SISSA
Scuola
Internazionale
Superiore di
Studi Avanzati

Physics Area - PhD course in
Theory and Numerical Simulation of Condensed Matter

Ab initio thermoelasticity of crystals at extremes

Candidate:
Xuejun GONG

Advisor:
Prof. Dr. Andrea Dal Corso

Academic Year 2020-2024

Contents

1 Introduction **20**

2 Theoretical approach **23**

2.1 Dynamical theory of crystal lattices 23
2.1.1 Atoms in crystal 23
2.1.2 Equations of motion 24
2.1.3 The phonons 25
2.2 Density functional pertubation theory (DFPT) 26
2.2.1 Adiabatic approximation 26
2.2.2 Density functional theory (DFT) 26
2.2.3 Hellmann-Feynman theorem and second derivatives of the energy . . 26
2.2.4 Self-consistent linear system 28
2.2.5 Dynamical matrix at finite $\mathbf{q}$ 28
2.2.6 Bloch theorem 30
2.2.7 Charge density response at finite $\mathbf{q}$ 31
2.2.8 First-order derivative of the wavefunctions 32
2.2.9 Linear response 32
2.3 Pseudopotentials 34
2.3.1 Plane waves in periodic solids 34
2.3.2 Spherical symmetry 35
2.3.3 Norm-conserving pseudopotentials 36
2.3.4 The logarithmic derivative 37
2.3.5 Pseudopotential in the solid 37
2.3.6 Transferability tests 38
2.3.7 Fully separable pseudopotentials 38
2.3.8 Ultrasoft pseudopotentials 39
2.3.9 PAW mapping: from pseudo-wave-functions to all-electron wave-functions 40
2.3.10 PAW Hamiltonian 40
2.4 Ab initio statistical thermodynamics 42
2.4.1 The canonical partition function 42
2.4.2 The thermodynamic functions 43
2.4.3 Volume as a function of temperature 45
2.4.4 Free energy minimization 45

2.4.5 Volume thermal expansion . . . 46
2.4.6 Isobaric heat capacity and isoentropic bulk modulus . . . 47
2.4.7 Thermal equation of state . . . 49
2.4.8 Finite temperature electronic excitation energy . . . 49
2.4.9 Strain and stress . . . 50
2.4.10 Uniform pressure . . . 51
2.4.11 Equation of state . . . 51
2.4.12 Crystal parameters as functions of the temperature and thermal expansion . . . 52
2.4.13 Isothermal elastic constants and compliances . . . 53
2.4.14 Thermal expansion from Grüneisen parameters . . . 53
2.4.15 Constant stress heat capacity . . . 54
2.4.16 Adiabatic elastic compliances . . . 54
2.4.17 Adiabatic elastic constants . . . 55
2.4.18 Polycrystalline averages . . . 56
2.4.19 Sound velocities . . . 57

3 Tungsten **58**
3.1 Computational parameters . . . 60
3.2 Results and discussion . . . 62

4 Molybdenum **70**
4.1 Computational parameters . . . 71
4.2 Results and discussion . . . 73

5 Tantalum **79**
5.1 Computational details . . . 80
5.2 Results and discussion . . . 81

6 Beryllium **91**
6.1 Thermodynamics and elastic constants . . . 92
6.1.1 HCP internal relaxations . . . 95
6.1.2 Elastic constants computation beyond ZSISA . . . 97
6.2 Computational details . . . 97
6.3 Results and discussion . . . 99

7 An alternative GPU acceleration for a pseudopotential plane-waves density functional theory code with applications to metallic systems **105**
7.1 Theory . . . 107
7.1.1 Davidson algorithm . . . 107
7.1.2 Application of Hamiltonian . . . 109
7.1.3 Density functional perturbation theory . . . 111
7.1.4 Preconditioned conjugate gradient . . . 112

7.2 GPU optimization . . . 113
7.3 Fast Fourier transform . . . 117
7.3.1 FFT on the device . . . 119
7.4 Matrix Diagonalization . . . 119
7.5 Results . . . 120
7.5.1 Benchmark Example . . . 120
7.5.2 FFT . . . 121
7.5.3 Diagonalization . . . 121
7.5.4 Application of the Hamiltonian and of S . . . 122
7.5.5 Total time . . . 123

8 Conclusions **125**
8.1 Tungsten . . . 125
8.2 Molybdenum . . . 126
8.3 Tantalum . . . 127
8.4 Beryllium . . . 127
8.5 GPU . . . 128

Appendices **130**

A Tungsten **131**
A.1 Phonon dispersions . . . 132
A.2 Equation of state . . . 132
A.3 Thermal expansion . . . 134
A.4 Isobaric heat capacity . . . 136
A.5 Bulk modulus . . . 137
A.6 Gruneisen parameter . . . 138
A.7 Elastic moduli and sound velocities . . . 139

B Molybdenum **145**
B.1 Phonon dispersion . . . 145
B.2 Thermal equation of state . . . 145
B.3 Thermal expansion . . . 146
B.4 Heat capacity . . . 148
B.5 Bulk modulus . . . 149
B.6 Grüneisen parameter . . . 150
B.7 Numerical issues . . . 151

C Beryllium **157**
C.1 Thermodynamic properties . . . 157

D GPU and CUDA Fortran **165**

Abstract

This thesis presents the study of the second-order elastic constants (ECs) of body centered cubic (BCC) refractory metals tungsten and molybdenum, and of the hexagonal close-packed (HCP) beryllium at extreme conditions (high temperature and high pressure), using density functional perturbation theory (DFPT) within the quasi-harmonic approximation (QHA). Some preliminary results are also presented for tantalum.

Moreover, we present the thermodynamic properties including the equation of states (EOS), phonon dispersion, thermal expansion (TE), bulk modulus, heat capacity and average Grüneisen parameter which are calculated by density functional theory (DFT) implemented in `Quantum ESPRESSO`. We find a reasonable agreement with available experiments with some exceptions discussed in the thesis. In general, the temperature dependent QHA ECs show a better description compared with quasi static approximation (QSA) ECs. The latest experimental sound velocity measurements on tungsten support our findings.

For beryllium, the accuracies of various approximations on crystal structure (zero static internal stress approximation (ZSISA) and volume-constrained zero static internal stress approximation (V-ZSISA)), or on elastic constants (QHA versus QSA) which are widely applied in ab initio thermodynamic calculations are quantified in detail. A numerical approach is given to compute the ECs in presence of internal relaxations when the free energy is minimized with respect to the strain.

An alternative `GPU` acceleration for plane waves pseudopotentials electronic structure codes designed for systems that have small unit cells but require a large number of **k** points to sample the Brillouin zone, such as metals, is presented.

All phonon calculations in the thesis have benefited from this implementation in `thermo_pw`. As a side product of this work, the PAW pseudo potentials of tungsten have been updated in `pslibrary`.

List of publications

This thesis resulted in the following publications:

- Xuejun Gong and Andrea Dal Corso. Pressure and temperature dependent ab initio quasiharmonic thermoelastic properties of tungsten. Journal of Physics: Condensed Matter, 36(28):285702, 2024. (Chapter 3)
- Xuejun Gong and Andrea Dal Corso. Ab initio quasiharmonic thermoelasticity of molybdenum at high temperature and pressure. The Journal of Chemical Physics, 160(24):244703, 2024. (Chapter 4)
- Xuejun Gong and Andrea Dal Corso. Ab initio quasiharmonic thermoelasticity of tantalum: A high pressure and high temperature study. In preparation. (Chapter 5)
- Xuejun Gong and Andrea Dal Corso. High temperature and high pressure thermoelasticity of hcp metals from ab initio quasiharmonic free energy calculations: The beryllium case. Physical Review B, 110(9):094109, 2024. (Chapter 6)
- Xuejun Gong and Andrea Dal Corso. An alternative GPU acceleration for a pseudopotential plane-waves density functional theory code with applica- tions to metallic systems. Computer Physics Communications, 308:109439, 2025. (Chapter 7)

Abbreviations and Symbols

abbreviation	meaning
DFT	Density Functional Theory
DFPT	Density Functional Perturbation Theory
ECs	Elastic Constants
TDECs	Temperature Dependent Elastic Constants
LDA	Local Density Approximation
GGA	Generalized Gradient Approximation
PBE	Perdew-Burke-Ernzerhof GGA
PBEsol	Revised Perdew-Burke-Ernzerhof GGA for Solids
PAW	Projector Augmented Wave
QHA	Quasi Harmonic Approximation
QSA	Quasi Static Approximation
TE	Thermal Expansion
EOS	Equation of State
ZSISA	Zero Static Internal Stress Approximation
V-ZSISA	Volume-Constrained Zero Static Internal Stress Approximation
FFEM	Full Free Energy Minimization
CPU	Central Processing Unit
GPU	Graphics Processing Unit
MD	Molecular Dynamics
ZPE	Zero-Point Energy
FCC	Face Centered Cubic
BCC	Body Centered Cubic
HCP	Hexagonal Close-Packed
QE	Quantum ESPRESSO
DOS	Density of States
PBCs	Periodic Boundary Conditions
KSDFT	Kohn-Sham DFT
PWs	Plane Waves
BZ	Brillouin Zone
PPs	PseudoPotentials

symbol	meaning
a_0	Lattice Constants
F	Free Energy
U	Internal Energy
T	Temperature
S	Entropy
H	Enthalpy
T_D	Debye Temperature
Ω	Volume of A Cell
C_v	Constant Volume Heat Capacity
C_p	Isobaric Heat Capacity
B_T	Isothermal Bulk Modulus
B_s	Adiabatic Bulk Modulus
β	Thermal Expansion
γ	Grüneisen Parameter
σ	Stress
ϵ	Strain
C	Elastic Constants
B	Bulk Modulus
E	Young's Modulus
G	Shear Modulus
V_P	Compressional Sound Velocity
V_S	Shear Sound Velocity
$\because$	Because
$\therefore$	Therefore

List of Figures

2.1 Equilibrium properties in a crystal: Beckmann diagram. (Based on figures seen in Ref.[144] and Ref.[104]) 43
2.2 The forces on the faces of a unit cube in a homogeneously stressed body. [1] 51

3.1 Upper: Pressure dependent PBEsol (dashed lines) and PBE (solid lines) density calculated for several temperatures (red 298 K, green 473 K, blue 673 K, yellow 873 K, and pink 1073 K) compared with the experimental data of Qi et al. [158]. Lower: The PBE density is shown after a shift of $\Delta\rho = 0.475$ g/cm^3 (indicated by the red arrow on the line at 298 K) to facilitate the comparison with experiment. The dashed lines are the PBEsol curves after a shift of -0.06 g/cm^3 also shown by a red arrow. 61
3.2 Pressure dependent ECs calculated at 0 K obtained from the second derivatives of the energy with respect to strain for the N_V geometries used for the quasi-harmonic approximation. ECs are calculated within LDA (red line), PBEsol (green line), and PBE (blue line). The red circles are the PBE data of Ref.[101]. 62
3.3 PBEsol (green lines) and PBE (blue lines) temperature dependent isothermal (dashed) and adiabatic (solid) elastic constants calculated within the quasi-harmonic approximation at zero pressure. The gold and red circles indicate the adiabatic experimental data of Ref.[20] and of Ref.[115], respectively. For C_{44} isothermal and adiabatic ECs coincide. 63
3.4 PBEsol (green lines) and PBE (blue lines) temperature dependent isothermal (dashed) and adiabatic (solid) polycrystalline averages of the macroscopic elastic properties (bulk modulus B, Young's modulus E, and shear modulus G) calculated within the quasi-harmonic approximation at zero pressure. The red circles are the adiabatic data of Ref.[115]. In the inset we compare the isothermal and adiabatic Poisson's ratio with experiment. 64

3.5 Temperature dependent longitudinal modulus calculated within the quasi-harmonic approximation as a function of pressure for several temperatures (red 298 K, green 473 K, blue 673 K, yellow 873 K, and pink 1073 K). The circles (with the same color code) are the data of Ref.[158], measured at the same temperatures and calculated as $L = B_S + 4/3G_S$ from the B_S and G_S in their Table III. To facilitate the comparison with experiment, theoretical lines translated by 437 kbar, as indicated by the red arrows, are also shown. PBEsol results are shown with dashed lines after a shift of 128 kbar. 65
3.6 Temperature dependent PBE shear modulus calculated within the quasi-harmonic approximation as a function of pressure for several temperatures (red 298 K, green 473 K, blue 673 K, yellow 873 K, and pink 1073 K). The circles (with the same color code) are the data of Ref.[158], measured at the same temperatures (from their Table III). To facilitate the comparison with experiment, theoretical lines translated by 204 kbar, as indicated by the red arrows, are also shown. The PBEsol results are shown with dashed lines after a shift of 122 kbar. 66
3.7 Temperature dependent compressional sound velocity (V_P) calculated within the quasi-harmonic approximation as a function of pressure for several temperatures (red 298 K, green 473 K, blue 673 K, yellow 873 K, and pink 1073 K). The circles (with the same color code) are the data of Ref.[158], measured at the same temperatures. To facilitate the comparison with experiment, theoretical lines translated by 146 m/s, as indicated by the red arrows, are also shown. PBEsol results are shown by dashed lines after a shift of 65 m/s. . . 67
3.8 Temperature dependent shear sound velocity (V_G) calculated within the quasi-harmonic approximation as a function of pressure for several temperatures (red 298 K, green 473 K, blue 673 K, yellow 873 K, and pink 1073 K). The circles (with the same color code) are the data of Ref.[158], measured at the same temperatures. To facilitate the comparison with experiment, theoretical lines translated by 149 m/s, as indicated by the red arrows, are also shown. PBEsol results are shown by dashed lines after a shift of 113 m/s. 68

4.1 Elastic constants as a function of pressure calculated within LDA (red lines), PBEsol (green lines) and PBE (blue lines) compared with the PBE results of Ref. [101]. 74
4.2 Quasi-harmonic isothermal (dashed lines) and adiabatic (solid line) elastic constants C_{11}, C_{12} and C_{44} as a function of temperature compared with experimental adiabatic data from Ref. [54] (yellow circles), Ref. [47] (green circles), Ref.[20] (blue circles), and Ref.[21] (red circles). 75
4.3 Quasi-static isothermal (dashed lines) and adiabatic (solid line) elastic constants C_{11}, C_{12}, and C_{44} as a function of temperature compared with adiabatic experimental data from Ref. [54] (gold circles), Ref. [47] (green circles), Ref.[20] (blue circles), and Ref.[21] (red circles). 76

4.4 Adiabatic bulk and shear modulus of polycrystalline molybdenum against pressure computed at 5 K (red line), 300 K (green line), 1000 K (blue line), 1500 K (yellow line), and 2000 K (pink line), compared with room temperature experimental values of Ref. [112] (red circles). 77
4.5 Compressional and shear sound velocities of polycrystalline molybdenum against pressure at 5 K (red line), 300 K (green line), 1000 K (blue line), 1500 K (yellow line), and 2000 K (pink line), compared with room temperature experimental values of Ref. [112] (red circles). 78

5.1 $T = 0$ K elastic constants C_{11}, C_{12} and C_{44} as a function of pressure calculated within PBE compared with experiment [58] (orange squares). As a reference we report also previous calculations the PBE results of Ref. [101] (blue diamond), Ref. [159] (red circles), Ref. [87] (yellow triangles), Ref. [175] (cyan squares) 83
5.2 Comparison of the PBE adiabatic QSA elastic constants C_{11}, C_{12}, and C_{44} (continuous blue line) as a function of temperature with experiments from Ref. [54] (red dots), Ref. [189] (yellow dots), Ref. [108] (light blue diamonds) and Ref. [176] (cyan dots). Dashed lines indicate the isothermal elastic constants. Dotted red line is the PBE QSA calculation of Ref. [193]. 84
5.3 Comparison of the PBE adiabatic QHA elastic constants C_{11}, C_{12}, and C_{44} (continuous blue line) as a function of temperature with experiments from Ref. [54] (red dots), Ref. [189] (yellow dots), Ref. [108] (light blue diamonds) and Ref. [176] (cyan dots). Dashed lines indicate the isothermal elastic constants. 85
5.4 Comparison of the PBE QSA (dashed blue line) and QHA (solid blue line) elastic constants C_{11}, C_{12} and C_{44} as a function of temperature. The experiments are from Ref. [54] (red dots), Ref. [189] (yellow dots), Ref. [108] (light blue diamonds) and Ref. [176] (cyan dots). Green dots are the PBE results of Ref. [73]. The dashed orange line is the calculation of Ref. [146]. 86
5.5 PBE adiabatic QSA (dashed line) and QHA (continuous line) combination of elastic constants $C = 0.5(C_{11} + C_{12} + 2C_{44})$ as a function of temperature after subtracting the $T = 0$ K value. The function is compared with experiments from Ref. [54] (red dots), Ref. [189] (yellow dots), Ref. [108] (light blue diamonds) and Ref. [176] (cyan dots). 87
5.6 PBE adiabatic QSA (dashed line) and QHA (continuous line) combination of elastic constants $C' = 0.5(C_{11} - C_{12})$ as a function of temperature after subtracting the $T = 0$ K value. The function is compared with experiments from Ref. [54] (red dots), Ref. [189] (yellow dots), Ref. [108] (light blue diamonds) and Ref. [176] (cyan dots). The QSA results of Ref. [95] are also shown (green dots) 88

5.7 PBE adiabatic QSA (dashed line) and QHA (continuous line) C_{44} elastic constant as a function of temperature after subtracting the $T = 0$ K value. Theory is compared with experiments from Ref. [54] (red dots), Ref. [189] (yellow dots), Ref. [108] (light blue diamonds) and Ref. [176] (cyan dots). The QSA results of Ref. [95] are also shown (green dots). The orange dashed line show the results of Ref. [146]. 89
5.8 QHA adiabatic elastic constants C_{11}, C_{12}, and C_{44} as a function of pressure calculated within PBE at 5 K (red line), 300 K (green line), 1000 K (blue line), and 1500 K (yellow line). 90

6.1 Contours of constant total energy (red lines) plotted in the plane a and c/a. The two blue dashed straight lines intersect at the position of the energy minimum. The orange curve is the "stress-pressure" isotherm at 0 K. The light-blue curve is the "stress-pressure" isotherm at 1500 K. The three green lines show the isobars at 0 kbar, 500 kbar, and 1000 kbar for temperatures going from 0 K to 1500 K. Points on the orange curve shows the values of a and c/a in which we have computed the quasi-harmonic TDECs. The 0 K ECs as well as the phonon dispersions have been calculated in these points and also in all the points of the two dimensional grid shown with dotted lines. 93
6.2 Stress-strain elastic constants of Be as a function of pressure at 0 K (continous lines) compared with previous calculations of Ref. [172] (diamonds), Ref. [77] (circles), and Ref. [116] (triangles). The dashed lines show C_{11} and C_{12} obtained by keeping the ions fixed at the uniformly strained positions. . 96
6.3 Adiabatic LDA elastic constants of Be as a function of temperature calculated within the QSA (red lines) along the 0 kbar isobar (with ZSISA atomic positions). For comparison we have reported also the QSA elastic constants interpolated (within V-ZSISA) only on the "stress-pressure" isotherm at 0 K (dashed blue lines). The dots are the experimental points of Ref. [165] (yellow dots) and [173] (green dots). Diamond are the theoretical PBE QSA calculation of Ref. [103]. 99
6.4 Elastic constants C_{11} and C_{12} of Be as a function of temperature calculated as second derivatives of the free energy (within the QHA) at fixed equilibrium geometry. We compare the results obtained with the ZSISA (red lines) and within the FFEM (green lines), a scheme in which the internal y parameter is relaxed at each strain and temperature by minimizing the free energy. . . . 100
6.5 Adiabatic elastic constants of Be as a function of temperature (red lines) calculated within the QHA. Atomic relaxations have been dealt with the ZSISA approximation. Calculations have been done only along the "stress-pressure" 0 K isotherm (V-ZSISA). The dots are the experimental points of Ref. [165] (yellow dots) and [173] (green dots). The diamond are the theoretical QHA results of Ref. [171] while the pink dots are the isothermal QHA elastic constants calculated in Ref. [161]. The isothermal elastic constants are also shown (blue dashed lines). 101

6.6 Temperature dependent elastic constants of Be as a function of temperature calculated within the V-ZSISA QHA (red lines) are compared with the V-ZSISA QSA (blue dashed lines). The dots are the experimental points of Ref. [165] (yellow dots) and [173] (green dots). 102
6.7 Adiabatic pressure dependent elastic constants of Be calculated within the V-ZSISA QHA at three temperatures: 4 K (red line), 500 K (green lines) 1000 K (blue lines). Calculations have been done along the "stress-pressure" isotherm. 103

7.1 Algorithms used in the standard approach and in our optimized `GPU` approach for the diagonalization of the Hamiltonian. 113
7.2 Flowchart of the routine that applies $H^{\mathbf{k}}_{KS}$ and $S^{\mathbf{k}}$ to the wavefunctions. Close to each routine we write the number of threads that are used to run it on the `GPU`. 114
7.3 Algorithms used in the standard phonon code and in our optimized `GPU` approach for solving the linear system that gives the perturbed wavefunctions. 116

A.1 Phonon dispersions interpolated at the 295 K lattice constant. The LDA (red curves), PBEsol (green curve), and PBE (blue curve) results are compared with the experimental inelastic neutron scattering data measured at 295 K (Refs. [105, 28, 29]). 131
A.2 V as a function of p at 300 K obtained by LDA (red), PBEsol (green), and PBE (blue) is compared with experiments (orange circles, [44] green circles, [110] and yellow triangles [51]) and previous calculations (blue diamonds (PBE) from Ref. [196], blue squares (LDA) from Ref. [166], and red squares (PBE) from Ref. [192]). In the inset the same curves at 3000 K are compared with the predictions of Refs. [48] (blue diamonds) and [110] (red circles). 132
A.3 V/V_0 as a function of p at 300 K obtained by LDA (red), PBEsol (green), and PBE (blue) is compared with experiments (orange circles, [44] green circles, [110] and yellow triangles [51]) and previous calculations (blue diamonds (PBE) from Ref. [196], and blue squares (LDA) from Ref. [166], and red squares (PBE) from Ref. [192]). In the inset the same curves at 3000 K are compared with the predictions of Refs. [48] (blue diamonds) and [110] (red circles). 133
A.4 Temperature dependent volumetric thermal expansion calculated by LDA (red curve), PBEsol (green curve), and PBE (blue curve) compared with the experimental data reported in Ref. [136] (red triangles), Ref. [170] (reversed yellow triangles), Ref. [131] (gold circles), Ref. [19] (magenta circles), Ref. [123] (cyan squares), and Ref. [185] (blue diamond). The thinner lines at the bottom indicate the differences between the thermal expansion calculated including or neglecting the electronic excitations term in the free energy. 134

A.5 Temperature dependent volumetric thermal expansion computed within the LDA (red line), PBEsol (green line), and PBE (blue line). The different curves (from top to bottom) correspond to pressures from 0 kbar to 3000 kbar in steps $\Delta p = 1000$ kbar. Theory is compared with the models of Refs. [48] (blue diamonds) and [110] (red circles). 135
A.6 LDA (red line), PBEsol (green line), and PBE (blue line) temperature dependent isobaric heat capacity compared with experiment from Ref. [194] (red triangles), Ref. [10] (gold circles), Ref. [27] (magenta circles), Ref. [11] (cyan diamonds). Thin lines at the bottom (with the same color conventions) indicate the contribution of electronic excitations to the heat capacity. 136
A.7 LDA (red line), PBEsol (green line), and PBE (blue line) temperature dependent isobaric heat capacity. From top to bottom the curves correspond to pressures from 0 kbar to 3000 kbar in steps $\Delta p = 1000$ kbar. DFT calculations are compared with the models of Refs. [48] (blue diamonds) and [110] (red circles). The green lines at the bottom are the PBEsol electronic contribution to C_V at the four pressures (from top to bottom) shifted by 15 J/(K · mol). 137
A.8 Temperature dependent adiabatic and isothermal bulk moduli calculated within LDA (red line), PBEsol (green line), and PBE (blue line) compared with the experimental adiabatic data of Ref. [16] (filled cyan squares), Ref. [54] (empty gold triangles), and Ref. [115] (empty magenta cycles). For each functional the higher curve is the adiabatic bulk modulus. 138
A.9 Temperature dependent adiabatic bulk modulus calculated within the LDA (red lines), PBEsol (green lines), and PBE (blue lines). From bottom to top the curves correspond to pressures from 0 kbar to 3000 kbar in steps $\Delta p = 1000$ kbar. DFT calculations are compared with the model predictions of Ref. [110] (red circles) and of Ref. [48] (blue diamonds). 139
A.10 Temperature dependent average Grüneisen parameter calculated within the LDA (red line below the green line), PBEsol (green line) and PBE (blue line). From top to bottom the curves correspond to pressures from 0 kbar to 3000 kbar in steps $\Delta p = 1000$ kbar. DFT calculations are compared with the model predictions of Refs. [48] (blue diamonds) and [110] (red circles). 140
A.11 Temperature dependent PBEsol (dashed lines) and PBE (solid lines) longitudinal modulus calculated within the quasi-harmonic approximation as a function of pressure for several temperatures (red 298 K, green 473 K, blue 673 K, yellow 873 K, and pink 1073 K). The circles (with the same color code) are the data of Ref.[158], measured at the same temperatures and calculated as $L = B_S + 4/3G_S$ from the B_S and G_S in their Table III. 141
A.12 Temperature dependent PBEsol (dashed lines) and PBE (solid lines) shear modulus calculated within the quasi-harmonic approximation as a function of pressure for several temperatures (red 298 K, green 473 K, blue 673 K, yellow 873 K, and pink 1073 K). The circles (with the same color code) are the data of Ref.[158], measured at the same temperatures (from their Table III). . . . 142

A.13 Temperature dependent PBEsol (dashed lines) and PBE (solid lines) compressional sound velocity (V_P) calculated within the quasi-harmonic approximation as a function of pressure for several temperatures (red 298 K, green 473 K, blue 673 K, yellow 873 K, and pink 1073 K). The circles (with the same color code) are the data of Ref.[158], measured at the same temperatures. 143
A.14 Temperature dependent PBEsol (dashed lines) and PBE (solid lines) shear sound velocity (V_G) calculated within the quasi-harmonic approximation as a function of pressure for several temperatures (red 298 K, green 473 K, blue 673 K, yellow 873 K, and pink 1073 K). The circles (with the same color code) are the data of Ref.[158], measured at the same temperatures. 144

B.1 Phonon dispersions interpolated at the 295 K lattice constant. The LDA (red curves), PBEsol (green curve), and PBE (blue curve) results are compared with the experimental inelastic neutron scattering data measured at 295 K (Ref. [155] blue diamonds and Ref.[197] green circles). 146
B.2 V as a function of p at 300 K obtained by LDA (red), PBEsol (green), and PBE (blue) compared with experiment (blue circles [79], cyan circles, [109] red triangles, [201] and green diamonds [45]) and previous calculations (red squares (PBE) from Ref. [192]). In the inset the same curves at 2000 K compared with the predictions of Ref. [109] (red circles) and of Ref. [49] (blue diamonds). 147
B.3 V/V_0 as a function of p at 300 K obtained by LDA (red), PBEsol (green), and PBE (blue) compared with experiment (blue circles [79], cyan circles, [109] red triangles, [201] and green diamonds [45]) and previous PBE calculations (red [192] squares). In the inset the same curves at 2000 K compared with the predictions of Ref. [109] (red circles) and of Ref. [49] (blue diamonds). . 148
B.4 Temperature dependent thermal expansion calculated by LDA (red curve), PBEsol (green curve), and PBE (blue curve) compared with the experimental data reported in Ref. [136] (cyan triangles) Ref. [97] (green circles), Ref. [130] (blue diamonds), Ref. [18] (red triangles). The thinner lines at the bottom indicate the differences between the thermal expansion calculated including or neglecting the electronic excitations term in the free energy. Pink dashed line on the PBE curve shows the result obtained with 8 geometries and $\Delta a = 0.02$ a.u. 149
B.5 Temperature dependent thermal expansion computed within the LDA (red line), PBEsol (green line), and PBE (blue line). The different curves (from top to bottom) correspond to pressures from 0 kbar to 3000 kbar in steps $\Delta p = 1000$ kbar. Theory is compared with the models of Ref. [109] (red circles) and of Ref. [177] (blue diamonds) and with the ab-initio PBE calculations of Ref. [198] (green triangles). 150

B.6 LDA (red line), PBEsol (green line), and PBE (blue line) temperature dependent isobaric heat capacity compared with experiment from Ref. [97] (green circles), Ref. [72] (red diamonds) and Ref. [18] (blue triangles). Thin lines at the bottom (with the same color conventions) indicate the contribution of electronic themal excitations to the heat capacity. Pink dashed line on the PBE curve shows the result obtained with 8 geometries and $\Delta a = 0.02$ a.u. . 151
B.7 LDA (red line), PBEsol (green line), and PBE (blue line) temperature dependent isobaric heat capacity. From top to bottom the curves correspond to pressures from 0 kbar to 3000 kbar in steps $\Delta p = 1000$ kbar. DFT calculations are compared with the model of Ref. [109] (red circles) and of Ref. [49] (blue diamond). The green lines at the bottom are the PBEsol electronic contribution to C_V at the four pressures (from top to bottom) shifted by 15 J/(K · mol). 152
B.8 Temperature dependent adiabatic and isothermal bulk moduli calculated within LDA (red line), PBEsol (green line), and PBE (blue line) compared with the experimental adiabatic data of Ref. [47] (blue triangles), Ref. [20] (green circles) and Ref. [21] (red diamonds). For each functional the higher curve is the adiabatic bulk modulus. 153
B.9 Temperature dependent adiabatic bulk modulus calculated within the LDA (red lines), PBEsol (green lines), and PBE (blue lines). From bottom to top the curves correspond to pressures from 0 kbar to 3000 kbar in steps $\Delta p = 1000$ kbar. DFT calculations are compared with the model predictions of Ref. [109] (red circles) and of Ref. [177] (blue diamond). 154
B.10 Temperature dependent average Grüneisen parameter calculated within the LDA (red line below the green line), PBEsol (green line) and PBE (blue line). From top to bottom the curves correspond to pressures from 0 kbar to 3000 kbar in steps $\Delta p = 1000$ kbar. DFT calculations are compared with the model predictions of Ref. [109] (red circles) and of Ref. [49] (blue diamond) and with the ab-initio PBE calculations of Ref. [198] (green triangles). 155
B.11 Value of the $T = 0$ K elastic constants calculated with different values of the strain interval for each strain type. 156

C.1 Equation of state calculated with our parameters at 4 K (red line) and 1500 K (green line) compared with experimental data of Ref. [52] (red points), Ref. [134] (blue diamond), and Ref. [106] (yellow triangles). The "stress-pressure" 0 K isotherm is shown with a dashed orange line. 159
C.2 c/a ratio as a function of pressure at 0 K (red line) compared with experimental data of Ref. [195] (red points) and of Ref. [134] (blue diamond) and with the theoretical calculations of Ref. [162] (blue squares) and Ref.[178] (yellow triangles). 160

C.3 Thermal expansion tensor of beryllium (red α_{xx} and green α_{zz} lines) calculated in the present work compared with the experimental data of Ref. [69]. The volume thermal expansion $\beta = 2\alpha_{xx} + \alpha_{zz}$ is also shown (blue line) and compared with the one calculated using only the 11 geometries along the "stress-pressure" 0 K isotherm (dashed orange line). 161
C.4 Isobaric heat capacity per cell (green line) compared with the experimental data in Ref. [81] (red diamond) and with the values recommended Ref. [18] from a critical evaluation of the experimental data (yellow circles). 162
C.5 Isothermal (dashed lines) and adiabatic (continuos lines) bulk modulus as a function of temperature calculated from the equation of state (red lines) by fitting the free energy along the "stress-pressure" 0 K isotherm with a fourth-order Birch-Murnaghan equation. The green (blue) lines are the bulk modulus obtained from the interpolation of the QHA elastic constants in 5 (8) geometries. The red squares (orange line) indicate the PBE isothermal (adiabatic) bulk modulus predicted in Ref. [162] The green dots is the bulk modulus predicted by Ref. [103]. The green (yellow) diamonds are the experimental values of Refs. [173] (Ref. [165]). The two dashed olive lines show the region where recent experimental values of the bulk modulus of polycristalline beryllium have been found. [133] 163
C.6 The flowchart of elastic constants calculations of hcp metals in `thermo_pw`. "SCF" and "Ph" on the left side of the bar represent doing a self-consistent field (SCF) calculation of DFT energy and/or phonon calculations at the corresponding structures. 164

List of Tables

3.1 The equilibrium lattice constants (a_0), the bulk moduli (B_T) and the pressure derivatives of the bulk moduli (B'_T) of tungsten calculated in this work compared with selected previous calculations and with experiment. 59

3.2 The 0 K elastic constants calculated with the different functionals compared with experiment and selected previous calculations. B, E, G, and ν are the bulk modulus, the Young's modulus, the shear modulus, and the Poisson's ratio, respectively. 60

4.1 The equilibrium lattice constants (a_0), the bulk moduli (B_T) and the pressure derivatives of the bulk moduli (B'_T) of molybdenum calculated in this work compared with previous calculations and with experiment. 72

4.2 The 0 K elastic constants calculated with the different functionals compared with experiment and one previous calculation. B, E, G, and ν are the bulk modulus, the Young's modulus, the shear modulus, and the Poisson's ratio, respectively. 73

5.1 The equilibrium lattice constants (a_0), the bulk moduli (B_T) and the pressure derivatives of the bulk moduli (B'_T) of tantalum calculated in this work compared with previous calculations and with experiment (in experiment B_S is measured at 300 K. At 0 K B_S and B_T have the same value). 81

5.2 The 0 K elastic constants calculated with the different functionals compared with experiment and one previous calculation. B, E, G, and ν are the bulk modulus, the Young's modulus, the shear modulus, and the Poisson's ratio, respectively. 82

6.1 The 0 K elastic constants compared with experiment and previous calculations. B, E, G, and ν are the bulk modulus, the Young's modulus, the shear modulus, and the Poisson's ratio, of polycrystalline beryllium calculated within the Voigt-Reuss-Hill approximation, respectively. 98

7.1 Comparison of the time spent by computing the FFT and the inverse `FFT` when applying the Hamiltonian operator in the Davidson algorithm and in the conjugate gradient algorithm for the example described in the paper. . . 121

7.2 Comparison of the time spent to diagonalize the reduced Hamiltonian using linear algebra routines (within the Davidson algorithm). 122
7.3 Comparison of the total time spent to apply H_{KS} and S to the wave-functions in the Davidson algorithm and in the conjugate gradient algorithm. 122
7.4 Total time spent in the standard `CPU` calculations. The number of `CPUs`, `GPUs`, `tasks`, and `pools` are also indicated. The number of core-hours is obtained multiplying the total time by the number of cores. 123
7.5 Total time spent in the standard `GPU` calculations. This includes also the time passed on the part of the code that are not GPU accelerated or are not GPU optimized. The number of `CPUs`, `GPUs`, `tasks`, and `pools` are equal. 124
7.6 Total time spent in the optimized `GPU` calculations. This includes also the time passed on the part of the code that are not GPU accelerated or are not GPU optimized. The number of `CPUs`, `GPUs`, `tasks`, and `pools` are equal. . . 124

C.1 The "stress-pressure" 0 K isotherm. In the configurations with * we have computed the QHA TDECs. For all other values of pressure we have interpolated them. 158

Chapter 1

Introduction

The theory for equilibrium thermodynamics of periodic crystals is an essential component of condensed matter physics. The crystal is viewed as a collection of ions and electrons, which is then studied via quantum mechanics and statistical mechanics to describe the observable physical quantities. Elastic constants (ECs) are an important quantity among these.

The ECs are theoretically defined as multiple strain derivatives of the state functions, and quantify the degree of deformation and stability of the crystal to an external stress. In particular, second-order ECs C_{ijkl} are a fourth-rank tensor which quantifies the stress-strain relation as a linear response in an elastic medium. From ECs and mass density, the velocity of sound waves is derived and widely used in seismology to detect the chemical composition in the internal structures of the Earth. Furthermore, ECs are key physical quantities for the design of any engineering application of materials. With the development of modern technology in high pressure physics, for many common pure elements ECs have been measured extensively at room temperature, for instance by ultrasound techniques. So do the pressure-dependent ECs. However the experimental information is still scarce at both high temperature and high pressure conditions.

In this thesis the ECs are calculated from the second derivatives of the energy with respect to strain at $T = 0$ K or from the second derivatives of the free energy at finite temperature. The Helmholtz free energy is expressed as $F = U - TS$, where U is the internal energy of the system and S is the entropy. The Helmholtz free energy contains the contributions from the vibrations of ions in solids. Therefore, lattice dynamics of strained crystal structures should be considered carefully.

Lattice dynamical calculations in a periodic system, using density functional perturbation theory (DFPT), within the quasi-harmonic approximation (QHA), are among the most popular choices to simulate thermodynamic properties of crystals.[12] In the temperature range far from the melting point, the Helmholtz free energy is written as the sum of electronic and vibrational terms within the adiabatic approximation. The electronic contributions at $T = 0$ K is given by density functional theory (DFT) and electronic excitations can be computed within the rigid bands approximation from the electronic density of states (DOS). The vibrational energy can be derived from the phonon spectra. Two advantages of DFPT, as compared to other nonperturbative methods for calculating the vibrational properties of

crystalline solids (such as the frozen phonon method or molecular dynamics spectral analysis method) are the responses to perturbations of different wavelengths are decoupled, and the response to a phonon at any wavelength is calculated in an unperturbed cell. The drawback of this method is that it only accounts partially for anharmonicity, but it is still a good approximation at low temperature ($T < T_D$, where T_D is Debye temperature), where the quantum effects appear.

On the other side, molecular dynamics (MD) provides an efficient and economical tool to study the crystal structures and properties in the thermodynamic equilibrium at the atomic scale. It can be applied to the system in which the nuclear motion is classical. One can easily simulate the system at finite temperature and pressure with MD, but MD can not provide a complete description of the thermodynamic functions at low temperature ($T < T_D$) due to the neglect of quantum effects. Hence the two above methodologies are naturally complementary to each other.

Our QHA+DFPT approach are implemented in `thermo_pw`, which is a driver of `Quantum ESPRESSO` routines for the automatic computation of ab-initio material properties. In 2016 `thermo_pw` successfully handled elastic constants at $T = 0$ K [39]. In the next few years, this technique has been extended to QHA temperature dependent ECs (TDECs) calculations, particularly applied to face centered cubic (FCC) system (Al, Cu, Ag, Au, Pd, Pt)[118, 119, 121, 120], silicon and BAs [122]. It was possible to calculate the ECs both within the quasi static approximation (QSA) as the second derivatives of the total energy and within the QHA as second derivatives of the free energy.

Despite the above developments on TDECs calculations, there were still several unsolved challenges. Firstly, the investigation of pressure dependent ECs was missing. Secondly, a roadmap for TDECs of anisotropic solids was unclear in `thermo_pw`. For complex systems, a method beyond zero static internal stress approximation (ZSISA) was needed to verify its accuracy. In addition, the computation of TDECs for metals was computationally intensive and required to exploit the power of graphical processing unit (GPU) accelerators.

We address these problems in this thesis. Ab initio calculations are carried out on both temperature and pressure dependent ECs of the body centered cubic (BCC) metals tungsten and molybdenum. Some preliminary results are presented also for tantalum. We compare our results with experimental temperature and pressure dependent sound velocities and find a good agreement between them. Another development presented in chapter 6 is dealing with anisotropic solids: hexagonal close-packed (HCP) beryllium. HCP metal has two lattice parameters and internal relaxations when strained. We numerically reexamine the TDECs of beryllium focusing on the analysis of the effects of the common approximations made for studying the ECs of anisotropic solids: ZSISA and the constant volume ZSISA (V-ZSISA) approximation (also called the statically constrained quasi-harmonic approximation). The accuracies of ZSISA and of V-ZSISA that are widely applied in ab initio thermodynamic calculations are quantified. In particular, the effect of ZSISA on the calculation of C_{11} and C_{12} is compared with a numerical approach beyond ZSISA that minimizes the free energy with respect to the atomic positions at each strain. In beryllium, minor deviations are found within ZSISA, which gives elastic constants (ECs) in good agreement with the full free energy

minimization (FFEM). A substantial difference is found between the QHA and the QSA, with the former closer to experiments.

In the chapter 7, we discuss the DFPT for calculations on metallic systems on (GPU). We present an alternative `GPU` acceleration for plane waves pseudopotentials electronic structure codes designed for systems that have small unit cells but require a large number of $\mathbf{k}$ points to sample the Brillouin zone as happens, for instance, in metals. We discuss the diagonalization of the Kohn and Sham equations and the solution of the linear system derived in density functional perturbation theory. Both problems take advantage from a rewriting of the routine that applies the Hamiltonian to the Bloch wave-functions to work simultaneously (in parallel on the `GPU` threads) on the wave-functions with different wave-vectors $\mathbf{k}$, as many as allowed by the `GPU` memory. Our implementation is written in `CUDA Fortran` and makes extensive use of GPU kernel functions. We compare our method with the `CPUs` only calculation and with the approach currently implemented in `Quantum ESPRESSO` that uses `GPU` accelerated libraries for the FFT and for the linear algebra tasks such as the matrix-matrix multiplications as well as `OpenACC` directives for loop parallelization. We show in a realistic example that our method can give a significant improvement in the cases for which it has been designed.

‘

Chapter 2

Theoretical approach

2.1 Dynamical theory of crystal lattices

In this section we briefly review lattice dynamics from the perspective of electronic structure theory. Lattice dynamics studies the vibrations of atoms in a periodic crystal system. The oscillations of atoms, also known as phonons, play an important role not only in the theory of solids, but also in determining a large number of solid properties and corresponding applications, such as thermodynamic functions, thermal expansion, infrared absorption, thermal conductivity, superconductivity, phase transitions and so on.

Electronic structure calculations provide the forces acting on atoms, which can be used to calculate the dynamical matrix and obtain phonon dispersion relations. These relations describe how phonon frequencies vary with the wavevector and are essential for understanding thermodynamic properties.

The QHA is often used to study the temperature dependence of various material properties. QHA requires the calculation of phonon frequencies at different volumes. Thermal expansion, heat capacities, and temperature-dependent elastic constants can be predicted using this approach.

In summary, electronic structure theory provides a robust foundation for understanding and predicting lattice dynamics. The interplay between electrons and phonons, described through various theoretical and computational approaches, is key to unraveling the complex behaviors of materials.

2.1.1 Atoms in crystal

In the example of a periodic crystal, the equilibrium positions of atoms are conventionally expressed as:

$$\mathbf{R}_I = \mathbf{R}_\mu + \mathbf{d}_s \quad (s = 1, \ldots, N_{at}), \tag{2.1}$$

where $\mathbf{R}_\mu$ are the Bravais lattice vectors, and $\mathbf{d}_s$ are the positions of the atoms in a unit cell. N_{at} is the total number of atoms in a unit cell. N unit cells are taken into account with

Born-von Karman periodic boundary conditions. Ω is the volume of one cell. Therefore:

$$V = N\Omega \tag{2.2}$$

is the total volume of the solid. Atom I is vibrating from its equilibrium position and $\mathbf{u}_I(t)$ represents the displacement of the atom I at a certain time t. The total energy of the electron system calculated at fixed nuclei positions acts as the potential energy for the nuclei:

$$E_{tot}\left(\mathbf{R}_I + \mathbf{u}_I\right). \tag{2.3}$$

The electrons are assumed to be in the ground state for each nuclear configuration. When $|\mathbf{u}_I|$ is small enough, E_{tot} is expanded into a Taylor series with respect to $\mathbf{u}_I$ assuming all vibrations are simple harmonic oscillators:

$$E_{\text{tot}}\ \left(\mathbf{R}_I + \mathbf{u}_I\right) = E_{\text{tot}}\ \left(\mathbf{R}_I\right) + \sum_{I\alpha} \frac{\partial E_{\text{tot}}}{\partial \mathbf{u}_{I\alpha}} \mathbf{u}_{I\alpha} + \frac{1}{2} \sum_{I\alpha, J\beta} \frac{\partial^2 E_{\text{tot}}}{\partial \mathbf{u}_{I\alpha} \partial \mathbf{u}_{I\beta}} \mathbf{u}_{I\alpha} \mathbf{u}_{I\beta} + \ldots \tag{2.4}$$

where the derivatives are calculated at equilibrium ($\mathbf{u}_I = 0$). α and β are Cartesian coordinates in three-dimensional space.

2.1.2 Equations of motion

When atoms are at equilibrium positions $\frac{\partial E_{tot}}{\partial \mathbf{u}_{I\alpha}} = 0$, the Hamiltonian of this quantum system becomes:

$$H = \sum_{I\alpha} \frac{\mathbf{P}_{I\alpha}^2}{2M_I} + \frac{1}{2} \sum_{I\alpha, J\beta} \frac{\partial^2 E_{tot}}{\partial \mathbf{u}_{I\alpha} \partial \mathbf{u}_{J\beta}} \mathbf{u}_{I\alpha} \mathbf{u}_{J\beta}, \tag{2.5}$$

where $\mathbf{P}_I$ are the momenta of the nuclei and M_I their masses. The classical motion of the nuclei is given by the $N \times 3 \times N_{at}$ functions $\mathbf{u}_{I\alpha}(t)$. These functions are the solutions of the Hamilton equations:

$$\begin{aligned} \dot{\mathbf{u}}_{I\alpha} &= \frac{\partial H}{\partial \mathbf{P}_{I\alpha}}, \\ \dot{\mathbf{P}}_{I\alpha} &= -\frac{\partial H}{\partial \mathbf{u}_{I\alpha}}. \end{aligned} \tag{2.6}$$

With our Hamiltonian:

$$\begin{aligned} \dot{\mathbf{u}}_{I\alpha} &= \frac{\mathbf{P}_{I\alpha}}{M_I}, \\ \dot{\mathbf{P}}_{I\alpha} &= -\sum_{J\beta} \frac{\partial^2 E_{tot}}{\partial \mathbf{u}_{I\alpha} \partial \mathbf{u}_{J\beta}} \mathbf{u}_{J\beta}, \end{aligned} \tag{2.7}$$

$$M_I \ddot{\mathbf{u}}_{I\alpha} = -\sum_{J\beta} \frac{\partial^2 E_{tot}}{\partial \mathbf{u}_{I\alpha} \partial \mathbf{u}_{J\beta}} \mathbf{u}_{J\beta}. \tag{2.8}$$

2.1.3 The phonons

We can search the solution in the form of a phonon. Let's introduce a vector $\mathbf{q}$ in the first Brillouin zone. For each $\mathbf{q}$ we can write:

$$\mathbf{u}_{\mu s\alpha}(t) = \frac{A(\mathbf{q},t)}{\sqrt{M_s}}\tilde{\mathbf{u}}_{s\alpha}(\mathbf{q})e^{i\mathbf{q}\cdot\mathbf{R}_\mu} = \mathbf{u}_{s\alpha}(\mathbf{q})e^{i\mathbf{q}\cdot\mathbf{R}_\mu}, \tag{2.9}$$

where the amplitude $A(\mathbf{q},t)$ of the displacement depends on time and the displacement of the atoms in each cell identified by the Bravais lattice $\mathbf{R}_\mu$ can be obtained from the displacements of the atoms in one unit cell, for instance the one that corresponds to $\mathbf{R}_\mu = 0$ $\left(\frac{A(\mathbf{q},t)}{\sqrt{M_s}}\tilde{\mathbf{u}}_{s\alpha}(\mathbf{q})\right)$ multiplying by a phase factor.

A Γ-point phonon has the same displacements in all unit cells ($\mathbf{q} = 0$). A zone border phonon with $\mathbf{q}_{ZB} = \mathbf{G}/2$, where $\mathbf{G}$ is a reciprocal lattice vector, has displacements which repeat periodically every two unit cells. A phonon with $\mathbf{q} = \mathbf{q}_{ZB}/2$ has displacements which repeat every four unit cells. A phonon at a general wavevector $\mathbf{q}$ could be incommensurate with the underlying lattice. Inserting this solution in the equations of motion and writing $I = (\mu, s), J = (\nu, s')$ we obtain the following equations for the $3 \times N_{at}$ variables $\tilde{u}_{s\alpha}(\mathbf{q})$:

$$\frac{d^2A(\mathbf{q},t)}{dt^2}\tilde{\mathbf{u}}_{s\alpha}(\mathbf{q}) = -A(\mathbf{q},t)\sum_{s'\beta} D_{s\alpha s'\beta}(\mathbf{q})\tilde{\mathbf{u}}_{s'\beta}(\mathbf{q}), \tag{2.10}$$

where:

$$D_{s\alpha s'\beta}(\mathbf{q}) = \frac{1}{\sqrt{M_s M_{s'}}}\sum_\nu \frac{\partial^2 E_{tot}}{\partial \mathbf{u}_{\mu s\alpha}\partial \mathbf{u}_{\nu s'\beta}} e^{i\mathbf{q}(\mathbf{R}_\nu - \mathbf{R}_\mu)}, \tag{2.11}$$

is the dynamical matrix of the solid. Diagonalizing the dynamical matrix:

$$\sum_{s'\beta} D_{s\alpha s'\beta}(\mathbf{q})\mathbf{e}^\eta_{s'\beta}(\mathbf{q}) = \omega^2_{\mathbf{q},\eta}\mathbf{e}^\eta_{s\alpha}(\mathbf{q}), \tag{2.12}$$

we find the eigenvalues $\omega^2_{\mathbf{q},\eta}$ and eigenvectors $\mathbf{e}^\eta_{s\alpha}(\mathbf{q})$. Setting $\tilde{\mathbf{u}}_{s\alpha}(\mathbf{q}) = \mathbf{e}^\eta_{s\alpha}(\mathbf{q})$ the equations of motion become:

$$\frac{d^2A^\eta(\mathbf{q},t)}{dt^2} = -\omega^2_{\mathbf{q},\eta}A^\eta(\mathbf{q},t), \tag{2.13}$$

which are (for each $\mathbf{q}$) the equations of $3 \times N_{at}$ decoupled harmonic oscillators whose solutions are for instance:

$$A^\eta(\mathbf{q},t) = A^\eta_{\mathbf{q}}\sin\left(\omega_{\mathbf{q},\eta}t - \delta^\eta_{\mathbf{q}}\right), \tag{2.14}$$

where $A^\eta_{\mathbf{q}}$ and $\delta^\eta_{\mathbf{q}}$ depends on the initial conditions. The final solution of the problem is:

$$\mathbf{u}_{\mu s\alpha}(t) = \sum_{\mathbf{q},\eta}\frac{1}{\sqrt{M_s}}A^\eta_{\mathbf{q}}\sin\left(\omega_{\mathbf{q},\eta}t - \delta^\eta_{\mathbf{q}}\right)\mathbf{e}^\eta_{s\alpha}(\mathbf{q})e^{i\mathbf{q}\cdot\mathbf{R}_\mu}. \tag{2.15}$$

2.2 Density functional pertubation theory (DFPT)

2.2.1 Adiabatic approximation

Adiabatic approximation, also known as the Born–Oppenheimer approximation, assumes the decoupling of motions of nuclei and electrons in a quantum mechanical system, based on the fact that the masses of nuclei are much heavier than the ones of electrons. Within the Born-Oppenheimer adiabatic approximation the nuclei move in a potential energy given by the total energy of the electron system calculated (for instance within DFT) at fixed nuclei.

2.2.2 Density functional theory (DFT)

Within DFT the ground state total energy of the solid, calculated at fixed nuclei, is:

$$E_{\text{tot}} = \sum_i \left\langle \psi_i \left| -\frac{1}{2}\nabla^2 \right| \psi_i \right\rangle + \int V_{loc}(\mathbf{r})\rho(\mathbf{r})d^3r + E_H[\rho] + E_{xc}[\rho] + U_{II}, \tag{2.16}$$

where V_{loc} is the potential of the nuclei acting on the electrons. $\rho(\mathbf{r})$ is the density of the electron gas (2 sums over spins):

$$\rho(\mathbf{r}) = 2\sum_i |\psi_i(\mathbf{r})|^2, \tag{2.17}$$

The sum over i is on the occupied states. $|\psi_i\rangle$ are the wavefunctions. E_H is the Hartree energy:

$$E_H = \frac{1}{2}\int d^3r d^3r' \frac{\rho(\mathbf{r})\rho(\mathbf{r}')}{|\mathbf{r}-\mathbf{r}'|}. \tag{2.18}$$

E_{xc} is the exchange and correlation energy and U_{II} is the ion-ion interaction.

2.2.3 Hellmann-Feynman theorem and second derivatives of the energy

According to the Hellmann-Feynman theorem, the first order derivative of the ground state energy with respect to an external parameter is:

$$\frac{\partial E_{tot}}{\partial \lambda} = \int \frac{\partial V_{\text{loc}}(\mathbf{r})}{\partial \lambda}\rho(\mathbf{r})d^3r + \frac{\partial U_{II}}{\partial \lambda}. \tag{2.19}$$

Deriving with respect to a second parameter μ, we get:

$$\begin{aligned}\frac{\partial^2 E_{\text{tot}}}{\partial\mu\partial\lambda} = &\int \frac{\partial^2 V_{\text{loc}}(\mathbf{r})}{\partial\mu\partial\lambda}\rho(\mathbf{r})d^3r + \frac{\partial^2 U_{ll}}{\partial\mu\partial\lambda} \\ &+ \int \frac{\partial V_{\text{loc}}(\mathbf{r})}{\partial\lambda}\frac{\partial\rho(\mathbf{r})}{\partial\mu}d^3r.\end{aligned} \tag{2.20}$$

So the new quantity that we need to calculate is the charge density induced, at first order, by the perturbation:

$$\frac{\partial \rho(\mathbf{r})}{\partial \mu} = 2\sum_i \left[\frac{\partial \psi_i^*(\mathbf{r})}{\partial \mu} \psi_i(\mathbf{r}) + \psi_i^*(\mathbf{r}) \frac{\partial \psi_i(\mathbf{r})}{\partial \mu} \right]. \tag{2.21}$$

To fix the ideas we can think that $\lambda = \mathbf{u}_{\mu s \alpha}$ and $\mu = \mathbf{u}_{\nu s' \beta}$. The wavefunctions obey the following equation:

$$\left[-\frac{1}{2}\nabla^2 + V_{KS}(\mathbf{r}) \right] \psi_i(\mathbf{r}) = \varepsilon_i \psi_i(\mathbf{r}), \tag{2.22}$$

where $V_{KS} = V_{\text{loc}}(\mathbf{r}) + V_H(\mathbf{r}) + V_{XC}(\mathbf{r})$. $V_{KS}(\mathbf{r}, \mu)$ depends on μ so that also $\psi_i(\mathbf{r}, \mu)$, and $\varepsilon_i(\mu)$ depend on μ. We can expand these quantities in a Taylor series:

$$\begin{aligned} V_{KS}(\mathbf{r}, \mu) &= V_{KS}(\mathbf{r}, \mu = 0) + \frac{\partial V_{KS}(\mathbf{r})}{\partial \mu} \mu + \ldots, \\ \psi_i(\mathbf{r}, \mu) &= \psi_i(\mathbf{r}, \mu = 0) + \frac{\partial \psi_i(\mathbf{r})}{\partial \mu} \mu + \ldots, \\ \varepsilon_i(\mu) &= \varepsilon_i(\mu = 0) + \frac{\partial \varepsilon_i}{\partial \mu} \mu + \ldots. \end{aligned} \tag{2.23}$$

Inserting these equations and keeping only the terms of first order in μ we obtain the following:

$$\left[-\frac{1}{2}\nabla^2 + V_{KS}(\mathbf{r}) - \varepsilon_i \right] \frac{\partial \psi_i(\mathbf{r})}{\partial \mu} = -\frac{\partial V_{KS}}{\partial \mu} \psi_i(\mathbf{r}) + \frac{\partial \varepsilon_i}{\partial \mu} \psi_i(\mathbf{r}), \tag{2.24}$$

where $\frac{\partial V_{KS}}{\partial \mu} = \frac{\partial V_{\text{loc}}}{\partial \mu} + \frac{\partial V_H}{\partial \mu} + \frac{\partial V_{xc}}{\partial \mu}$ and

$$\begin{aligned} \frac{\partial V_H}{\partial \mu} &= \int \frac{1}{|\mathbf{r} - \mathbf{r}'|} \frac{\partial \rho(\mathbf{r}')}{\partial \mu} d^3 r', \\ \frac{\partial V_{xc}}{\partial \mu} &= \frac{dV_{xc}}{d\rho} \frac{\partial \rho(\mathbf{r})}{\partial \mu}, \end{aligned} \tag{2.25}$$

depend self-consistently on the charge density induced by the perturbation. This is the case for LDA. GGA is discussed in the Ref. [40]. The induced charge density depends only on $P_c \frac{\partial \psi_i}{\partial \mu}$ where $P_c = 1 - P_v$ is the projector on the conduction bands and $P_v = \sum_i |\psi_i\rangle \langle \psi_i|$ is the projector on the valence bands. In fact:

$$\begin{aligned} \frac{\partial \rho(\mathbf{r})}{\partial \mu} &= 2\sum_i \left[\left(P_c \frac{\partial \psi_i(\mathbf{r})}{\partial \mu} \right)^* \psi_i(\mathbf{r}) + \psi_i^*(\mathbf{r}) P_c \frac{\partial \psi_i(\mathbf{r})}{\partial \mu} \right] \\ &\quad + 2\sum_i \left[\left(P_v \frac{\partial \psi_i(\mathbf{r})}{\partial \mu} \right)^* \psi_i(\mathbf{r}) + \psi_i^*(\mathbf{r}) P_v \frac{\partial \psi_i(\mathbf{r})}{\partial \mu} \right]. \\ \frac{\partial \rho(\mathbf{r})}{\partial \mu} &= 2\sum_i \left[\left(P_c \frac{\partial \psi_i(\mathbf{r})}{\partial \mu} \right)^* \psi_i(\mathbf{r}) + \psi_i^*(\mathbf{r}) P_c \frac{\partial \psi_i(\mathbf{r})}{\partial \mu} \right] \\ &\quad + 2\sum_{ij} \psi_j^*(\mathbf{r}) \psi_i(\mathbf{r}) \left(\left\langle \frac{\partial \psi_i}{\partial \mu} \middle| \psi_j \right\rangle + \left\langle \psi_i \middle| \frac{\partial \psi_j}{\partial \mu} \right\rangle \right), \end{aligned} \tag{2.26}$$

and the last term vanishes because the term inside parenthesis is $\frac{d}{d\mu}\langle\psi_i|\psi_j\rangle = 0$.

2.2.4 Self-consistent linear system

Now we can solve the self-consistent linear system:

$$\left[-\frac{1}{2}\nabla^2 + V_{KS}(\mathbf{r}) - \varepsilon_i\right] P_c \frac{\partial\psi_i(\mathbf{r})}{\partial\mu} = -P_c\frac{\partial V_{KS}}{\partial\mu}\psi_i(\mathbf{r}), \tag{2.27}$$

where

$$\frac{\partial V_{KS}}{\partial\mu} = \frac{\partial V_{loc}}{\partial\mu} + \frac{\partial V_H}{\partial\mu} + \frac{\partial V_{xc}}{\partial\mu}, \tag{2.28}$$

and

$$\frac{\partial\rho(\mathbf{r})}{\partial\mu} = 2\sum_i \left[\left(P_c\frac{\partial\psi_i(\mathbf{r})}{\partial\mu}\right)^* \psi_i(\mathbf{r}) + \psi_i^*(\mathbf{r}) P_c\frac{\partial\psi_i(\mathbf{r})}{\partial\mu}\right]. \tag{2.29}$$

2.2.5 Dynamical matrix at finite q

The dynamical matrix is:

$$D_{s\alpha s'\beta}(\mathbf{q}) = \frac{1}{\sqrt{M_s M_{s'}}}\sum_\nu e^{-i\mathbf{q}\mathbf{R}_\mu}\frac{\partial^2 E_{tot}}{\partial\mathbf{u}_{\mu s\alpha}\partial\mathbf{u}_{\nu s'\beta}}e^{i\mathbf{q}\mathbf{R}_\nu}. \tag{2.30}$$

Inserting the expression of the second derivative of the total energy we have:

$$\begin{aligned} D_{s\alpha s'\beta}(\mathbf{q}) = \frac{1}{\sqrt{M_S M_{s'}}}\Bigg[&\frac{1}{N}\int_V d^3r \sum_{\mu\nu}\left(e^{-i\mathbf{q}\mathbf{R}_\mu}\frac{\partial^2 V_{loc}(\mathbf{r})}{\partial\mathbf{u}_{\mu s\alpha}\partial\mathbf{u}_{\nu s'\beta}}e^{i\mathbf{q}\mathbf{R}_\nu}\right)\rho(\mathbf{r}) \\ &+\frac{1}{N}\int_V d^3r\left(\sum_\mu e^{-i\mathbf{q}\mathbf{R}_\mu}\frac{\partial V_{loc}(\mathbf{r})}{\partial\mathbf{u}_{\mu s\alpha}}\right)\left(\sum_\nu \frac{\partial\rho(\mathbf{r})}{\partial\mathbf{u}_{\nu s'\beta}}e^{i\mathbf{q}\mathbf{R}_\nu}\right)\Bigg] + D^{I,I}_{s\alpha s'\beta}(\mathbf{q}). \end{aligned} \tag{2.31}$$

We now show that these integrals can be done over Ω. Defining:

$$\frac{\partial^2 V_{loc}(\mathbf{r})}{\partial\mathbf{u}^*_{s\alpha}(\mathbf{q})\partial\mathbf{u}_{s'\beta}(\mathbf{q})} = \sum_{\mu\nu} e^{-i\mathbf{q}\mathbf{R}_\mu}\frac{\partial^2 V_{loc}(\mathbf{r})}{\partial\mathbf{u}_{\mu s\alpha}\partial\mathbf{u}_{\nu s'\beta}}e^{i\mathbf{q}\mathbf{R}_\nu}, \tag{2.32}$$

we can show (see below) that $\frac{\partial^2 V_{\text{loc}}(\mathbf{r})}{\partial\mathbf{u}^*_{s\alpha}(\mathbf{q})\partial\mathbf{u}_{s'\beta}(\mathbf{q})}$ is a lattice-periodic function. Then we can define

$$\frac{\partial\rho(\mathbf{r})}{\partial\mathbf{u}_{s'\beta}(\mathbf{q})} = \sum_\nu \frac{\partial\rho(\mathbf{r})}{\partial\mathbf{u}_{\nu s'\beta}}e^{i\mathbf{q}\mathbf{R}_\nu}, \tag{2.33}$$

and show that

$$\frac{\partial\rho(\mathbf{r})}{\partial\mathbf{u}_{s'\beta}(\mathbf{q})} = e^{i\mathbf{q}\mathbf{r}}\frac{\partial\widetilde{\rho}(\mathbf{r})}{\partial\mathbf{u}_{s'\beta}(\mathbf{q})}, \tag{2.34}$$

where $\frac{\partial\widetilde{\rho}(\mathbf{r})}{\partial\mathbf{u}_{s'\beta}(\mathbf{q})}$ is a lattice-periodic function.

By defining lattice-periodic function in the same way:

$$\frac{\partial V_{loc}(\mathbf{r})}{\partial \mathbf{u}_{s\alpha}(\mathbf{q})} = \sum_{\mu} \frac{\partial V_{loc}(\mathbf{r})}{\partial \mathbf{u}_{\mu S\alpha}} e^{i\mathbf{q}\mathbf{R}_{\mu}}, \tag{2.35}$$

we can write the dynamical matrix at finite $\mathbf{q}$ as:

$$\begin{aligned} D_{s\alpha s'\beta}(\mathbf{q}) = \frac{1}{\sqrt{M_s M_{s'}}} \Bigg[& \int_{\Omega} d^3r \frac{\partial^2 V_{loc}(\mathbf{r})}{\partial \mathbf{u}^*_{s\alpha}(\mathbf{q}) \partial \mathbf{u}_{s'\beta}(\mathbf{q})} \rho(\mathbf{r}) \\ & + \int_{\Omega} d^3r \left(\frac{\partial \tilde{V}_{loc}(\mathbf{r})}{\partial \mathbf{u}_{s\alpha}(\mathbf{q})} \right)^* \frac{\partial \tilde{\rho}(\mathbf{r})}{\partial \mathbf{u}_{s'\beta}(\mathbf{q})} \Bigg] + D^{I,I}_{s\alpha s'\beta}(\mathbf{q}). \end{aligned} \tag{2.36}$$

We have:

$$\frac{\partial^2 V_{loc}(\mathbf{r})}{\partial \mathbf{u}^*_{s\alpha}(\mathbf{q}) \partial \mathbf{u}_{s'\beta}(\mathbf{q})} = \sum_{\mu\nu} e^{-i\mathbf{q}\mathbf{R}_{\mu}} \frac{\partial^2 V_{loc}(\mathbf{r})}{\partial \mathbf{u}_{\mu s\alpha} \partial \mathbf{u}_{\nu s'\beta}} e^{i\mathbf{q}\mathbf{R}_{\nu}} \tag{2.37}$$

is a lattice-periodic function because the local potential can be written as

$$V_{\mathrm{loc}}\left(\mathbf{r}\right) = \sum_{\mu} \sum_{s} v^{s}_{\mathrm{loc}}\left(\mathbf{r} - \mathbf{R}_{\mu} - \mathbf{d}_{s} - \mathbf{u}_{\mu s}\right), \tag{2.38}$$

and $\frac{\partial^2 V_{loc}(\mathbf{r})}{\partial \mathbf{u}_{\mu s\alpha} \partial \mathbf{u}_{\nu s'\beta}}$ vanishes if $\mu \neq \nu$ or $s \neq s'$. Since $\mu = \nu$ the two phase factors cancel, and we remain with a lattice-periodic function:

$$\frac{\partial^2 V_{loc}(\mathbf{r})}{\partial \mathbf{u}^*_{s\alpha}(\mathbf{q}) \partial \mathbf{u}_{s'\beta}(\mathbf{q})} = \delta_{s,s'} \sum_{\mu} \left. \frac{\partial^2 v^{s}_{loc}(\mathbf{r} - \mathbf{R}_{\mu} - \mathbf{d}_{s} - \mathbf{u}_{\mu s})}{\partial \mathbf{u}_{\mu s\alpha} \partial \mathbf{u}_{\mu s\beta}} \right|_{\mathbf{u}=0}. \tag{2.39}$$

In order to show that:

$$\frac{\partial \rho(\mathbf{r})}{\partial \mathbf{u}_{s'\beta}(\mathbf{q})} = \sum_{\nu} \frac{\partial \rho(\mathbf{r})}{\partial \mathbf{u}_{\nu s'\beta}} e^{iq\mathbf{R}_{\nu}} = e^{i\mathbf{q}\mathbf{r}} \frac{\partial \widetilde{\rho}(\mathbf{r})}{\partial \mathbf{u}_{s'\beta}(\mathbf{q})}, \tag{2.40}$$

where $\frac{\partial \widetilde{\rho}(\mathbf{r})}{\partial \mathbf{u}_{s'\beta}(\mathbf{q})}$ is a lattice-periodic function, we can calculate the Fourier transform of $\frac{\partial \rho(\mathbf{r})}{\partial \mathbf{u}_{s'\beta}(\mathbf{q})}$ and show that it is different from zero only at vectors $\mathbf{q} + \mathbf{G}$, where $\mathbf{G}$ is a reciprocal lattice vector. We have

$$\frac{\partial \rho}{\partial \mathbf{u}_{s'\beta}(\mathbf{q})}(\mathbf{k}) = \frac{1}{V} \int_{V} d^3r e^{-i\mathbf{k}\mathbf{r}} \sum_{\nu} \frac{\partial \rho(\mathbf{r})}{\partial \mathbf{u}_{\nu s'\beta}} e^{i\mathbf{q}\mathbf{R}_{\nu}}. \tag{2.41}$$

Due to the translational invariance of the solid, if we displace the atom s' in the direction β in the cell $\nu = 0$ and probe the charge at the point $\mathbf{r}$, or we displace in the same direction the atom s' in the cell ν and probe the charge at the point $\mathbf{r} + \mathbf{R}_{\nu}$, we should find the same value. Therefore

$$\frac{\partial \rho(\mathbf{r} + \mathbf{R}_{\nu})}{\partial \mathbf{u}_{\nu s'\beta}} = \frac{\partial \rho(\mathbf{r})}{\partial \mathbf{u}_{0 s'\beta}}, \tag{2.42}$$

or, taking $\mathbf{r} = \mathbf{r}' - \mathbf{R}_\nu$, we have

$$\frac{\partial \rho(\mathbf{r}')}{\partial \mathbf{u}_{\nu s' \beta}} = \frac{\partial \rho(\mathbf{r}' - \mathbf{R}_\nu)}{\partial \mathbf{u}_{0 s' \beta}}, \tag{2.43}$$

which can be inserted in the expression of the Fourier transform to give:

$$\frac{\partial \rho}{\partial \mathbf{u}_{s' \beta}(\mathbf{q})}(\mathbf{k}) = \frac{1}{V} \int_V d^3 r e^{-i\mathbf{k}\mathbf{r}} \sum_\nu \frac{\partial \rho(\mathbf{r} - \mathbf{R}_\nu)}{\partial \mathbf{u}_{0 s' \beta}} e^{i\mathbf{q}\mathbf{R}_\nu}. \tag{2.44}$$

Changing variable in the integral setting $\mathbf{r}' = \mathbf{r} - \mathbf{R}_\nu$, we have

$$\frac{\partial \rho}{\partial \mathbf{u}_{s' \beta}(\mathbf{q})}(\mathbf{k}) = \frac{1}{V} \int_V d^3 r' e^{-i\mathbf{k}\mathbf{r}'} \sum_\nu \frac{\partial \rho(\mathbf{r}')}{\partial \mathbf{u}_{0 s' \beta}} e^{i(\mathbf{q}-\mathbf{k})\mathbf{R}_\nu}, \tag{2.45}$$

The sum over ν: $\sum_\nu e^{i(\mathbf{q}-\mathbf{k})\mathbf{R}_\nu}$ gives N if $\mathbf{k} = \mathbf{q} + \mathbf{G}$ and 0 otherwise. Hence $\frac{\partial \rho}{\partial \mathbf{u}_{s' \beta}(\mathbf{q})}(\mathbf{k})$ is non-vanishing only at $\mathbf{k} = \mathbf{q} + \mathbf{G}$. It follows that:

$$\frac{\partial \rho(\mathbf{r})}{\partial \mathbf{u}_{s' \beta}(\mathbf{q})} = e^{i\mathbf{q}\mathbf{r}} \sum_{\mathbf{G}} \frac{\partial \rho}{\partial \mathbf{u}_{s' \beta}(\mathbf{q})}(\mathbf{q} + \mathbf{G}) e^{i\mathbf{G}\mathbf{r}}, \tag{2.46}$$

and the sum over $\mathbf{G}$ gives a lattice-periodic function.

2.2.6 Bloch theorem

According to the Bloch theorem, the solution of the Kohn and Sham equations in a periodic potential $V_{KS}(\mathbf{r} + \mathbf{R}_\mu) = V_{KS}(\mathbf{r})$:

$$\left[-\frac{1}{2}\nabla^2 + V_{KS}(\mathbf{r}) \right] \psi_{\mathbf{k}v}(\mathbf{r}) = \epsilon_{\mathbf{k}v} \psi_{\mathbf{k}v}(\mathbf{r}), \tag{2.47}$$

can be indexed by a $\mathbf{k}$-vector in the first Brillouin zone and by a band index v, and:

$$\begin{aligned} \psi_{\mathbf{k}v}(\mathbf{r} + \mathbf{R}_\mu) &= e^{i\mathbf{k}\mathbf{R}_\mu} \psi_{\mathbf{k}v}(\mathbf{r}), \\ \psi_{\mathbf{k}v}(\mathbf{r}) &= e^{i\mathbf{k}\mathbf{r}} u_{\mathbf{k}v}(\mathbf{r}), \end{aligned} \tag{2.48}$$

where $u_{\mathbf{k}v}(\mathbf{r})$ is a lattice-periodic function. Periodic Boundary Conditions (PBCs) imply that:

$$\psi_{\mathbf{k}v}(\mathbf{r} + N_j \mathbf{a}_j) = \psi_{\mathbf{k}v}(\mathbf{r}). \tag{1.59}$$

$\therefore$

$$e^{iN_j \mathbf{k}\cdot\mathbf{a}_j} = 1, \tag{1.60}$$

hence, after introducing the vectors $\mathbf{b}_j$ such that $\mathbf{a}_i \cdot \mathbf{b}_j = 2\pi\delta_{ij}$, the allowed wave vectors are expressed as:

$$\mathbf{k} = \frac{m_1}{N_1}\mathbf{b}_1 + \frac{m_2}{N_2}\mathbf{b}_2 + \frac{m_3}{N_3}\mathbf{b}_3 \tag{1.61}$$

where m_j are integers such that $0 \leq m_j < N_j$. By time reversal symmetry, we also have:

$$\psi^*_{-\mathbf{k}v}(\mathbf{r}) = \psi_{\mathbf{k}v}(\mathbf{r}). \tag{2.49}$$

2.2.7 Charge density response at finite q

The lattice-periodic part of the induced charge density at finite $\mathbf{q}$ can be calculated as follows. We have:

$$\begin{aligned}\frac{\partial\rho(\mathbf{r})}{\partial\mathbf{u}_{s'\beta}(\mathbf{q})} = 2\sum_{\mathbf{k}v}\Bigg[&\left(P_c\sum_{\nu}\frac{\partial\psi_{\mathbf{k}v}(\mathbf{r})}{\partial\mathbf{u}_{\nu s'\beta}}e^{-i\mathbf{q}\mathbf{R}_\nu}\right)^*\psi_{\mathbf{k}v}(\mathbf{r})\\&+\psi^*_{\mathbf{k}v}(\mathbf{r})P_c\left(\sum_{\nu}\frac{\partial\psi_{\mathbf{k}v}(\mathbf{r})}{\partial\mathbf{u}_{\nu s'\beta}}e^{i\mathbf{q}\mathbf{R}_\nu}\right)\Bigg].\end{aligned} \tag{2.50}$$

Changing $\mathbf{k}$ with $-\mathbf{k}$ in the first term, using time reversal symmetry $\psi_{-\mathbf{k}v}(\mathbf{r}) = \psi^*_{\mathbf{k}v}(\mathbf{r})$, and defining:

$$\frac{\partial\psi_{\mathbf{k}v}(\mathbf{r})}{\partial\mathbf{u}_{s'\beta}(\mathbf{q})} = \sum_{\nu}\frac{\partial\psi_{\mathbf{k}v}(\mathbf{r})}{\partial\mathbf{u}_{\nu s'\beta}}e^{i\mathbf{q}\mathbf{R}_\nu}, \tag{2.51}$$

we have:

$$\frac{\partial\rho(\mathbf{r})}{\partial\mathbf{u}_{s'\beta}(\mathbf{q})} = 4\sum_{\mathbf{k}v}\psi^*_{\mathbf{k}v}(\mathbf{r})P_c\frac{\partial\psi_{\mathbf{k}v}(\mathbf{r})}{\partial\mathbf{u}_{s'\beta}(\mathbf{q})} \tag{2.52}$$

We can now use the following identities to extract the periodic part of the induced charge density:

$$\begin{aligned}\frac{\partial\psi_{\mathbf{k}v}(\mathbf{r})}{\partial\mathbf{u}_{s'\beta}(\mathbf{q})} &= e^{i\mathbf{k}\mathbf{r}}\frac{\partial u_{\mathbf{k}v}(\mathbf{r})}{\partial\mathbf{u}_{s'\beta}(\mathbf{q})} = e^{i\mathbf{k}\mathbf{r}}\sum_{\nu}\frac{\partial u_{\mathbf{k}v}(\mathbf{r})}{\partial\mathbf{u}_{\nu s'\beta}}e^{i\mathbf{q}\mathbf{R}_\nu}\\&= e^{i(\mathbf{k}+\mathbf{q})\mathbf{r}}\frac{\partial\widetilde{u}_{\mathbf{k}v}(\mathbf{r})}{\partial\mathbf{u}_{s'\beta}(\mathbf{q})},\end{aligned} \tag{2.53}$$

where $\frac{\partial\widetilde{u}_{\mathbf{k}v}(\mathbf{r})}{\partial\mathbf{u}_{s'\beta}(\mathbf{q})}$ is a lattice-periodic function. The projector in the conduction band $P_c = 1 - P_v$ is:

$$\begin{aligned}P_c &= \sum_{\mathbf{k}'c}\psi_{\mathbf{k}'c}(\mathbf{r})\psi^*_{\mathbf{k}'c}\left(\mathbf{r}'\right)\\&= \sum_{\mathbf{k}'c}e^{i\mathbf{k}'\mathbf{r}}u_{\mathbf{k}'c}(\mathbf{r})u^*_{\mathbf{k}'c}\left(\mathbf{r}'\right)e^{-i\mathbf{k}'\mathbf{r}'}\\&= \sum_{\mathbf{k}'}e^{i\mathbf{k}'\mathbf{r}}P_c^{\mathbf{k}'}e^{-i\mathbf{k}'\mathbf{r}'},\end{aligned} \tag{2.54}$$

but only the term $\mathbf{k}' = \mathbf{k}+\mathbf{q}$ gives a non-zero contribution when applied to $\frac{\partial\psi_{\mathbf{k}v}(\mathbf{r})}{\partial\mathbf{u}_{s'\beta}(\mathbf{q})}$. We have therefore:

$$\frac{\partial\rho(\mathbf{r})}{\partial\mathbf{u}_{s'\beta}(\mathbf{q})} = e^{i\mathbf{q}\mathbf{r}}4\sum_{\mathbf{k}v}u^*_{\mathbf{k}v}(\mathbf{r})P_c^{\mathbf{k}+\mathbf{q}}\frac{\partial\widetilde{u}_{\mathbf{k}v}(\mathbf{r})}{\partial\mathbf{u}_{s'\beta}(\mathbf{q})}, \tag{2.55}$$

so the lattice-periodic part of the induced charge density, written in terms of lattice-periodic functions is:

$$\frac{\partial\widetilde{\rho}(\mathbf{r})}{\partial\mathbf{u}_{s'\beta}(\mathbf{q})} = 4\sum_{\mathbf{k}v}u^*_{\mathbf{k}v}(\mathbf{r})P_c^{\mathbf{k}+\mathbf{q}}\frac{\partial\widetilde{u}_{\mathbf{k}v}(\mathbf{r})}{\partial\mathbf{u}_{s'\beta}(\mathbf{q})}. \tag{2.56}$$

2.2.8 First-order derivative of the wavefunctions

$\frac{\partial \tilde{u}_{\mathbf{k}v}(\mathbf{r})}{\partial \mathbf{u}_{s'\beta}(\mathbf{q})}$ is a lattice-periodic function which can be calculated with the following considerations. From first order perturbation theory we get, for each displacement $\mathbf{u}_{\nu s'\beta}$, the equation:

$$\left[-\frac{1}{2}\nabla^2 + V_{KS}(\mathbf{r}) - \epsilon_{\mathbf{k}v}\right] P_c \frac{\partial \psi_{\mathbf{k}v}(\mathbf{r})}{\partial \mathbf{u}_{\nu s'\beta}} = -P_c \frac{\partial V_{KS}(\mathbf{r})}{\partial \mathbf{u}_{\nu s'\beta}} \psi_{\mathbf{k}v}(\mathbf{r}). \tag{2.57}$$

Multiplying every equation by $e^{i\mathbf{q}\mathbf{R}_\nu}$ and summing on ν, we get:

$$\begin{aligned}\left[-\frac{1}{2}\nabla^2 + V_{KS}(\mathbf{r}) - \epsilon_{\mathbf{k}v}\right] P_c \frac{\partial \psi_{\mathbf{k}v}(\mathbf{r})}{\partial \mathbf{u}_{s'\beta}(\mathbf{q})} \\ = - P_c \frac{\partial V_{KS}(\mathbf{r})}{\partial \mathbf{u}_{s'\beta}(\mathbf{q})} \psi_{\mathbf{k}v}(\mathbf{r}).\end{aligned} \tag{2.58}$$

Using the translational invariance of the solid we can write

$$\frac{\partial V_{KS}(\mathbf{r})}{\partial \mathbf{u}_{s'\beta}(\mathbf{q})} = \sum_\nu \frac{\partial V_{KS}(\mathbf{r})}{\partial \mathbf{u}_{\nu S'\beta}} e^{i\mathbf{q}\mathbf{R}_\nu} = e^{i\mathbf{q}\mathbf{r}} \frac{\partial \tilde{V}_{KS}(\mathbf{r})}{\partial \mathbf{u}_{s'\beta}(\mathbf{q})}, \tag{2.59}$$

where $\frac{\partial \tilde{V}_{KS}(\mathbf{r})}{\partial \mathbf{u}_{s'\beta}(\mathbf{q})}$ is a lattice-periodic function. The right-hand side of the linear system becomes:

$$-e^{i(\mathbf{k}+\mathbf{q})\mathbf{r}} P_c^{\mathbf{k}+\mathbf{q}} \frac{\partial \tilde{V}_{KS}(\mathbf{r})}{\partial \mathbf{u}_{s'\beta}(\mathbf{q})} u_{\mathbf{k}v}(\mathbf{r}). \tag{2.60}$$

In the left-hand side we have

$$P_c \sum_\nu \frac{\partial \psi_{\mathbf{k}v}(\mathbf{r})}{\partial \mathbf{u}_{\nu s'\beta}} e^{i\mathbf{q}\mathbf{R}_\nu} = e^{i(\mathbf{k}+\mathbf{q})\mathbf{r}} P_c^{\mathbf{k}+\mathbf{q}} \frac{\partial \tilde{u}_{\mathbf{k}v}(\mathbf{r})}{\partial \mathbf{u}_{s'\beta}(\mathbf{q})}, \tag{2.61}$$

and defining:

$$H^{\mathbf{k}+\mathbf{q}} = e^{-i(\mathbf{k}+\mathbf{q})\mathbf{r}} \left[-\frac{1}{2}\nabla^2 + V_{KS}(\mathbf{r})\right] e^{i(\mathbf{k}+\mathbf{q})\mathbf{r}}, \tag{2.62}$$

we obtain the linear system:

$$\left[H^{\mathbf{k}+\mathbf{q}} - \epsilon_{\mathbf{k}v}\right] P_c^{\mathbf{k}+\mathbf{q}} \frac{\partial \tilde{u}_{\mathbf{k}v}(\mathbf{r})}{\partial \mathbf{u}_{s'\beta}(\mathbf{q})} = -P_c^{\mathbf{k}+\mathbf{q}} \frac{\partial \tilde{V}_{KS}(\mathbf{r})}{\partial \mathbf{u}_{s'\beta}(\mathbf{q})} u_{\mathbf{k}v}(\mathbf{r}). \tag{2.63}$$

2.2.9 Linear response

The lattice-periodic component of the induced self-consistent potential can be obtained with the same techniques seen above. We have:

$$\begin{aligned}\frac{\partial V_{KS}(\mathbf{r})}{\partial \mathbf{u}_{\nu s'\beta}} = \frac{\partial V_{loc}(\mathbf{r})}{\partial \mathbf{u}_{\nu s'\beta}} + \int d^3r' \frac{1}{|\mathbf{r}-\mathbf{r}'|} \frac{\partial \rho(\mathbf{r}')}{\partial \mathbf{u}_{\nu s'\beta}} \\ + \frac{\partial V_{xc}}{\partial \rho} \frac{\partial \rho(\mathbf{r})}{\partial \mathbf{u}_{\nu s'\beta}}.\end{aligned} \tag{2.64}$$

Multiplying by $e^{i\mathbf{q}\mathbf{R}_\nu}$ and summing on ν, we obtain:

$$\begin{aligned}\frac{\partial V_{KS}(\mathbf{r})}{\partial \mathbf{u}_{s'\beta}(\mathbf{q})} = \frac{\partial V_{loc}(\mathbf{r})}{\partial \mathbf{u}_{s'\beta}(\mathbf{q})} + \int d^3r' \frac{1}{|\mathbf{r}-\mathbf{r}'|} \frac{\partial \rho(\mathbf{r}')}{\partial \mathbf{u}_{s'\beta}(\mathbf{q})} \\ + \frac{\partial V_{xc}}{\partial \rho} \frac{\partial \rho(\mathbf{r})}{\partial \mathbf{u}_{s'\beta}(\mathbf{q})}.\end{aligned} \tag{2.65}$$

Keeping only the lattice periodic parts gives:

$$\begin{aligned}e^{i\mathbf{q}\mathbf{r}} \frac{\partial \tilde{V}_{KS}(\mathbf{r})}{\partial \mathbf{u}_{s'\beta}(\mathbf{q})} = e^{i\mathbf{q}\mathbf{r}} \frac{\partial \tilde{V}_{loc}(\mathbf{r})}{\partial \mathbf{u}_{s'\beta}(\mathbf{q})} + \int d^3r' \frac{1}{|\mathbf{r}-\mathbf{r}'|} e^{i\mathbf{q}\mathbf{r}'} \frac{\partial \tilde{\rho}(\mathbf{r}')}{\partial \mathbf{u}_{s'\beta}(\mathbf{q})} \\ + \frac{\partial V_{xc}}{\partial \rho} e^{i\mathbf{q}\mathbf{r}} \frac{\partial \tilde{\rho}(\mathbf{r})}{\partial \mathbf{u}_{s'\beta}(\mathbf{q})},\end{aligned} \tag{2.66}$$

or equivalently:

$$\begin{aligned}\frac{\partial V_{KS}(\mathbf{r})}{\partial \mathbf{u}_{s'\beta}(\mathbf{q})} = \frac{\partial \tilde{V}_{loc}(\mathbf{r})}{\partial \mathbf{u}_{s'\beta}(\mathbf{q})} + \int d^3r' \frac{1}{|\mathbf{r}-\mathbf{r}'|} e^{i\mathbf{q}(\mathbf{r}'-\mathbf{r})} \frac{\partial \tilde{\rho}(\mathbf{r}')}{\partial \mathbf{u}_{s'\beta}(\mathbf{q})} \\ + \frac{\partial V_{xc}(\mathbf{r})}{\partial \rho} \frac{\partial \tilde{\rho}(\mathbf{r})}{\partial \mathbf{u}_{s'\beta}(\mathbf{q})}.\end{aligned} \tag{2.67}$$

The above contents are summarized from the literature on DFPT. [13, 62, 68, 12, 33]

2.3 Pseudopotentials

Modern pseudopotentials are constructed on isolated atoms. The radial Kohn and Sham equations are initially solved for all the electrons, then the orbitals are divided into core and valence parts. For the valence orbitals, a pseudopotential is calculated which reproduces the all-electron results.

We formulated the theory with a local external potential in the previous section. However, modern pseudopotentials (PPs) are non-local. These references [62, 34, 33] contains more detailed descriptions of DFPT with modern PPs.

In this section we introduce the main forms of the available PPs in `pslibrary`. Modern pseudopotentials are divided into three types:

- Norm-conserving pseudopotentials
- Ultrasoft pseudopotentials
- The projector augmented-wave data sets (PAW)

The basics of three atomic pseudopotentials are discussed in the following subsections.

2.3.1 Plane waves in periodic solids

In order to solve the KS equations, it is useful to expand the wave functions on a given basis set. One of the most widely used is the Plane Waves (PWs) basis set: PWs are indeed an orthogonal basis by construction and represent the most natural choice while dealing with crystalline solids. The translational invariance of the Bravais lattice imposes further constraints on the wave vectors that enter in the expansion of a lattice-periodic function in the PWs basis set. Indeed, PWs $e^{i\mathbf{k}\cdot\mathbf{r}}$ are lattice-periodic only for a given set of wave vectors $\mathbf{G}$, called reciprocal lattice vectors and defined by the condition $e^{i\mathbf{G}\cdot\mathbf{R}_\mu}=1$. The $\mathbf{G}$ vectors form a lattice in the reciprocal space, its primitive vectors being $\mathbf{b}_1, \mathbf{b}_2$, and $\mathbf{b}_3$ introduced above. The Wigner-Seitz primitive cell of the reciprocal lattice is called Brillouin Zone (BZ): all the wave vectors $\mathbf{k}$ allowed in PBCs can be refolded into it and, as a consequence, a band index v needs to be introduced to label the wave functions, $\psi_{\mathbf{k}v}(\mathbf{r})$.

The periodic part of the wave function can be expanded in PWs, to get:

$$\psi_{\mathbf{k}v}(\mathbf{r}) = \frac{1}{\sqrt{V}} \sum_{\mathbf{G}} c_{\mathbf{k}+\mathbf{G}v} e^{i(\mathbf{k}+\mathbf{G})\cdot\mathbf{r}} \tag{2.68}$$

where V is the volume of the solid. If we substitute $\psi_{\mathbf{k}v}(\mathbf{r})$ given by Eq. 2.68 into Eq. 2.47, we obtain the following expression for the KS equations in reciprocal space for a local potential:

$$\sum_{\mathbf{G}'} \left[\frac{1}{2}|\mathbf{k}+\mathbf{G}|^2 \delta_{\mathbf{G}\mathbf{G}'} + V_{\mathrm{KS}}\left(\mathbf{G}-\mathbf{G}'\right) \right] c_{\mathbf{k}+\mathbf{G}'v} = \epsilon_{\mathbf{k}v} c_{\mathbf{k}+\mathbf{G}v} \tag{2.69}$$

where $V_{\mathrm{KS}}\left(\mathbf{G}-\mathbf{G}'\right) (V_{\mathrm{KS}} = V_{\mathrm{H}} + V_{\mathrm{xc}} + V_{\mathrm{ext}})$ is the matrix elements of the KS potential between two PWs with wave vectors $\mathbf{k}+\mathbf{G}$ and $\mathbf{k}+\mathbf{G}'$ (For non local potential we can refer

to Ref. [33]). Hence it corresponds to the $\mathbf{G}-\mathbf{G}'$ Fourier component of the KS potential defined in real space:

$$V_{\mathrm{KS}}\left(\mathbf{G}-\mathbf{G}'\right)=\frac{1}{\Omega}\int_{\Omega}d^3r e^{-i\left(\mathbf{G}-\mathbf{G}'\right)\cdot\mathbf{r}}V_{\mathrm{KS}}(\mathbf{r}) \tag{2.70}$$

The charge density can be written in terms of the single-particle wave functions (Eq. 2.68) and, following the expansion in PWs introduced above, it reads:

$$n(\mathbf{r})=\frac{1}{V}\sum_{\mathbf{k}v}\sum_{\mathbf{G}\mathbf{G}'}f_{\mathbf{k}v}c^{*}_{\mathbf{k}+\mathbf{G}'v}c_{\mathbf{k}+\mathbf{G}v}e^{i\left(\mathbf{G}-\mathbf{G}'\right)\cdot\mathbf{r}} \tag{2.71}$$

or, equivalently:

$$n(\mathbf{r})=\sum_{\mathbf{G}}n(\mathbf{G})e^{i\mathbf{G}\cdot\mathbf{r}} \tag{2.72}$$

The PWs expansion in Eq. (1.62) is formally exact, but it requires an infinite number of PWs. Clearly, in order for such an approach to be computationally affordable, the number of basis elements has to be finite: in electronic structure codes, this is usually achieved by considering only the PWs with $\mathbf{G}$ vectors such that:

$$\frac{1}{2}|\mathbf{k}+\mathbf{G}|^2<E_{\mathrm{cut}} \tag{2.73}$$

where E_{cut} is a kinetic energy cut-off that is chosen accordingly to the desired accuracy on the wave functions, which naturally affects the accuracy of computed quantities such as, e.g., the ground state energy and the forces. The representation of the wave functions with a truncated basis set implies that also the charge density is computed with a limited number of PWs. By comparing Eqs. 2.71 and 2.72 it follows that the kinetic energy cut-off for the charge density is 4 times larger than the one for the wave functions, namely:

$$\frac{1}{2}|\mathbf{G}|^2<4E_{\mathrm{cut}} \tag{2.74}$$

2.3.2 Spherical symmetry

The Kohn and Sham (KS) equation is (in atomic units):

$$\left[-\frac{1}{2}\nabla^2+V_{ext}(\mathbf{r})+V_H(\mathbf{r})+V_{xc}(\mathbf{r})\right]\psi_i(\mathbf{r})=\epsilon_i\psi_i(\mathbf{r}). \tag{2.75}$$

For an atom $V_{\mathrm{ext}}\left(\mathbf{r}\right)=-Z/r$, where Z is the nuclear charge and $r=|\mathbf{r}|$. Assuming a spherically symmetric charge density $\rho(\mathbf{r})=\rho(r)$, one can show that the Hartree and exchange and correlation potentials are spherically symmetric too. In this hypothesis, the solutions of this equation have the form:

$$\psi_{n\ell m}(\mathbf{r})=\frac{\psi_{n\ell}(r)}{r}Y_{\ell m}\left(\Omega_{\mathbf{r}}\right), \tag{2.76}$$

where $(r, \Omega_{\mathbf{r}})$ are the spherical coordinates of $\mathbf{r}$. Here n, the main quantum number, is a positive integer, $0 \leq \ell \leq n-1$ indicates the orbital angular momentum and $-\ell \leq m \leq \ell$ its projection on a quantization axis. $Y_{\ell m}(\Omega_{\mathbf{r}})$ are the spherical harmonics, eigenstates of $\mathbf{L}^2$ and L_z :

$$\begin{aligned} \mathbf{L}^2 Y_{\ell m} &= \ell(\ell+1) Y_{\ell m}, \\ \mathbf{L}_z Y_{\ell m} &= m Y_{\ell m}. \end{aligned} \tag{2.77}$$

Inserting this solution in the KS equation, we obtain, for each value of ℓ, an ordinary differential equation for $\psi_{n\ell}(r)$:

$$\left[-\frac{1}{2}\frac{d^2}{dr^2} + \frac{\ell(\ell+1)}{2r^2} + V_{KS}(r) \right] \psi_{n\ell}(r) = \epsilon_{n\ell} \psi_{n\ell}(r), \tag{2.78}$$

where $V_{KS}(r) = V_{\text{ext}}(r) + V_H(r) + V_{xc}(r)$. The charge density is determined by the total number of electrons and by their distribution among the available orbitals defined by the occupation numbers $f_{n\ell}$. The maximum value of $f_{n\ell}$ is $2, 6, 10, 14$ for $\ell = 0, 1, 2, 3$ (s, p, d, f states) respectively. Note that we assumed a spherically symmetric atom, so we cannot specify the occupation of a state with a given m. For open-shell configurations, a uniform distribution of electrons among the available orbitals is implicitly assumed. The charge density is:

$$\tilde{\rho}(r) = 4\pi r^2 \rho(r) = \sum_{n\ell} f_{n\ell} \left| \psi_{n\ell}(r) \right|^2. \tag{2.79}$$

The radial equation is solved by the Numerov's method, discretizing the r coordinate by a logarithmic radial grid from $r_{\min}$ to $r_{\max}$. The grid is:

$$r_i = \frac{1}{Z} e^{x_{\min}} e^{(i-1)dx}, \quad i = 1, \cdots, N_p. \tag{2.80}$$

From input, it is possible to change the default values of $x_{\min}$, dx and $r_{\max}$ but, usually, this is not needed. The output of the calculation are the eigenvalues $\epsilon_{n\ell}$, the radial orbitals $\psi_{n\ell}(r)$, the charge density $\tilde{\rho}(r)$, and the total energy.

2.3.3 Norm-conserving pseudopotentials

Let us now consider, for each orbital angular momentum ℓ, the equation:

$$\left[-\frac{1}{2}\frac{d^2}{dr^2} + \frac{\ell(\ell+1)}{2r^2} + V_{ps,\ell}(r) \right] \phi_{\ell}(r) = \epsilon_{\ell} \phi_{\ell}(r), \tag{2.81}$$

We would like to find an ℓ dependent pseudopotential $V_{ps,\ell}(r)$ with the following properties:

- For each ℓ, the lowest eigenvalue ϵ_ℓ coincides with the valence eigenvalue $\epsilon_{n\ell}$ in the all-electron equation. n identifies the valence state.
- For each ℓ, it is possible to find a $r_{c,\ell}$ such that $\phi_\ell(r) = \psi_{n\ell}(r)$ for $r > r_{c,\ell}$.

The solution of the problem is not unique. There are several recipes to construct a pseudopotential. First of all, it is convenient to note that at sufficiently large $r, V_{ps,\ell}(r)$ coincides with the all-electron potential because $\phi_\ell(r) = \psi_{n\ell}(r)$ for $r > r_{c,\ell}$ and $\epsilon_\ell = \epsilon_{n\ell}$. We can therefore choose a $V_{\text{eff}}(r)$ such that $V_{\text{eff}}(r) = V_{KS}(r)$ for $r > r_{loc}$ and rewrite the radial equation in the form:

$$\left[-\frac{1}{2}\frac{d^2}{dr^2} + \frac{\ell(\ell+1)}{2r^2} + V_{eff}(r) + \Delta V_{ps,\ell}(r)\right]\phi_\ell(r) = \epsilon_\ell \phi_\ell(r). \tag{2.82}$$

Then suppose that we have a recipe to get a node-less $\phi_\ell(r)$ for $r < r_{c,\ell}$. Then:

$$\Delta V_{ps,\ell}(r) = \frac{1}{\phi_\ell(r)}\left[\epsilon_\ell + \frac{1}{2}\frac{d^2}{dr^2} - \frac{\ell(\ell+1)}{2r^2} - V_{eff}(r)\right].\phi_\ell(r) \tag{2.83}$$

There are some guidelines to follow in the choice of the form of $\phi_\ell(r)$ and one important condition. First of all the function must be as smooth as possible, with continuity of a certain number of derivatives at the matching point $r_{c,\ell}$. Then it is useful to search a function whose Fourier transform decays as rapidly as possible. However, the most important constraint is the norm-conserving condition [2] that is:

$$\int_0^{r_{c,\ell}} dr\,|\phi_\ell(r)|^2 = \int_0^{r_{c,\ell}} dr\,\left|\psi_{n,\ell}(r)\right|^2. \tag{2.84}$$

2.3.4 The logarithmic derivative

In order to illustrate the importance of the norm-conserving condition, it is useful to define the concept of logarithmic derivative. Let us consider the two equations:

$$\begin{aligned}\left[T_\ell + V_{KS}(r)\right]\psi_\epsilon(r) &= \epsilon\psi_\epsilon(r),\\ \left[T_\ell + V_{eff}(r) + \Delta V_{ps,\ell}(r)\right]\phi_\epsilon(r) &= \epsilon\phi_\epsilon(r).\end{aligned} \tag{2.85}$$

where we defined $T_\ell = -\frac{1}{2}\frac{d^2}{dr^2} + \frac{\ell(\ell+1)}{2r^2}$. By construction, we know that at $\epsilon = \epsilon_{n\ell}$, the solution $\phi_\epsilon(r)$ coincides with the $\psi_\epsilon(r)$ for $r > r_{c,\ell}$. But what about the other energies? The transferability of the pseudopotential depends on the fact that $\phi_\epsilon(r)$ reproduces $\psi_\epsilon(r)$ for a certain range of energies about $\epsilon_{n\ell}$. Since norm conservation implies that the derivative with respect to energy of the logarithmic derivatives coincide, all-electron and pseudo logarithmic derivatives usually coincide for a quite extended range of energies, of the order of a few Rydberg making the pseudopotential concept quite useful in practice.

2.3.5 Pseudopotential in the solid

In order to use the pseudopotential in the solid we have to subtract from $V_{\text{eff}}(r)$ the Hartree and exchange and correlation potentials.

$$V_{\text{loc}}(r) = V_{\text{eff}}(r) - V_H(r) - V_{xc}(r). \tag{2.86}$$

Usually only the valence atomic charge is used to calculate $V_H(r)$ and $V_{xc}(r)$. This however can introduce a significant error if there is a large overlap of the core and valence charge. In this case it is also possible to use the total charge $\rho_c(r)+\rho_v(r)$ in the calculation of $V_{xc}(r)$. The technique is known as nonlinear core correction. In order to improve the plane wave convergence a pseudized version of $\rho_c(r)$ is generally used for $r \leq r_{\text{core}}$. $V_{\text{loc}}\,(r)$ behaves as $-Z_V/r$ for large r, while $\Delta V_{ps,l}(r)$ is localized and goes to zero for $r \geq \max\left(r_{loc}, r_{c,\ell}\right)$. In order to apply the nonlocal part of the potential, that is different for different ℓ, we use projectors into subspaces of well defined ℓ :

$$P_\ell = \sum_{m=-\ell}^{m=\ell} |Y_{\ell m}\rangle \langle Y_{\ell m}| \,. \tag{2.87}$$

Therefore the resulting potential is nonlocal (actually it is called semilocal because it is local in the radial variable and nonlocal in the angular variables). We can write:

$$\begin{aligned} V_{ps}\left(\mathbf{r},\mathbf{r}'\right) = & \sum_I V_{loc}^I\left(|\mathbf{r}-\mathbf{R}_I|\right)\delta\left(\mathbf{r}-\mathbf{r}'\right) \\ & + \sum_I \sum_{lm} \Delta V_{ps,\ell}^I\left(|\mathbf{r}-\mathbf{R}_I|\right)\delta\left(|\mathbf{r}-\mathbf{R}_I| - \left|\mathbf{r}'-\mathbf{R}_I\right|\right) \\ & \times Y_{\ell m}\left(\Omega_{\mathbf{r}-\mathbf{R}_I}\right) Y_{\ell m}^*\left(\Omega_{\mathbf{r}'-\mathbf{R}_I}\right). \end{aligned} \tag{2.88}$$

Note that $V_{\text{loc}}\,(\mathbf{r})$ is applied to all angular momenta larger than $\ell_{\max}$, the maximum angular momentum included in the nonlocal part.

2.3.6 Transferability tests

The energy range in which the logarithmic derivatives coincide give an estimate of the pseudopotential quality. However, the logarithmic derivative is calculated at fixed charge density. Before using the pseudopotential in the solid, we can check its transferability on the atom by predicting the eigenvalues and the total energy of atomic configurations different from the reference one used for the generation. We can also check spin-polarized atomic configurations. An accuracy of a few mRy on the eigenvalues of atomic configurations that differ in energy up to a few Ry from the reference configuration is within the possibilities of the method.

2.3.7 Fully separable pseudopotentials

The semilocal form of the pseudopotential is not very efficient for practical calculations. It requires to keep in memory the matrix $\langle \mathbf{k}+\mathbf{G}\,|V_{ps}|\,\mathbf{k}+\mathbf{G}'\rangle$ that becomes rapidly big for large systems and matrix-vector multiplications to apply it to the wavefunctions. It is convenient to write the nonlocal part of the pseudopotential in the fully separable form [5]:

$$V_{NL}\left(\mathbf{r},\mathbf{r}'\right) = \sum_I \sum_{\ell m} E_\ell^I \left\langle \mathbf{r} \mid \beta_\ell^I Y_{\ell,m}^I \right\rangle \left\langle \beta_\ell^I Y_{\ell,m}^I \mid \mathbf{r}' \right\rangle. \tag{2.89}$$

In this way we can keep in memory only the vectors $\left\langle \mathbf{k}+\mathbf{G} \mid \beta_\ell^I Y_{\ell,m}^I \right\rangle$ which are the Fourier transform of $\left\langle \mathbf{r} \mid \beta_\ell^I Y_{\ell,m}^I \right\rangle$ and to apply the nonlocal pseudopotential by doing a few scalar products with the vectors which represent the wavefunction.

In the atom, we can define $\beta_\ell(r) = \Delta V_{ps,\ell}(r)\phi_\ell(r)$ and $E_\ell = \left[\int_0^\infty dr \phi_\ell(r)\Delta V_{ps,\ell}(r)\phi_\ell(r)\right]^{-1}$ so that the fully separable potential:

$$V_{NL} = E_\ell \left|\beta_\ell\right\rangle \left\langle\beta_\ell\right|, \tag{2.90}$$

has the following property:

$$\left\langle r \left| V_{NL} \right| \phi_\ell \right\rangle = \Delta V_{ps,\ell}(r)\phi_\ell(r). \tag{2.91}$$

As a consequence, the equation

$$\left[T_\ell + V_{\text{eff}}\left(r\right)\right]\Phi_\ell(r) + \left\langle r \left| V_{NL} \right| \Phi_\ell \right\rangle = \epsilon \Phi_\ell(r). \tag{2.92}$$

has ϵ_ℓ as an eigenvalue and $\phi_\ell(r)$ as an eigenfunction.

2.3.8 Ultrasoft pseudopotentials

Fitting the pseudopotential at more than one energy for each ℓ, one can relax the norm-conserving condition. The orbitals obey a generalized orthogonality constraint:

$$\left\langle \tilde{\psi}_i | S | \tilde{\psi}_j \right\rangle = \delta_{ij}. \tag{2.93}$$

The resulting Hamiltonian is the following:

$$H = -\frac{1}{2}\nabla^2 + \tilde{V}_{\text{eff}}\left(\mathbf{r}\right) + \sum_{I,mn}\left(\int d^3r \tilde{V}_{\text{eff}}\left(\mathbf{r}\right) Q_{mn}^I(\mathbf{r}) + D_{I,mn}^{(0)}\right)\left|\beta_m^I\right\rangle\left\langle\beta_n^I\right|, \tag{2.94}$$

and one solves a generalized eigenvalue equation:

$$H\left|\tilde{\psi}_i\right\rangle = \varepsilon_i S \left|\tilde{\psi}_i\right\rangle. \tag{2.95}$$

The augmentation functions:

$$Q_{mn}^I(\mathbf{r}) = \psi_m^{IAE}(\mathbf{r})\psi_n^{IAE}(\mathbf{r}) - \phi_m^{IPS}(\mathbf{r})\phi_n^{IPS}(\mathbf{r}) \tag{2.96}$$

are used to recover the correct charge density:

$$\rho(\mathbf{r}) = \sum_i \left|\tilde{\psi}_i(\mathbf{r})\right|^2 + \sum_{I,mn} Q_{mn}^I(\mathbf{r})\left\langle\tilde{\psi}_i \mid \beta_m^I\right\rangle\left\langle\beta_n^I \mid \tilde{\psi}_i\right\rangle. \tag{2.97}$$

2.3.9 PAW mapping: from pseudo-wave-functions to all-electron wave-functions

In the PAW scheme one starts from the following mapping between all-electron and pseudo wavefunction:

$$|\Psi_i\rangle = \left|\tilde{\Psi}_i\right\rangle + \sum_{I,m} \left[\left|\psi_m^{IAE}\right\rangle - \left|\phi_m^{IPS}\right\rangle\right] \left\langle \beta_m^I \mid \tilde{\Psi}_i \right\rangle. \tag{2.98}$$

and obtains that the expectation values of all-electrons operators O can be computed as the expectation values between pseudo wavefuctions of pseudo operators $\tilde{O}$ according to the

$$\langle \psi_{\mathbf{k}v} | O | \psi_{\mathbf{k}v} \rangle = \left\langle \tilde{\psi}_{\mathbf{k}v} \middle| \tilde{O} \middle| \tilde{\psi}_{\mathbf{k}v} \right\rangle. \tag{2.99}$$

$$\tilde{O} = O + \sum_{Imn} |\beta_m^I\rangle \left(\left\langle \psi_m^{IAE} \middle| O \middle| \psi_n^{IAE} \right\rangle - \left\langle \varphi_m^{IPS} \middle| O \middle| \varphi_n^{IPS} \right\rangle \right) \left\langle \beta_n^I \right|. \tag{2.100}$$

When

$$O \to 1, \tag{2.101}$$

we obtain the pseudo operator,

$$S = 1 + \sum_{Imn} q_{mn}^I \left|\beta_m^I\right\rangle \left\langle \beta_n^I \right|. \tag{2.102}$$

When

$$O \to |\mathbf{r}\rangle \langle \mathbf{r}|, \tag{2.103}$$

we get

$$\rho = \tilde{\rho} + \rho^{(1)} + \tilde{\rho}^{(1)}. \tag{2.104}$$

$$\rho = \sum_{\mathbf{k}v} \left|\tilde{\psi}_{\mathbf{k}v}\right|^2. \tag{2.105}$$

$$\rho^{(1)} = \sum_{Imn} \rho_{mn}^I \psi_m^{IAE}(\mathbf{r}) \psi_n^{IAE}(\mathbf{r}). \tag{2.106}$$

$$\tilde{\rho}^{(1)} = \sum_{Imn} \rho_{mn}^I \varphi_m^{IPS}(\mathbf{r}) \varphi_n^{IPS}(\mathbf{r}). \tag{2.107}$$

where

$$\rho_{mn}^I = \sum_{\mathbf{k}v} \left\langle \tilde{\psi}_{\mathbf{k}v} | \beta_m^I \right\rangle \left\langle \beta_n^I | \tilde{\psi}_{\mathbf{k}v} \right\rangle. \tag{2.108}$$

2.3.10 PAW Hamiltonian

In the PAW scheme one still solves a generalized eigenvalue equation $(H - \epsilon_i S)\left|\tilde{\Psi}_i\right\rangle = 0$, with the Hamiltonian

$$H = -\frac{1}{2}\nabla^2 + \tilde{V}_{\text{eff}} + \sum_{I,mn} \left(\int d^3 r \tilde{V}_{\text{eff}}\,(\mathbf{r}) Q_{mn}^I(\mathbf{r}) + D_{I,mn}^1 - \tilde{D}_{I,mn}^1 \right) \left|\beta_m^I\right\rangle \left\langle \beta_n^I \right|, \tag{2.109}$$

where

$$
\begin{aligned}
D^1_{I,mn} &= \left\langle \psi^{I,AE}_m \left| \frac{\mathbf{p}^2}{2} + V^I_{\mathrm{KS}} \right| \psi^{I,AE}_n \right\rangle, \\
\tilde{D}^1_{I,mn} &= \left\langle \phi^{I,PS}_m \left| \frac{\mathbf{p}^2}{2} + \tilde{V}^I_{\mathrm{eff}} \right| \phi^{I,PS}_n \right\rangle + \int_{\Omega_I} d^3r \hat{Q}^I_{mn}(\mathbf{r}) \tilde{V}^I_{\mathrm{eff}}(\mathbf{r}).
\end{aligned}
\tag{2.110}
$$

Some contents in references [154, 76, 94, 98, 188, 17, 102, 186, 160] are included in this section.

2.4 Ab initio statistical thermodynamics

A crystal in thermal equilibrium at ambient conditions has the corresponding lattice structure that minimizes the Gibbs free energy. We can calculate this energy starting from the DFT energy, the phonon frequencies, and the band structure. In this section, we summarize the main thermodynamic relations used in this thesis.

The Beckmann diagram in Fig. 2.1 below represents the coupled interrelationships between the mechanical, thermal, and electrical properties of a crystal. In this diagram:

- the variables on the outer triangle represents intensive variables;
- the variables on the inner triangle represents extensive variables;
- the round brackets ( ) represents the ranks of the tensors of variables;
- the square brakets [ ] represents the ranks of tensors of properties between variables;

In this thesis we focus on the properties allocated in the pink trapezoid at the bottom of this triangle diagram, including thermal expansion $\beta(T,p)$, bulk modulus $B(T,p)$, isobaric heat capacity $C_p(T,p)$, elastic constants $C_{ijkl}(T,p)$ and so on.

2.4.1 The canonical partition function

Let us start from the canonical partition function of a solid. The vibrational energy of a solid whose phonon modes have frequencies $\omega_{\mathbf{q},\nu}$ depends on the number of phonons $n_{\mathbf{q},\nu}$ in each mode:

$$E_i = \sum_{\mathbf{q},\nu} \left(n_{\mathbf{q},\nu} + \frac{1}{2} \right) \hbar \omega_{\mathbf{q},\nu}, \tag{2.111}$$

where i indicates the set of integer numbers $n_{\mathbf{q},\nu}$. At a given temperature T the probability that the solid has a certain energy E_i can be calculated by statistical methods and it is:

$$P(E_i) = \frac{1}{Z} e^{-\beta E_i}, \tag{2.112}$$

where Z is the canonical partition function defined as

$$Z = \sum_i e^{-\beta E_i}, \tag{2.113}$$

the sum is over all the possible sets of integers $n_{\mathbf{q},\nu}$ and $\beta = 1/K_B T$ (K_B is the Boltzmann constant). We can write

$$Z = \sum_i e^{-\beta E_i} = \prod_{\mathbf{q},\nu} \left(\sum_{n=0}^{\infty} e^{-(n+1/2)\beta\hbar\omega_{\mathbf{q},\nu}} \right). \tag{2.114}$$

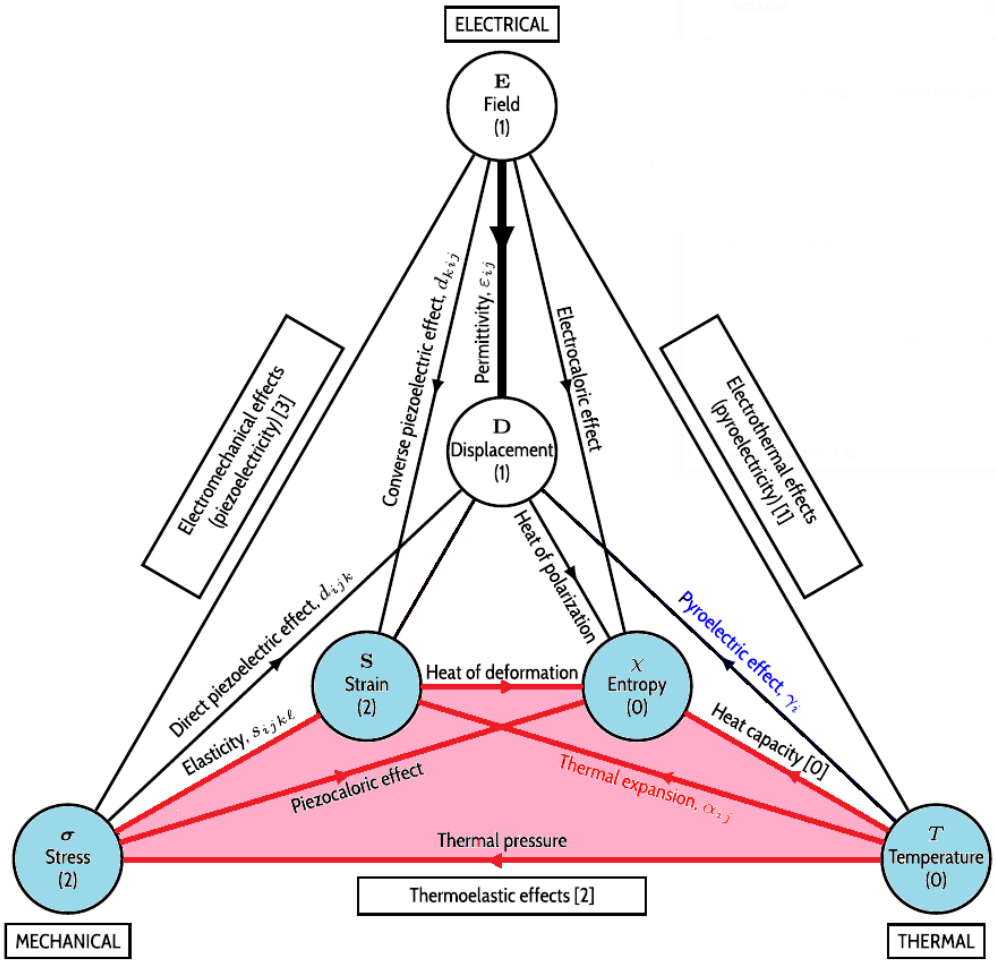

Figure 2.1: Equilibrium properties in a crystal: Beckmann diagram. (Based on figures seen in Ref.[144] and Ref.[104])

Making the sum over n and taking the logarithm gives:

$$\begin{aligned}\ln Z &= \sum_{\mathbf{q},\nu} \ln\left[\frac{e^{-\frac{1}{2}\beta\hbar\omega_{\mathbf{q},\nu}}}{1-e^{-\beta\hbar\omega_{\mathbf{q},\nu}}}\right] = -\sum_{\mathbf{q},\nu} \ln\left[2\sinh\left(\frac{\beta\hbar\omega_{\mathbf{q},\nu}}{2}\right)\right] \\ &= -\beta\sum_{\mathbf{q},\nu}\frac{\hbar\omega_{\mathbf{q},\nu}}{2} - \sum_{\mathbf{q},\nu}\ln\left[1-e^{-\beta\hbar\omega_{\mathbf{q},\nu}}\right].\end{aligned} \tag{2.115}$$

2.4.2 The thermodynamic functions

Using the expression of $\ln Z$ in terms of the phonon frequencies, the vibrational energy per cell becomes:

$$U = \frac{1}{N}\sum_i E_i P(E_i) = -\frac{1}{N}\frac{\partial \ln Z}{\partial \beta} = \frac{1}{N}\sum_{\mathbf{q},\nu}\frac{\hbar\omega_{\mathbf{q},\nu}}{2} + \frac{1}{N}\sum_{\mathbf{q},\nu}\frac{\hbar\omega_{\mathbf{q},\nu}}{e^{\beta\hbar\omega_{\mathbf{q},\nu}-1}}, \tag{2.116}$$

while the Helmholtz free energy per cell becomes

$$F = -\frac{1}{N}\frac{\ln Z}{\beta} = \frac{1}{N}\sum_{\mathbf{q},\nu}\frac{\hbar\omega_{\mathbf{q},\nu}}{2} + \frac{1}{N\beta}\sum_{\mathbf{q},\nu}\ln\left[1 - e^{-\beta\hbar\omega_{\mathbf{q},\nu}}\right], \tag{2.117}$$

or

$$F = \frac{1}{N\beta}\sum_{\mathbf{q},\nu}\ln\left[2\sinh\left(\frac{\beta\hbar\omega_{\mathbf{q},\nu}}{2}\right)\right]. \tag{2.118}$$

The entropy per cell can be computed as:

$$S = \frac{1}{T}(U - F), \tag{2.119}$$

while the isochoric heat capacity is:

$$\begin{aligned} C_V = \frac{\partial U}{\partial T} &= \frac{1}{N}\sum_{\mathbf{q},\nu}\hbar\omega_{\mathbf{q},\nu}\frac{\partial}{\partial T}\left[\frac{1}{e^{\beta\hbar\omega_{\mathbf{q},\nu}} - 1}\right] \\ &= \frac{K_B}{N}\sum_{\mathbf{q},\nu}\left[\frac{\beta\hbar\omega_{\mathbf{q},\nu}}{2\sinh\left(\beta\hbar\omega_{\mathbf{q},\nu}/2\right)}\right]^2. \end{aligned} \tag{2.120}$$

Introducing the phonon density of states per cell:

$$g(\omega) = \frac{1}{N}\sum_{\mathbf{q},\nu}\delta\left(\omega - \omega_{\mathbf{q},\nu}\right) \tag{2.121}$$

we can write the thermodynamic fuctions as one dimensional integrals over the frequencies:

$$\begin{aligned} U &= \int_0^\infty d\omega g(\omega)\frac{\hbar\omega}{2} + \int_0^\infty d\omega g(\omega)\frac{\hbar\omega}{e^{\beta\hbar\omega} - 1}, \\ F &= \frac{1}{\beta}\int_0^\infty d\omega g(\omega)\ln\left[2\sinh\left(\frac{\beta\hbar\omega}{2}\right)\right]. \end{aligned} \tag{2.122}$$

The isochoric heat capacity of one unit cell:

$$\begin{aligned} C_V = \left.\frac{\partial U}{\partial T}\right|_V &= K_B\int_0^\infty d\omega g(\omega)\left[\frac{\beta\hbar\omega/2}{\sinh\left(\frac{\beta\hbar\omega}{2}\right)}\right]^2 \\ &= K_B\int_0^\infty d\omega g(\omega)e^{\beta\hbar\omega}\left[\frac{\beta\hbar\omega}{e^{\beta\hbar\omega} - 1}\right]^2. \end{aligned} \tag{2.123}$$

All these functions are plotted by the `thermo_pw` software after a phonon dispersion calculation. Some other codes that compute these quantities from the phonon density of states are available inside the QE package or on the internet. Before computing these thermodynamic properties for a solid, it is essential to check that there is no imaginary frequencies so that the system is dynamically stable.

2.4.3 Volume as a function of temperature

We consider a solid at temperature T and at pressure p. If the volume of the solid changes by $d\Omega$ the solid does a work $pd\Omega$ against the pressure p. To keep the temperature constant the solid absorbs some heat dQ. According to the second law of thermodynamic $dQ = TdS$ where S is the entropy. According to the first law of thermodynamic the change of the internal energy is equal to the adsorbed heat minus the work done $dU = TdS - pd\Omega$. Therefore, at constant temperature:

$$p = -\left(\frac{dU}{d\Omega} - T\frac{dS}{d\Omega}\right)\Big|_T = -\left.\frac{\partial F(\Omega,T)}{\partial \Omega}\right|_T. \tag{2.124}$$

At temperature T and zero pressure, the solid is in equilibrium at the volume Ω that minimizes the free energy. The total free energy per unit cell of volume Ω is:

$$F(\Omega,T) = U_0(\Omega) + F_{ph}(\Omega,T) + F_{el}, \tag{2.125}$$

where $U_0(\Omega)$ is the DFT total energy, $F_{ph}(\Omega,T)$ is the vibrational free energy, and F_{el} is the electron excitation energy, needed only for metals and computed from the electron density of states.

Within the quasi-harmonic approximation the vibrational free energy depends on volume since the phonon frequencies depend on volume.

Minimizing $F(\Omega,T)$ at each T, we obtain the equilibrium volume as a function of temperature, $\Omega_0(T)$.

2.4.4 Free energy minimization

Usually the minimization of the free energy is carried out by fitting it with an equation of state (EOS). EOS depends on the bulk modulus an on its derivertives with respect to pressure. The bulk modulus B_0^T is the inverse of the compressibility.

Calculated at constant temperature it is:

$$\frac{1}{B_0^T} = K^T = -\frac{1}{\Omega}\left(\frac{\partial \Omega}{\partial p}\right)_T. \tag{2.126}$$

A widely used EOS is the Murnaghan equation:

$$F(\Omega) = F(\Omega_0) + \frac{B_0\Omega}{B_0'}\left[\frac{1}{B_0'-1}\left(\frac{\Omega_0}{\Omega}\right)^{B_0'} + 1\right] - \frac{B_0\Omega_0}{B_0'-1}, \tag{2.127}$$

obtained assuming a constant derivative of the bulk modulus B_0' with respect to pressure, depends on Ω_0, B_0, and B_0'. For high pressure studies, we use forth-order Birch-Murnaghan equation:

$$E = a_0 + a_1 f + a_2 f^2 + a_3 f^3 + a_4 f^4 + \ldots, \tag{2.128}$$

where f is Eulerian finite strain:

$$f = -\varepsilon_{\mathrm{E2}} = \frac{1}{2}\left[\left(\frac{\Omega_0}{\Omega}\right)^{\frac{2}{3}} - 1\right]. \tag{2.129}$$

The state variables temperature, volume, and pressure are not independent quantities; they are connected by an implicit function:

$$f(P, \Omega, T) = 0 \tag{2.130}$$

At T = 0 K, pressure is the volume derivative of energy:

$$P = -\left(\frac{\partial E}{\partial \Omega}\right)_{T=0} \tag{2.131}$$

The bulk modulus and its derivatives are given by[93] [54]:

$$B_{T_0} = -\Omega \frac{dP}{d\Omega}, \qquad B'_{T_0} = \frac{dB_{T_0}}{dP}, \qquad B''_{T_0} = \frac{d^2 B_{T_0}}{dP^2}, \tag{2.132}$$

and we have:

$$a_0 = a_1 = 0, \tag{2.133}$$

$$a_2 = \frac{9}{2} B_0 \Omega_0, \tag{2.134}$$

$$a_3 = a_2(B'_0 - 4), \tag{2.135}$$

$$a_4 = a_2\left(\frac{9{B'_0}^2 - 63B'_0 + 9B_0 B''_0 + 143}{12}\right) \tag{2.136}$$

By fitting and minimizing the free energy at each temperature we obtain $\Omega_0(T), B_0^T(T)$, $B_0'^T(T)$, and $B_0''^T(T)$.

2.4.5 Volume thermal expansion

The volume thermal expansion is defined as:

$$\beta = \frac{1}{\Omega_0(T)} \frac{d\Omega_0(T)}{dT}. \tag{2.137}$$

It can be calculated by numerical differentition from $\Omega_0(T)$ deduced from the EOS or in terms of Grüneisen parameters. The Grüneisen parameters are defined by:

$$\gamma_{\mathbf{q},\nu} = -\frac{\Omega}{\omega_{\mathbf{q},\nu}} \frac{d\omega_{\mathbf{q},\nu}}{d\Omega}. \tag{2.138}$$

Thermal expansion in terms of Grüneisen parameters is:

$$\beta = \frac{1}{\Omega(T)}\frac{\partial \Omega(T)}{\partial T}\bigg|_p = -\frac{1}{\Omega(T)}\frac{\partial \Omega(T)}{\partial p(T)}\bigg|_T \frac{\partial p(T)}{\partial T}\bigg|_\Omega = -\frac{1}{B_0(T)}\frac{\partial^2 F(\Omega,T)}{\partial T \partial \Omega}. \tag{2.139}$$

Only the vibrational part of the free energy depends on T (the electronic excitations are discussed below). So we get :

$$\beta = \frac{1}{B_0(T)}\sum_{\mathbf{q},\nu} c_{\mathbf{q},\nu}\gamma_{\mathbf{q},\nu} \tag{2.140}$$

where $c_{\mathbf{q},\nu}$ is given by:

$$c_{\mathbf{q},\nu} = \frac{\hbar\omega_{\mathbf{q},\nu}}{\Omega}\frac{\partial}{\partial T}\left[\frac{1}{e^{\beta\hbar\omega_{\mathbf{q},\nu}}-1}\right]. \tag{2.141}$$

It is also common to define the average Grüneisen parameter as:

$$\gamma = \frac{\sum_{\mathbf{q},\nu} c_{\mathbf{q},\nu}\gamma_{\mathbf{q},\nu}}{\sum_{\mathbf{q},\nu} c_{\mathbf{q},\nu}}, \tag{2.142}$$

or, in terms of macroscopic quantities,

$$\gamma = \frac{\beta(T)B_0(T)\Omega}{C_V(T)}. \tag{2.143}$$

2.4.6 Isobaric heat capacity and isoentropic bulk modulus

From the definitions of C_p and C_v:

$$C_p - C_v = \frac{dQ}{dT}\bigg|_P - \frac{dQ}{dT}\bigg|_V, \tag{2.144}$$

Substitution of the definition of entropy gives the following:

$$C_p - C_v = T\left[\frac{\partial S}{\partial T}\bigg|_P - \frac{\partial S}{\partial T}\bigg|_V\right]. \tag{2.145}$$

These partials are converted from the total differential obtained from $S = f(T,V)$:

$$dS = \frac{\partial S}{\partial T}\bigg|_V dT + \frac{\partial S}{\partial V}\bigg|_T dV, \tag{2.146}$$

which when divided by dT at $\mathrm{dP} = 0$, it becomes:

$$\frac{\partial S}{\partial T}\bigg|_P - \frac{\partial S}{\partial T}\bigg|_V = \frac{\partial S}{\partial V}\bigg|_T \frac{\partial V}{\partial T}\bigg|_P. \tag{2.147}$$

Substituting 2.147 into 2.145 gives

$$C_p - C_v = T\frac{\partial S}{\partial V}\bigg|_T \frac{\partial V}{\partial T}\bigg|_P. \tag{2.148}$$

The Maxwell Relationship $\frac{\partial S}{\partial V}\Big|_T = \frac{\partial P}{\partial T}\Big|_V$ further transforms 2.148 to

$$C_p - C_v = T\frac{\partial P}{\partial T}\bigg|_V \frac{\partial V}{\partial T}\bigg|_P. \tag{2.149}$$

The total differential from $P = (T, V)$ at $\mathrm{dP} = 0$ gives:

$$0 = \frac{\partial P}{\partial V}\bigg|_T \frac{\partial V}{\partial T}\bigg|_P + \frac{\partial P}{\partial T}\bigg|_V, \tag{2.150}$$

and

$$\frac{\partial P}{\partial T}\bigg|_V = -\frac{\partial P}{\partial V}\bigg|_T \frac{\partial V}{\partial T}\bigg|_P = -\frac{\frac{\partial V}{\partial T}\big|_P}{\frac{\partial V}{\partial P}\big|_T} = \beta B_T. \tag{2.151}$$

Therefore, 2.149 can be written as

$$Cp - Cv = \beta^2 TV B_T. \tag{2.152}$$

Using $p(V,T)$, obtained by deriving the fitted free energy, we compute the isothermal bulk modulus:

$$B_T(V,T) = -V\frac{\partial p(V,T)}{\partial V}\bigg|_T, \tag{2.153}$$

the adiabatic bulk modulus:

$$B_S(V,T) = -V\frac{\partial p(V,T)}{\partial V}\bigg|_S, \tag{2.154}$$

The relation between B_T and B_S is given by:

$$B_S(p,T) = B_T(V,T) + \frac{\beta(p,T)^2 B_T(V,T)^2 VT}{C_V(V,T)}. \tag{2.155}$$

The difference between the bulk modulus measured at constant entropy (without heat exchange) or at constant temperature can be obtained as:

$$\frac{1}{B_0^S} - \frac{1}{B_0^T} = -\frac{T\Omega\beta^2}{C_P}, \tag{2.156}$$

Inserting in the second equation $T\Omega\beta^2$ from the 2.152, one finds:

$$\frac{B_0^S}{B_0^T} = \frac{C_P}{C_V}. \tag{2.157}$$

2.4.7 Thermal equation of state

From the free energy at each T we can obtain the following:

$$p(\Omega,T) = -\frac{\partial F(\Omega,T)}{\partial \Omega} \tag{2.158}$$

which is the thermal equation of state. It is also possible to minimize (for each p) the auxiliary function:

$$G_p(\Omega,T) = F(\Omega,T) + p\Omega \tag{2.159}$$

obtaining the function $\Omega(p,T)$. This equation remains valid when F depends on several crystal parameters in anisotropic solids and can be generalized for a generic strain.

The volume that minimizes $G_p(V,T)$ is the volume at pressure p and temperature T, written as $V(p,T)$. Using $V(p,T)$ we obtain the volume thermal expansion $\beta_V(p,T)$ at pressure p as:

$$\beta_V(p,T) = \frac{1}{V(p,T)} \frac{\partial V(p,T)}{\partial T}\bigg|_p . \tag{2.160}$$

2.4.8 Finite temperature electronic excitation energy

The electronic excitation energy due to the finite temperature U_{el} is negligible in semiconductors and insulators. For metals it gives a finite contribution to the heat capacity that we estimate by a model of independent electrons whose energy-wave vector dispersion is given by the band structure. We assume Fermi-Dirac occupations of the available electronic levels:

$$f(E,T,\mu) = \tilde{\theta}\left(\frac{\mu - E}{k_B T}\right), \tag{2.161}$$

where μ is the chemical potential and the function $\tilde{\theta}(x)$ is

$$\tilde{\theta}(x) = \frac{1}{1+e^{-x}}. \tag{2.162}$$

Given the density of electronic states $N(E)$, we determine the chemical potential $\mu(T)$ at each temperature from the condition

$$N_{el} = \int_{-\infty}^{\infty} N(E) f(E,T,\mu) dE, \tag{2.163}$$

where N_{el} is the number of electrons per unit cell. The electronic excitation energy U_{el} is given by

$$U_{el} = \int_{-\infty}^{\infty} E N(E) f(E,T,\mu) dE - \int_{-\infty}^{E_F} E N(E) dE, \tag{2.164}$$

where E_F is the Fermi energy. The electronic entropy is given:

$$S_{el} = -k_B \int_{-\infty}^{\infty} [f(E,T,\mu)\ln f(E,T,\mu) + (1-f(E,T,\mu))\ln(1-f(E,T,\mu))] N(E) dE. \tag{2.165}$$

The electron Helmholtz free-energy is calculated by $F_{el} = U_{el} - TS_{el}$. Finally the constant volume electronic specific heat capacity is estimated by:

$$C_{V,el} = \int_{-\infty}^{\infty} (E-\mu) N(E) \frac{\partial f(E,T,\mu)}{\partial T} dE, \tag{2.166}$$

where the partial derivative with respect to the temperature:

$$\frac{\partial f(E,T,\mu)}{\partial T} = \frac{E-\mu}{k_B T^2} \tilde{\theta}' \left(\frac{\mu - E}{k_B T} \right) \tag{2.167}$$

indicates that, in computing the derivative, we neglect the temperature dependence of the chemical potential, and

$$\bar{\theta}'(x) = \frac{1}{1 + e^x + e^{-x}}. \tag{2.168}$$

2.4.9 Strain and stress

For anisotropic solids the previous approach is still valid. However for a certain volume there are several independent crystallographic parameters to be determined. For tetragonal, hexagonal, and trigonal solids there are two parameters ($a, c/a$, or $a, \cos\alpha$). For orthorombic solids we have three lattice parameters (a, b/a, and c/a). For monoclinic solids there are four ($a, b/a, c/a, \cos\gamma$), and for triclinic solids six parameters ($a, b/a, c/a, \cos\alpha, \cos\beta, \cos\gamma$).

There are three approaches:

- Change only a and keep all angles and ratios constant. This is a simple but quite approximated way.
- Optimize all the parameters at $T = 0$ K and fix the volume so that the stress is a uniform pressure. This is the so-called V-ZSISA approximation (volume-constrained zero static internal stress approximation), which is less approximated than the option above.
- Compute the free energy as a function of all crystal parameters, and optimize them at each T. This is called full free energy minimization (FFEM). This is an exact but heavy approach which provides us the accurate numerical solution within the quasi-harmonic approximation.

Instead of changing the volume, we change the size and the shape of the unit cell. The strain applied to a solid is described by a symmetric 3×3 tensor $\epsilon_{i,j}$. Calling $\mathbf{a}_1, \mathbf{a}_2, \mathbf{a}_3$ the primitive vectors of the unperturbed solid, and $\mathbf{a}'_1, \mathbf{a}'_2, \mathbf{a}'_3$ those of the strained solid, we have:

$$\mathbf{a}'_{j,i} = \mathbf{a}_{j,i} + \sum_{k=1}^{3} \epsilon_{j,k} \mathbf{a}_{k,i}, \tag{2.169}$$

Since $\epsilon_{j,k}$ is a symmetric tensor we can describe it with the Voigt notation where $\epsilon_1 = \epsilon_{1,1}, \epsilon_2 = \epsilon_{2,2}, \epsilon_3 = \epsilon_{3,3}, \epsilon_4 = 2\epsilon_{2,3}$, $\epsilon_5 = 2\epsilon_{1,3}$, and $\epsilon_6 = 2\epsilon_{1,2}$.

We call stress $\sigma_{i,j}$ the force ($\mathbf{f}$) per unit area A_j (j indicates the perpendicular to the surface) present in a solid. The work per cell made by a solid with a stress $\sigma_{i,j}$ to change its strain by $d\epsilon_{i,j}$ is $dW = -\Omega \sum_{i,j} \sigma_{i,j} d\epsilon_{i,j}$, where Ω is the unperturbed unit cell volume.

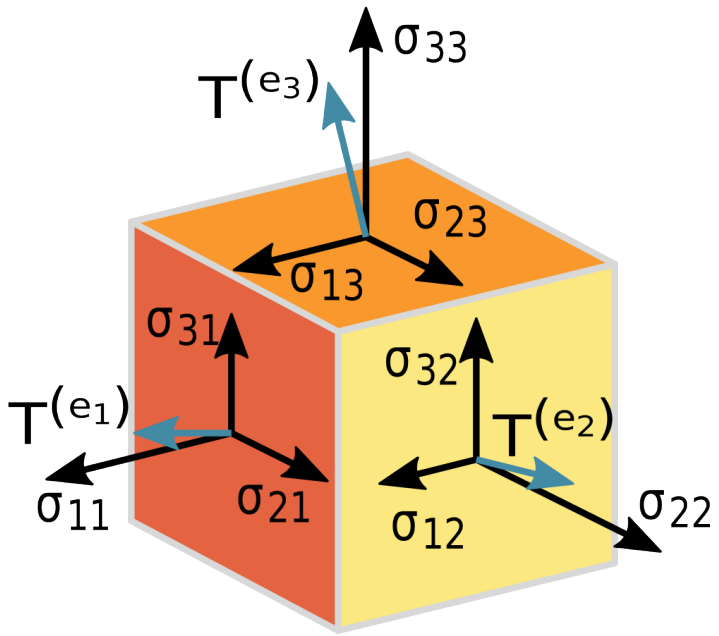

Figure 2.2: The forces on the faces of a unit cube in a homogeneously stressed body. [1]

2.4.10 Uniform pressure

A uniform pressure corresponds to a diagonal stress ($\sigma_{i,j} = 0$ for $i \neq j$) with:

$$\sigma_{i,i} = -p; \quad p = -\frac{1}{3}\operatorname{tr}(\sigma_{i,j}) = -\frac{1}{3}\sum_{i=1}^{3}\sigma_{i,i}. \tag{2.170}$$

The work made by the solid becomes:

$$dW = -\Omega\sum_{i,j}\sigma_{i,j}d\epsilon_{i,j} = \Omega p\sum_{i=1}^{3}d\epsilon_{i,i} = pd\Omega. \tag{2.171}$$

2.4.11 Equation of state

When the strain of the solid changes of $d\epsilon_{i,j}$, at constant T and stress $\sigma_{i,j}$, the solid makes some work and adsorb some heat to keep the temperature constant so the internal energy of the solid changes as:

$$dU = TdS + \Omega\sum_{i,j}\sigma_{i,j}d\epsilon_{i,j} \tag{2.172}$$

From this equation we obtain the equation of state (at constant temperature):

$$\sigma_{i,j} = \frac{1}{\Omega}\left(\frac{\partial U}{\partial\epsilon_{i,j}} - T\frac{\partial S}{\partial\epsilon_{i,j}}\right)_T = \frac{1}{\Omega}\frac{\partial F}{\partial\epsilon_{i,j}}\bigg|_T. \tag{2.173}$$

For a solid with no stress, the strain minimizes the Helmholtz free energy.

2.4.12 Crystal parameters as functions of the temperature and thermal expansion

Considering only strains that do not change the Bravais lattice, we fit the free energy with a quadratic or quartic polynomial of the crystal parameters and minimize it. From the minimum we obtain $a(T), b(T), c(T)$ etc. Thermal expansion measures the strain induced by a change of temperature at constant stress:

$$\alpha_{ij} = \left.\frac{\partial \epsilon_{ij}}{\partial T}\right|_{\sigma}. \tag{2.174}$$

In order to relate the thermal expansion tensor to the change of crystal parameters, we can use the following considerations. If $\vec{\mathbf{l}}$ is a vector in a given direction, the thermal expansion in that direction is:

$$\alpha_{\mathbf{l}} = \sum_{ij} \alpha_{ij} l_i l_j \tag{2.175}$$

Taking $\vec{\mathbf{l}}$ perpendicular to a set of lattice planes whose distance is h, we also have:

$$\alpha_{\mathbf{l}} = \frac{1}{h}\frac{dh}{dT}. \tag{2.176}$$

In a cubic solid taking $\mathbf{l} = (1,0,0)$ we have $\alpha_{\mathbf{l}} = \alpha_{11}$ and $h = a$ or $h = a/2$ so

$$\alpha_{11} = \frac{1}{a(T)}\frac{da(T)}{dT}. \tag{2.177}$$

In a tetragonal, hexagonal or trigonal solid taking $\mathbf{l} = (1,0,0)$ or $\mathbf{l} = (0,0,1)$ we have:

$$\alpha_{11} = \frac{1}{a(T)}\frac{da(T)}{dT}, \tag{2.178}$$

$$\alpha_{33} = \frac{1}{c(T)}\frac{dc(T)}{dT}. \tag{2.179}$$

In an orthorombic solid taking $\mathbf{l} = (1,0,0), \mathbf{l} = (0,1,0)$, or $\mathbf{l} = (0,0,1)$ we have:

$$\alpha_{11} = \frac{1}{a(T)}\frac{da(T)}{dT}, \tag{2.180}$$

$$\alpha_{22} = \frac{1}{b(T)}\frac{db(T)}{dT}, \tag{2.181}$$

$$\alpha_{33} = \frac{1}{c(T)}\frac{dc(T)}{dT}. \tag{2.182}$$

From the thermal expansion tensor, we can derive the volume thermal expansion:

$$\beta = \left.\frac{1}{\Omega}\frac{\partial \Omega}{\partial T}\right|_{p} = \left.\sum_{i=1}^{3}\frac{\partial \epsilon_{i,i}}{\partial T}\right|_{\sigma} = \sum_{i=1}^{3}\alpha_{i,i} = \mathrm{Tr}(\alpha). \tag{2.183}$$

2.4.13 Isothermal elastic constants and compliances

The concepts that generalize to anisotropic solids the bulk modulus and the compressibility are the elastic constants and compliances. The elastic constants, at finite temperature, are defined as the stress induced by a strain:

$$C^T_{ijkl} = \left.\frac{\partial \sigma_{ij}}{\partial \epsilon_{k,l}}\right|_T, \tag{2.184}$$

The inverse of the elastic tensor are called elastic compliances that measure the strain induced by a stress:

$$S^T_{ijkl} = \left.\frac{\partial \epsilon_{ij}}{\partial \sigma_{k,l}}\right|_T, \tag{2.185}$$

We compute the elastic constants from:

$$C^T_{ijkl} = \left.\frac{\partial^2 F}{\partial \epsilon_{ij} \partial \epsilon_{kl}}\right|_T, \tag{2.186}$$

correcting for finite pressure effects to obtain the stress-strain ECs: [14]

$$C^T_{ijkl} = \tilde{C}^T_{ijkl} + \frac{p}{2}\left(2\delta_{i,j}\delta_{k,l} - \delta_{i,l}\delta_{j,k} - \delta_{i,k}\delta_{j,l}\right). \tag{2.187}$$

The second derivatives of the free energy are calculated as described in Ref. [119] taking a subset of the volumes V_i as equilibrium configurations. The ECs at any other volume at temperature T and pressure p are obtained by interpolation by a fourth-degree polynomial.

2.4.14 Thermal expansion from Grüneisen parameters

Using these quantities we can determine the thermal expansion from Grüneisen parameters. Define the mode Grüneisen parameters as:

$$\gamma^{ij} = -\frac{1}{\omega_{\mathbf{q}\nu}} \frac{d\omega_{\mathbf{q}\nu}}{d\epsilon_{ij}}. \tag{2.188}$$

So we have

$$\alpha_{ij} = \left.\frac{d\epsilon_{ij}}{dT}\right|_\sigma = -\sum_{kl} \left.\frac{\partial \epsilon_{ij}}{\partial \sigma_{kl}}\right|_T \left.\frac{\partial \sigma_{kl}}{\partial T}\right|_\epsilon = -\frac{1}{\Omega}\sum_{kl} S^T_{ijkl} \frac{\partial^2 F}{\partial \epsilon_{kl} \partial T}, \tag{2.189}$$

therefore,

$$-\frac{1}{\Omega}\frac{\partial^2 F}{\partial \epsilon_{ij} \partial T} = \sum_{\mathbf{q}\upsilon} C_{\mathbf{q}\nu} \gamma^{ij}_{\mathbf{q}\upsilon}, \tag{2.190}$$

$$\alpha_{ij} = \sum_{kl} S^T_{ijkl} \sum_{\mathbf{q}\nu} C_{\mathbf{q}\nu} \gamma^{ij}_{\mathbf{q}\nu}. \tag{2.191}$$

2.4.15 Constant stress heat capacity

Then we use these quantities to derive the relationship between constant stress and constant strain heat capacity. We have:

$$dS = \sum_{ij} \left.\frac{\partial S}{\partial \epsilon_{ij}}\right|_T d\epsilon_{ij} + \left.\frac{\partial S}{\partial T}\right|_\epsilon dT = \sum_{ij} \left.\frac{\partial S}{\partial \sigma_{ij}}\right|_T d\sigma_{ij} + \left.\frac{\partial S}{\partial T}\right|_\sigma dT \tag{2.192}$$

Dividing both sides of equation by dT, assuming a constant stress condition, and multiplying by T we have:

$$C_\sigma - C_\epsilon = T \sum_{ij} \left.\frac{\partial S}{\partial \epsilon_{ij}}\right|_T \left.\frac{\partial \epsilon_{ij}}{\partial T}\right|_\sigma \tag{2.193}$$

We know that $dU = TdS + \Omega \sum_{ij} \sigma_{ij} d\epsilon_{ij}$ and $dF = -SdT + \Omega \sum_{ij} \sigma_{ij} d\epsilon_{ij}$ and $S = -\left.\frac{\partial F}{\partial T}\right|_\epsilon$, then

$$\begin{aligned} C_\sigma - C_\epsilon &= -T \sum_{ij} \frac{\partial^2 F}{\partial \epsilon_{ij} \partial T} \left.\frac{\partial \epsilon_{ij}}{\partial T}\right|_\sigma \\ &= -\Omega T \sum_{ij} \left.\frac{d\sigma_{ij}}{\partial T}\right|_\epsilon \left.\frac{\partial \epsilon_{ij}}{\partial T}\right|_\sigma \\ &= -\Omega T \sum_{ijkl} \left.\frac{\partial \sigma_{ij}}{\partial T}\right|_\epsilon \left.\frac{\partial T}{\partial \epsilon_{kl}}\right|_\sigma \left.\frac{\partial \epsilon_{ij}}{\partial T}\right|_\sigma \left.\frac{\epsilon_{ij}}{\partial T}\right|_\sigma \\ &= \Omega T \sum_{ijkl} \left.\frac{\partial \sigma_{ij}}{\partial \epsilon_{kl}}\right|_T \left.\frac{\partial \epsilon_{kl}}{\partial T}\right|_\sigma \left.\frac{\partial \epsilon_{ij}}{\partial T}\right|_\sigma, \end{aligned} \tag{2.194}$$

therefore,

$$\begin{aligned} C_\sigma - C_\epsilon &= \Omega T \sum_{ijkl} C^T_{ijkl} \left.\frac{\partial \epsilon_{ij}}{\partial T}\right|_\sigma \left.\frac{\partial \epsilon_{kl}}{\partial T}\right|_\sigma \\ &= \Omega T \sum_{ijkl} \alpha_{ij} C^T_{ijkl} \alpha_{kl}. \end{aligned} \tag{2.195}$$

2.4.16 Adiabatic elastic compliances

Express $d\epsilon_{ij}$ as a function of stress and entropy or of stress and temperature we get:

$$\begin{aligned} d\epsilon_{ij} &= \sum_{kl} \left.\frac{\partial \epsilon_{ij}}{d\sigma_{kl}}\right|_T d\sigma_{kl} + \left.\frac{\partial \epsilon_{ij}}{\partial T}\right|_\sigma dT, \\ &= \sum_{kl} \left.\frac{\partial \epsilon_{ij}}{\partial \sigma_{kl}}\right|_S d\sigma_{kl} + \left.\frac{\partial \epsilon_{ij}}{\partial S}\right|_\sigma dS. \end{aligned} \tag{2.196}$$

By dividing for $d\sigma_{kl}$ with constant entropy,

$$S^S_{ijkl} - S^T_{ijkl} = \left.\frac{\partial \epsilon_{ij}}{\partial T}\right|_\sigma \left.\frac{\partial T}{\partial \sigma_{kl}}\right|_S, \tag{2.197}$$

Introducing the enthalphy of the solid:

$$H = U - \Omega \sum_{ij} \sigma_{ij} \epsilon_{ij} \tag{2.198}$$

we get:

$$\begin{aligned} dH &= TdS + \Omega \sum_{ij} \sigma_{ij} d\epsilon_{ij} - \Omega \sum_{ij} \sigma_{ij} d\epsilon_{ij} - \Omega \sum_{ij} d\sigma_{ij} \epsilon_{ij} \\ &= TdS - \Omega \sum_{ij} d\sigma_{ij} \epsilon_{ij}. \end{aligned} \tag{2.199}$$

$\therefore$

$$\begin{aligned} S^S_{ijkl} - S^T_{ijkl} &= \alpha_{ij} \frac{\partial^2 H}{\partial \sigma_{kl} \partial S} \\ &= -\alpha_{ij} \Omega \left. \frac{\partial \epsilon_{kl}}{\partial S} \right|_\sigma \left. \frac{\partial S}{\partial T} \right|_\sigma \frac{1}{\left. \frac{\partial S}{\partial T} \right|_\sigma} \\ &= -\alpha_{ij} \Omega \left. \frac{\partial \epsilon_{kl}}{\partial T} \right|_\sigma \frac{T}{C_\sigma}. \end{aligned} \tag{2.200}$$

Finally, the difference between the isoentropic and isothermal elastic compliances is:

$$S^S_{ijkl} - S^T_{ijkl} = -\frac{T \Omega \alpha_{ij} \alpha_{kl}}{C^\sigma} \tag{2.201}$$

2.4.17 Adiabatic elastic constants

Similarilly, isoentropic elastic constants can be calculated from the stress as function of strain and entropy or of strain and temperature. Here we have:

$$\begin{aligned} d\sigma_{ij} &= \sum_{kl} \left. \frac{\partial \sigma_{ij}}{\partial \epsilon_{kl}} \right|_T d\epsilon_{kl} + \left. \frac{\partial \sigma_{ij}}{\partial T} \right|_\epsilon dT \\ &= \sum_{kl} \left. \frac{\partial \sigma_{ij}}{\partial \epsilon_{kl}} \right|_S d\epsilon_{kl} + \left. \frac{\partial \sigma_{ij}}{\partial S} \right|_\epsilon dS. \end{aligned} \tag{2.202}$$

Dividing both sides by $d\epsilon_{kl}$ at constant entropy,

$$C^S_{ijkl} - C^T_{ijkl} = \left. \frac{\partial \sigma_{ij}}{\partial T} \right|_\epsilon \left. \frac{\partial T}{\partial \epsilon_{kl}} \right|_S, \tag{2.203}$$

$\because$

$$\left. \frac{\partial T}{\partial \epsilon_{kl}} \right|_S = \frac{\partial^2 U}{\partial \epsilon_{kl} \partial S} = \Omega \left. \frac{\partial \sigma_{kl}}{\partial S} \right|_\epsilon, \tag{2.204}$$

$\therefore$

$$C^S_{ijkl} - C^T_{ijkl} = b_{ij} \Omega \left. \frac{\partial \sigma_{kl}}{\partial S} \right|_\epsilon \left. \frac{\partial S}{\partial T} \right|_\epsilon \frac{1}{\left. \frac{\partial S}{\partial T} \right|_\epsilon}, \tag{2.205}$$

The difference between the isoentropic and isothermal elastic constants is:

$$C^S_{ijkl} - C^T_{ijkl} = \frac{T\Omega b_{ij} b_{kl}}{C_\epsilon}, \tag{2.206}$$

where b_{ij} is the thermal stress:

$$\begin{aligned} b_{ij} &= \left.\frac{\partial \sigma_{ij}}{\partial T}\right|_\epsilon \\ &= \sum_{kl} \left.\frac{\partial \sigma_{ij}}{\partial T}\right|_\epsilon \left.\frac{\partial T}{\partial \epsilon_{kl}}\right|_\sigma \left.\frac{\partial \epsilon_{kl}}{\partial T}\right|_\sigma \\ &= -\sum_{kl} C^T_{ijkl} \left.\frac{\partial \epsilon_{kl}}{\partial T}\right|_\sigma \\ &= -\sum_{kl} C^T_{ijkl} \alpha_{kl}. \end{aligned} \tag{2.207}$$

2.4.18 Polycrystalline averages

From the elastic constants of a solid it is possible to estimate those of a polycrystalline solid through the Voigt-Reuss-Hill method [135]. From the average elastic constants:

$$\langle C'_{11} \rangle = \frac{3}{15}(C_{11}+C_{22}+C_{33}) + \frac{2}{15}(C_{12}+C_{13}+C_{23}) + \frac{4}{15}(C_{44}+C_{55}+C_{66}), \tag{2.208}$$

$$\langle C'_{12} \rangle = \frac{1}{15}(C_{11}+C_{22}+C_{33}) + \frac{4}{15}(C_{12}+C_{13}+C_{23}) - \frac{2}{15}(C_{44}+C_{55}+C_{66}), \tag{2.209}$$

$$\langle C'_{44} \rangle = \frac{1}{15}(C_{11}+C_{22}+C_{33}) - \frac{1}{15}(C_{12}+C_{13}+C_{23}) + \frac{3}{15}(C_{44}+C_{55}+C_{66}), \tag{2.210}$$

one obtains the Voigt approximations of the Bulk modulus (B_V), of the Young modulus (E_V), of the shear modulus (G_V), and of the Poisson ratio (ν_V) as:

$$B_V = \frac{\langle C'_{11} \rangle + 2\langle C'_{12} \rangle}{3}, \tag{2.211}$$

$$E_V = \frac{(\langle C'_{11} \rangle - \langle C'_{12} \rangle)(\langle C'_{11} \rangle + 2\langle C'_{12} \rangle)}{\langle C'_{11} \rangle + \langle C'_{12} \rangle}, \tag{2.212}$$

$$G_V = \langle C'_{44} \rangle, \tag{2.213}$$

$$\nu_V = \frac{E_V}{2G_V} - 1. \tag{2.214}$$

The Reuss approximation of these quantities is given in terms of the elastic compliances:

$$B_R = \frac{1}{S_{11}+S_{22}+S_{33}+2S_{12}+2S_{13}+2S_{23}}, \tag{2.215}$$

$$E_R = \frac{15}{3(S_{11}+S_{22}+S_{33})+2(S_{12}+S_{13}+S_{23})+(S_{44}+S_{55}+S_{66})}, \tag{2.216}$$

$$G_R = \frac{15}{4(S_{11}+S_{22}+S_{33})-4(S_{12}+S_{13}+S_{23})+3(S_{44}+S_{55}+S_{66})}, \tag{2.217}$$

$$\nu_R = \frac{E_R}{2G_R} - 1. \tag{2.218}$$

Finally the Hill approximation is the average of the Voigt and Reuss estimates.

2.4.19 Sound velocities

From the Hill estimate of these quantities we obtain the average sound velocities:

$$V_P = \left[\frac{B_S + \frac{4G_S}{3}}{\rho}\right]^{1/2}, \tag{2.219}$$

$$V_S = \left[\frac{G_S}{\rho}\right]^{1/2}, \tag{2.220}$$

where V_P and V_S are the compressional and shear sound velocities and ρ is the density. We compute the polycrystalline average of the bulk modulus B_S, of the shear modulus G_S, of the Young's modulus E_S, and of the Poisson's ratio ν_S with adiabatic ECs. Sometimes it is useful to define the bulk sound velocity as:

$$V_B = \left[\frac{B_S}{\rho}\right]^{1/2}. \tag{2.221}$$

Using G_S and B_S, we calculate the Pugh ratio $P = G_S/B_S$ that provides a criterium to predict if a solid is ductile ($P < 0.57$) or brittle ($P > 0.57$). This section is learned from [12, 143, 46, 191].

Chapter 3

Tungsten

Tungsten, a body-centered-cubic (bcc) *5d*-metal, finds various applications, both pure and in alloys, due to its high melting point and corrosion resistance. It is expected to become a plasma facing material in thermonuclear fusion reactors [153] and is used as a high-pressure gauge in diamond anvil cells. [44] Its thermodynamic properties have been investigated by experiment, [44, 136, 170, 131, 19, 123, 185, 194, 27, 11, 10, 132, 79, 157, 51, 50] model theory, [48, 110, 158, 71] and ab-initio. [44, 43, 196, 74, 101]

The ECs and the bulk modulus of tungsten are known from ultrasonic experiments at room pressure up to 2073 K [54, 115, 20] and have been calculated, at zero temperature, for several pressures. [101] However information on high pressure and high temperature thermoelastic properties of tungsten is still incomplete.

The pressure derivatives of the elastic constants at room temperature are known, [91] but only recently density as well as compressional and shear sound velocities have been measured by Qi et al. [158] in polycrystalline tungsten up to 1073 K and 105 kbar using ultrasonic interferometry and X-ray diffraction. These measurements give experimental values of the adiabatic bulk and shear moduli at high pressures and temperatures. So far these data have not been compared with ab-initio calculations, but such comparison is timely both to test the ab-initio methods at high pressure and to further support the experimental measurement. Unfortunately, temperature dependent elastic constants (TDECs) within the quasi-harmonic approximation are numerically heavy to compute and the examples in the literature are focused mainly on materials of geophysical interest.[88, 89] To our knowledge, no quasi-harmonic calculation of the TDECs of tungsten exists and theoretical results are presently limited to molecular dynamics based on embedded atom method potentials at room pressure. [126]

Table 3.1: The equilibrium lattice constants (a_0), the bulk moduli (B_T) and the pressure derivatives of the bulk moduli (B'_T) of tungsten calculated in this work compared with selected previous calculations and with experiment.

		T (K)	a_0 (a.u.)	B_T (kbar)	B'_T
This study	LDA	0	5.930	3398	3.97
		295	5.939	3330	4.02
	PBEsol	0	5.965	3276	3.98
		295	5.974	3210	4.01
	PBE	0	6.021	3073	4.01
		295	6.030	3008	4.05
Calc. [101]	PBE	0	6.016	3290	3.89
Calc. [157]	PBE	0	6.010	3068	4.10
Calc. [74]	PBE	0	6.026	3010	4.04
Calc. [192][1]	PBE	0	6.032		
Calc. [166][1]	LDA	0	5.959	3065	
Calc. [196]	LDA	0	5.936		
	PBE	0	6.030		
Calc. [96]	LDA	0	5.94	3370	
	PW91	0	6.02	3070	
Calc. [75]	LDA	0	5.939		
	PBEsol	0	5.975		
	PBE	0	6.030		
Model [48]		300	5.981	3060	4.18
Model [110]		300	5.981	3080	4.20
Expt. [132]		300	5.984	3070	4.32
Expt. [44]		300	5.982	2960	4.30
Expt. [54]		0		3142	
Expt. [92]				3084	4.5 [2]/3.9 [3]

[1] These data are used to calculate the equations of state reported in Fig. 3 of the supplementary material.
[2] Ultrasonic experiment.
[3] Shock wave experiment.

In this chapter we report an ab-initio investigation of the thermoelastic properties of tungsten extending this computational scheme to high pressures. We compute the temperature dependent isothermal ECs from the second strain derivatives of the Helmholtz free energy, including both the quasi-harmonic (QHA) vibrational term and the contribution

of electronic thermal excitations. These calculations, being carried out on several reference geometries at high and low pressures, can be used to interpolate the isothermal ECs at an arbitrary volume and therefore to study their temperature and pressure dependence. Adiabatic TDECs are calculated by thermodynamic relationships for comparison with experiments. From these ECs we derive the elastic parameters of polycrystalline tungsten, and compare with experiment.

Finally, from the density and the polycrystalline elastic parameters we determine the compressional and shear sound velocities that are compared with the results of Qi et al.. [158] We confirm some of the experimental results, but we also find some discrepancies that might require further theoretical and/or experimental investigations.

3.1 Computational parameters

In this paper we use `thermo_pw` [38] to calculate the thermodynamic properties.

Table 3.2: The 0 K elastic constants calculated with the different functionals compared with experiment and selected previous calculations. B, E, G, and ν are the bulk modulus, the Young's modulus, the shear modulus, and the Poisson's ratio, respectively.

	T (K)	a_0 (a.u.)	C_{11} (kbar)	C_{12} (kbar)	C_{44} (kbar)	B (kbar)	E (kbar)	G (kbar)	ν
LDA	0	5.930	5682	2201	1520	3362	4154	1605	0.294
PBEsol	0	5.965	5476	2131	1519	3246	4076	1579	0.291
PBE	0	6.021	5140	1997	1444	3045	3852	1494	0.289
PBE [157]	0	6.010	5285	1934	1487	3051	3997	1559	0.282
PBE [101]	0	6.016	5130	1990	1400	3037	3788	1466	0.292
LDA [166]	0	5.981	5289	1953	1705	3065	4283	1690	0.267
expt.[115]	0 (extr.)	5.972	5321	2047	1638	3138	4184	1637	0.277
expt.[115]	273.15		5235	2045	1608	3108	4103	1603	0.280
expt.[54]	0	5.972	5326	2050	1631	3142	4178	1634	0.278

The calculations of the TDECs presented in this work were done by using DFT implemented in Quantum ESPRESSO [60, 59] with the PBE [149] exchange and correlation functional. In addition, we present also some results using the LDA [152] and PBEsol, [150] a functional that, modifying the PBE exchange, gives a better description of solids [168] at the expense of the accuracy in molecules. We employ the projector augmented wave (PAW) method [17] and a plane-wave basis with pseudopotentials generated by us starting from those available in `pslibrary`. [37, 35] We called these pseudopotentials `W.pz-spn-kjpaw_psl.1.0.1.UPF`, `W.pbesol-spn-kjpaw_psl.1.0.1.UPF`, and `W.pbe-spn-kjpaw_psl.1.0.1.UPF` for LDA, PBEsol,

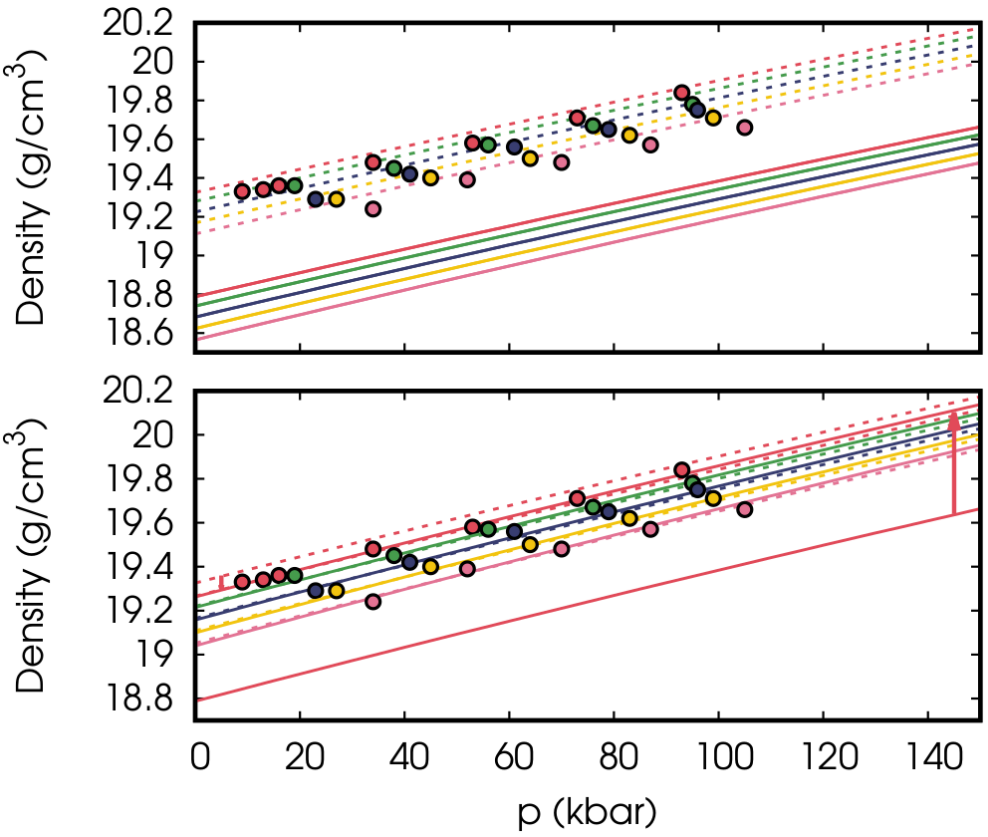

Figure 3.1: Upper: Pressure dependent PBEsol (dashed lines) and PBE (solid lines) density calculated for several temperatures (red 298 K, green 473 K, blue 673 K, yellow 873 K, and pink 1073 K) compared with the experimental data of Qi et al. [158]. Lower: The PBE density is shown after a shift of $\Delta\rho = 0.475$ g/cm^3 (indicated by the red arrow on the line at 298 K) to facilitate the comparison with experiment. The dashed lines are the PBEsol curves after a shift of -0.06 g/cm^3 also shown by a red arrow.

and PBE respectively and added them to `pslibrary`. They can be obtained from the web page given in Ref. [35]. They have $5s$, $5p$, $5d$, and $6s$ valence states, while the $4f$ states are frozen in the core and accounted for by the nonlinear core correction. [114] For the wave functions cut-offs, we use 70 Ry, 90 Ry, 90 Ry while for the charge density we use 280 Ry, 360 Ry, 360 Ry, for LDA, PBE, and PBEsol, respectively.

The Fermi surface has been dealt with by a smearing approach [128] with a smearing parameter $\sigma = 0.02$ Ry. With this smearing, the Brillouin zone integrals converge with a $40 \times 40 \times 40$ **k**-point mesh. Density functional perturbation theory (DFPT) [12, 34] is used to calculate the dynamical matrices on a $8 \times 8 \times 8$ **q**-point grid. These dynamical matrices have been Fourier interpolated on a $200 \times 200 \times 200$ **q**-point mesh to evaluate the free-energy and thermodynamic quantities.

For quasi-harmonic calculations, the free energy was calculated in $N_V = 15$ geometries with lattice constants ranging from $a_0 - 1.2$ a.u. to $a_0 + 0.2$ a.u. in steps of $\Delta a = 0.1$ a.u.,

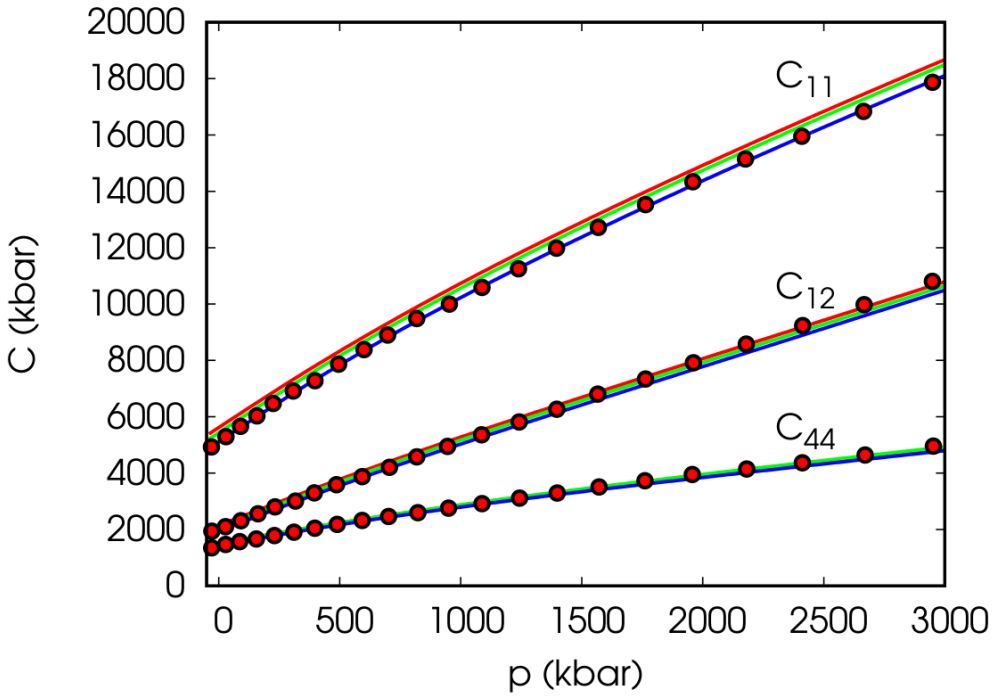

Figure 3.2: Pressure dependent ECs calculated at 0 K obtained from the second derivatives of the energy with respect to strain for the N_V geometries used for the quasi-harmonic approximation. ECs are calculated within LDA (red line), PBEsol (green line), and PBE (blue line). The red circles are the PBE data of Ref.[101].

where a_0 is the equilibrium 0 K lattice constant (see Table 3.1).

The ECs C_{11}, C_{12}, and C_{44} are calculated by using six strained configurations for each type of strain (see Ref. [119]) with $\delta\varepsilon = 0.005$. Therefore, each reference configuration requires the phonon dispersions and the electronic density of states for 18 geometries, 6 with a body-center cubic lattice, 6 with centered tetragonal lattice, and 6 with a rhombohedral lattice. Phonons are calculated on a $8\times8\times8$ **q**-point grid, sampling the Brillouin zone by a $45\times45\times45$ **k**-point mesh. Among the $N_V = 15$ geometries used for anharmonic calculations, we computed the QHA ECs for six reference geometries: 1, 5, 8, 12, 13, and 14. The phonon frequencies of geometries 1, 5, 8, and 12 have been computed on Marconi100 at CINECA with an accelerated `GPU` version of `thermo_pw` optimized for calculations with a dense grid of **k**-points. [66] The method is presented in chapter 7 of this thesis.

3.2 Results and discussion

We start in Table 3.1 by comparing the LDA, PBEsol, and PBE equilibrium lattice constants, bulk moduli, and pressure derivatives of the bulk moduli obtained from the interpolation of $U(V)$ with selected previous calculations and experiments. Using $a_{exp} = 5.972$ a.u. as the

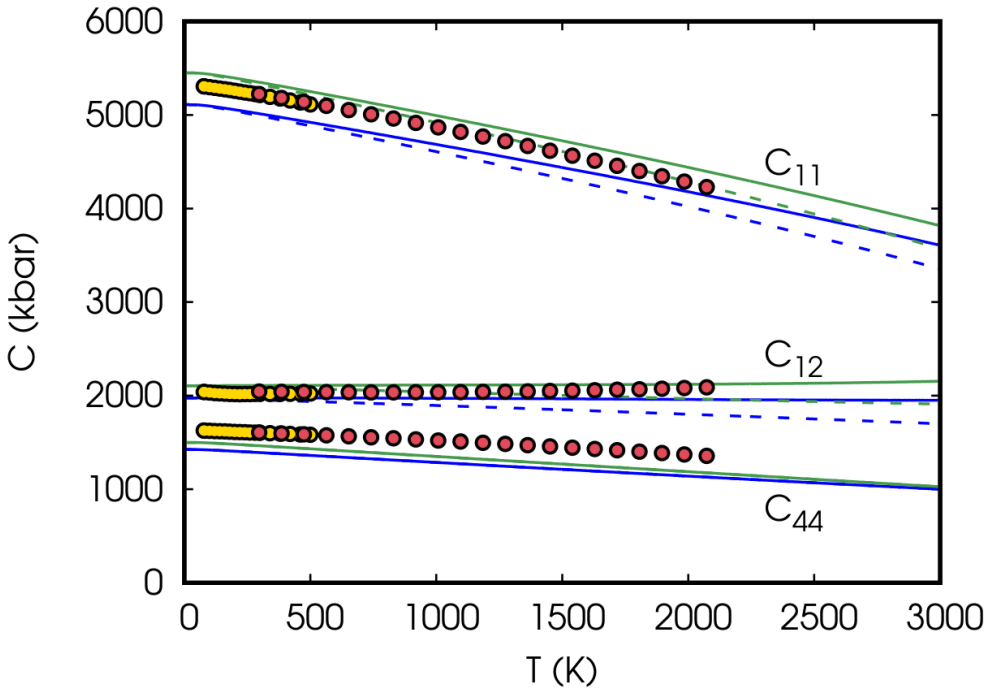

Figure 3.3: PBEsol (green lines) and PBE (blue lines) temperature dependent isothermal (dashed) and adiabatic (solid) elastic constants calculated within the quasi-harmonic approximation at zero pressure. The gold and red circles indicate the adiabatic experimental data of Ref.[20] and of Ref.[115], respectively. For C_{44} isothermal and adiabatic ECs coincide.

0 K experimental lattice constants obtained subtracting 0.009 a.u., the thermal expansion contribution, to the reported 300 K value of Ref. [110], LDA underestimates the lattice constant by 0.7% while PBE overestimates it by 0.8%. PBEsol is closer to the experiment underestimating it by 0.1%. This agrees with the all-electron LAPW calculation of Ref. [75]. Using $B = 3142$ kbar as the 0 K experimental bulk modulus (the value given in Ref. [54]), the LDA and PBEsol overestimations are about 8% and 4%, while PBE underestimation is about 2%. The three functionals give similar values for the pressure derivative of the bulk modulus which are in reasonable agreement with the experiment. In the appendix we show, as a reference, the phonon dispersions, the thermal EOS, the volume thermal expansion, the isobaric heat capacity, the bulk modulus, and the average Grüneisen parameter calculated with LDA, PBEsol, and PBE and compare them with the available experiments and previous calculations. We refer to these data when needed in the following.

The PBE and PBEsol thermal EOS in the range of pressures and for the temperatures measured in the experiment of Qi et al. [158] (298 K, 473 K, 673 K, 873 K, and 1073 K) are shown in the upper part of Fig. 3.1. Since the PBE functional overestimates the volume, its predicted densities are all below experiment. The PBEsol densities are much closer to the experimental data although slightly higher. In order to facilitate the comparison of the temperature and pressure dependence of the theoretical densities and experiment we

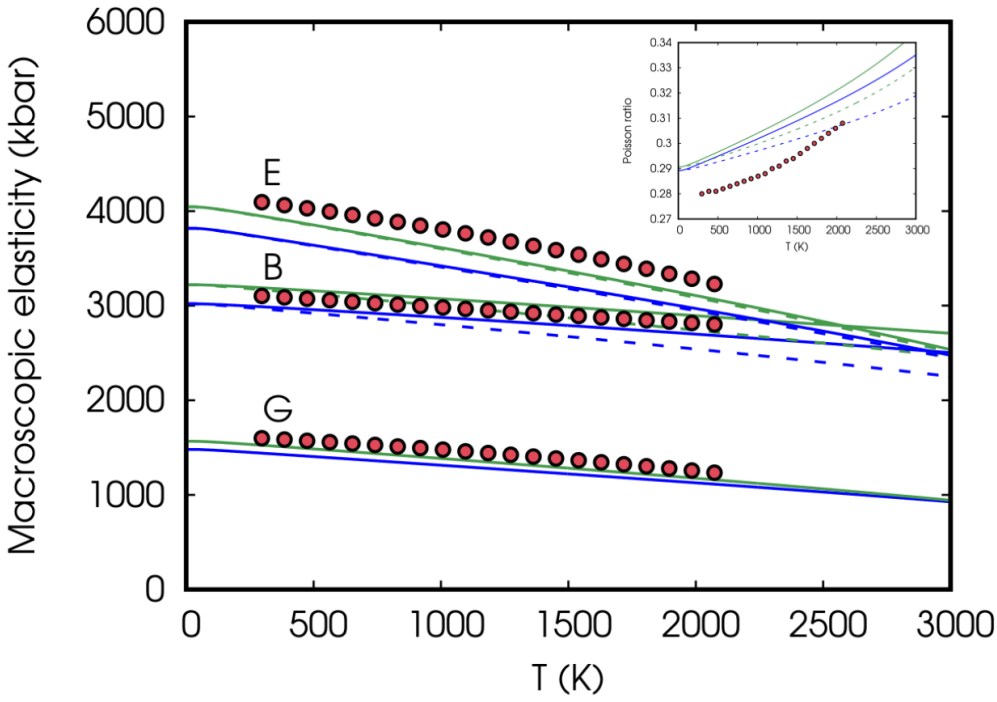

Figure 3.4: PBEsol (green lines) and PBE (blue lines) temperature dependent isothermal (dashed) and adiabatic (solid) polycrystalline averages of the macroscopic elastic properties (bulk modulus B, Young's modulus E, and shear modulus G) calculated within the quasi-harmonic approximation at zero pressure. The red circles are the adiabatic data of Ref.[115]. In the inset we compare the isothermal and adiabatic Poisson's ratio with experiment.

superimpose the two sets of curves in the lower part of Fig. 3.1 making a upper shift of $\Delta\rho = 0.475$ g/cm^3 of all the PBE curves and of $\Delta\rho = -0.06$ g/cm^3 of all the PBEsol curves so that the two curves at 298 K overlap with experiments at the point at 53 kbar. This comparison shows that the slope of the lines and the distance between lines are very similar to experiment for both functionals as expected from the bulk moduli and thermal expansion. The pressure slope of the PBEsol density is slightly smaller than the PBE one (in agreement with the different bulk moduli), but the difference is not significant in the comparison with experiment in this range of pressures.

The LDA, PBEsol, and PBE ECs calculated at the 0 K equilibrium volume are reported in Tab. 3.2 and compared with experiments and selected earlier calculations. The experimental values of Lowrie and Gonas [115] refer to 273.15 K, but they can be extrapolated at 0 K using our PBE differences between 0 K and 273 K. We obtain a good agreement with the 0 K values of Ref. [54] and take these extrapolated values as experimental reference. The LDA errors are 361 kbar (7%), 154 kbar (8%), and −118 kbar (−7%) for C_{11}, C_{12}, and C_{44}, respectively. PBEsol errors are 155 kbar (3%), 84 kbar (4%), and −119 kbar (−7%) while PBE errors are −181 kbar (−3%), −50 kbar (−2%), and −194 (−12%). In Tab. 3.2 we also report the bulk, shear, and Young's moduli of polycrystalline tungsten derived from the

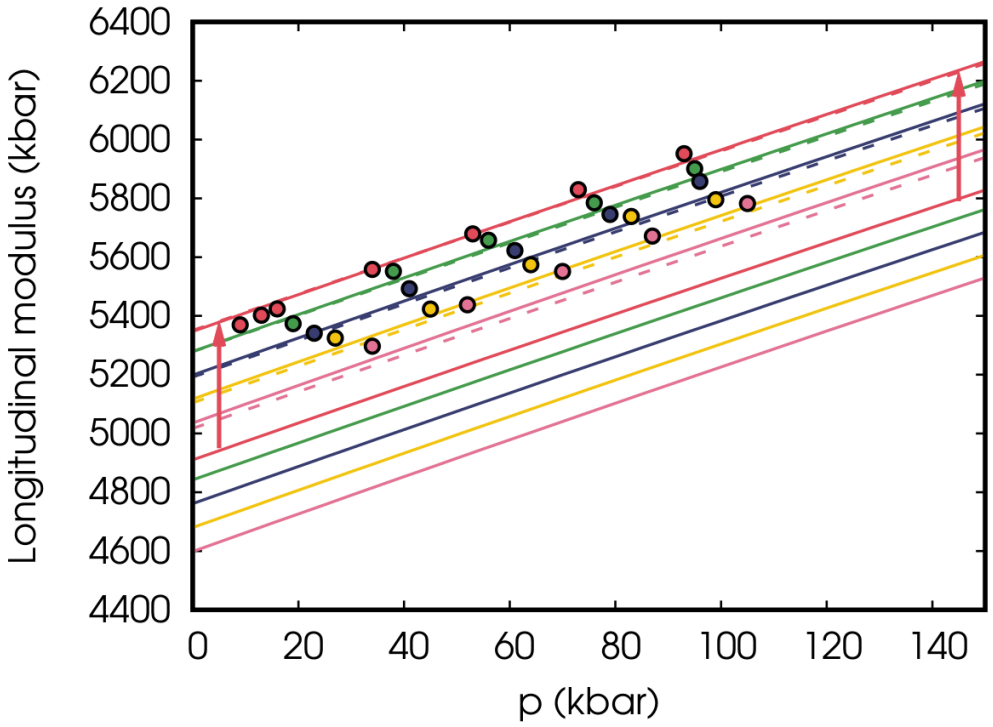

Figure 3.5: Temperature dependent longitudinal modulus calculated within the quasi-harmonic approximation as a function of pressure for several temperatures (red 298 K, green 473 K, blue 673 K, yellow 873 K, and pink 1073 K). The circles (with the same color code) are the data of Ref.[158], measured at the same temperatures and calculated as $L = B_S + 4/3G_S$ from the B_S and G_S in their Table III. To facilitate the comparison with experiment, theoretical lines translated by 437 kbar, as indicated by the red arrows, are also shown. PBEsol results are shown with dashed lines after a shift of 128 kbar.

ECs. The bulk moduli derived from the ECs are about 1% smaller than those reported in Tab. 3.1 derived from the Birch-Murnaghan interpolation. This shows the accuracy of our ECs calculations. The difference is within the numerical uncertainty of the Birch-Murnaghan fitting.

Pressure dependent ECs calculated with the three functionals are reported in Fig. 3.2 and compared with the previous PBE calculation [101]. On the scale of this figure the three functionals are almost equivalent and in good agreement with earlier results. The numerical effort to calculate the temperature and pressure dependent ECs is large and we could afford only two functionals, so we chose PBEsol and PBE which have smaller errors than LDA. Presently, we do not include phonon-phonon anharmonic effects in the free energy, so our results are expected to be reliable only up to 1500 K, a temperature for which, as shown in the appendix, the quasi-harmonic approximation is sufficient to describe accurately the other thermodynamic properties of this system. In Fig. 3.3 we report the temperature dependent isothermal and adiabatic ECs as a function of temperature at room pressure. As is well

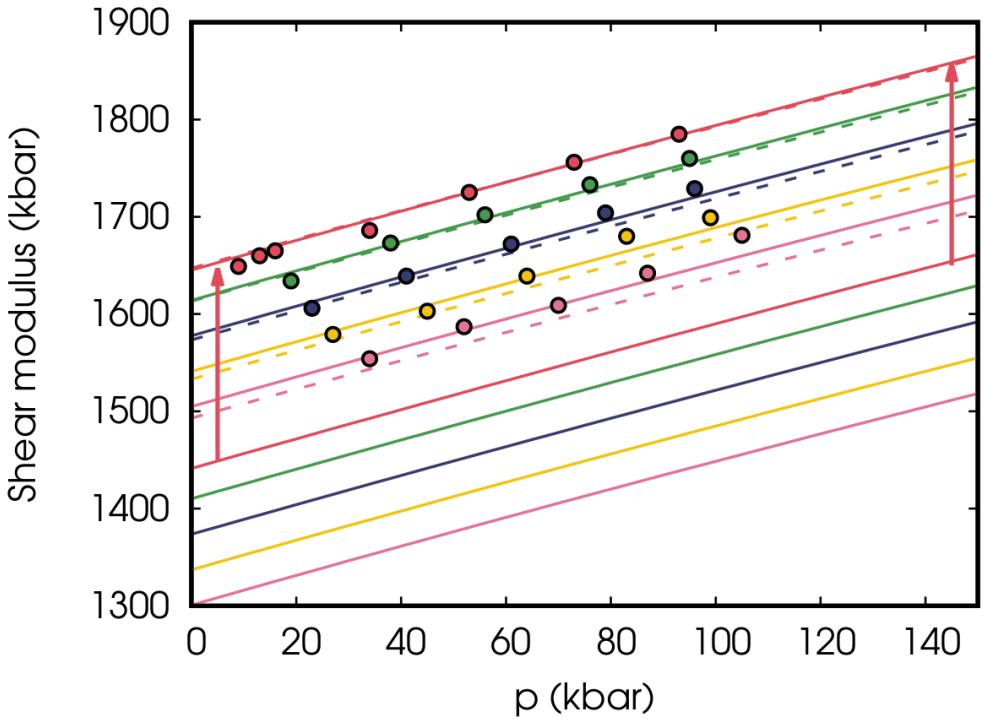

Figure 3.6: Temperature dependent PBE shear modulus calculated within the quasi-harmonic approximation as a function of pressure for several temperatures (red 298 K, green 473 K, blue 673 K, yellow 873 K, and pink 1073 K). The circles (with the same color code) are the data of Ref.[158], measured at the same temperatures (from their Table III). To facilitate the comparison with experiment, theoretical lines translated by 204 kbar, as indicated by the red arrows, are also shown. The PBEsol results are shown with dashed lines after a shift of 122 kbar.

known from theory, in cubic systems adiabatic and isothermal elastic constants differ only for C_{11} and C_{12} while they coincide for symmetry reasons for C_{44}. Experimentally ECs are derived from sound velocities and are adiabatic. We compare our data with Lowrie and Gonas [115] which provided analytic fits of their experiments on single crystal tungsten. The points shown in the figure have been obtained from these fits. The temperature dependence of the ECs is well reproduced, theory and experiment differ only for a rigid shift. From 297 K to 2073 K the experimental values decrease by 993 kbar (19 %), -44 kbar (-2 %), and 250 kbar (15 %) for C_{11}, C_{12}, and C_{44} while the theoretical ones decrease by 953 kbar (18 %), -12 kbar (-0.6 %) and 289 kbar (20 %) with PBEsol and by 874 kbar (17 %), 17 kbar (0.8 %), and 263 kbar (16 %) with PBE. The behavior of C_{12} is quite unusual. In experiment C_{12} is almost constant with a slight enhancement with temperature. We find an almost constant curve, slightly increasing with PBEsol and slightly decreasing with PBE.

The bulk modulus, shear modulus, and Young's modulus of polycrystalline tungsten calculated by the Voigt-Reuss-Hill approximation are shown against temperature in Fig. 3.4

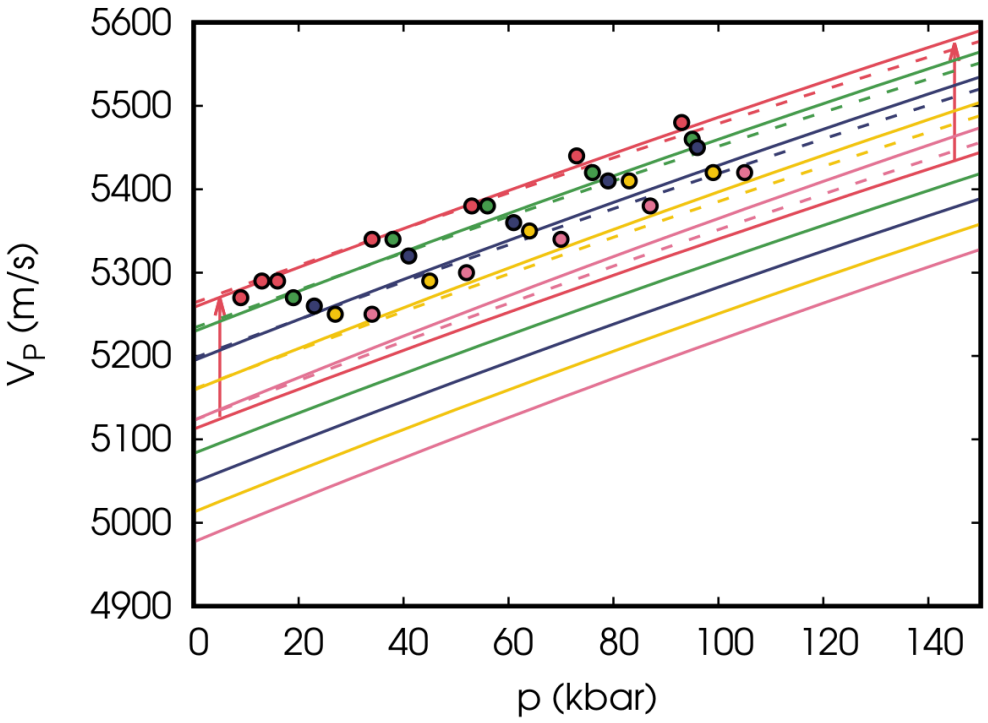

Figure 3.7: Temperature dependent compressional sound velocity (V_P) calculated within the quasi-harmonic approximation as a function of pressure for several temperatures (red 298 K, green 473 K, blue 673 K, yellow 873 K, and pink 1073 K). The circles (with the same color code) are the data of Ref.[158], measured at the same temperatures. To facilitate the comparison with experiment, theoretical lines translated by 146 m/s, as indicated by the red arrows, are also shown. PBEsol results are shown by dashed lines after a shift of 65 m/s.

and compared with the analytic fits of the experimental data of Ref. [115]. Again except for the absolute positions, the temperature dependence of B, E, and G is reproduced reasonably well. From 297 K to 2073 K, these quantities decrease by 10%, 21%, and 23% both in experiment and in our PBE calculation. With PBEsol these figures become 10%, 22%, and 24%, but the absolute position is closer to experiment. The same is found for the Poisson's ratio ν, shown in the inset where the increase is 10% in experiment and 9% (PBE) and 10 % (PBEsol) in theory. At 300 K and 0 kbar, the pressure derivative of the adiabatic bulk modulus is $\frac{dB_S}{dp} = 4.2$ (4.2), while the temperature derivative is $\frac{dB_S}{dT} = -0.15$ kbar/K (-0.16 kbar/K) for PBE (PBEsol) (experimental $\frac{dB_S}{dp} = 4.45$ and $\frac{dB_S}{dT} = -0.076$ kbar/K [158]). For the shear modulus the values become: $\frac{dG_S}{dp} = 1.5$ (1.5) and $\frac{dG_S}{dT} = -0.18$ kbar/K (-0.19 kbar/K) for PBE (PBEsol) (experimental $\frac{dG_S}{dp} = 1.8$ and $\frac{dG_S}{dT} = -0.175$ kbar/K).

In Fig. 3.5 we show the pressure dependent longitudinal modulus that derives from our elastic constants. This modulus is computed as $L = B_S + \frac{4}{3}G_S$. A similar calculation is done also with the experimental data of Ref. [158]. Also in these curves it is easier to

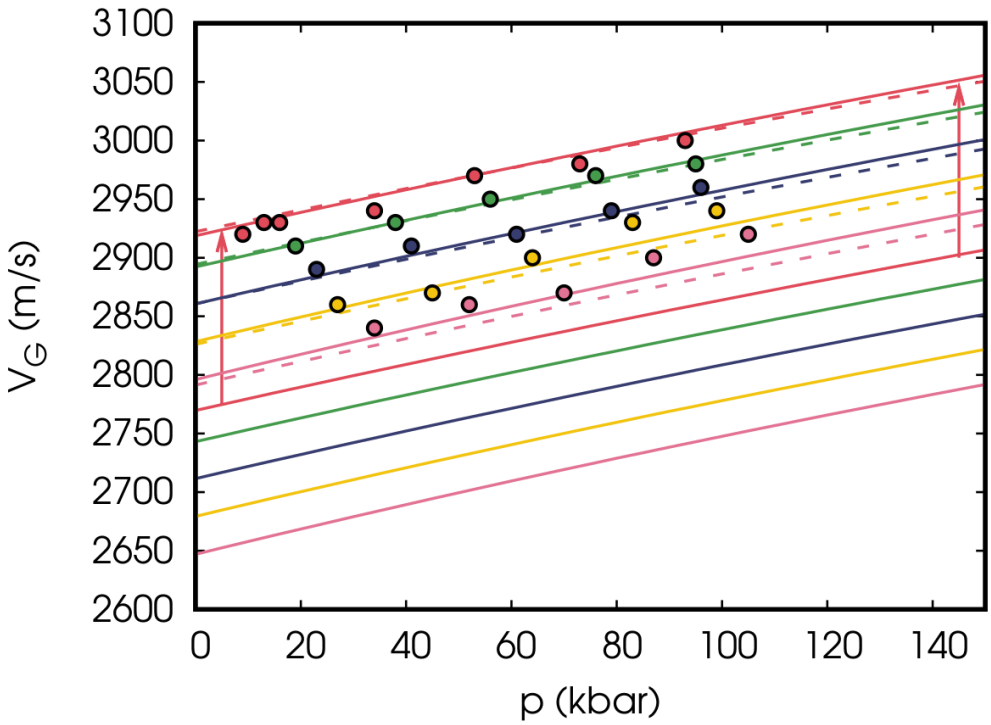

Figure 3.8: Temperature dependent shear sound velocity (V_G) calculated within the quasi-harmonic approximation as a function of pressure for several temperatures (red 298 K, green 473 K, blue 673 K, yellow 873 K, and pink 1073 K). The circles (with the same color code) are the data of Ref.[158], measured at the same temperatures. To facilitate the comparison with experiment, theoretical lines translated by 149 m/s, as indicated by the red arrows, are also shown. PBEsol results are shown by dashed lines after a shift of 113 m/s.

compare the two functionals and experiment by doing a shift that removes the differences due to the $T = 0$ K elastic constants. The figure with unshifted curves is presented in the appendix. We make a shift of 437 kbar for PBE and of 128 kbar for PBEsol so that the 298 K curves and the experimental point at 53 kbar and 298 K coincide. The theoretical data reproduce accurately the pressure dependence of the experimental data and both functionals give curves with the same slope, however our calculation predicts a larger variation of L with temperature than experiment. This difference is mainly due to the bulk modulus as can be deduced by comparing the shear modulus (see Fig. 3.6). After a shift of 204 kbar for PBE and of 122 kbar for PBEsol (again to make the curve at 298 K to pass through the point at 53 kbar), the temperature and pressure dependence of the shear modulus follows with experiment with the PBEsol shear modulus that decreases slightly faster than the PBE one with temperature.

Finally, in Figs. 3.7 and 3.8 we present a comparison between the sound velocity data and our results (Eqs. 2.219 and 2.220). We show our theoretical PBE results and the same curves shifted by 146 m/s (Fig. 3.7) and 149 m/s (Fig. 3.8) so that the 298 K curves are

above the experimental data at 53 kbar. In the same figures we show also the PBEsol data shifted by 65 m/s (V_P) and 113 m/s (V_G). As expected from previous analysis, we find that the pressure dependence is well reproduced for both the compressional and the shear sound velocities. The temperature dependence of the shear sound velocity is also very well accounted for, while the distances between compressional velocities at different temperatures agree with our curves at low temperatures, but the experimental points at 873 K and those at 1073 K have higher values than our theoretical curves. These findings are due to the values of $\frac{dB_S}{dT}$ and $\frac{dG_S}{dT}$, the latter in quite good agreement with experiment, while the former only in fair agreement.

Chapter 4

Molybdenum

Molybdenum, as a refractory $4d$ transition metal in the same group of tungsten, finds several applications, pure or in alloys with other metals, for its high melting point, mechanical properties, and corrosion resistance. Its thermodynamic properties have been studied by several authors, both experimentally and by theory. [132, 45, 201, 109, 82, 79, 136, 18, 198, 199, 200, 192, 25]

In molybdenum, the temperature dependent bulk modulus and ECs have been measured by ultrasonic technique at room pressure. [54, 20, 47, 21] Data are available almost until melting (2898 K). [21] Pressure derivatives of the ECs are known at room temperature [91] and compressional and shear sound velocities in polycrystalline molybdenum have been measured up to 120 kbar at room temperature. [112] A simultaneous measurement of the density allow to derive from these data the bulk and shear moduli at high pressure. However, information on pressure dependent elasticity at high temperatures is still missing in the literature.

Theoretically temperature dependent ECs of molybdenum have been calculated within the quasi-static approximation (QSA) at room pressure, [193] while the pressure dependent ECs have been calculated by Koči et al. [101] at zero temperature. The measurements on polycrystalline molybdenum have been modeled by ab-initio calculations [112] and the ECs along the Hugoniot together with the corresponding compressional and shear sound velocities have been calculated within the QSA. [199] Due to the time-consuming phonon calculations for deformed configurations of metallic systems needed for the ab-initio quasi-harmonic (QHA) ECs no paper has addressed these quantities for molybdenum so far.

In this chapter, we present a comparison of the temperature dependence of the QSA and the QHA ECs and use the calculated QHA adiabatic ECs to predict the temperature and pressure dependence of the bulk and shear moduli of polycrystalline molybdenum as well as its compressional and shear sound velocities, providing a theoretical prediction that could be useful in future investigations of the thermoelastic properties at high pressure and temperature.

4.1 Computational parameters

The temperature and pressure dependent thermodynamic properties and ECs are calculated by the open source software `thermo_pw`, which has been discussed in previous publications. [39, 148, 118, 119, 120, 121, 65]

The calculations presented in this work are done by using DFT as implemented in the Quantum ESPRESSO (QE) package. [60, 59] The exchange and correlation functionals are the LDA [152] and the generalized gradient approximations PBEsol [150] and PBE. [149]

We employ the projector augmented wave (PAW) method [17] and a plane-wave basis with pseudopotentials from `pslibrary`. [35] We use `Mo.pz-spn-kjpaw_psl.1.0.0.UPF`, `Mo.pbesol-spn-kjpaw_psl.1.0.0.UPF`, and `Mo.pbe-spn-kjpaw_psl.1.0.0.UPF` for LDA, PBEsol, and PBE, respectively. These pseudopotentials have the $4s$, $4p$, $4d$, and $5s$ states in the valence, while the other states are frozen in the core and accounted for by the nonlinear core correction. [114] The lattice constants of 14 reference geometries from 4.784 a.u. to 6.084 a.u. with LDA, from 4.8162 a.u. to 6.1162 a.u. for PBEsol, and from 4.8922 a.u. to 6.1922 a.u. with PBE with an interval of 0.1 a.u. between geometries have been chosen to calculate the free energies. For the wave functions cutoffs, we use 100 Ry, 90 Ry, 120 Ry while for the charge density we use 400 Ry, 360 Ry, 480 Ry, for LDA, PBEsol, and PBE, respectively. The Fermi surface has been dealt with by the smearing approach of Methfessel and Paxton [128] with a smearing parameter $\sigma = 0.02$ Ry. With this smearing, the Brillouin zone integrals converge with a $40 \times 40 \times 40$ **k**-point mesh.

For 6 reference geometries (with $i = 1$, 4, 7, 11, 12, 13), temperature dependent ECs are calculated by 3 strain types that lead to a body-center cubic, a centered tetragonal, and a rhombohedral strained lattices. Each strain type is sampled by 6 strains, from $\epsilon = -0.15$ to $\epsilon = 0.15$ with stepsize $\delta_\epsilon = 0.05$. A thicker **k**-point mesh of $45 \times 45 \times 45$ is employed on strained configurations. Each one of the 108 strained configurations requires calculations of phonon frequencies and electronic density of states. Phonon frequencies are calculated by density functional perturbation theory (DFPT) [12, 34] getting the dynamical matrices on a $8 \times 8 \times 8$ **q**-point grid. These dynamical matrices have been Fourier interpolated on a $200 \times 200 \times 200$ **q**-point mesh to evaluate the free-energy and the thermodynamic quantities. The calculations are all performed on the Leonardo supercomputer at CINECA with a GPU version of `thermo_pw` that optimizes some routines of QE for problems with dense **k**-points sampling in metallic systems. [66] This alternative approach will be discussed in Chapter 7.

Table 4.1: The equilibrium lattice constants (a_0), the bulk moduli (B_T) and the pressure derivatives of the bulk moduli (B'_T) of molybdenum calculated in this work compared with previous calculations and with experiment.

		T (K)	a_0 (a.u.)	B_T (kbar)	B'_T
This study	LDA	0	5.884	2949	4.00
		295	5.894	2874	4.09
	PBEsol	0	5.916	2826	4.02
		295	5.926	2753	4.10
	PBE	0	5.975	2617	4.08
		295	5.986	2543	4.16
Calc. [198]	PW91	0	5.988	2666	4.42
Calc. [199]	PBE	0	5.996	2633	4.21
Calc. [101]	PBE	0	6.001	2610	4.5
Calc. [192][1]	PBE	0	5.992		
Calc. [75]	LDA	0	5.888		
	PBEsol	0	5.920		
	PBE	0	5.979		
Calc. [45]	LDA	0	5.880	3010	3.99
		298[2]	5.891	2950	4.01
	PBEsol	0	5.914	2870	4.02
		298[2]	5.925	2800	4.05
	PBE	0	5.981	2620	4.14
		298[2]	5.993	2550	4.17
Model [109]		300	5.945	2600	4.21
Model [177]		300	5.944	2605	4.05
Expt. [45][1]		300	5.944	2610	4.06
Expt. [132]		300	5.951	2608	4.46
Expt. [54]		0		2653	
Expt. [92]				2610	4.65[3]/3.95[4]

[1] These data are used to calculate the equations of state which we report in Fig. S2 and Fig. S3 of the supplementary material.

[2] Values estimated using a Debye model.

[3] Ultrasonic experiment.

[4] Shock Wave experiment.

Table 4.2: The 0 K elastic constants calculated with the different functionals compared with experiment and one previous calculation. B, E, G, and ν are the bulk modulus, the Young's modulus, the shear modulus, and the Poisson's ratio, respectively.

	T (K)	a_0 (a.u.)	C_{11} (kbar)	C_{12} (kbar)	C_{44} (kbar)	B (kbar)	E (kbar)	G (kbar)	ν
LDA	0	5.884	5183	1815	1094	2938	3402	1301	0.307
PBEsol	0	5.916	4976	1727	1081	2810	3318	1273	0.303
PBE	0	5.974	4637	1589	1016	2605	3111	1196	0.301
PW91 [198]	0	5.988	4723	1604	1060	2644	3211	1237	0.297
Expt. [54]	0		4500.2	1729.2	1250.3	2653	3358	1303	0.289
Expt. [47]	273.15		4637	1578	1092	2598	3232	1250	0.293
Expt. [47] (Extrapolated)	0		4800	1558	1124	2639	3354	1302	0.288
Expt. [20]	300		4696	1676	1068	2683	3194	1227	0.302
Expt. [20] (Extrapolated)	0		4832	1656	1100	2715	3306	1275	0.297
Expt. [91]	300		4648	1616	1089	2627	3222	1244	0.296
Expt. [91] (Extrapolated)	0		4784	1596	1121	2659	3334	1291	0.291
Expt. [112]	300					2607		1251	

4.2 Results and discussion

In Table 4.1, the equilibrium lattice constants, bulk moduli, and pressure derivatives of the bulk moduli of molybdenum obtained as parameters of a fourth-order Birch-Murnaghan interpolation of the static energy $U(V)$ are listed together with a few selected values from previous calculations and experiment. Our PAW LDA, PBEsol, and PBE values of the lattice constant differ by less than 0.1% from the all-electron values reported in Ref. [75]. With respect to experiment ($a = 5.936$ a.u. at 0 K) the LDA, PBEsol, and PBE errors are -0.9%, -0.3% and 0.7%, with LDA and PBEsol below experiment and PBE above. For the bulk modulus these errors become 10% (LDA), 7% (PBEsol), and -1% (PBE) with respect to the 0 K value 2653 kbar. [54]

In Table 4.2, we report the values of the ECs C_{11}, C_{12}, and C_{44} calculated with the three functionals together with the values of the bulk modulus, Young's modulus, shear modulus, and Poisson's ratio of polycrystalline molybdenum calculated using the Voigt-Reuss-Hill approximation. The temperature dependent ECs have been measured in Refs. [20, 54, 47, 21]. Although there is not perfect agreement among these data, the 0 K values of Ref.[47, 21, 91] are quite close to each other. Taking as a reference the values of Ref. [91] extrapolated to 0 K, by adding the theoretical difference between 0 K and 300 K, we find that the LDA errors for C_{11}, C_{12}, and C_{44} are 399 kbar (8 %), 219 kbar (14 %) and -27 kbar (-2 %) while the PBE errors are -147 kbar (-3 %), -7 kbar (-0.4 %) and -105 kbar (-9 %). PBEsol has errors 192 kbar (4 %), 131 kbar (8 %), and -40 kbar (-4 %) smaller than LDA, but bigger than PBE. The PBE values of C_{11} and C_{12}, and hence of its bulk modulus, are the closest to experiment. Since the calculation of the TDEC is computationally heavy, we calculated

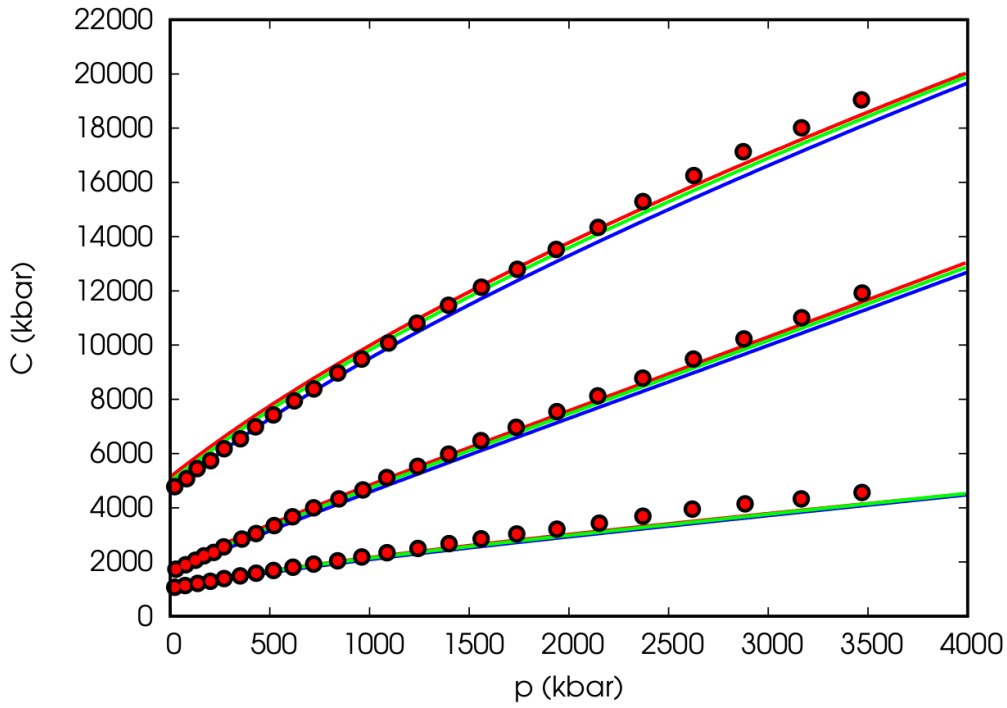

Figure 4.1: Elastic constants as a function of pressure calculated within LDA (red lines), PBEsol (green lines) and PBE (blue lines) compared with the PBE results of Ref. [101].

them using only this functional. Actually, as shown in Ref. [121] for several metals and as we confirmed in a recent study of tungsten, [65] different functionals give different 0 K values of the ECs but the temperature and pressure dependence is almost independent from the functional.

In Fig. 4.1 we present the pressure dependent ECs at 0 K calculated with the three functionals and compare them with the PBE results of Koči et al.. [101] There is a reasonable agreement between the two calculations expecially at low pressure. At 3000 kbar our ECs are smaller than those of Koči et al. but quite close to them. At zero pressure, the pressure derivatives of the ECs are: $\frac{dC_{11}}{dp} = 5.8$, $\frac{dC_{12}}{dp} = 3.3$, $\frac{dC_{44}}{dp} = 1.3$, for all three functionals to be compared to the experimental values: [91] $\frac{dC_{11}}{dp} = 6.41$, $\frac{dC_{12}}{dp} = 3.45$, and $\frac{dC_{44}}{dp} = 1.396$.

We show in Fig. 4.2 the QHA isothermal and adiabatic ECs compared with the adiabatic experimental values. Keeping into account the zero point motion on both the lattice constant and on the ECs themselves, we find $C_{11} = 4564$ kbar, $C_{12} = 1589$ kbar, and $C_{44} = 996$ kbar at 4 K, while computing the ECs from the strain derivatives of the energies at the lattice constant expanded by zero point motion effects within the QSA we get $C_{11} = 4593$ kbar, $C_{12} = 1565$ kbar, and $C_{44} = 996$ kbar.

As can be seen from Fig. 4.2, there is a good agreement between our calculated temperature dependence and the experimental data. From 24 K and 2022 K, the experimental values [21] decrease of 1264 kbar (27 %), -63 kbar (-4 %), and 231 kbar (21 %) for C_{11},

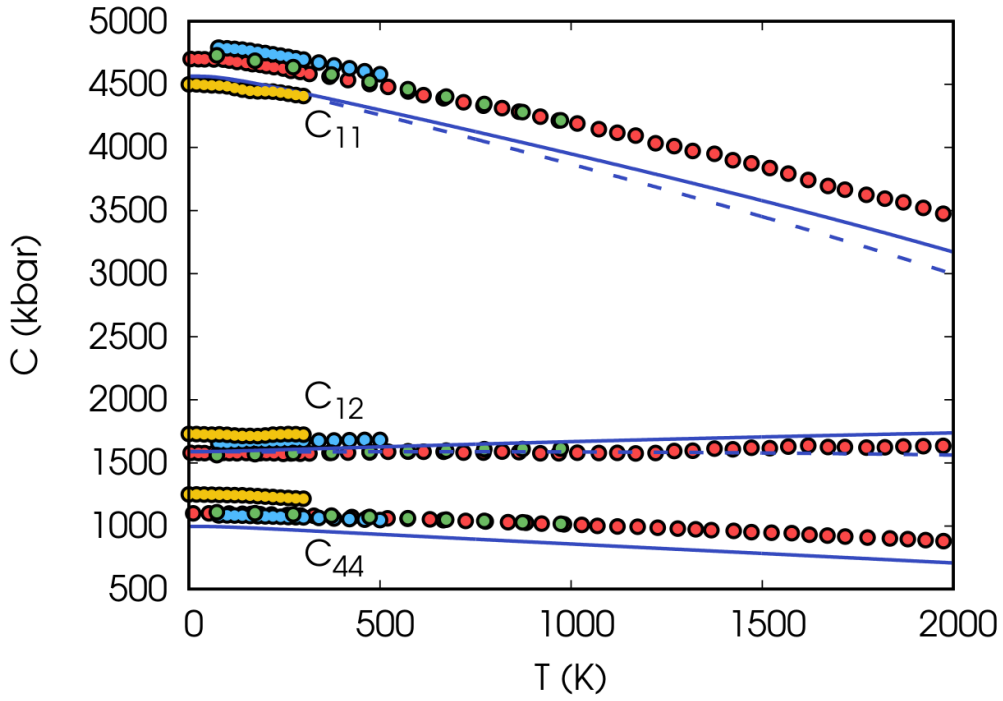

Figure 4.2: Quasi-harmonic isothermal (dashed lines) and adiabatic (solid line) elastic constants C_{11}, C_{12} and C_{44} as a function of temperature compared with experimental adiabatic data from Ref. [54] (yellow circles), Ref. [47] (green circles), Ref.[20] (blue circles), and Ref.[21] (red circles).

C_{12}, and C_{44} respectively, while our values decrease by 1400 kbar (31 %), -141 kbar (-9 %), and 287 kbar (29 %). In particular the increase of C_{12} with temperature is found also in our QHA calculation, slightly overestimated with respect to experiment.

For comparison we show in Fig. 4.3 the ECs calculated with the PBE functional within the QSA which are in good agreement with those calculated in Ref. [193]. In this case, from 4 K to 2000 K, the decreases of C_{11}, C_{12}, and C_{44} are 380 kbar (8 %), 127 kbar (8 %), and 132 kbar (13 %). The decrease of C_{11}, and C_{44} is much smaller than in experiments (and within QHA) while C_{12} decreases with temperature instead of increasing as in experiment. We can understand this behavior using the QHA ECs calculated at fixed volume that do not contain any thermal expansion effect. For these ECs C_{11} and C_{44} decrease with temperature, while C_{12} increases. Since QSA has only the effect of thermal espansion for C_{11} and C_{44} it misses the QHA contribution that give a larger decrease, while for C_{12} it has no increasing QHA term. The QHA predicts an almost constant C_{12} that is the results of the cancellation between the decrease due to thermal expansion and the increase due to the use of the free energy derivatives instead of the energy derivatives.

Using the QHA ECs we have calculated the properties of polycrystalline molybdenum. In Fig. 4.4 we show the pressure dependence of the bulk modulus and of the shear modulus in the range of pressures (up to 140 kbar) measured in Ref. [112]. In addition to the 300 K

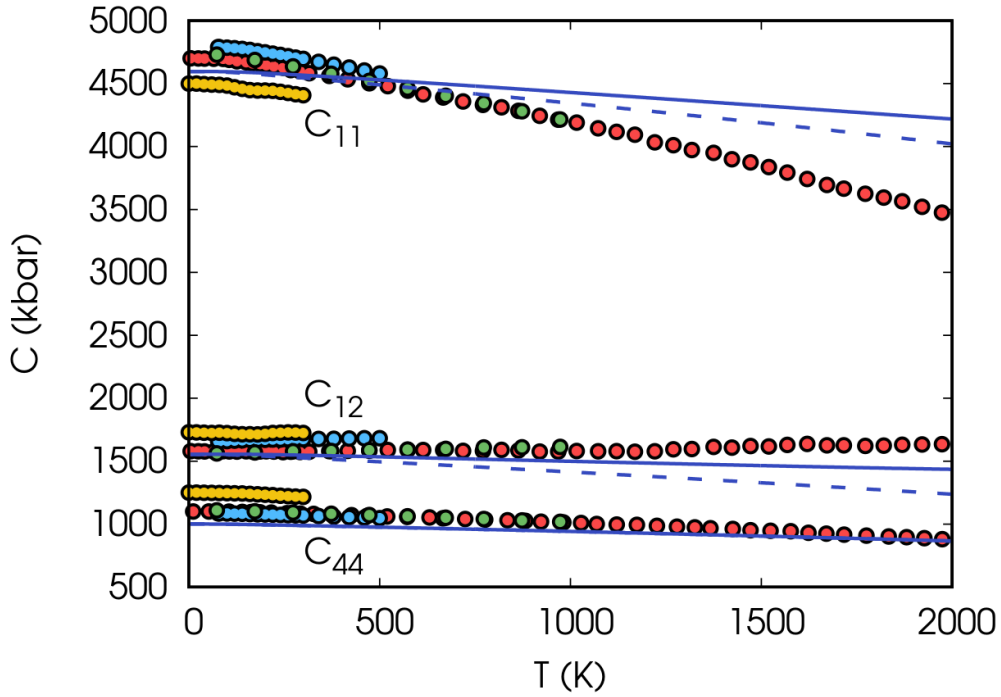

Figure 4.3: Quasi-static isothermal (dashed lines) and adiabatic (solid line) elastic constants C_{11}, C_{12}, and C_{44} as a function of temperature compared with adiabatic experimental data from Ref. [54] (gold circles), Ref. [47] (green circles), Ref.[20] (blue circles), and Ref.[21] (red circles).

calculation (green line), which can be compared with experiment, we show our predictions for 4 K, 1000 K, 1500 K and 2000 K. We can see that the derivatives of the bulk and shear modulus with respect to pressure are well followed by our curves. Our values at 300 K are $\frac{dB_S}{dp} = 4.24$ and $\frac{dG_S}{dp} = 1.33$ against experimental values (obtained by a linear fit) $\frac{dB_S}{dp} = 4.54$ and $\frac{dG_S}{dp} = 1.5$, respectively. These data are in agreement with the experimental values reported in Ref. [91]: $\frac{dB_S}{dp} = 4.44$ and $\frac{dG_S}{dp} = 1.43$ and with the 0 K PBE theoretical results of Ref. [112] $\frac{dB}{dp} = 4.4$ and $\frac{dG}{dp} = 1.7$. Regarding the temperature dependence of the adiabatic bulk and shear modulus we find the following derivatives at 298 K: $\frac{dB_S}{dT} = -0.15$ kbar/K and $\frac{dG_S}{dT} = -0.22$ kbar/K.

Finally using Eq. 2.219 and Eq. 2.220, we computed the compressional and shear sound velocities as a function of pressure for the same set of temperatures used in the previous picture. They are presented in Fig. 4.5. Even in this case the pressure dependence of the sound velocity at 300 K is well reproduced by the calculation and the other curves are our prediction.

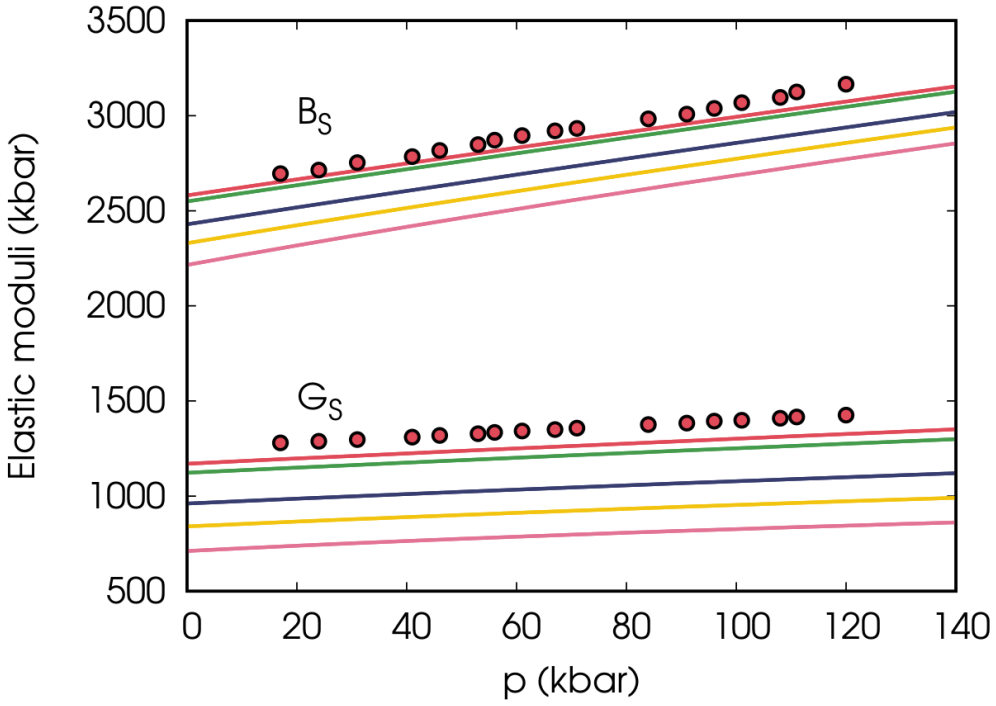

Figure 4.4: Adiabatic bulk and shear modulus of polycrystalline molybdenum against pressure computed at 5 K (red line), 300 K (green line), 1000 K (blue line), 1500 K (yellow line), and 2000 K (pink line), compared with room temperature experimental values of Ref. [112] (red circles).

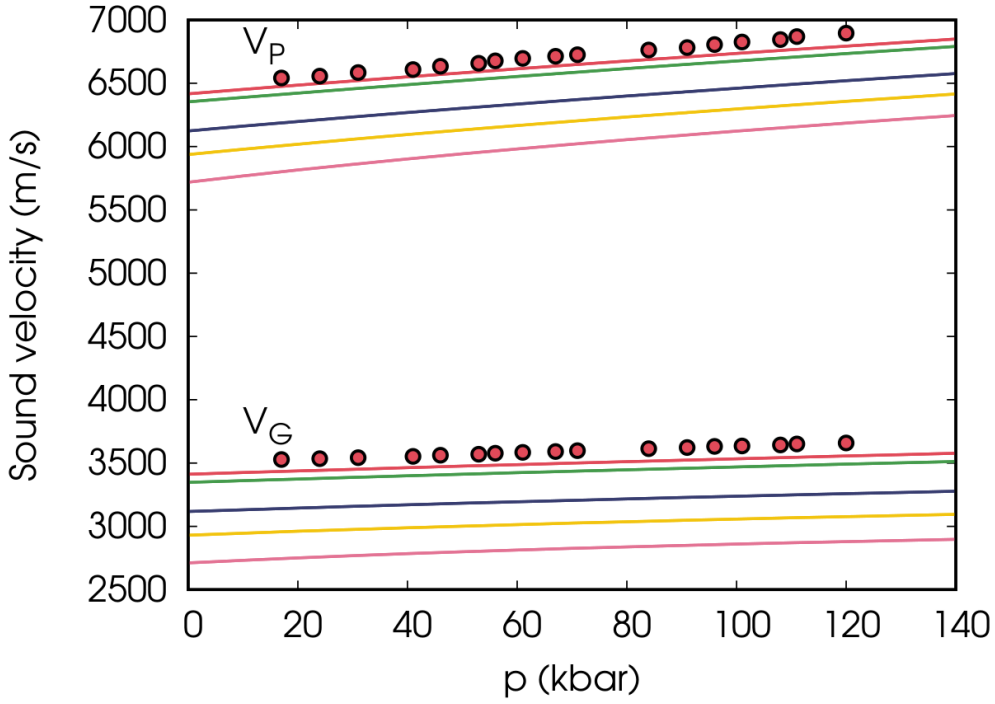

Figure 4.5: Compressional and shear sound velocities of polycrystalline molybdenum against pressure at 5 K (red line), 300 K (green line), 1000 K (blue line), 1500 K (yellow line), and 2000 K (pink line), compared with room temperature experimental values of Ref. [112] (red circles).

Chapter 5

Tantalum

Tantalum, as a member of the refractory metals family (melting temperature $T_M = 3269$ K), is known for its high corrosion resistance and applications for electronics, environmental chemical processing, and medicine. [23] Tantalum is also widely used component of metallic alloys. Its thermodynamic properties have been studied in detail, both experimentally [9, 44, 32] and ab-initio [113, 55, 181, 15, 31].

Temperature dependent elastic constants (TDECs) of tantalum present characteristic features such as a change of slope at high temperature [176, 189] that have been the subject of extensive investigations. At room pressure, TDECs have been measured from 0 K to 300 K in Refs. [54, 108, 6]. The range from 300 K to 725 K has been reported in Ref. [176] showing a linear dependence on temperature but with a somewhat different slope with respect to the values measured between 0 K and 300 K. This change of slope has been confirmed also in Ref. [189] where the measurement has been extended from 300 K up to 3000 K. Pressure dependent elastic constants have been measured at room temperature in Ref. [58, 90], but no experimental information is available for the high-temperature, high-pressure regime.

Pressure dependent elastic constants at 0 K calculated ab-initio [99, 87, 159] are in reasonable agreement among themselves and with the available experiments. TDECs have been computed within the quasi static approximation (QSA) [193, 95] and there are claims that the QSA ECs can explain the anomalous temperature behavior found in experiment [95], in particular the minimum in the $C_{44}(T)$ curve. TDECs of tantalum have been computed in Ref. [146] by using the QHA but phonons obtained with a model generalized pseudopotential theory (MGPT). In this case, reasonable agreement with experiment has been found. Finally, QHA TDEC have been calculated within the PIC model [73], but these calculations cover a too large range of temperatures and pressure to help the interpretation of the experimental data at room pressure.

In this chapter we present a comparison of the QSA and QHA TDECs of tantalum and use them to interpret the experimental data. Moreover we show our prediction for the high temperature - high pressure regime. We include both the vibrational and the electronic excitation contributions in the free energy and we find that, on a large scale the QSA TDECs seem in better agreement with experiment than the QHA ones. On a closer examination, however, the QHA predicts accurately the temperature variation of the elastic constants

from 0 K until approximately 600 K, but then fail to predict the change of slope found in experiments at higher temperatures. Our QHA ECs have a normal behavior: the elastic constants decrease linearly with temperature and follow the slope they had until 600 K also at higher temperatures. This results may point to the existence of relevant effects not accounted for by the QHA, such as the anharmonic phonon-phonon interations.

For completeness, standard thermodynamic properties such has the thermal equation of state, thermal expansion, isobaric heat capacity, adiabatic bulk modulus, and average Grüneisen parameter, calculated by density functional theory using the local density approximation (LDA), the PBE, and the PBEsol generalized gradient approximations, are presented in supplemental material.

5.1 Computational details

We employ the projector augmented wave (PAW) method [17] and a plane-wave basis with pseudopotentials from `pslibrary` [35]. We use `Ta.pz-spn-kjpaw_psl.1.0.0.UPF`, `Ta.pbesol-spn- kjpaw_psl.1.0.0.UPF`, and `Ta.pbe-spn-kjpaw_psl.1.0.0.UPF` for LDA, PBEsol, and PBE, respectively. These pseudopotentials have the $5s$, $5p$, $5d$, and $6s$ states in the valence, while the other states are frozen in the core and accounted for by the nonlinear core correction. [114] For the wave functions cutoffs, we use 70 Ry, 80 Ry, 90 Ry while for the charge density we use 280 Ry, 320 Ry, 360 Ry, for LDA, PBEsol, and PBE, respectively. The Fermi surface has been dealt with by a smearing approach [128] with a smearing parameter $\sigma = 0.02$ Ry. With this smearing, the Brillouin zone integrals converge with a $30 \times 30 \times 30$ **k**-point mesh.

Density functional perturbation theory (DFPT) [12, 34] is used to calculate the dynamical matrices on a $10 \times 10 \times 10$ **q**-point grid. These dynamical matrices have been Fourier interpolated on a $200 \times 200 \times 200$ **q**-point mesh to evaluate the free-energy and the thermodynamic quantities.

The harmonic and anharmonic thermodynamic quantities are calculated by the `thermo_pw` code. [38] For quasi-harmonic calculations the free energy, and therefore the electronic density of states and the phonon dispersions, are calculated in $N_V = 17$ geometries with lattice constants from $a_0 - 0.7$ a.u. to $a_0 + 0.7$ a.u. in steps of $\Delta a = 0.1$ a.u., where a_0 is the equilibrium 0 K lattice constant (see Table 5.1).

QHA TDEC have been calculated on six geometries from $N_i = 9$ to $N_i = 14$. TDECs at higher pressures could not be computed for the appearance of imaginary frequencies in some distorted configurations. At geometry $N_i = 9$ the pressure is about 700 kbar, so QHA ECs should be reliable in the range of pressures presented here.

All calculations have been performed on the Leonardo supercomputer at CINECA with a GPU optimized version of `thermo_pw` [66].

Table 5.1: The equilibrium lattice constants (a_0), the bulk moduli (B_T) and the pressure derivatives of the bulk moduli (B'_T) of tantalum calculated in this work compared with previous calculations and with experiment (in experiment B_S is measured at 300 K. At 0 K B_S and B_T have the same value).

		T (K)	a_0 (a.u.)	B_T (kbar)	B'_T
This study	LDA	0	6.140	2165	3.51
		295	6.152	2100	3.70
	PBEsol	0	6.192	2072	3.47
		295	6.205	2007	3.64
	PBE	0	6.264	1948	3.53
		295	6.277	1902	3.60
Calc. [75]	LDA	0	6.155		
	PBEsol	0	6.208		
	PBE	0	6.280		
Calc. [73]	PBE	0	6.100		
Calc. [113]	PBE	0	6.293	1944	3.06
Expt. [32]		300	6.245	1947	3.4
Expt. [54]		0		1942	
		300	6.247	1919	
Expt. [108]		0		1964	
		300		1939	

5.2 Results and discussion

We report in Table 5.1 the equilibrium lattice constants, bulk moduli, and pressure derivatives of the bulk moduli obtained as parameters of a fourth-order Birch-Murnaghan interpolation of the static energy and compare them with a few selected values from previous calculations and experiment. Taking the all-electron calculation of the lattice constants of Ref.[75] as reference, our PAW values are smaller than 0.2% with all functionals. With respect to the experiment of Ref. [32] corrected for zero point and temperature effect by subtracting 0.013 a.u. that gives 6.232 a.u. the errors of LDA, PBEsol, and PBE are -1.4%, -0.6%, and 0.6%, respectively. Taking as experimental value of the bulk modulus 1942 kbar reported by Ref. [54], the errors of LDA, PBEsol, and PBE are 11%, 6%, and 0.8%. All functionals overestimate the bulk modulus, but PBE is quite close to experiment.

In Table 5.2 we report the calculated elastic constants at the equilibrium 0 K lattice constant. Assuming as 0 K experimental values $C_{11} = 2663$ kbar, $C_{12} = 1582$ kbar, and

Table 5.2: The 0 K elastic constants calculated with the different functionals compared with experiment and one previous calculation. B, E, G, and ν are the bulk modulus, the Young's modulus, the shear modulus, and the Poisson's ratio, respectively.

		a_0	C_{11}	C_{12}	C_{44}	B	E	G	ν
	(K)	(a.u.)	(kbar)	(kbar)	(kbar)	(kbar)	(kbar)	(kbar)	
LDA	0	6.138	3021	1743	710	2169	1849	681	0.358
PBEsol	0	6.189	2862	1673	755	2069	1853	686	0.351
PBE	0	6.262	2647	1595	740	1946	1743	645	0.351
PBE [101]	0		2650	1590	740	1943	1748	647	0.350
Expt. [54]	0		2663	1582	874	1942	1924	721	0.335
Expt. [108]	0		2701	1595	873	1964	1941	727	0.335
Expt. [189]	0		2665	1582	873	1943	1924	721	0.335
Expt. [176]	300		2602	1544	826	1897	1848	691	0.338
Expt. [58]	300		2536	1627	719	1930	1627	598	0.359

$C_{44} = 874$ kbar of Ref. [54] the LDA errors are 358 kbar (13%), 161 kbar (10%), and 164 kbar (19%) the PBEsol errors are 199 kbar (7%), 91 kbar (6%), and 119 kbar (14%), while the PBE one are -16 kbar (0.6%), 13 kbar (0.8%), and 134 kbar (15%). With the exception of C_{44} for which the three functionals have similar errors, the PBE functional is the closest to experiment. As we have shown in a previous paper [65] the temperature dependence of the ECs is not strongly influenced by the functional that instead can change the 0 K values. Therefore, in the following, we limit the calculations of the TDECs, which are numerically quite heavy, to this functional.

In Fig. 5.1 we report the 0 K ECs calculated as a function of pressure. At room pressure we find $\frac{dC_{11}}{dp} = 4.9$, $\frac{dC_{12}}{dp} = 3.1$ and $\frac{dC_{44}}{dp} = 1.0$ to be compared with the experimental values $\frac{dC_{11}}{dp} = 5.1$, $\frac{dC_{12}}{dp} = 3.14$ and $\frac{dC_{44}}{dp} = 0.995$ from Ref. [91]. Our data are in good agreement with Ref. [101]. C_{11} and C_{12} are also in good agreement with Ref. [159] while our C_{44} values are slightly above those of this reference.

In Fig. 5.2 we compare the QSA adiabatic TDECs with experiment and with the previous PBE calculation of Ref. [193]. The two calculations are in substantial agreement, with slightly different values of the 0 K ECs. On the scale of this figure the QSA ECs follow well the experimental results of Ref. [176] and of Ref. [189] since the QSA ECs have a slope that agree with the high temperature slope of the tantalum ECs. Passing from 5 K to 2000 K the decrease is $\Delta C_{11} = 298$ kbar (11%), $\Delta C_{12} = 7$ kbar (0.4%), and $\Delta C_{44} = 169$ kbar (22%), to be compared with the experimental values of Ref. [189] $\Delta C_{11} = 408$ kbar (15%), $\Delta C_{12} = 102$ kbar (6%), and $\Delta C_{44} = 188$ kbar (22 %). For comparison we report also the calculated isothermal ECs. They decrease more rapidly than the isoentropic ones since the anharmonic correction in Eq. 2.206 is positive.

The QHA adiabatic ECs are shown in Fig. 5.3 and compared with the experimental results. As can be seen from the figure the QHA ECs decrease with temperature more than the QSA ones. Passing from 5 K to 2000 K we have $\Delta C_{11} = 595$ kbar (22%), $\Delta C_{12} = 260$

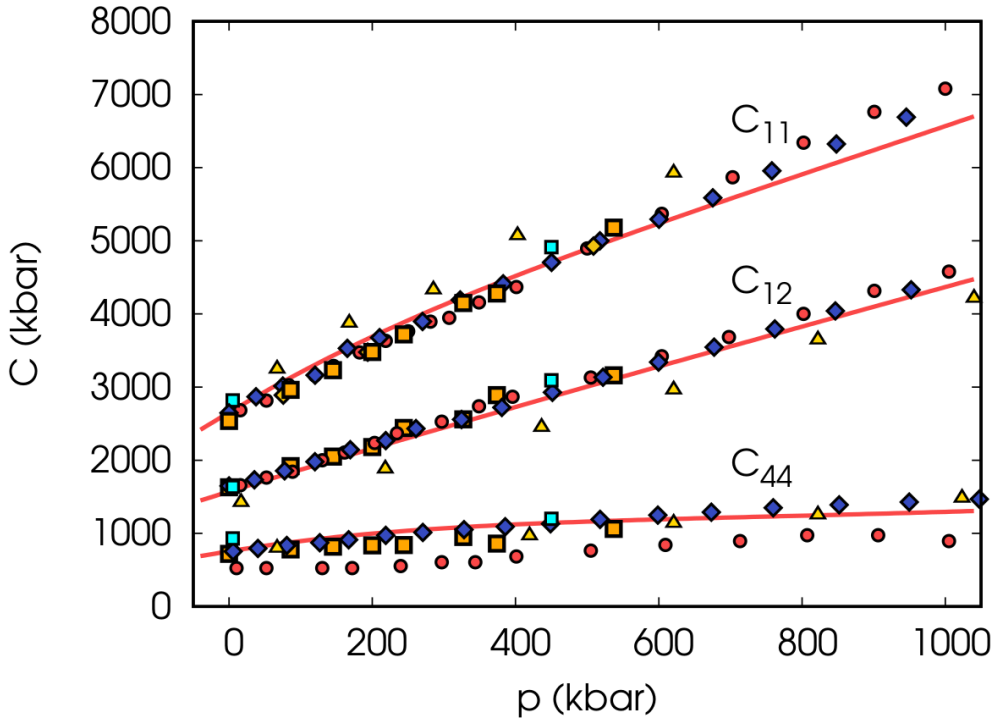

Figure 5.1: $T = 0$ K elastic constants C_{11}, C_{12} and C_{44} as a function of pressure calculated within PBE compared with experiment [58] (orange squares). As a reference we report also previous calculations the PBE results of Ref. [101] (blue diamond), Ref. [159] (red circles), Ref. [87] (yellow triangles), Ref. [175] (cyan squares) .

kbar (16%), and $\Delta C_{44} = 423$ kbar (58%). Therefore on this scale the QSA ECs are in better agreement with experiment than the QHA ECs.

A direct comparison of the QSA and QHA TDECs is presented in Fig. 5.4. Note that in this picture we have limited the scale of temperatures at 1200 K, a range where the QHA is expected to be a good approximation. The difference among the two approximation is not large, but still the QHA seem to worsen the agreement with experiment.

In order to better interpret the results, we present in Figs. 5.5, 5.6, and 5.7 the combination of elastic constants $C = \frac{1}{2}(C_{11} + C_{12} + 2C_{44})$, $C' = \frac{1}{2}(C_{11} - C_{12})$ and C_{44} to which their value at 0 K has been subtracted. These combinations are measured directly in experiments. In this enlarged scale we plot both the QSA and the QHA results. The QHA results for C and C_{44} follow well the experimental data from 0 K to about 500 K, but then fail to predict the change of slope measured in experiment. For C' instead the QHA slope is in better agreement with experiment than the QSA.

Finally we present in Fig. 5.8 the adiabatic QHA elastic constants as a function of pressure at different temperatures for 5 K to 1500 K.

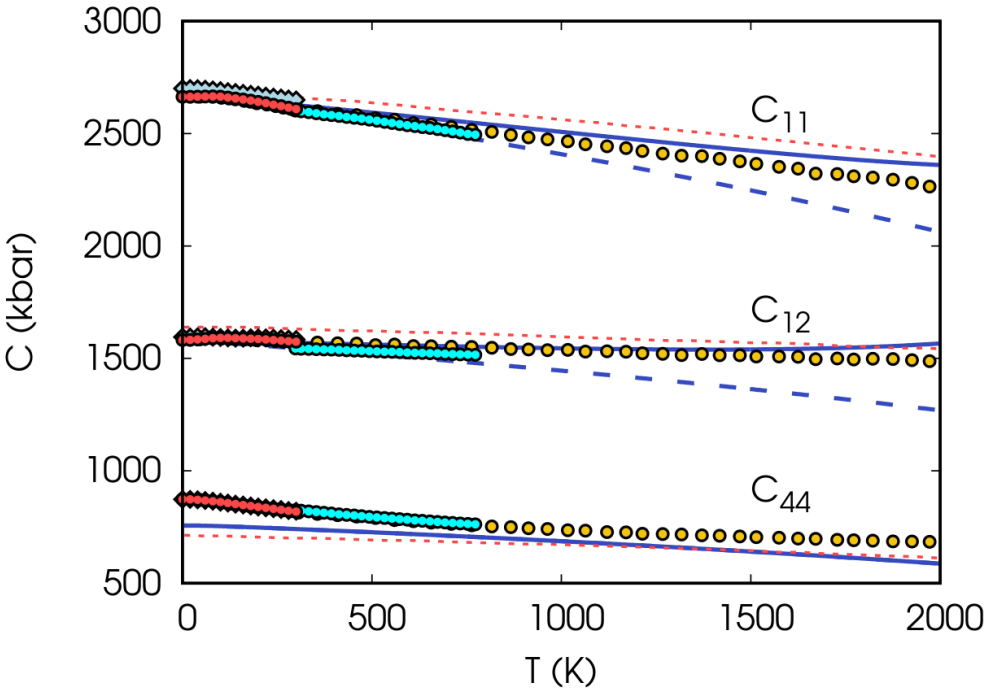

Figure 5.2: Comparison of the PBE adiabatic QSA elastic constants C_{11}, C_{12}, and C_{44} (continuous blue line) as a function of temperature with experiments from Ref. [54] (red dots), Ref. [189] (yellow dots), Ref. [108] (light blue diamonds) and Ref. [176] (cyan dots). Dashed lines indicate the isothermal elastic constants. Dotted red line is the PBE QSA calculation of Ref. [193].

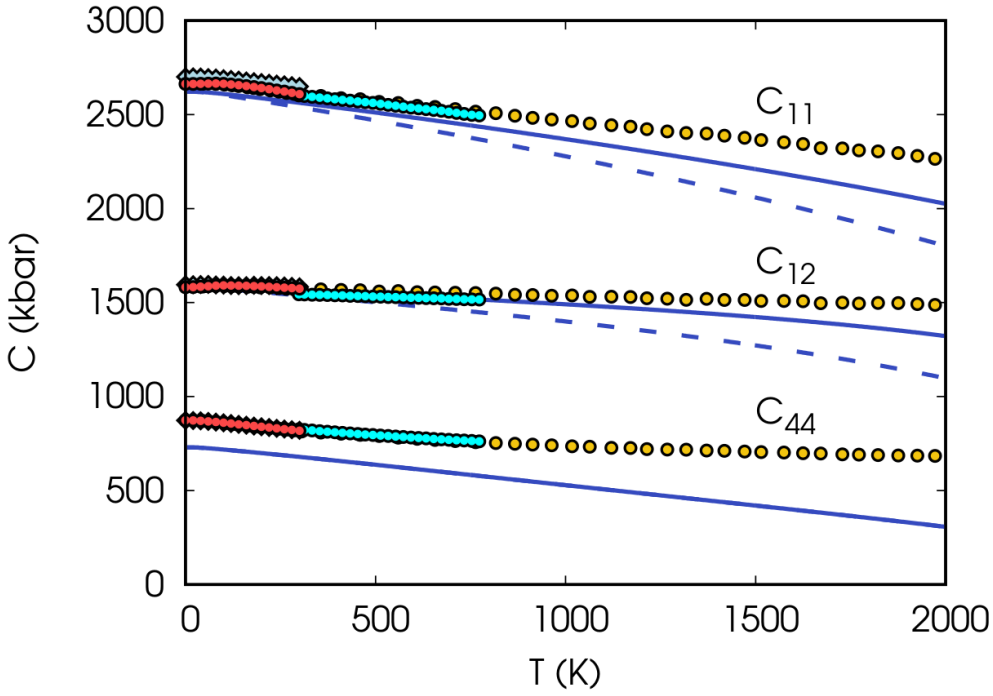

Figure 5.3: Comparison of the PBE adiabatic QHA elastic constants C_{11}, C_{12}, and C_{44} (continuous blue line) as a function of temperature with experiments from Ref. [54] (red dots), Ref. [189] (yellow dots), Ref. [108] (light blue diamonds) and Ref. [176] (cyan dots). Dashed lines indicate the isothermal elastic constants.

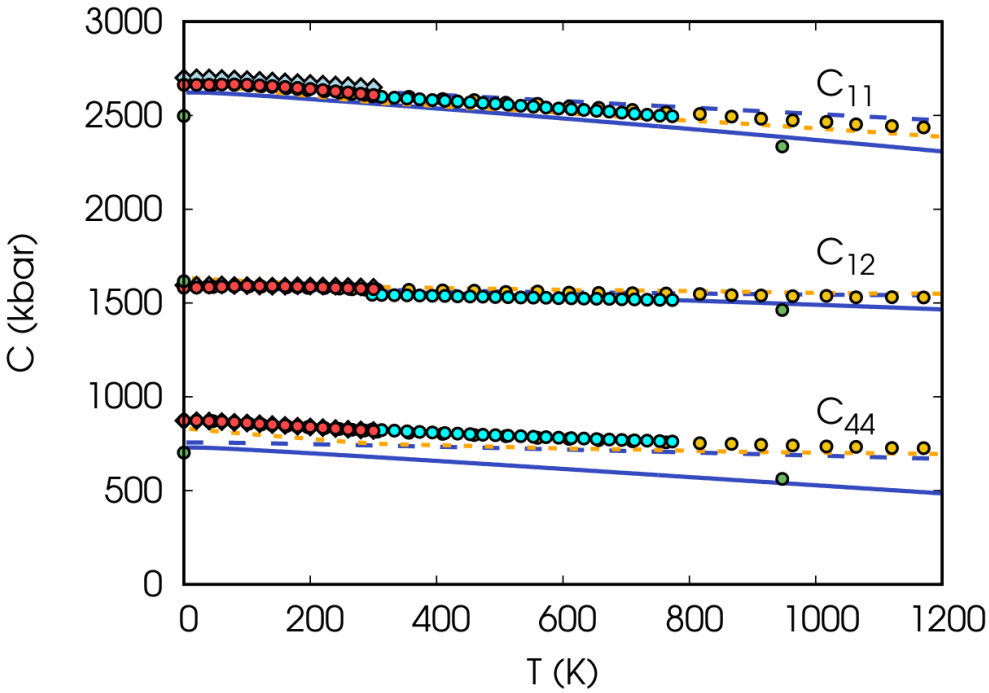

Figure 5.4: Comparison of the PBE QSA (dashed blue line) and QHA (solid blue line) elastic constants C_{11}, C_{12} and C_{44} as a function of temperature. The experiments are from Ref. [54] (red dots), Ref. [189] (yellow dots), Ref. [108] (light blue diamonds) and Ref. [176] (cyan dots). Green dots are the PBE results of Ref. [73]. The dashed orange line is the calculation of Ref. [146].

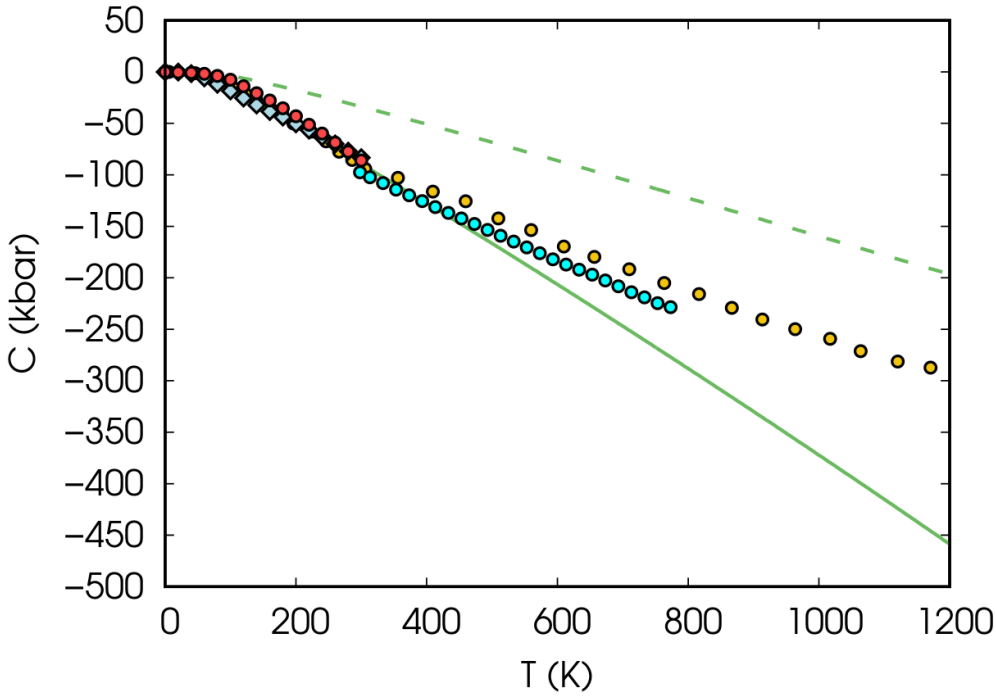

Figure 5.5: PBE adiabatic QSA (dashed line) and QHA (continuous line) combination of elastic constants $C = 0.5(C_{11} + C_{12} + 2C_{44})$ as a function of temperature after subtracting the $T = 0$ K value. The function is compared with experiments from Ref. [54] (red dots), Ref. [189] (yellow dots), Ref. [108] (light blue diamonds) and Ref. [176] (cyan dots).

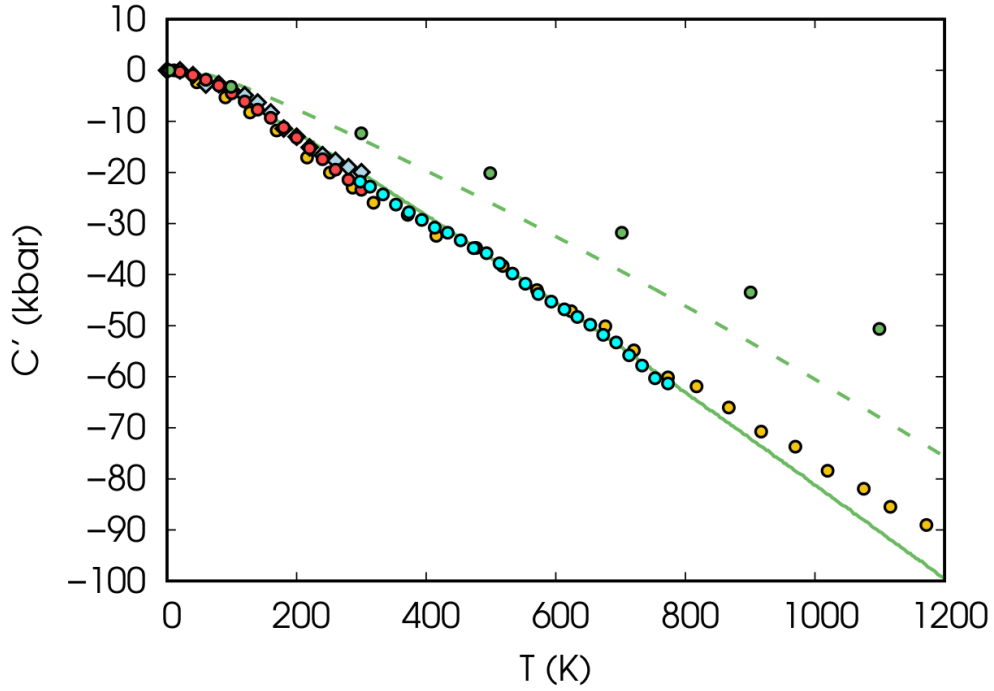

Figure 5.6: PBE adiabatic QSA (dashed line) and QHA (continuous line) combination of elastic constants $C' = 0.5(C_{11} - C_{12})$ as a function of temperature after subtracting the $T = 0$ K value. The function is compared with experiments from Ref. [54] (red dots), Ref. [189] (yellow dots), Ref. [108] (light blue diamonds) and Ref. [176] (cyan dots). The QSA results of Ref. [95] are also shown (green dots) .

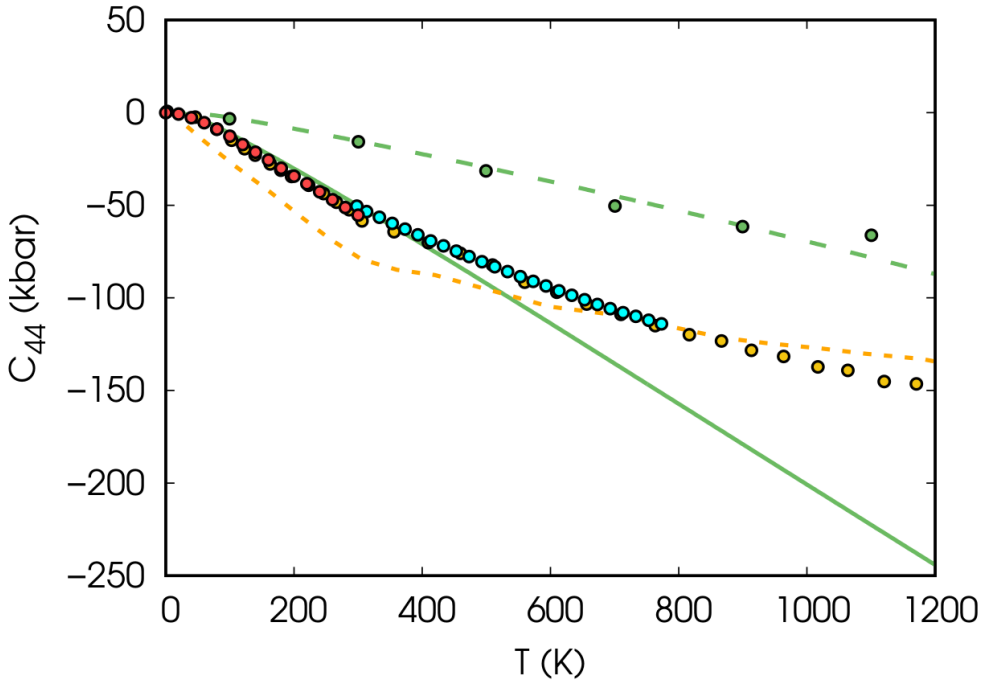

Figure 5.7: PBE adiabatic QSA (dashed line) and QHA (continuous line) C_{44} elastic constant as a function of temperature after subtracting the $T = 0$ K value. Theory is compared with experiments from Ref. [54] (red dots), Ref. [189] (yellow dots), Ref. [108] (light blue diamonds) and Ref. [176] (cyan dots). The QSA results of Ref. [95] are also shown (green dots). The orange dashed line show the results of Ref. [146].

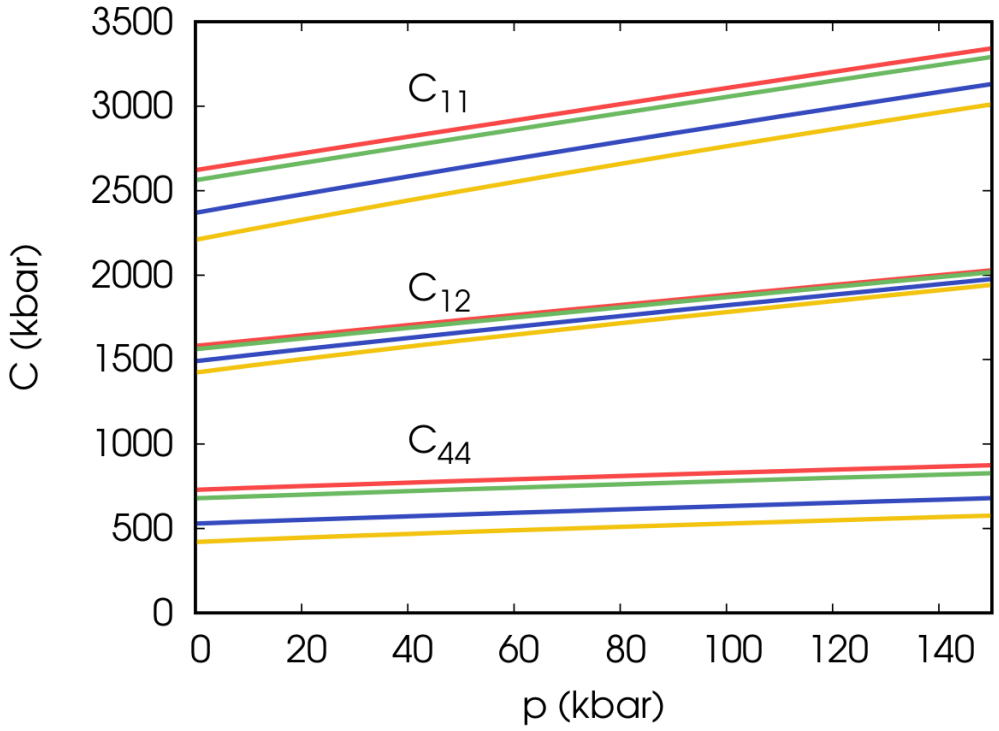

Figure 5.8: QHA adiabatic elastic constants C_{11}, C_{12}, and C_{44} as a function of pressure calculated within PBE at 5 K (red line), 300 K (green line), 1000 K (blue line), and 1500 K (yellow line).

Chapter 6

Beryllium

Beryllium is a lightweight metal with a very low density, high elasticity and thermal conductivity, extremely low Poisson ratio and several other noteworthy physical properties that make it quite attractive for applications in aircrafts, satellites, and spacecraft. It is also used in nuclear power industry as a neutron reflector and moderator. Its thermodynamic properties are well explored, experimentally [8, 18, 180, 106] and theoretically [116, 77, 103, 172, 161, 171, 195], but the knowledge of its elastic constants (ECs) is still improvable.

Room temperature ECs, measured several times (see Ref. [129] for a recent account) have been calculated at 0 K by many authors. As one of us discussed previously [39], the reported results are not always in agreement among themselves, sometimes due to different numerical techniques but sometimes also due to the different treatment of internal relaxations.

Pressure dependent ECs at 0 K have been calculated in Refs. [172, 77, 116] with the first two papers in substantial agreement while the third that predicts a somewhat different pressure dependence.

For the temperature dependent elastic constants (TDECs), two sets of experimental data exist at room pressure. The first [173] covering the low temperature range from 0 K to 300 K and the second [165] the range from 298 K to 573 K. Ref. [165] reported a quite strong decrease in ECs with temperature, a fact that motivated further theoretical investigations [103, 161, 171] using the quasi-static approximation (QSA) in Ref. [103] and the quasi-harmonic approximation (QHA) in Refs. [161, 171]. None of these studies could obtain the rapid decrease of the ECs claimed by Ref. [165] and a reexamination of the experimental data was suggested. Ref. [133] measured the compressional and shear sound velocities of polycrystalline beryllium and derived the bulk and shear modulus from them. Although the experimental errors are still quite large, the results are more in line with the theoretical data than with Ref. [165].

At high pressure and high temperature the situation is even more obscure. We are not aware of any experimental or theoretical paper available so far.

In this chapter we reexamine the TDECs of beryllium focusing on the analysis of the effects of the common approximations made for studying the ECs of anisotropic solids: the zero static internal stress approximation (ZSISA) [4] and the constant volume (V-ZSISA) [124]

approximation (also called the statically constrained quasi-harmonic approximation [24]). Within ZSISA one avoids the calculation of the free energy as a function of the atomic positions in strains that decrease the symmetry enough to let the atoms free to move. For each strain, the atomic positions are calculated at 0 K from energy minimization and the free energy is computed at one atomic configuration. Using the V-ZSISA the equilibrium configurations are obtained at 0 K by optimizing (using energy) the crystal parameters in a set of volumes V_i (or pressure p_i) and computing the free energy only on the optimized geometries.

After the optimization of the crystal parameters and atomic positions, the ECs can be calculated within the QSA (from the second strain derivatives of the energy) or within the QHA (from the second strain derivatives of the free energy). We report both the QSA and QHA TDECs calculated within V-ZSISA along the "stress-pressure" 0 K isotherm determined so that the stress is a uniform pressure along it. The effect of V-ZSISA is tested on the QSA TDECs by identifying in the plane of parameters a and c/a the isotherm at 1500 K and interpolating the ECs along the "stress-pressure" isotherm at 0 K (within V-ZSISA) or along the correct isobar at 0 kbar that joins the two isotherms.

In hexagonal close packed (hcp) crystals, relaxation of atomic positions affects only the ECs C_{11} and C_{12}. On these, we test the ZSISA, by comparing its predictions with the ECs calculated with atomic positions that minimize the free energy. We find that both V-ZSISA and ZSISA in beryllium are accurate and have only minor effects on the final QHA ECs.

As in other metals [119, 121, 65, 63], QHA gives results closer to experiment than the QSA, but even if the QHA gives a faster decrease with temperature of C_{11}, C_{33}, and C_{44}, the derivatives with respect to temperature of these ECs are still lower than in experiment and in substantial agreement with previous calculations.

Finally, we present the pressure-dependent QHA ECs at 4 K, 500 K, and at 1000 K, in hopes that these theoretical data can help and stimulate the experimental measurement of these quantities.

6.1 Thermodynamics and elastic constants

In this chapter, the `thermo_pw` [38] software developed by ourselves is employed to calculate all thermodynamic properties. The QHA, as implemented in `thermo_pw`, has been discussed in previous publications [39, 147, 148, 118, 119, 120, 121]. Here, we summarize the main formulas and discuss the thermodynamic relationships needed for computing the ECs of hcp solids. Except for a few relationships that are more easily written in Cartesian coordinates, we will use the Voigt notation with indices going from 1 to 6.

Within QHA, the Helmholtz free energy $F(\xi,T)$ of a solid is a function of temperature T and (unit cell) parameters ξ that in the hexagonal lattice are a and c/a. It can be written as the sum of three contributions:

$$F(\xi,T) = U(\xi) + F_{ph}(\xi,T) + F_{el}(\xi,T), \tag{6.1}$$

where $U(\xi)$ is the static energy, $F_{ph}(\xi,T)$ is the vibrational free energy, and $F_{el}(\xi,T)$ is the

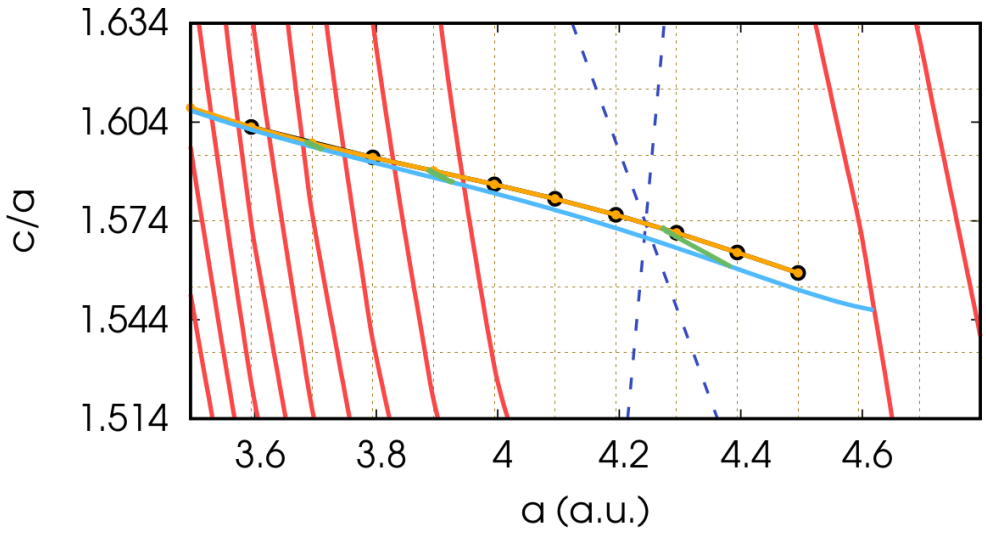

Figure 6.1: Contours of constant total energy (red lines) plotted in the plane a and c/a. The two blue dashed straight lines intersect at the position of the energy minimum. The orange curve is the "stress-pressure" isotherm at 0 K. The light-blue curve is the "stress-pressure" isotherm at 1500 K. The three green lines show the isobars at 0 kbar, 500 kbar, and 1000 kbar for temperatures going from 0 K to 1500 K. Points on the orange curve shows the values of a and c/a in which we have computed the quasi-harmonic TDECs. The 0 K ECs as well as the phonon dispersions have been calculated in these points and also in all the points of the two dimensional grid shown with dotted lines.

electronic excitations contribution to the free energy. $U(\xi)$ is computed via density functional theory (DFT), $F_{ph}(\xi,T)$ is written in terms of the phonon frequencies $\omega_\eta(\mathbf{q},\xi)$:

$$\begin{aligned} F_{vib}(\xi,T) &= \frac{1}{2N}\sum_{\mathbf{q}\eta}\hbar\omega_\eta(\mathbf{q},\xi) \\ &+ \frac{1}{N\beta}\sum_{\mathbf{q}\eta}\ln\left[1-\exp\left(-\beta\hbar\omega_\eta(\mathbf{q},\xi)\right)\right], \end{aligned} \tag{6.2}$$

and $F_{el}(\xi,T)$ can be computed within the rigid bands approximation from the electronic density of states (see Ref. [121]). In beryllium we expect small effects of electronic excitations [103] and in this chapter we do not consider them. In Eq. 6.2, $\hbar$ is the reduced Planck's constant, $\beta = \frac{1}{k_B T}$, where k_B is the Boltzmann constant, $\mathbf{q}$ are the phonon wavevectors and η indicates the different modes. N is the number of cells of the solid (equal also to the number of phonon wavevectors $\mathbf{q}$). These free energies are computed for a grid of parameters $\xi_i = (a_i, c_i/a_i)$, $i = 1, N_p$. $U(\xi)$ as well as the vibrational free energy are interpolated by a fourth-degree polynomial.

Considering the stress tensor $\boldsymbol{\sigma}$ as a fixed set of parameters, and the strain as a function

of the crystal parameters minimization of the functional:

$$G_{\boldsymbol{\sigma}}(\xi,T) = F(\xi,T) - V\sum_j \boldsymbol{\sigma}_j \epsilon_j \tag{6.3}$$

with respect to the parameters ξ gives the EOS:

$$\boldsymbol{\sigma}_j = \frac{1}{V}\frac{\partial F(\xi,T)}{\partial \epsilon_j}. \tag{6.4}$$

Hence the crystal parameters that minimizes $G_{\boldsymbol{\sigma}}(\xi,T)$ are those that give stress $\boldsymbol{\sigma}$. Using for the stress a uniform pressure we find the crystal parameters at any pressure and temperature ($\xi_p(T)$). From the $\xi_p(T)$ we can compute also the volume as a function of p that is the equation of state (EOS): $V(p,T) = V(\xi_p(T))$.

Using $V(p,T)$ we obtain the volume thermal expansion $\beta(p,T)$ at pressure p as:

$$\beta(p,T) = \frac{1}{V(p,T)}\frac{\partial V(p,T)}{\partial T}\bigg|_p. \tag{6.5}$$

For an hexagonal system, the thermal expansion tensor is diagonal and has two different components. We get:

$$\alpha_1 = \alpha_2 = \frac{1}{a}\frac{da}{dT}, \tag{6.6}$$

$$\alpha_3 = \frac{1}{c}\frac{dc}{dT}. \tag{6.7}$$

The isothermal ECs are calculated from the second strain derivatives of the free energy.

$$\tilde{C}^T_{ij} = \frac{1}{V}\frac{\partial^2 F}{\partial\varepsilon_i \partial\varepsilon_j}\bigg|_T, \tag{6.8}$$

Actually using the following five strain types: $(\epsilon,0,0,0,0,0)$, $(0,0,\epsilon,0,0,0)$, $(\epsilon,0,\epsilon,0,0,0)$, $(\epsilon,\epsilon,0,0,0,0)$, and $(0,0,0,\epsilon,0,0)$, $\frac{1}{V}\frac{\partial^2 F}{\partial\epsilon^2}$ is equal to $\tilde{C}_{11}$, $\tilde{C}_{33}$, $\tilde{C}_{11}+\tilde{C}_{33}+2\tilde{C}_{13}$, $2\tilde{C}_{11}+2\tilde{C}_{12}$, and $\tilde{C}_{44}$ respectively. When the equilibrium reference configuration has a non vanishing stress $\sigma^{(0)}_i$ (or $\sigma^{(0)}_{ij}$ in cartesian notation), the stress-strain ECs C^T_{ij} are obtained as (in cartesian notation) [14]:

$$\begin{aligned} C^T_{ijkl} = \tilde{C}^T_{ijkl} &- \frac{1}{2}\Big(2\sigma^{(0)}_{ij}\delta_{kl} - \frac{1}{2}\sigma^{(0)}_{ik}\delta_{jl} - \frac{1}{2}\sigma^{(0)}_{il}\delta_{jk} \\ &- \frac{1}{2}\sigma^{(0)}_{jk}\delta_{il} - \frac{1}{2}\sigma^{(0)}_{jl}\delta_{ik}\Big). \end{aligned} \tag{6.9}$$

An hexagonal lattice with an arbitrary a and c/a has a diagonal stress tensor with two equal components $\sigma^{(0)}_1 = \sigma^{(0)}_2$, while $\sigma^{(0)}_3$ can be different. From Eq. 6.9 we find $C^T_{11} = \tilde{C}^T_{11}$,

$C^T_{33} = \tilde{C}^T_{33}$ while $C^T_{12} = \tilde{C}^T_{12} - \sigma^{(0)}_1$, $C^T_{21} = \tilde{C}^T_{21} - \sigma^{(0)}_1$, $C^T_{13} = \tilde{C}^T_{13} - \sigma^{(0)}_1$, $C^T_{31} = \tilde{C}^T_{31} - \sigma^{(0)}_3$, $C^T_{44} = \tilde{C}^T_{44} + \frac{1}{4}(\sigma^{(0)}_1 + \sigma^{(0)}_3)$. Since $\tilde{C}_{ij}$ is symmetric in the exchange of the two indices, C^T_{ij} is not. For an hexagonal lattice we have $C^T_{12} = C^T_{21}$, but $C^T_{31} \neq C^T_{13}$. Symmetry is recovered only along the "stress-pressure" isotherm where $\sigma^{(0)}_1 = \sigma^{(0)}_3 = -p$. Along this curve Eq. 6.9 becomes (in Cartesian notation):

$$C^T_{ijkl} = \tilde{C}^T_{ijkl} + \frac{p}{2}\left(2\delta_{i,j}\delta_{k,l} - \delta_{i,l}\delta_{j,k} - \delta_{i,k}\delta_{j,l}\right). \tag{6.10}$$

The second derivatives of the free energy are calculated as described in Ref. [39] taking as equilibrium configuration a subset of parameters ξ_i along the "stress-pressure" 0 K isotherm. The values of ξ_i along this curve are given in the appendix, together with the pressure present in each configuration. The ECs at any other set of parameters ξ_p at temperature T and pressure p are obtained by projection on the 'stress-pressure" 0 K isotherm ($a(T)$ is unchanged while $c/a(T)$ is substituted with $c/a(a(T))$) and interpolation by a fourth-degree polynomial.

Adiabatic ECs are calculated from the isothermal ones as:

$$C^S_{ij} = C^T_{ij} + \frac{TVb_ib_j}{C_V}, \tag{6.11}$$

where b_i are the thermal stresses:

$$b_i = -\sum_j C^T_{ij}\alpha_j. \tag{6.12}$$

6.1.1 HCP internal relaxations

The application of a strain $(\epsilon, 0, 0, 0, 0, 0)$ to the hcp structure transforms the hexagonal lattice into a base centered orthorhombic lattice and the positions of the two atoms in the unit cell are no more constrained in the y direction. The energy can be written in the form

$$E(\epsilon, y) = \frac{1}{2}VC^{(0)}_{11}\epsilon^2 + \Lambda\epsilon y + \frac{1}{2}\mu\omega^2 y^2 + E(0,0), \tag{6.13}$$

where $C^{(0)}_{11}$ is the frozen ion ECs obtained by keeping the two atoms of the hcp unit cell in the strained position. In this equation y is the deviation of the positions of the two atoms from their strained position (that for the y coordinate coincides with the equilibrium position) $a\frac{1}{2\sqrt{3}}$ where a is the hexagonal unstrained lattice parameter (We refer to Fig.2 of Ref. [39] for an illustration of the geometry). By minimizing the energy with respect to y we find:

$$y = -\frac{\Lambda\epsilon}{\mu\omega^2}, \tag{6.14}$$

that inserted in Eq. 6.13 gives the correction to the $C^{(0)}_{11}$ EC.

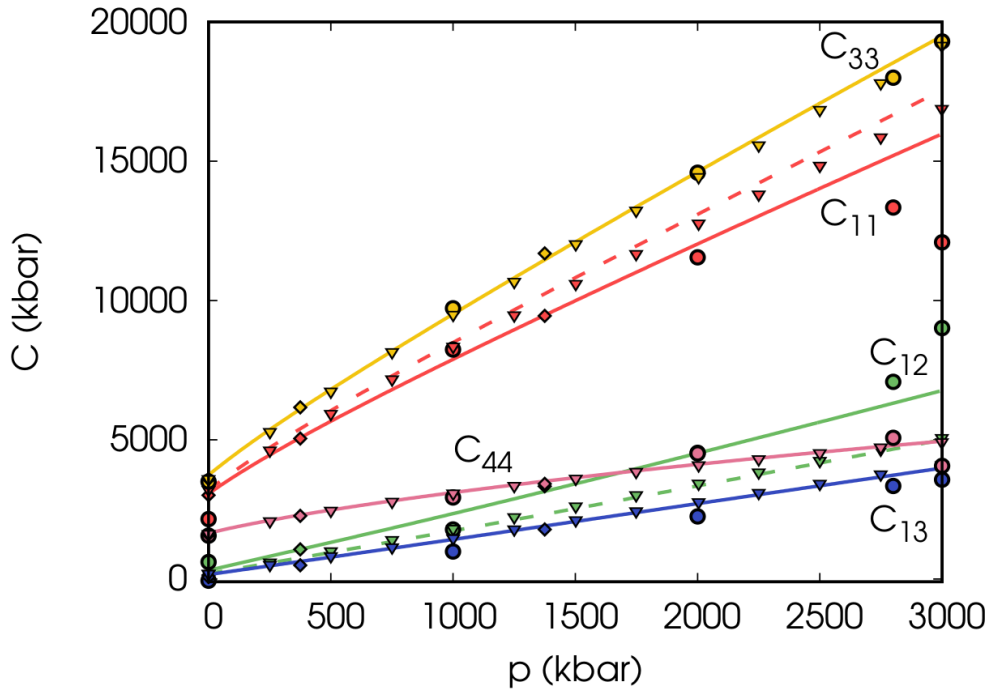

Figure 6.2: Stress-strain elastic constants of Be as a function of pressure at 0 K (continous lines) compared with previous calculations of Ref. [172] (diamonds), Ref. [77] (circles), and Ref. [116] (triangles). The dashed lines show C_{11} and C_{12} obtained by keeping the ions fixed at the uniformly strained positions.

We find:

$$C_{11} = C_{11}^{(0)} - \frac{\Lambda^2}{V\mu\omega^2}. \tag{6.15}$$

Similarly, within the QHA approximation, we can use the free energy instead of the energy and write:

$$\begin{aligned} F(\epsilon, y, T) &= \frac{1}{2} V C_{11}^{F(0)}(T)\epsilon^2 + \Lambda_F(T)\epsilon y + \frac{1}{2}\mu\omega_F^2(T)y^2 \\ &+ F(0,0,T), \end{aligned} \tag{6.16}$$

By minimizing the free energy at each temperature we find:

$$y^F = -\frac{\Lambda_F(T)\epsilon}{\mu\omega_F^2(T)}, \tag{6.17}$$

and we obtain the correction to the $C_{11}^{F(0)}$ EC:

$$C_{11}^F(T) = C_{11}^{F(0)}(T) - \frac{\Lambda_F^2(T)}{V\mu\omega_F^2(T)}. \tag{6.18}$$

Using for y Eq. 6.14 instead of Eq. 6.17 is the ZSISA approximation.

6.1.2 Elastic constants computation beyond ZSISA

The equations in the previous subsection provide a method to compute the ECs accounting for internal relaxations without ZSISA. Similarly to what was done in Ref. [122], for each strain, it is possible to calculate the free energy for a finite number of atomic positions. The free energy as a function of strain and atomic coordinates is then interpolated at each temperature with a polynomial as in Eq. 6.16. The mixed second derivatives $\Lambda_F(T)$ and the frequencies $\mu\omega_F^2(T)$ are calculated from the interpolating polynomial and the correction to the frozen ions ECs derived from Eq. 6.18.

In this chapter, we propose an alternative method to compute the ECs in presence of internal relaxation that we call full free energy minimization (FFEM). For each strain, the energy (or free energy) as a function of the internal position y is interpolated with a second or fourth degree polynomial and the minimum is found. The value of the minimum (free-) energy is assigned to the given strain and used to calculate the TDECs via Eq. 6.8. This approach, which at 0 K is equivalent to the relaxed-ions calculation, has the advantage that it can be carried out at any temperature and, at variance with the approach of Ref. [122], does not require the knowledge of the form of the interpolating polynomial, that might be structure dependent and has to be analyzed on a case by case basis. Therefore, using the full free energy minimization (FFEM) we obtain the relaxations and ECs beyond the ZSISA and compare them with the ZSISA ones. A similar method that goes beyond ZSISA has been applied for the calculation of the internal thermal expansion of ZnO [111].

6.2 Computational details

The calculations presented in this work are done by using DFT as implemented in the Quantum ESPRESSO (QE) package. [60, 59] The exchange and correlation functional is the LDA. [152] We employ a plane-wave basis with the pseudopotential `Be.pz-n-vbc.UPF` obtained from the QE website. This pseudopotential has the $2s$ states in valence, while the $1s$ electrons are frozen in the core and accounted for by the nonlinear core correction [114]. For the wave functions and charge density cutoffs, we use 35 Ry and 140 Ry respectively. The Fermi surface has been dealt with by the smearing approach of Methfessel and Paxton [128] with a smearing parameter $\sigma = 0.02$ Ry. With this smearing, the Brillouin zone integrals give reasonable values of the ECs with a $64 \times 64 \times 40$ **k**-point mesh.

We first determine the "stress-pressure" 0 K isotherm in the crystal parameters space by computing the total energy in a mesh of 14×7 grid of values of a and c/a covering a pressure range from about -200 kbar to 1800 kbar. On this grid of geometries, we compute also the phonon dispersions and the 0 K ECs. This give us the thermal expansion tensor and the "stress-pressure" isotherm at any temperature, as well as the QSA ECs without the V-ZSISA approximation.

Along the "stress-pressure" isotherm at 0 K, we choose 11 values of a and c/a as given in Tab. I in the appendix. In these geometries we compute the phonon dispersions, the free energy and the 0 K ECs. In 8 of these 11 geometries we also compute the QHA TDECs as

second strain derivatives of the free energy. These ECs are then used to interpolate the ECs for any other pressure and temperature within the V-ZSISA approximation. The 8 reference geometries have $i = 2$, 4, 6, 7, 8, 9, 10, and 11 (where geometry 1 is the point at highest pressure) and the QHA TDECs are calculated by 5 strain types that lead to base centered orthorhombic (strain types 1 and 3), hexagonal (strain types 2 and 4) and monoclinic (strain type 5) lattices. Each strain type is sampled by 6 strains, from $\epsilon = -0.0125$ to $\epsilon = 0.0125$ with a stepsize $\delta\epsilon = 0.005$. Each of the $30 \times 8 = 240$ strained configurations requires calculations of the phonon frequencies by density functional perturbation theory (DFPT) [12, 34] to obtain the dynamical matrices on a $6 \times 6 \times 6$ **q**-point grid. This grid leads to 28 inequivalent **q**-points in the hexagonal cell, 52 in the base centered orthorombic cell and to 68 in the monoclinic cell.

To calculate FFEM ECs, for each equilibrium geometry, free energies are needed on 78 strained configurations. This number is determined by considering that for strain type 1 and 3, six values of strain ϵ are sampled and, in addition, we calculate 5 different values of y. Therefore, the five strain types of hcp structure will require $30+6+30+6+6 = 78$ phonon dispersions.

The dynamical matrices calculated by DFPT are Fourier interpolated into a $200 \times 200 \times 200$ **q**-point mesh to evaluate the free energy and its strain derivatives. The calculations are all performed on the Leonardo supercomputer at CINECA with a GPU version of `thermo_pw` that optimizes some routines of QE for problems with dense **k**-points sampling in metallic systems [66]. Please refer to the appendix for a workflow of the present calculations.

Recently, some methods to calculate the dynamical matrices in strained configurations [124] or to reduce the number of calculated phonon dispersions needed for QHA thermal expansion [164] and for QHA TDECs [125, 52] have been proposed. It could also be useful to try them in order to speed up the calculations in our problem.

Table 6.1: The 0 K elastic constants compared with experiment and previous calculations. B, E, G, and ν are the bulk modulus, the Young's modulus, the shear modulus, and the Poisson's ratio, of polycrystalline beryllium calculated within the Voigt-Reuss-Hill approximation, respectively.

	T (K)	a_0 (a.u.)	$\frac{a_0}{c_0}$	C_{11} (kbar)	C_{12} (kbar)	C_{13} (kbar)	C_{33} (kbar)	C_{44} (kbar)	B (kbar)	E (kbar)	G (kbar)	ν
This study (LDA)	0	4.244	1.573	3074	280	163	3674	1639	1223	3259	1543	0.06
Ref. [172]	0	4.281	1.573	3008	141	71	3595	1602	1127	3182	1545	0.06
Ref. [77](LDA)	0	4.312	1.567	2150	610	-60	3500	1560	970	2532	1114	0.06
Ref. [116](LDA)	0	4.248	1.57	3109	195	191	3595	1621	1215	3267	1552	0.05
Ref. [103](PBE)	0		1.577	2882	254	0	3652	1567	1100	3080	1490	0.03
Ref. [161](PBE)	0		1.575	2965	194	83	3612	1632	1137	3177	1536	0.03
Ref. [171](LDA)				2966	403	209	3323	1798	1210	3214	1520	0.06
Ref. [129] (Expt.)		4.319[1]	1.568[1]	2936	268	140	3567	1622	1168	3152	1501	0.05

[1] Ref. [117].

6.3 Results and discussion

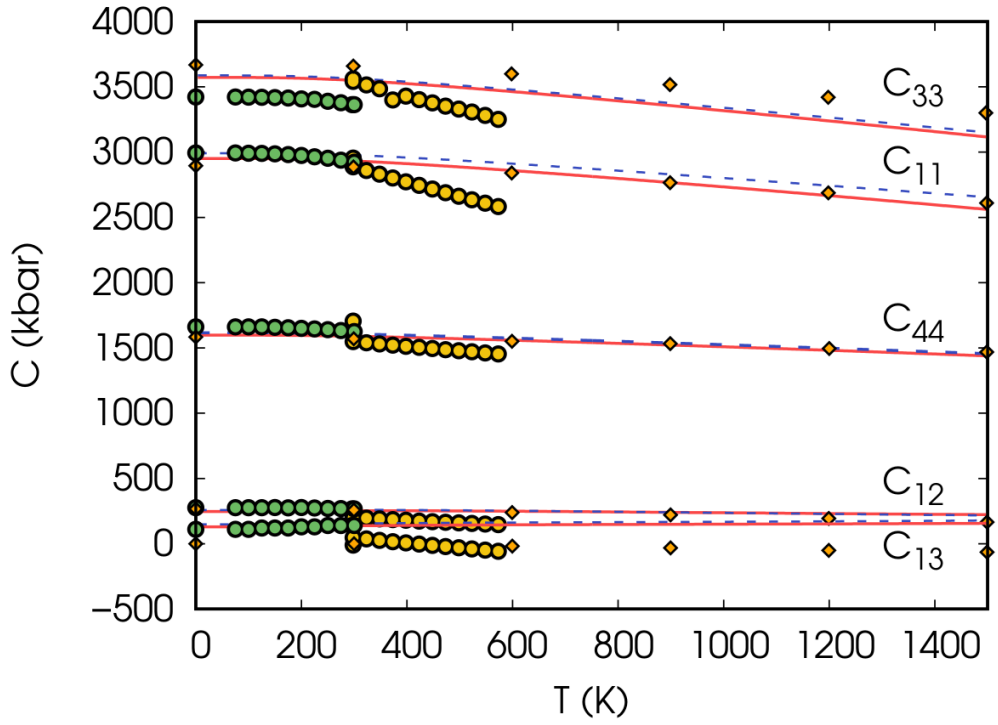

Figure 6.3: Adiabatic LDA elastic constants of Be as a function of temperature calculated within the QSA (red lines) along the 0 kbar isobar (with ZSISA atomic positions). For comparison we have reported also the QSA elastic constants interpolated (within V-ZSISA) only on the "stress-pressure" isotherm at 0 K (dashed blue lines). The dots are the experimental points of Ref. [165] (yellow dots) and [173] (green dots). Diamond are the theoretical PBE QSA calculation of Ref. [103].

The equilibrium crystal parameters at 0 K obtained from the total energy minimization are reported in Tab. 6.1 together with our calculated ECs. For comparison, we also show the ECs of selected references that are discussed below. A more complete account of the data available in the literature and of the effects of parameters such as exchange and correlation energy, the pseudopotentials, the **k**-point sampling, and the atomic relaxations method is presented in Ref. [39]. When compared with the recent experiment of Ref. [129], our computed ECs at 0 K match experiment with errors $\Delta C_{11} = 138$ kbar (4%), $\Delta C_{12} = 12$ kbar (4%), $\Delta C_{13} = 23$ kbar (16 %), $\Delta C_{33} = 107$ kbar (3 %), and $\Delta C_{44} = 17$ kbar (1 %). All errors are within 10% with the exception of C_{13}, whose value is, however, quite variable also among different experimental reports [129].

The crystal parameters as a function of pressure $a(p)$ and $\frac{c}{a}(p)$ are calculated from the minimization of the Gibbs energy (Eq. 6.3). The "stress-pressure" isotherm at 0 K is shown in Fig. 6.1 (orange curve) together with the constant energy contours in the plane a, c/a

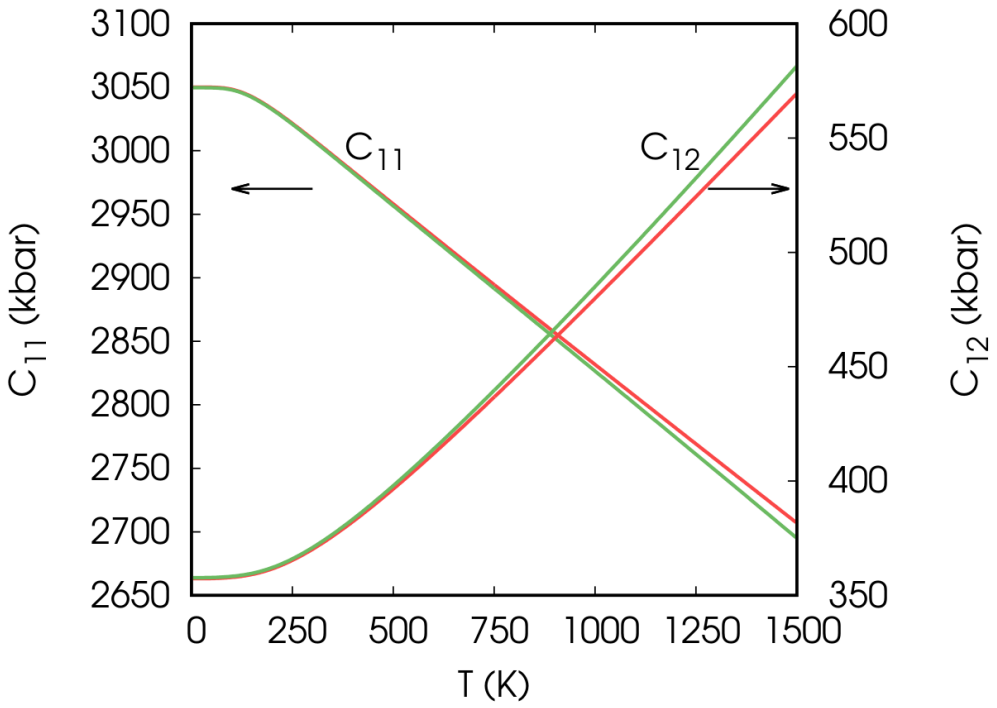

Figure 6.4: Elastic constants C_{11} and C_{12} of Be as a function of temperature calculated as second derivatives of the free energy (within the QHA) at fixed equilibrium geometry. We compare the results obtained with the ZSISA (red lines) and within the FFEM (green lines), a scheme in which the internal y parameter is relaxed at each strain and temperature by minimizing the free energy.

and the position of the energy minimum. Pressure dependent ECs are calculated in a set of points along this curve. The resulting equations of state (EOS) and $c/a(p)$ are reported in the supplementary material.

Fig. 6.2 shows the pressure dependent ECs at 0 K compared with those already published. Our LDA data are in good agreement with the LDA results of Sin'ko et al. [172] available until 1500 kbar, and with the PBE ones [149] of Hao et al. [77] at least until 2000 kbar. At variance with Ref. [77] we find no strong deviation from linearity at higher pressures. The LDA values of C_{33}, C_{13}, and C_{44} of Luo et al. [116] agree with ours while C_{11} and C_{12} are different. For the latter, better agreement is found by computing the ECs with the ions frozen in their strained positions. We mention also that the ECs given in Table II of Ref. [112] are the second derivatives of the total energy with respect to the Lagrangian strains (we call them $\mathring{C}_{ijkl}$). In order to compare with our stress-strain results, we have used the following expression [14]:

$$C^T_{ijkl} = \mathring{C}_{ijkl} + p(\delta_{ij}\delta_{kl} - \delta_{ik}\delta_{jl} - \delta_{il}\delta_{jk}). \tag{6.19}$$

The data of Refs. [172, 77], instead, are the stress-strain ECs and no modification is done.

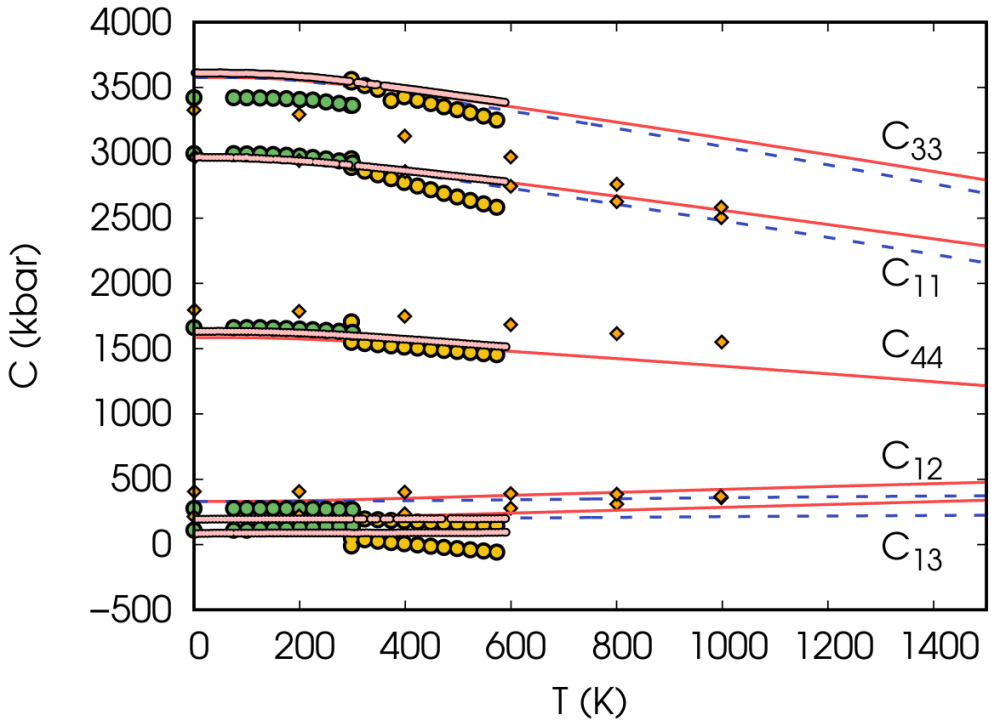

Figure 6.5: Adiabatic elastic constants of Be as a function of temperature (red lines) calculated within the QHA. Atomic relaxations have been dealt with the ZSISA approximation. Calculations have been done only along the "stress-pressure" 0 K isotherm (V-ZSISA). The dots are the experimental points of Ref. [165] (yellow dots) and [173] (green dots). The diamond are the theoretical QHA results of Ref. [171] while the pink dots are the isothermal QHA elastic constants calculated in Ref. [161]. The isothermal elastic constants are also shown (blue dashed lines).

Ref. [77] uses the PBE functional, so some care should be used to compare with our results. However, in other materials [65, 63], we found that on the scale of this figure the differences among functionals are small, and the pressure derivative of the ECs are similar.

Computing the phonon dispersions on all the points of the two-dimensional grid shown in Fig. 6.1, we obtain a set of Gibbs energies that can be interpolated with a fourth-degree polynomial whose minimum gives $a(T)$ and $\frac{c}{a}(T)$ at any temperature and pressure. The "stress-pressure" isotherm at 1500 K is shown in Fig. 6.1. In this parameter space, the "stress-pressure" isotherms at 0 K and at 1500 K are close to each other. This fact is exploited in the literature, where TDECs are calculated only in a few points along the isotherm at 0 K. This is the so-called V-ZSISA approximation. We estimated the effect of this approximation on the QSA adiabatic ECs.

Fig. 6.3 shows two sets of QSA TDECs. In the red curves, the 0 K ECs are calculated at all points of the two-dimensional grid shown in Fig. 6.1 and interpolated at the crystal parameters that minimize the Gibbs energy. At zero pressure, we interpolate along the green

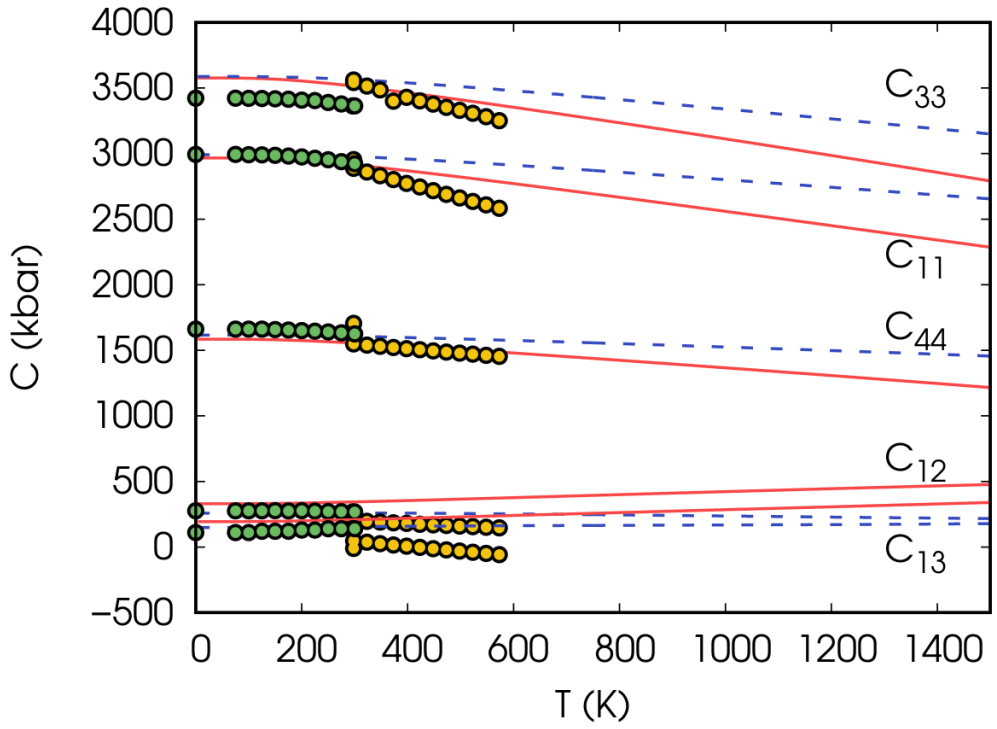

Figure 6.6: Temperature dependent elastic constants of Be as a function of temperature calculated within the V-ZSISA QHA (red lines) are compared with the V-ZSISA QSA (blue dashed lines). The dots are the experimental points of Ref. [165] (yellow dots) and [173] (green dots).

isobar shown in Fig. 6.1 close to the energy minimum. Note that at 0 K this curve does not start exactly on the energy minimum because of zero-point effects.

In V-ZSISA, instead, the ECs are calculated only in a few points on the "stress-pressure" isotherm at 0 K and interpolated at $a(T)$ for each temperature. Along this line c/a is a function of a. At each temperature we use $a(T)$, but $c/a(T) = c/a(a(T))$. The change of c/a that one would have moving from the "stress-pressure" isotherm at 0 K to the "stress-pressure" isotherm at temperature T is neglected [103]. The results are shown with a blue dashed line in Fig. 6.3. Differences with respect to the complete interpolation are quite small and the temperature dependence is weakly influenced. The changes from 0 K to 1500 K are: $\Delta C_{11} = 391$ kbar (13%), $\Delta C_{12} = 24$ kbar (10%), $\Delta C_{13} = -26$ kbar (-20 %), $\Delta C_{33} = 457$ kbar (13 %), and $\Delta C_{44} = 159$ kbar (10 %) with the interpolation on the two-dimensional grid and $\Delta C_{11} = 336$ kbar (11%), $\Delta C_{12} = 41$ kbar (16%), $\Delta C_{13} = -29$ kbar (-19 %), $\Delta C_{33} = 438$ kbar (12 %), and $\Delta C_{44} = 160$ kbar (10 %) within V-ZSISA. These data agree reasonably well with the QSA calculation of Ref. [103] which finds, in the same temperature range, $\Delta C_{11} = 286$ kbar (10%), $\Delta C_{12} = 101$ kbar (40%), $\Delta C_{33} = 368$ kbar (10 %), and $\Delta C_{44} = 115$ kbar (7 %). In this reference C_{13} is almost zero and does not change with temperature.

The other approximation that we tested is the ZSISA. In Fig. 6.4 we show the ECs C_{11}

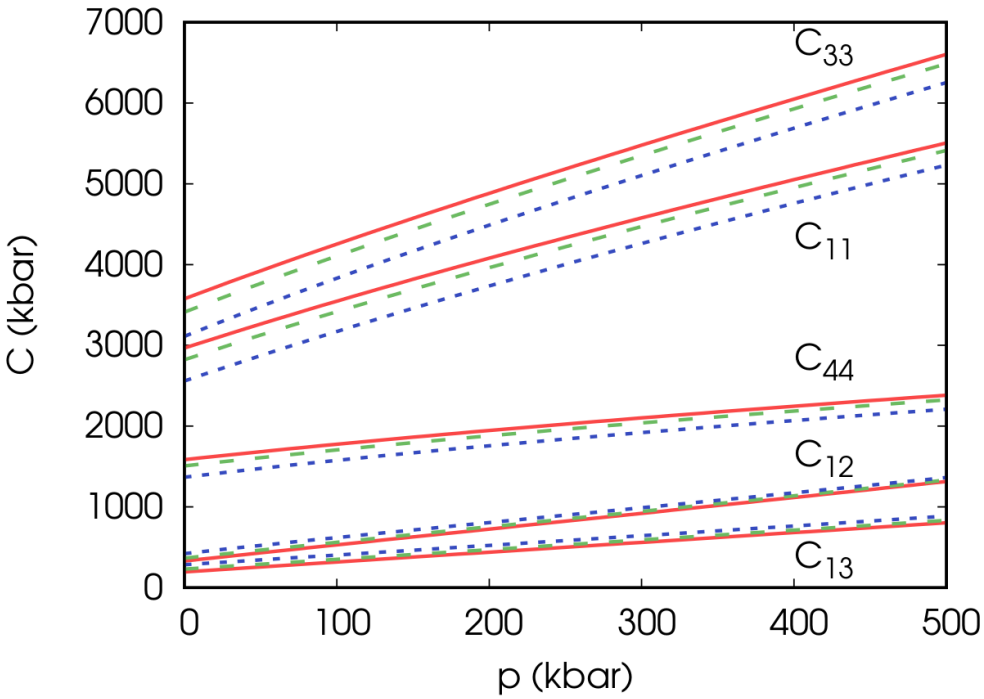

Figure 6.7: Adiabatic pressure dependent elastic constants of Be calculated within the V-ZSISA QHA at three temperatures: 4 K (red line), 500 K (green lines) 1000 K (blue lines). Calculations have been done along the "stress-pressure" isotherm.

and C_{12} calculated within QHA with and without the ZSISA. These ECs are computed at one reference geometry: the 0 K crystal parameters (Tab. 6.1). Hence these ECs have only the contribution of the free energy to the temperature variation. As explained above, C_{11} is calculated using the strain $(\epsilon,0,0,0,0,0)$ and is different from the frozen ion value because there is a non-zero internal relaxation, while C_{12} is calculated only later from the strain $(\epsilon,\epsilon,0,0,0,0)$ that does not allow any internal relaxation. It is different from its frozen-ions value because the second derivatives with respect to this strain provide $2C_{11}+2C_{12}$ to which C_{11} must be subtracted.

For the first (and the third) strain type, we calculate the phonon dispersion in five different atomic positions. For each equilibrium geometry and strain type, the calculation of these ECs requires the calculation of the phonon dispersion in 30 distorted geometries and is therefore much heavier that the ZSISA calculation that requires only 6 distorted geometries per strain type. The ZSISA C_{11} is slightly higher than the FFEM, less than 1 kbar at 4 K while at 1500 K the difference are $\Delta C_{11} = -12$ kbar (-0.4%), $\Delta C_{12} = 12$ kbar (2%, negligible on the scale of the other figures).

Fig. 6.5 shows the adiabatic QHA TDECs calculated within ZSISA and V-ZSISA. In the same picture, for reference, we show also the isothermal elastic constants. From 0 K to 1500 K we have the following decreases $\Delta C_{11} = 678$ kbar (22%), $\Delta C_{12} = -145$ kbar (-44%), $\Delta C_{13} = -146$ kbar $(-75\ \%)$, $\Delta C_{33} = 784$ (22 %), and $\Delta C_{44} = 369$ (23 %). Our data are

compared with the QHA results of Ref. [171] (up to 1000 K) and of Ref. [161] (until 600 K). From 0 K to 600 K, the temperature dependence predicted by this latter reference agrees very well with our result, although the values at 0 K of C_{12} and C_{13} are different from ours. Comparing with Ref. [171] we have a similar temperature dependence for C_{11}, C_{13} and C_{44}, while we find a smaller temperature derivative for C_{33} and a C_{12} that increases with temperature instead of decreasing. From 0 K to 1000 K Ref. [171] finds: $\Delta C_{11} = 464$ kbar (16%), $\Delta C_{12} = 37$ kbar (9%), $\Delta C_{13} = -145$ kbar (-56 %), $\Delta C_{33} = 743$ (22 %), and $\Delta C_{44} = 206$ (12 %), to be compared with our adiabatic values: $\Delta C_{11} = 407$ kbar (13%), $\Delta C_{12} = -92$ kbar (-27%), $\Delta C_{13} = -91$ kbar (-46 %), $\Delta C_{33} = 465$ (13 %), and $\Delta C_{44} = 219$ (13 %).

The comparison between the QHA and the QSA elastic constants is shown in Fig. 6.6. The $T = 0$ K ECs increase with pressure, so we expect a decrease with temperature that in beryllium expands the volume. Actually this is the picture that one finds in the quasi static approximation (QSA) for the isothermal ECs. The QHA C_{11}, C_{33}, and C_{44} decrease faster with temperature than the QSA ones. Actually, at fixed structure, QHA C_{11}, C_{33}, and C_{44} decrease with temperature, and this decrease adds to that due to thermal expansion, the only effect present in the QSA calculation. Instead the QHA C_{12} and C_{13} both increases with temperature. At fixed geometry, the QHA C_{12} increase and since the thermal expansion causes a decrease as seen for the QSA C_{12}, the temperature dependence of the QHA C_{12} is the result of the cancellation of two effects and therefore the sign might be difficult to predict. Experimental there seem to be a decrease of C_{12} with temperature. The adiabatic C_{13} increases both within QSA and also within QHA at fixed volume. In the first case this is due to the adiabatic corrections that increase with temperature more than the decrease of the isothermal C_{13}. So the two increases add up and the QHA C_{13} increases more than the QSA one.

Finally, in Fig. 6.7 we report the QHA ECs as a function of pressure at 4 K, 500 K, and 1000 K. In the pressure range from 0 kbar to 500 kbar, shown in the figure, the nonlinearities are small. There is no previous information on these elastic constants and we hope that the present calculation will stimulate their measurement at high temperature and pressure, together with a reassessment of the zero pressure high temperature behavior.

Chapter 7

An alternative GPU acceleration for a pseudopotential plane-waves density functional theory code with applications to metallic systems

We present an alternative GPU acceleration for plane waves pseudopotentials electronic structure codes designed for systems that have small unit cells but require a large number of **k** points to sample the Brillouin zone as happens, for instance, in metals. We discuss the diagonalization of the Kohn and Sham equations and the solution of the linear system derived in density functional perturbation theory. Both problems take advantage from a rewriting of the routine that applies the Hamiltonian to the Bloch wave-functions to work simultaneously (in parallel on the GPU threads) on the wave-functions with different wave-vectors **k**, as many as allowed by the GPU memory. Our implementation is written in CUDA Fortran and makes extensive use of kernel routines that run on the GPU (GLOBAL and DEVICE routines). We compare our method with the CPUs only calculation and with the approach currently implemented in Quantum ESPRESSO that uses GPU accelerated libraries for the FFT and for the linear algebra tasks such as the matrix-matrix multiplications as well as OpenACC directives for loop parallelization. We show in a realistic example that our method can give a significant improvement in the cases for which it has been designed.

Density functional theory [80] (DFT) and the availability of more and more powerful computers has made the study of material properties from first-principles a well established reality. Several tools have been refined over the years to solve the one electron Kohn and Sham equations that derive from DFT, [100] the most widespread being based on a plane waves basis and pseudopotentials. Well tested, freely available [60, 59, 67] or commercial [102, 30] packages implement the theory and allow the calculation of material properties.

In the last ten years, high performance computers aiming to reach the exaflops (10^{18} floating point operations per second) switched to a hybrid technology in which the graphic processing units (GPUs) support the central processing units (CPUs) in the floating point operations. In theory, the GPUs can deliver one or two orders of magnitude more flops

than the CPUs themselves, and to harness this power many electronic structure groups are modifying their codes to run on the GPUs. [190, 61, 174, 169, 3, 2]

Extensions of common programming languages such as C/C++ or Fortran have provided commands to allocate data on the GPU, to move data from the CPU to the GPU and vice versa, and to perform calculations on these data with the GPU. CUDA Fortran commands, [142] declarations, and compiler directives and OpenACC compiler directives [145] are two of the most commonly used Fortran extensions. Recently also applications based on openMP started to appear in the literature. [41] Actually OpenACC and OpenMP have the additional benefit of being transferable to GPUs architectures of different vendors such as NVIDIA and AMD and sometimes are preferred to CUDA Fortran that is limited to NVIDIA GPUs.

So far, in several plane-waves pseudopotentials and quantum chemistry codes, the GPUs have been exploited by allocating the variables on the GPU and by substituting the calls to linear algebra and fast Fourier transform (FFTs) routines with calls to optimized library routines (such as cuBlas, [139] cuSolver, [141] cuFFT, [140] and MAGMA [86]) developed by the GPUs vendors and capable to run on the GPU. [84, 61, 41, 83, 53] Sometimes the routines of these libraries have the same names and arguments of the corresponding CPU libraries and it suffices to allocate the variables on the GPU to call the GPU routines with minimal changes to the underlying codes and algorithms. Single loops using variables allocated on the GPUs can also be accelerated by compiler directives.

In Quantum ESPRESSO [60, 59] work on this kind of acceleration started more than ten years ago [179] and has been improved over the years [163] leading to a well tested package (that in the following we call standard GPU implementation). [61] Accelerations of 2X or higher with respect to the CPU are often found in pseudopotential plane waves codes that adopt this approach. However, test systems are usually big supercells with many atoms for which the time spent to make calculations on the GPU is larger than the time needed to transfer data from the CPU to the GPU, while small size systems are left out from these tests. For some applications, metallic systems with small unit cells need tens or hundreds thousands $\mathbf{k}$ points to sample the Fermi surface. [128, 65, 63, 119, 121, 183, 184, 39, 64] The calculation of the phonon dispersions of these systems for many geometries as required for thermodynamic calculations is a problem that could take advantage from the new supercomputers, but for small systems we found that the use of the GPUs with the present codes is not always convenient and sometimes it can also slow down the calculation with respect to the CPUs alone. We have therefore tried to improve the situation and in this chapter we present the solution that we have found: an alternative approach to the acceleration of the pseudopotentials plane waves codes that is useful to deal with metallic system when there are many $\mathbf{k}$ points. We load on the GPU many wave-functions (i.e. $\mathbf{k}$ points), all the available ones if the GPU memory is large enough or as many as possible until there is free GPU memory. Then we make the calculations simultaneously on all these data (application of the Hamiltonian to the wave-functions) with each GPU thread working on a single wave-function or on a part of it. To obtain the precise control of the GPU threads that is needed we wrote a set of kernel functions (called GLOBAL in the CUDA language) that implement the theory and run on the GPU. These kernel functions need to call linear

algebra and FFT libraries from the GPU. Unfortunately, libraries such as cuFFT, cuSolver, or MAGMA, which are called from the CPU and automatically control the number of threads, are not suited for our algorithm. We need functions that can be called from the GPU threads (DEVICE functions in the CUDA language). We only find the C++ library cuFFTDx [137] that implements such functionalities, but it does not provide a FORTRAN interface so far. For the moment, we transformed to the DEVICE form the FORTRAN sources of fftpack5.1 and of selected LAPACK routines. Finally, we obtained a code significantly faster than the standard one for small systems with many **k** points.

We start with a brief introduction of the main equations that are solved in a plane-waves pseudopotential code. We stress in particular the algorithms that are relevant for the following discussion, neglecting the parts that have not changed or that are still calculated on the CPU. We then discuss how, in our method, the different parts of the code have been accelerated on the GPU. Finally, we present a test of our implementation and compare the times required by our approach with those taken by the CPUs only calculations and by the previously available GPU implementation.

7.1 Theory

The solutions of the Kohn and Sham (KS) equations minimize the DFT total energy. These equations are an eigenvalue problem for norm conserving pseudopotentials, [98] and a generalized eigenvalue problem for ultrasoft [188] or projector-augmented wave (PAW) pseudopotentials. [17, 102] For periodic solids they can be written as:

$$H_{KS}\psi_{\mathbf{k}\nu} = \varepsilon_{\mathbf{k}\nu} S\psi_{\mathbf{k}\nu}, \tag{7.1}$$

where $\mathbf{k}$ is a wave vector and ν is a band index. H_{KS} is the Kohn and Sham Hamiltonian and S is the overlap matrix. We are interested in finding the lowest N_b (number of bands) eigenvalues and eigenvectors of these equations. The Kohn and Sham Hamiltonian depends itself from a potential that is calculated from the charge density (that also depends on the wavefunctions). It is possible to solve this problem by a self-consistent procedure in which the wavefunctions are first calculated with an approximate potential. Then these wavefunctions are used to recompute the charge density and a new potential. The latter is mixed with the potential of the previous iterations and the procedure is repeated until one reaches self-consistency. At each step of the procedure however one has to diagonalize a fixed Hamiltonian which is progressively improved.

In the standard algorithm the problem is solved sequentially for each $\mathbf{k}$ vector and the charge density is computed at the end when all wave-functions are available.

7.1.1 Davidson algorithm

There are several algorithms currently implemented in electronic structure codes to find the eigenvalues and eigenfunctions in Eq. 7.1, but here we limit the discussion to the Davidson algorithm. [42] In this algorithm an initial set of N_b functions $|\phi_i^{(n)}\rangle$ are progressively

improved by enlarging the set applying $H_{KS} - \varepsilon_i S$ and solving the generalized eigenvalue problem $\tilde{H}_{ij} - \varepsilon \tilde{S}_{ij}$ on the basis formed by the original and the newly calculated vectors. A standard software library for numerical linear algebra, such as `LAPACK`, [7] is employed for the diagonalization. The algoritm is the following and has to be repeated for each **k** point:

- Given N_b trial eigenpairs: $\left\{ \left| \phi_i^{(n)} \right\rangle, \varepsilon_i^{(n)} \right\}$ of the reduced Hamiltonian calculate:

$$\tilde{H}_{ij} = \left\langle \phi_i^{(n)} \left| H_{KS} \right| \phi_j^{(n)} \right\rangle, \quad \tilde{S}_{ij} = \left\langle \phi_i^{(n)} | S | \phi_j^{(n)} \right\rangle. \tag{7.2}$$

- Build the correction vectors $\left| \tilde{\phi}_i^{(n)} \right\rangle$:

$$\left| \tilde{\phi}_i^{(n)} \right\rangle = \left(H_{diag} - \varepsilon_i^{(n)} S_{diag} \right)^{-1} \left(H_{KS} - \varepsilon_i^{(n)} S \right) \left| \phi_i^{(n)} \right\rangle, \tag{7.3}$$

  where H_{diag} and S_{diag} are the diagonal elements of H_{KS} and S in the plane waves representation.

- Normalize the correction vectors:

$$|\tilde{\phi}_i^{(n)}\rangle = \frac{|\tilde{\phi}_i^{(n)}\rangle}{\sqrt{\langle \tilde{\phi}_i^{(n)} | \tilde{\phi}_i^{(n)} \rangle}}. \tag{7.4}$$

- Build an extended reduced Hamiltonian and overlap matrix:

$$\tilde{H}_{ij} = \left\langle \phi_i^{(n)} / \tilde{\phi}_i^{(n)} \left| H_{KS} \right| \phi_j^{(n)} / \tilde{\phi}_j^{(n)} \right\rangle, \quad \tilde{S}_{ij} = \left\langle \phi_i^{(n)} / \tilde{\phi}_i^{(n)} | S | \phi_j^{(n)} / \tilde{\phi}_j^{(n)} \right\rangle. \tag{7.5}$$

- Set N_{base} equal to the number of basis vector. Diagonalize the small $N_{base} \times N_{base}$ reduced Hamiltonian to get the new estimate for the lowest N_b eigenpairs:

$$(\tilde{H} - \varepsilon \tilde{S}) v = 0 \longrightarrow \quad \left\{ \left| \phi_i^{(n+1)} \right\rangle, \varepsilon_i^{(n+1)} \right\}. \tag{7.6}$$

- Calculate $|\tilde{\phi_i}^{(n+1)}\rangle$ for all i for which $\left| \varepsilon_i^{(n+1)} - \varepsilon_i^{(n)} \right| > \varepsilon_{th}$ where ε_{th} is the accuracy required for the eigenvalues and call N_{nc} the number of new vectors.

- If $N_{nc} > 0$ repeat with the basis $|\phi_i^{(n)} / \tilde{\phi_i}^{(n)} / \tilde{\phi_i}^{(n+1)}\rangle$ of size $N_{base} + N_{nc}$ and continue with progressively larger basis. When the size of the basis becomes too large for the allocated memory instead of adding $\left\{ \left| \tilde{\phi_i}^{(n+1)} \right\rangle \right\}$ to the basis, restart with $\left\{ \left| \phi_i^{(n+1)} \right\rangle, \varepsilon_i^{(n+1)} \right\}$. If $N_{nc} = 0$ exit with eigenpairs $\left\{ \left| \phi_i^{(n+1)} \right\rangle, \varepsilon_i^{(n+1)} \right\}$

The most time consuming step of this algorithm is the application of the operators H_{KS} and S to the wave-functions as discussed in the next subsection.

7.1.2 Application of Hamiltonian

The KS Hamiltonian can be written as: [154]

$$H_{KS}\psi_{\mathbf{k}\nu} = \underbrace{-\frac{1}{2}\nabla^2\psi_{\mathbf{k}\nu}}_{kinetic\ energy} + \underbrace{V_{eff}\psi_{\mathbf{k}\nu}}_{local\ energy} + \underbrace{V_{NL}\psi_{\mathbf{k}\nu}}_{non-local\ energy}, \tag{7.7}$$

where the effective potentials is the sum of the local, Hartree, and exchange and correlation potentials:

$$V_{eff} = V_{loc} + V_H + V_{XC}, \tag{7.8}$$

while the nonlocal pseudopotential is defined in term of the projector functions $\left|\beta_m^I\right\rangle$ and pseudopotential coefficients D_{mn}^I: [98, 188]

$$V_{NL}\left|\psi_{\mathbf{k}\nu}\right\rangle = \sum_{Imn} D_{mn}^I \left|\beta_m^I\right\rangle \left\langle\beta_n^I\right|\psi_{\mathbf{k}\nu}\rangle. \tag{7.9}$$

Here I indicates the different atoms in the solid and m and n run on all the β_m^I functions of a given atom.

The overlap matrix can be calculated in a similar way: [188]

$$S\left|\psi_{\mathbf{k}\nu}\right\rangle = \left|\psi_{\mathbf{k}\nu}\right\rangle + \sum_{mn} q_{mn}^I \left|\beta_m^I\right\rangle \left\langle\beta_n^I\right|\psi_{\mathbf{k}\nu}\rangle, \tag{7.10}$$

where the coefficients q_{mn}^I are defined together with the pseudopotential.

Kinetic energy

The kinetic energy is calculated in reciprocal space. Using the Bloch theorem we write the Bloch wave-functions as:

$$\psi_{\mathbf{k}\nu}(\mathbf{r}) = e^{i\mathbf{k}\mathbf{r}} u_{\mathbf{k}\nu}(\mathbf{r}) = \frac{1}{\sqrt{V}} \sum_{\mathbf{G}} C_{\mathbf{k}+\mathbf{G}\nu} e^{i(\mathbf{k}+\mathbf{G})\mathbf{r}}, \tag{7.11}$$

where $u_{\mathbf{k}\nu}(\mathbf{r})$ is a lattice periodic function expanded in plane waves (here V is the volume of the solid) and the sum is over the reciprocal lattice vectors contained into a sphere defined by the relationship:

$$\frac{1}{2}|\mathbf{k}+\mathbf{G}|^2 < E_{cut}, \tag{7.12}$$

where E_{cut} is the kinetic energy cut-off. Then we have:

$$-\frac{1}{2}\nabla^2\psi_{\mathbf{k}\nu}(\mathbf{r}) = \frac{1}{\sqrt{V}} \sum_{\mathbf{G}} C'_{\mathbf{k}+\mathbf{G}\nu} e^{i(\mathbf{k}+\mathbf{G})\mathbf{r}}, \tag{7.13}$$

where:

$$C'_{\mathbf{k}+\mathbf{G}\nu} = \frac{1}{2}|\mathbf{k}+\mathbf{G}|^2 C_{\mathbf{k}+\mathbf{G}\nu}. \tag{7.14}$$

Local potential

The fast Fourier transform (FFT) transforms functions in real space into reciprocal space and the inverse FFT makes the inverse transformation.
From the coefficients $C_{\mathbf{k}+\mathbf{G}\nu}$, applying an inverse FFT we obtain the Bloch function in real space (up to a factor $1/\sqrt{V}$):

$$C_{\mathbf{k}+\mathbf{G}\nu} \xrightarrow{FFT^{-1}} u_{\mathbf{k}\nu}(\mathbf{r}) = \sum_{\mathbf{G}} C_{\mathbf{k}+\mathbf{G}\nu} e^{i\mathbf{G}\mathbf{r}}. \tag{7.15}$$

The effective potential is applied in real space as:

$$u'_{\mathbf{k}\nu}(\mathbf{r}) = V_{eff}(\mathbf{r}) u_{\mathbf{k}\nu}(\mathbf{r}), \tag{7.16}$$

and a final FFT computes the plane wave expansion of $u'_{\mathbf{k}\nu}(\mathbf{r})$:

$$u'_{\mathbf{k}\nu}(\mathbf{r}) \xrightarrow{FFT} C'_{\mathbf{k}+\mathbf{G}\nu} = \frac{1}{N_{\mathbf{r}}} \sum_{\mathbf{r}} u'_{\mathbf{k}\nu}(\mathbf{r}) e^{-i\mathbf{G}\mathbf{r}}, \tag{7.17}$$

where $N_{\mathbf{r}}$ is the number of points of the FFT grid (see below).

The actual calculation of V_{eff} requires the calculation of the charge density in terms of the wave-functions $\psi_{\mathbf{k}\nu}$. However since we have not modified this part of the calculation we do not discuss it in detail. We assume only to have a function V_{eff} defined in the points of the FFT grid $\mathbf{r}$.

Non local pseudopotential and overlap matrix

The application of the non local potential needs three matrix-matrix multiplications:

$$\lambda^I_{n\mathbf{k}\nu} = \left\langle \beta^I_n \middle| \psi_{\mathbf{k}\nu} \right\rangle = \sum_{\mathbf{G}} \beta^I_n(\mathbf{k}+\mathbf{G})^* C_{\mathbf{k}+\mathbf{G}\nu}, \tag{7.18}$$

$$\gamma^I_{m\mathbf{k}\nu} = \sum_n D^I_{mn} \lambda^I_{n\mathbf{k}\nu}, \tag{7.19}$$

$$V_{NL} \left| \psi_{\mathbf{k}\nu} \right\rangle = \sum_{Im} \gamma^I_{m\mathbf{k}\nu} \left| \beta^I_m \right\rangle. \tag{7.20}$$

Similarly, the application of the S matrix is:

$$\delta^I_{m\mathbf{k}\nu} = \sum_n q^I_{mn} \lambda^I_{n\mathbf{k}\nu}, \tag{7.21}$$

$$S \left| \psi_{\mathbf{k}\nu} \right\rangle = \left| \psi_{\mathbf{k}\nu} \right\rangle + \sum_{Im} \delta^I_{m\mathbf{k}\nu} \left| \beta^I_m \right\rangle. \tag{7.22}$$

where $\lambda^I_{n\mathbf{k}\nu}$ are those calculated in Eq. 7.18.

7.1.3 Density functional perturbation theory

The phonon frequencies and displacement modes are obtained by diagonalization of the dynamical matrix:

$$\omega_{\mathbf{q}}^2 \mathbf{u}_{s\alpha}(\mathbf{q}) = \sum_{s'\beta} D_{s\alpha s'\beta}(\mathbf{q}) \mathbf{u}_{s'\beta}(\mathbf{q}), \tag{7.23}$$

where $D_{s\alpha s'\beta}(\mathbf{q})$ is the dynamical matrix:

$$D_{s\alpha s'\beta}(\mathbf{q}) = \frac{1}{\sqrt{M_s M_{s'}}} \sum_{\nu} \frac{\partial^2 E_{tot}}{\partial \mathbf{u}_{\mu s\alpha} \partial \mathbf{u}_{\nu s'\beta}} e^{i\mathbf{q}(\mathbf{R}_\nu - \mathbf{R}_\mu)}, \tag{7.24}$$

where E_{tot} is the DFT total energy, $\mathbf{q}$ is a wave vector in the Brillouin zone (BZ), $\mathbf{R}_\mu$ are the Bravais lattice vectors, M_s are the atomic masses, and $\mathbf{u}_{\mu s\alpha}$ are the atomic displacements.

The second derivative of the DFT total energy can be written in terms of the change of the wave-functions due to a phonon perturbation projected on the conduction band. These functions are the solutions of a linear system: [12, 33]

$$\left[H_{KS}^{\mathbf{k}+\mathbf{q}} + \alpha Q^{\mathbf{k}+\mathbf{q}} - \varepsilon_{\mathbf{k}\nu} S\right] P_c^{\mathbf{k}+\mathbf{q}} \frac{\partial u_{\mathbf{k}\nu}(\mathbf{r})}{\partial \mathbf{u}_{s'\beta}(\mathbf{q})} = -P_c^{\mathbf{k}+\mathbf{q}} \left[\frac{\partial V_{KS}}{\partial \mathbf{u}_{s'\beta}(\mathbf{q})} - \varepsilon_{\mathbf{k},\nu} \frac{\partial S}{\partial \mathbf{u}_{s'\beta}(\mathbf{q})}\right] u_{\mathbf{k}\nu}(\mathbf{r}), \tag{7.25}$$

where $P_c^{\mathbf{k}+\mathbf{q}}$ is the projector in the conduction band and $\frac{\partial V_{KS}}{\partial \mathbf{u}_{s'\beta}(\mathbf{q})} = \frac{\partial V_{\text{loc}}}{\partial \mathbf{u}_{s'\beta}(\mathbf{q})} + \frac{\partial V_H}{\partial \mathbf{u}_{s'\beta}(\mathbf{q})} + \frac{\partial V_{\text{xc}}}{\partial \mathbf{u}_{s'\beta}(\mathbf{q})} + \frac{\partial V_{\text{NL}}}{\partial \mathbf{u}_{s'\beta}(\mathbf{q})}$. The change of the Hartree and exchange and correlation potential are:

$$\begin{aligned} \frac{\partial V_H}{\partial \mathbf{u}_{s'\beta}(\mathbf{q})} &= \int \frac{e^{i\mathbf{q}(\mathbf{r}'-\mathbf{r})}}{|\mathbf{r}-\mathbf{r}'|} \frac{\partial \rho(\mathbf{r}')}{\partial \mathbf{u}_{s'\beta}(\mathbf{q})} d^3 r', \\ \frac{\partial V_{xc}}{\partial \mathbf{u}_{s'\beta}(\mathbf{q})} &= \frac{dV_{xc}}{d\rho} \frac{\partial \rho(\mathbf{r})}{\partial \mathbf{u}_{s'\beta}(\mathbf{q})}, \end{aligned} \tag{7.26}$$

and depend self-consistently on the charge density induced by the perturbation:

$$\frac{\partial \rho(\mathbf{r})}{\partial \mathbf{u}_{s'\beta}(\mathbf{q})} = 4 \sum_{\mathbf{k}\nu} \left[u_{\mathbf{k}\nu}^*(\mathbf{r}) P_c^{\mathbf{k}+\mathbf{q}} \frac{\partial u_{\mathbf{k}\nu}(\mathbf{r})}{\partial \mathbf{u}_{s'\beta}(\mathbf{q})}\right] + \Delta_{\mathbf{u}_{s'\beta}(\mathbf{q})}(\mathbf{r}), \tag{7.27}$$

where the last term represents the change of the augmentation charge calculated in the ultrasoft and PAW case but not accelerated in the present work. [33] $Q^{\mathbf{k}+\mathbf{q}}$ is a projection in the valence manifold, [12] while the change of the nonlocal pseudopotential is described in more detail in the given references (see for instance Ref. [33]).

$\alpha Q^{\mathbf{k}+\mathbf{q}}$ can be written in the form:

$$\alpha Q^{\mathbf{k}+\mathbf{q}} = \alpha \sum_{\mu} S|u_{\mathbf{k}+\mathbf{q}\mu}\rangle\langle u_{\mathbf{k}+\mathbf{q}\mu}|S, \tag{7.28}$$

and its application to a set of wave functions $|x_{\mathbf{k+q}\nu j}\rangle$ (here j indicates the different perturbations $s'\beta$) can be calculated easily using the fact that $S|x_{\mathbf{k+q}\nu j}\rangle$ is already known from the routine that applies $H_{KS}^{\mathbf{k+q}}$ and S. We have a first matrix-matrix multiplication:

$$\mu_{\mathbf{k+q}j\mu\nu} = \langle u_{\mathbf{k+q}\mu}|S|x_{\mathbf{k+q}\nu j}\rangle\alpha, \tag{7.29}$$

then a second one:

$$|y_{\mathbf{k+q}\nu j}\rangle = \sum_{\mu} |u_{\mathbf{k+q}\mu}\rangle\mu_{\mathbf{k+q}j\mu\nu}, \tag{7.30}$$

and finally we must apply S to the vectors $|y_{\mathbf{k+q}\nu j}\rangle$ and we have:

$$\alpha Q^{\mathbf{k+q}}|x_{\mathbf{k+q}\nu j}\rangle = S|y_{\mathbf{k+q}\nu j}\rangle = |y_{\mathbf{k+q}\nu j}\rangle + \sum_{Imn} q^I_{mn}|\beta^I_m\rangle\langle\beta^I_n|y_{\mathbf{k+q}\nu j}\rangle, \tag{7.31}$$

and this requires other three matrix-matrix multiplications as illustrated above.

The self-consistent linear system (Eq. 7.25) is solved by iterations. From an initial guess of the potentials, of $\frac{\partial V_H}{\partial \mathbf{u}_{s'\beta}(\mathbf{q})} + \frac{\partial V_{xc}}{\partial \mathbf{u}_{s'\beta}(\mathbf{q})}$, the linear system is solved and new induced charge and potentials are obtained. Mixing the latter with the potentials used in the linear system it is possible to reach a self-consistent solution.

The most time consuming step of this process is however the solution of the linear system at fixed $\frac{\partial V_H}{\partial \mathbf{u}_{s'\beta}(\mathbf{q})} + \frac{\partial V_{xc}}{\partial \mathbf{u}_{s'\beta}(\mathbf{q})}$ so we will focus on this step.

7.1.4 Preconditioned conjugate gradient

The algorithm used for the solution of Eq. 7.25 with a given right hand side is a preconditioned conjugate-gradient iterative algorithm. [156, 78, 57] Given a starting guess x of the solution of the problem $Ax = b$, we improve it with the following algorithm:

$$\begin{aligned}
r &\leftarrow Ax - b, && (7.32)\\
d &\leftarrow M^{-1}r, && (7.33)\\
\rho &\leftarrow d^T r, && (7.34)\\
\gamma &\leftarrow \frac{\rho}{\rho_{old}}, && (7.35)\\
d &\leftarrow d + \gamma d_{old}, && (7.36)\\
t &\leftarrow Ad, && (7.37)\\
\lambda &\leftarrow -\frac{d^T r}{d^T t}, && (7.38)\\
x &\leftarrow x + \lambda d, && (7.39)\\
r &\leftarrow r + \lambda t, && (7.40)\\
d_{old} &\leftarrow d, && (7.41)\\
\rho_{old} &\leftarrow \rho, && (7.42)
\end{aligned}$$

Figure 7.1: Algorithms used in the standard approach and in our optimized GPU approach for the diagonalization of the Hamiltonian.

Algorithm 1 CPU and standard GPU diagonalization

for ik = 1,nks **do** ▷ nks = #k points per pool
  build $H^{\mathbf{k}}_{KS}$ and $S^{\mathbf{k}}$
  compute $\varepsilon_{\mathbf{k}\nu}$ and $\psi_{\mathbf{k}\nu}$ by Davidson (N_b)
end for

Algorithm 2 Optimized GPU diagonalization

for ikb = 1,nkblock **do** ▷ nkblock = #k points blocks
  build in parallel $H^{\mathbf{k}}_{KS}$ and $S^{\mathbf{k}}$ on GPU threads (N_k)
  compute $\varepsilon_{\mathbf{k}\nu}$ and $\psi_{\mathbf{k}\nu}$ by Davidson on GPU threads ($N_b \times N_k$)
end for

and iterate from Eq. 7.33 until the modulus of ρ is smaller than an input threshold. Here the arrows indicate that the variables on the left are substituted with those on the right. r is the negative of the residual vector while d contains minus the preconditioned residual in Eqs. 7.33 to 7.36 and minus the search direction from Eq. 7.36. Eqs. 7.35 and 7.36 are executed only from the second iteration onwards. The algorithm requires memory sufficient to save the vectors r, d, t, d_{old} of the same size of the input vector x. ρ and ρ_{old}, as well as γ and λ, are instead scalars. Moreover, we need two external routines to apply A and M^{-1}. The most time consuming step is the application of the matrix A to d. In our case $A = H^{\mathbf{k}+\mathbf{q}}_{KS} + \alpha Q^{\mathbf{k}+\mathbf{q}} - \varepsilon_{\mathbf{k}\nu} S$ so again the acceleration rests on the routine that applies $H^{\mathbf{k}+\mathbf{q}}_{KS}$ and S described above. For the preconditioning the following matrix diagonal in reciprocal space $M_{\mathbf{G},\mathbf{G}} = MAX(1.0, \frac{|\mathbf{k}+\mathbf{q}+\mathbf{G}|^2}{2\langle\psi_{\mathbf{k}+\mathbf{q}\nu}|-\frac{1}{2}\nabla^2|\psi_{\mathbf{k}+\mathbf{q}\nu}\rangle})$ is used and this vector is passed to the routine. The conjugate gradient algorithm is applied to each $\mathbf{k}$ point and to each N_{pe} perturbations. The N_b bands of a given $\mathbf{k}$ point are optimized together but the different $\mathbf{k}$ points and different perturbations are treated in sequence, one after the other. Only one $\mathbf{q}$ is calculated in each run. This algorithm has been used in the last thirty years in Quantum ESPRESSO to solve the linear system. Similar algorithms, with appropriate modifications, can be used also to minimize the total energy and solve the Kohn and Sham equations. [182]

7.2 GPU optimization

Quantum ESPRESSO has several levels of parallelization on the CPU. It is possible to divide the $\mathbf{k}$-points in groups (called pools) and assign each group to a set of cores. These cores may be further divided in groups, with each group dealing with a set of bands (bands parallelization) and finally each group of cores dealing with a set of bands can further divide the reciprocal lattice vectors ($\mathbf{G}$) and work only on a subset of these ($\mathbf{G}$ vectors parallelization). It is at this point that one can introduce the GPU acceleration. The standard method to use

Figure 7.2: Flowchart of the routine that applies $H^{\mathbf{k}}_{KS}$ and $S^{\mathbf{k}}$ to the wavefunctions. Close to each routine we write the number of threads that are used to run it on the `GPU`.

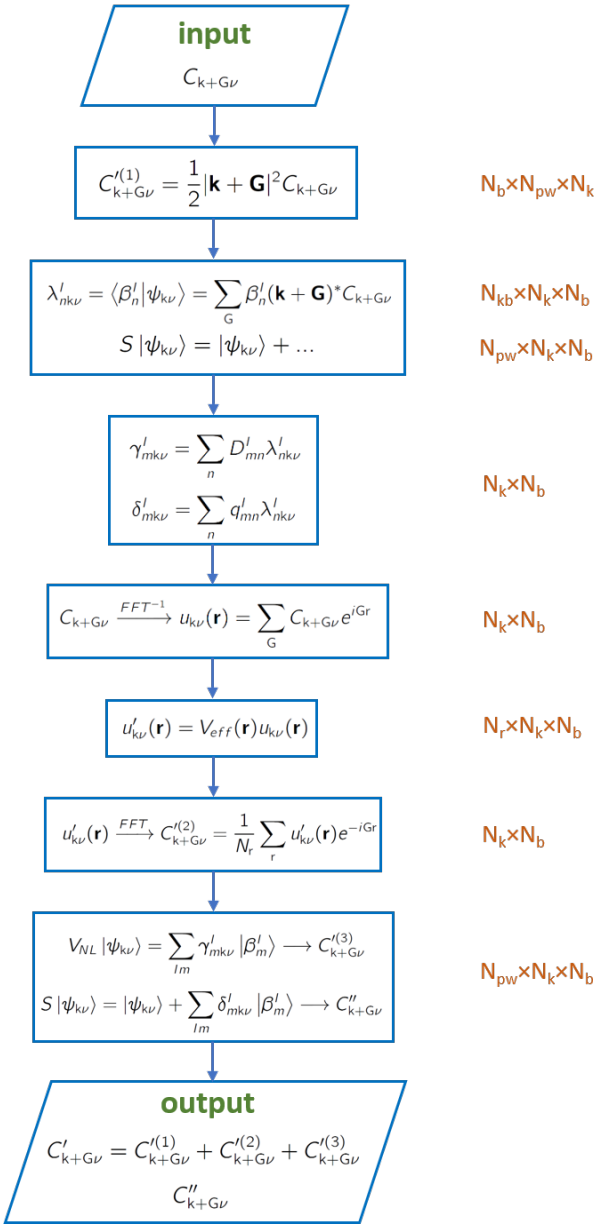

the GPU consists into allocating variables on the device memory (the GPU) and to call from HOST routines developed by NVidia that perform linear algebra (cuBLAS) operations or FFTs (cuFFT) on the data allocated on the device. It is also possible to add compiler directives to run loops in parallel on the GPU without changing the code.

The standard Davidson algorithm works sequentially on each **k** point of a pool and solves for all the bands (calling the routines that apply H_{KS} and S for a subset of bands, if bands parallelization is used). Therefore the number of times in which the GPU memory is loaded increases linearly with the number of **k** points. When the size of the problem is small, it can happen that the library matrix-matrix multiplications and FFTs routines cannot exploit all the capacity of the GPU because they have too few data to work on. As a result a GPU calculation might become even slower than a CPUs only calculation. Parallelizing on the **G** vectors just reduces further the size of the data allocated on the GPU for each **k** point and does not help in this case. Moreover, presently the GPU acceleration does not work well if many CPUs use the same GPU, so we use as many CPUs as GPUs.

Our strategy for accelerating the code on the GPU is illustrated schematically in Fig. 7.1. We put on the GPU memory as many wave-functions (i.e. **k** points) as possible in a block of N_k **k** points and run simultaneously on all these **k** points the operations of the Davidson algorithm needed to diagonalize the Hamiltonian. Each pool of CPUs cores works on its set of **k** points as assigned by the pool parallelization of Quantum ESPRESSO and only these **k** points are divided in blocks for the GPU acceleration. Bands paralellization and **G** vector parallelization presently are not supported by our approach. The main GPU optimization has been performed on the routine that applies H_{KS} and S to the wave-functions $\psi_{\mathbf{k}\nu}$, but some acceleration has been obtained also carrying out the operations of the Davidson algorithm in parallel on many **k** points. In our approach, the routine that applies H_{KS} and S is a HOST routine (i.e. a routine running on the CPU) that receives as input $C_{\mathbf{k+G}\nu}$ for N_k **k** points, and gives as output the coefficients $C'_{\mathbf{k+G}\nu}$ and $C''_{\mathbf{k+G}\nu}$ of the plane waves expansion of $H_{KS}\psi_{\mathbf{k}\nu}$ and of $S\psi_{\mathbf{k}\nu}$. This routine calls in sequence several GLOBAL routines (that is routines that run on the GPU and for which we can specify how many threads run in parallel). The sequence of routines and the formula that they implement is illustrated in Fig. 7.2. The first computes the kinetic energy and runs $N_{pw} \times N_k \times N_b$ threads each one dealing with a **G** vector of one **k** point and of one band (here N_{pw} is the number of **G** vectors used to expand the wave-functions). A second routine computes the scalar product in Eq. 7.18 and runs $N_{kb} \times N_k \times N_b$ threads, where N_{kb} is the total number of projectors $|\beta_m^I\rangle$. The latter are loaded on the GPU for all the N_k points before calling the Davidson algorithm. Another GLOBAL routine computes Eqs. 7.19 and 7.21 and runs $N_k \times N_b$ threads, while the sum over n is made inside the routine. A routine copies $C_{\mathbf{k+G}\nu}$ in $C''_{\mathbf{k+G}\nu}$ and this is made in parallel running $N_{pw} \times N_k \times N_b$ threads. This is the first term of the application of S to the wave functions. A routine sets to zero the FFT grid running $N_{\mathbf{r}} \times N_k \times N_b$ threads and another one sets the non zero elements of this grid running $N_k \times N_b$ threads, each one dealing with all the $N_{\mathbf{r}}$ grid points for one **k** point and one band. Then a set of three routines applies an inverse FFT to the wave-functions as detailed below, and a routine applies V_{eff} running $N_{\mathbf{r}} \times N_k \times N_b$ threads. Another set of three routines applies the FFT to return to reciprocal

Figure 7.3: Algorithms used in the standard phonon code and in our optimized GPU approach for solving the linear system that gives the perturbed wavefunctions.

Algorithm 3 CPU and standard GPU phonon algorithm

for ik = 1,nks **do**
  build $H_{KS}^{\mathbf{k+q}}$ and $S^{\mathbf{k+q}}$
  for ipert = 1,npe **do** ▷ npe = #perturbations
    build $P_c^{\mathbf{k+q}} \frac{\partial V_{KS}}{\partial u_{s\alpha}(\mathbf{q})} u_{\mathbf{k}v}$ (N_b)
    compute $\frac{\partial u_{\mathbf{k}v}}{\partial u_{s\alpha}(\mathbf{q})}$ by conjugate gradient (CG) (N_b)
  end for
end for

Algorithm 4 Optimized GPU phonon algorithm

for ikb = 1,nkblock **do** ▷ N_k = #k points per block
  build in parallel $H_{KS}^{\mathbf{k+q}}$ and $S^{\mathbf{k+q}}$ on GPU threads (N_k)
  build in parallel $P_c^{\mathbf{k+q}} \frac{\partial V_{KS}}{\partial u_{s\alpha}(\mathbf{q})} u_{\mathbf{k}v}$ on GPU threads $(N_b \times N_k \times N_{pe})$
  compute $\frac{\partial u_{\mathbf{k}v}}{\partial u_{s\alpha}(\mathbf{q})}$ by CG on GPU threads $(N_b \times N_k \times N_{pe})$
end for

space and a routine collects the results from the grid and adds them to $C'_{\mathbf{k+G}\nu}$. This is made in parallel on the GPU running $N_k \times N_b$ threads. Finally Eq. 7.20 is calculated by a routine that runs $N_{pw} \times N_k \times N_b$ threads and adds the result to $C'_{\mathbf{k+G}\nu}$. In the ultrasoft or PAW PPs case, the same routine calculates also the second term in the right hand side of Eq. 7.22 and adds it to $C''_{\mathbf{k+G}\nu}$.

In this algorithm, N_k must be carefully chosen and depends on the amount of GPU memory and on the size of the FFT grid. N_k is mainly limited by the necessity to allocate on the GPU $N_k \times N_b$ FFT grids to apply, in parallel, the local potential to the Bloch functions. The allocation of this memory is done by the HOST routine that implements the Davidson algorithm.

We have also optimized some parts of the Davidson algorithm. The standard routine has been generalized introducing several loops on the N_k $\mathbf{k}$ points and part of these loops have been transformed into GLOBAL routines that perform the calculation in parallel using $N_k \times N_b$ threads. We have accelerated only the loops that took a significant amount of time. The other loops call the linear algebra cuBlas routines as in the standard approach.

The acceleration of the phonon code instead has been carried out essentially on the algorithm that solves the linear system in Eq. 7.25. We proceed as in the Davidson algorithm (see the scheme in Fig. 7.3). However, in the phonon case the calculation of the induced charge density requires two FFT grids per band, one to contain $u^*_{\mathbf{k}\nu}(\mathbf{r})$ and one to contain $P_c^{\mathbf{k+q}} \frac{\partial u_{\mathbf{k}\nu}(\mathbf{r})}{\partial \mathbf{u}_{s'\beta}(\mathbf{q})}$ so usually we use N_k smaller than in the Davidson algorithm. The GPU optimization of the preconditioned conjugate gradient algorithm starts by allocating the COMPLEX vectors g, d, d_{old}, and t on the GPU. For each variable $N_k \times N_b \times N_{pe}$ arrays are allocated.

This memory is much larger than the one of the standard algorithm that requires only N_b copies of each variable, but this space is allocated only on the `GPU`. The algorithm is then divided in loops over the N_k $\mathbf{k}$ points, the N_{pe} perturbations, and the N_b bands. Loop one executes Eqs. 7.33 and Eqs. 7.34, loop two executes Eq. 7.36, and loop three computes $d^T r$ and $d^T t$ that appear in the numerator and denominator of Eq. 7.38. Finally loop four computes Eqs. 7.39, 7.40, and 7.41. Each loop is transformed into routine with the `GLOBAL` attribute that runs $N_k \times N_b \times N_{pe}$ threads, each one computing one perturbation to one band of one $\mathbf{k}$ point. Since each thread executes only a scalar product or an operation of the type $x \leftarrow x + \lambda d$ we have programmed these routines in `CUDA Fortran` without calling any other library routine. The array themselves instead are not split and each thread works on all the $\mathbf{G}$ vectors of each wave-function. All the other steps of the algorithm involve only scalar operations that are performed by the `CPU`.

Eq. 7.32 and Eq. 7.37 require an external routine to apply A to the vectors x (or d). For this operator we use the same routine that applies H_{KS} and S in the Davidson algorithm. The routine works in general for an arbitrary number of wavefunctions so when called from the conjugate gradient algorithm, in parallel on the `GPU` threads, it deals with the $N_k \times N_{pe}$ set of wavefunctions, each one composed by N_b bands. We have then written a `HOST` routine that receives as input the coefficients $C'_{\mathbf{k+q}\nu j}$ and $C''_{\mathbf{k+q}\nu j}$ of the Fourier transform of $H_{KS}^{\mathbf{k+q}}|x_{\mathbf{k+q}\nu j}\rangle$ and $S|x_{\mathbf{k+q}\nu j}\rangle$ and gives as output the Fourier coefficients of $A|x_{\mathbf{k+q}\nu j}\rangle$. This routine calls a series of `GLOBAL` routines for which we can control the number GPU threads that run in parallel. The first routine computes Eq. 7.29 and runs $N_k \times N_{pe} \times N_b \times N_b$ threads. A second routine computes $|a_{\mathbf{k+q}\nu j}\rangle = H_{KS}^{\mathbf{k+q}}|x_{\mathbf{k+q}\nu j}\rangle - \varepsilon_{\mathbf{k}\nu} S|x_{\mathbf{k+q}\nu j}\rangle$ and runs $N_k \times N_{pe} \times N_b$ threads. To complete the operator A we have to calculate the operator $\alpha Q^{\mathbf{k+q}}|x_{\mathbf{k+q}\nu j}\rangle$ and we optimized also this part to run in many threads on the `GPU` in parallel on the $\mathbf{k}$ vectors, the bands, and the perturbations. This is done by calling another set of `GLOBAL` routines. The first computes Eq. 7.30 running on $N_k \times N_{pe} \times N_b$ threads, another one computes the scalar products $\langle \beta_n^I | y_{\mathbf{k+q}\nu j}\rangle$ that appear in Eq. 7.31 and runs $N_k \times N_{pe} \times N_{kb} \times N_b$ threads, and a third routine calculates Eq. 7.21 using the scalar products just calculated and runs on $N_k \times N_{pe} \times N_b$ threads. Finally a `GLOBAL` routine computes Eq. 7.31 and adds it to $|a_{\mathbf{k+q}\nu j}\rangle$ running in $N_k \times N_{pe} \times N_b \times N_{pw}$ threads.

7.3 Fast Fourier transform

The application of $V_{eff}(\mathbf{r})$ to one Bloch wave-function requires two Fourier transforms. It is convenient to introduce a mesh in reciprocal space:

$$\mathbf{G}_{m_1,m_2,m_3} \equiv m_1\mathbf{b}_1 + m_2\mathbf{b}_2 + m_3\mathbf{b}_3, \tag{7.43}$$

where $\mathbf{b}_1$, $\mathbf{b}_2$, and $\mathbf{b}_3$ are the principal reciprocal lattice vectors and m_1, m_2, and m_3 are integers, and a mesh in real space:

$$\mathbf{r}_{l_1,l_2,l_3} = \frac{l_1}{N_1}\mathbf{a}_1 + \frac{l_2}{N_2}\mathbf{a}_2 + \frac{l_3}{N_3}\mathbf{a}_3, \tag{7.44}$$

where $\mathbf{a}_1$, $\mathbf{a}_2$, and $\mathbf{a}_3$ are the direct lattice vectors, and l_1, l_2, and l_3 are integers. The integers N_1, N_2, and N_3 define the size of the mesh in real space and, equivalently, the size of the mesh in reciprocal space. They must be sufficiently large so that the vectors $\mathbf{G}_{m_1,m_2,m_3}$ contain all the vectors $\mathbf{G}-\mathbf{G}'$ defined by the basis set.

Given a function in reciprocal space, defined on the $\mathbf{G}$ vectors $\tilde{f}(m_1,m_2,m_3) \equiv f(\mathbf{G}_{m_1,m_2,m_3})$, its real space form $f(l_1,l_2,l_3) = f(\mathbf{r}_{l_1,l_2,l_3})$ is given by:

$$f(l_1,l_2,l_3) = \sum_{m_1=0}^{N_1-1} \sum_{m_2=0}^{N_2-1} \sum_{m_3=0}^{N_3-1} \tilde{f}(m_1,m_2,m_3) e^{i2\pi l_1 m_1/N_1} e^{i2\pi l_2 m_2/N_2} e^{i2\pi l_3 m_3/N_3}. \tag{7.45}$$

The transform is made in three steps. In the first step, we compute $N_1 \times N_2$ one dimensional FFTs along z:

$$\bar{f}(m_1,m_2,l_3) = \sum_{m_3=0}^{N_3-1} \tilde{f}(m_1,m_2,m_3) e^{i2\pi l_3 m_3/N_3}. \tag{7.46}$$

We run $N_1 \times N_b \times N_k$ threads on the `GPU` by calling a `GLOBAL` routine, and each thread computes N_2 FFTs. Each FFT (sum over m_3) is carried out by calling an FFT library routine (`cfft1b` from `fftpack.5.1`) which is declared as a `DEVICE` routine. In the second step, we compute:

$$\hat{f}(m_1,l_2,l_3) = \sum_{m_2=0}^{N_2-1} \bar{f}(m_1,m_2,l_3) e^{i2\pi l_2 m_2/N_2}. \tag{7.47}$$

In this case we run $N_1 \times N_b \times N_k$ threads each one doing N_3 FFTs. Each FFT (sum over m_2) is carried out by the `DEVICE` FFT library routine `cfft1b`. Finally, to complete the three dimensional Fourier transform, in the third step we calculate:

$$f(l_1,l_2,l_3) = \sum_{m_1=0}^{N_1-1} \hat{f}(m_1,l_2,l_3) e^{i2\pi l_1 m_1/N_1}. \tag{7.48}$$

In this case we run $N_k \times N_b$ threads on the `GPU` each one computing $N_2 \times N_3$ FFTs. Each one dimensional FFT (sum over m_1) is carried out by the `DEVICE` FFT library routine `cfft1b`. In a similar way one can make a three dimensional Fourier transform to obtain the reciprocal space function from its real space form:

$$\tilde{f}(m_1,m_2,m_3) = \frac{1}{N_\mathbf{r}} \sum_{l_1=0}^{N_1-1} \sum_{l_2=0}^{N_2-1} \sum_{l_3=0}^{N_3-1} f(l_1,l_2,l_3) e^{-i2\pi l_1 m_1/N_1} e^{-i2\pi l_2 m_2/N_2} e^{-i2\pi l_3 m_3/N_3}, \tag{7.49}$$

where $N_\mathbf{r} = N_1 N_2 N_3$. In this case we call the `DEVICE` function `cfft1f` to actually carry out the one dimensional FFTs.

The product of V_{eff} with the wave-function:

$$u'_{\mathbf{k}\nu}(l_1,l_2,l_3) = V_{eff}(l_1,l_2,l_3) u_{\mathbf{k}\nu}(l_1,l_2,l_3), \tag{7.50}$$

is made by running $N_\mathbf{r} \times N_k \times N_b$ threads on the `GPU`, each thread computing one product. After computing the product, an FFT as in Eq. 7.49 gives the Fourier components of the product that can be added to those obtained by applying the kinetic energy. This FFT is performed by three routines similar to those described for the inverse FFT.

7.3.1 FFT on the device

Eqs. 7.46,7.47,7.48 cannot be implemented as written since they involve N_i^2 operations, where N_i is N_1, N_2 or N_3. These sums can be done more efficiently with an FFT algorithm that requires $N_i log(N_i)$ operations. [156] The `FFTXlib` of `Quantum ESPRESSO` contains both the three dimensional FFT driver and a copy of an old `FFTW` library. [56] It also supports the newer `FFTW3` library, some vendor-specific FFT libraries, and it can call `GPU` routines in `cuFFT` [61, 140]. Moreover, it can carry out the FFT in parallel when the FFT mesh (and $\mathbf{G}$ vectors) are distributed among different `MPI` processes. However, these routines are called from the `CPU HOST` with actual argument variables that are allocated on the `GPU` and they take care of launching the threads on the `GPU`. In our approach, the FFT routines are called from `GLOBAL` routines that already run on the `GPU` and therefore must have the `DEVICE` attribute, hence `FFTXlib` cannot be used. The library that offers this functionality `cuFFTDx` is written in `C++` and it has not yet a `FORTRAN` interface. Therefore, we have taken the `fftpack5.1` [187] which is distributed under the GNU GPL licence together with its `Fortran` source and we have modified each routine and function of this library by adding the `ATTRIBUTES(DEVICE)`. We have also constructed an interface for each routine so that the routines that include the interface can know that the routines of `fftpack` are actually `DEVICE` routines and accept variables allocated on the `GPU`. The modified library is distributed together with the `thermo_pw` package.

7.4 Matrix Diagonalization

The Davidson algorithm requires the solution of a generalized eigenvalue problem in a reduced basis:

$$Ax = \lambda Bx, \tag{7.51}$$

where A and B are Hermitian matrices and λ and x are the eigenvalues and eigenvectors. Usually, the `CPU` makes this calculation by calling `LAPACK` routines [7] such as `ZHEGVX` that computes selected eigenvalues and, optionally, eigenvectors of a complex generalized Hermitian-definite eigenproblem, or `ZHEGV` that computes all eigenvalues and eigenvectors of the same matrices. It is also possible to call `GPU` routines of the `cuSolver` library. A `HOST` driver that calls these routines is contained in the `LAXlib` library distributed with `Quantum ESPRESSO`. We have tested this approach creating a loop over the N_k $\mathbf{k}$ points that calls these routines, but found that it is possible to obtain a significant speed up by simultaneously diagonalizing the generalized eigenvalue problem for many $\mathbf{k}$ points. We run therefore a `GLOBAL` routine with as many threads as possible (ideally N_k, but see below). In order to solve the generalized eigenvalue problem inside a `GLOBAL` routine we cannot call `HOST` routines such as those available in `cuSolver` or in `MAGMA` [86] what is needed is a library that can be called from the `GPU` threads (with `DEVICE` routines). Since we are not aware of any `DEVICE` implementation of `LAPACK`, we took the routines `ZHEGVX` and `ZHEGV` together with those called by them, transformed them into `DEVICE` routines, and wrote the corresponding `Fortran` interfaces. We found only one problem with this approach: The routine `ZPOTRF2`,

which performs the Cholesky factorization of a Hermitian positive definite matrix A, is recursive. Since CUDA Fortran does not allow for recursive DEVICE routines or functions, we rewrote it with a non recursive algorithm.

The number of $\mathbf{k}$ points that can be diagonalized simultaneously is usually lower than N_k since the LAPACK DEVICE routines use a certain amount of GPU resources. So we divided the N_k $\mathbf{k}$ points in blocks of maximum size determined empirically on the available machine.

7.5 Results

7.5.1 Benchmark Example

We have implemented our approach in the thermo_pw code [38] which is a driver of Quantum ESPRESSO routines to calculate materials properties. To activate the new approach, it suffices to set the flag many_k to .TRUE. and the input variable memgpu to the amount of GPU memory (in GBytes). Both variables are written in the thermo_control input file. The new routines are in the directory qe of thermo_pw, while the LAPACK and fftpack5.1 routines modified with the ATTRIBUTES(DEVICE) together with their interfaces are distributed in separate subdirectories of the thermo_pw package. For further details please refer to the thermo_pw user's guide.

Our benchmark is a part of the calculations carried out to compute the quasi-harmonic temperature dependent elastic constants of tungsten. [65] Our system is body centered cubic (bcc) tungsten simulated with the PBEsol exchange and correlation functional [150] at the lattice constant $a = 5.965$ a.u.. Tungsten is described with a PAW pseudopotential that has 14 valence electrons and we compute $N_b = 11$ bands. [35] We use cut-offs for the wave-functions/charge density of 90/360 Ry, a $\mathbf{k}$-point mesh of $45 \times 45 \times 45$ and deal with the Fermi surface with the smearing approach ([128]) with a smearing parameter $\sigma = 0.02$ Ry. The FFT mesh has size $32 \times 32 \times 32$ for a total of $N_\mathbf{r} = 32768$ mesh points. We compute the phonon frequencies for the point $\mathbf{q} = \frac{2\pi}{a}(-1/8, -1/4, 3/8)$. The small space group of this $\mathbf{q}$ point has no rotational symmetry in it, so we need to use the complete mesh of $45^3 = 91125$ $\mathbf{k}$ points when computing the perturbed wave-functions. Since we need also the eigenvalues and eigenfunctions at $\mathbf{k}+\mathbf{q}$ we compute the band structure of 182250 $\mathbf{k}$ points.

We report the time obtained with version 7.3 of Quantum ESPRESSO together with thermo_pw version 2.0.0. All tests have been performed on the Leonardo supercomputer at CINECA. Each node of the machine has a CPU with 32 cores and 4 Ampère GPUs. In the Leonardo manual, the theoretically declared peak performance of one node (32 cores) is 1680 Gflops while the four GPUs of one node can provide 75000 Gflops. There is therefore a maximum theoretical acceleration of a factor of 45. We run on the GPUs using as many CPU cores as GPUs and each CPU runs one MPI process. [127] MPI processes can communicate among themselves with MPI library calls. Each MPI process communicates with one GPU, multiple MPI processes using the same GPU are not allowed. Moreover we do not use direct GPU-GPU communication. When several MPI processes run, the total number of $\mathbf{k}$ points is divided in a number of pools equal to the number of MPI processes. The code is compiled

with the PGI Fortran compiler contained in the Nvidia SDK [138].

7.5.2 FFT

Table 7.1: Comparison of the time spent by computing the FFT and the inverse FFT when applying the Hamiltonian operator in the Davidson algorithm and in the conjugate gradient algorithm for the example described in the paper.

	CPU					GPU				optimized GPU			
#CPU	32	32	32	64	64	1	2	4	8	1	2	4	8
#GPU	0	0	0	0	0	1	2	4	8	1	2	4	8
#task(np)	32	32	32	64	64	1	2	4	8	1	2	4	8
#pool(nk)	8	16	32	32	64	1	2	4	8	1	2	4	8
time (s)	6771	6280	4539	3269	2213	13415	6866	3441	1744	7532	3574	2068	934

In Table 7.1, we report the time necessary to compute the FFTs to apply the local potential. We consider three cases: CPUs only, standard GPU code that calls the cuFFT library, and the optimized GPU code that uses the fftpack.5.1 routines declared as DEVICE routines. In the GPUs runs, we consider 1, 2, 4 or 8 GPUs. For the CPUs only runs, we use all the CPUs of one (32) or two nodes (64). Further, with 32 cores, the **k** points are divided into 8, 16, or 32 pools, with 64 cores, into 32 or 64 pools. When comparing CPUs and GPUs, we compare 4 or 8 GPUs with the best times obtained with 32 or 64 cores, respectively. We start by discussing the CPUs only case. With both 32 or 64 cores, the minimum FFT time is obtained when the number of pools is equal to the number of cores. This indicates that in this system it is not useful to divide the **G** vectors among CPUs. The second observation is that when we pass from one to two nodes the time halves, showing a good scaling with the number of nodes. We call T_{cpu} the best time obtained with one or two nodes. Passing now to the GPU times, we see that both with the standard algorithm and with the optimized one the computational time is inversely proportional to the number of GPUs. Comparing now the time taken by the standard GPU algorithm, we see that it is 0.76 T_{cpu} (4 GPUs), 0.79 T_{cpu} (8 GPUs). So, as far as the FFT is concerned, it is convenient to use the GPUs The FFTXlib of Quantum ESPRESSO instead of the CPUs although the gain is not big. The optimized GPU algorithm gives times that are 0.46 T_{cpu} (4 GPU), 0.42 T_{cpu} (8 GPUs). This is much less than the theoretical capacity of the GPU, but still it makes convenient to use the latter. When computing the FFT, the optimized GPU algorithm is 1.9 times faster (8 GPUs) than the standard GPU version that calls the CuFFT routines in sequence on the **k** points.

7.5.3 Diagonalization

In Table 7.2, we report the time spent by the diagonalization of the reduced Hamiltonian carried out by the LAPACK routines on the CPU, by the cuSolver library running on GPU called by the LAXlib package, and by the optimized GPU version of the code in which the

Table 7.2: Comparison of the time spent to diagonalize the reduced Hamiltonian using linear algebra routines (within the Davidson algorithm).

	CPU					GPU				optimized GPU			
#CPU	32	32	32	64	64	1	2	4	8	1	2	4	8
#GPU	0	0	0	0	0	1	2	4	8	1	2	4	8
#task(np)	32	32	32	64	64	1	2	4	8	1	2	4	8
#pool(nk)	8	16	32	32	64	1	2	4	8	1	2	4	8
time (s)	81	44	20	21	10	1286	684	348	178	220	118	60	29

Hamiltonians of many **k**-vectors are diagonalized simultaneously by the `LAPACK` routines declared as `DEVICE` routines. The effect of using pools and several `CPUs` is also illustrated. The sizes of the matrices to be diagonalized vary, depending on the istantaneous size of the basis set in the Davidson algorithm. The routine must find the lowests $N_b = 11$ eigenpairs in a matrix that can have a maximum size equal to $4N_b = 44$. This is repeated for all **k** points for all Davidson iterations and all self-consistent iterations in addition to a band structure calculation before the phonon calculation (in which there are about 2×10^5 **k** points). The `CPU` diagonalization time scales linearly with the number of **k** points and therefore depends only on the number of pools. Using 64 or 32 cores gives exactly the same time when we use 32 pools, but if we use a number of pools equal to the number of cores with two nodes we halves the diagonalization time with respect to one node. A good scaling is also shown by the `GPU` calculation. Increasing the number of `GPUs` increases the number of pools and therefore decreases the number of **k** points per `pool`. With both the standard `GPU` algorithm and with the optimized one we could not run faster than the `CPU`. With the standard algorithm the size of the matrix to diagonalize is so small that the time to initialize the `GPU` greatly exceeds the `CPU` diagonalization time. In this particular example, the time of the standard `GPU` calculation is 18 T_{cpu}. With our optimization we could reduce this time to 3 T_{cpu}. In our example however the total time for the diagonalization is small with respect to all other times and we have not tried to further optimize this part.

7.5.4 Application of the Hamiltonian and of S

Table 7.3: Comparison of the total time spent to apply H_{KS} and S to the wave-functions in the Davidson algorithm and in the conjugate gradient algorithm.

	CPU					GPU				optimized GPU			
#CPU	32	32	32	64	64	1	2	4	8	1	2	4	8
#GPU	0	0	0	0	0	1	2	4	8	1	2	4	8
#task(np)	32	32	32	64	64	1	2	4	8	1	2	4	8
#pool(nk)	8	16	32	32	64	1	2	4	8	1	2	4	8
time (s)	7907	7319	5519	3780	2702	36157	18465	9263	4694	9138	4375	2472	1138
time -time$_{\rm FFT}$ (s)	1136	1039	980	511	489	22742	11599	5822	2950	1606	801	404	204

In Table 7.3 we show the time required for the application of the Hamiltonian and of the overlap matrix S to the wave-functions. This time comprises the time needed to apply the FFT and inverse FFT to the wave-functions, the time needed to apply the kinetic energy and the nonlocal pseudopotential as well as the time needed to apply the overlap matrix S. In the same table we report also the difference between these times and the times needed to carry out the FFT reported in Table 7.1. In the time reported in the table, we apply the operator H_{KS} and S about 8×10^7 times (as reported by the code when we do not use the optimized algorithm and 7.3×10^4 when we use the optimized algorithm and many **k**-points are calculated concurrently). This is reasonable since we have 1×10^5 **k** points, about 16 self-consistent iterations and $N_{pe} = 3$ modes. This gives an average of 16 conjugate gradient steps per iteration. To count the number of operations is more difficult since the number of bands is not always constant. If take as an average value $N_b = 11$ bands, the number of plane waves $N_{pw} = 2093$ and a number of projector functions $N_{kb} = 18$ we see that Eq. 7.38 is the multiplication of a matrix 18×2023 and a matrix 2023×11. We start by considering the `CPU` times when FFT time is subtracted. These times depend on the number of cores, but less on how these cores are distributed between **G** vectors and **k**-point pools. Still using only **k**-point pools gives the shortest times but the differences are small. Comparing with the standard `GPU` version, we see that the application of the nonlocal potential and of the S matrix require too many small size matrix-matrix multiplications and this part of the calculation is quite slow on the `GPU`. For this calculation the required time is 6 T_{cpu}. The optimized `GPU` algorithm is much faster and needs about 0.42 T_{cpu}. Adding also the speedup obtained with the `FFT`, the optimized `GPU` algorithm takes about 0.44 T_{cpu}. Comparing the two `GPU` algorithms, the optimized one is 4 times faster in applying H_{KS} and 14 times faster in applying the nonlocal pseudopotential and the S matrix.

7.5.5 Total time

Table 7.4: Total time spent in the standard `CPU` calculations. The number of `CPUs`, `GPUs`, `tasks`, and `pools` are also indicated. The number of core-hours is obtained multiplying the total time by the number of cores.

	CPU						
#CPU	32	32	32	64	64	128	256
#GPU	0	0	0	0	0	0	0
#task(np)	32	32	32	64	64	128	256
#pool(nk)	8	16	32	32	64	128	256
time (s)	11400	10560	8040	5640	4500	2280	1182
time (m)	190	176	134	94	75	38	20
core-hours	101	94	71	100	80	81	85

In this section we present some benchmarks of the entire run, considering both the self consistent and the phonon frequencies calculations. We report in Tables 7.4, 7.5, 7.6 the total time. This time is approximately twice the time required by the application of H_{KS}

Table 7.5: Total time spent in the standard `GPU` calculations. This includes also the time passed on the part of the code that are not GPU accelerated or are not GPU optimized. The number of `CPUs`, `GPUs`, `tasks`, and `pools` are equal.

	GPU					
#CPU	1	2	4	8	16	32
time (s)	107640	54780	27720	14100	7500	3720
time (m)	1794	913	462	235	125	62
core-hours	239	243	246	250	267	265

Table 7.6: Total time spent in the optimized `GPU` calculations. This includes also the time passed on the part of the code that are not GPU accelerated or are not GPU optimized. The number of `CPUs`, `GPUs`, `tasks`, and `pools` are equal.

	optimized GPU					
#CPU	1	2	4	8	16	32
time (s)	16080	7860	4680	2153	1140	585
time (m)	268	131	78	36	19	10
core-hours	36	35	42	38	41	43

and S in the `CPU` and in the optimized `GPU` cases and three times in the standard `GPU` case. Considering now the total T_{cpu}, we see that the faster time is obtained when the number of pools is equal to the number of cores. The scaling with the number of nodes is good: from 32 to 64 cores the code is 1.8 times faster. The standard `GPU` approach takes 3.4 T_{cpu} (one node) or 3.1 T_{cpu} (two nodes), while the optimized `GPU` approach takes 0.58 T_{cpu} (one node) and 0.48 T_{cpu} (two nodes). The difference between one and two nodes is due to the different number of `CPUs` cores available in the two cases. The parts that are not accelerated are calculated faster when more cores are available. Comparing now the two `GPU` algorithms we see that the optimized one is about 6 times faster.

In the table we have indicated also the cost of each run in core-hours. This cost is obtained by multiplying the total time by the number of core used (in the `GPU` case, each `GPU` costs 8 cores). We have also added the time needed with 4 and 8 nodes (128 and 256 cores). We find that increasing the number of nodes the total cost tend to increase (even if there are some fluctuations) since it is difficult to achieve an exact linear scaling with the number of `pools`. In the optimized `GPU` case the optimum is obtained with 2 nodes. It is therefore convenient to carry out this calculations with a small number of nodes per **q** point and calculate in parallel on different nodes different **q** points and geometries. However, even with an ideal scaling with the `pools` and a computer that can provide as many `GPUs` as desired, it is still convenient to use pools that contain a number of **k** point sufficient to occupy the `GPU` memory and use it (gaining about a factor `2X`), than split the calculations so that each `pool` has a single **k** point.

Chapter 8

Conclusions

The DFPT + QHA methodology for ECs calculations in software `thermo_pw` has been extended to high temperature and high pressure conditions. The ECs as a function of temperature at finite pressure and as a function of pressure at finite temperature is available.

This new techniques have been illustrated in BCC solids W, Mo, and Ta. The first has been chosen for its wide range of applications, in particular as a plasma-facing material in fusion reactor. Mo is a metal in the same group of periodic table as W but no ECs information was available under the high-pressure or high-temperature conditions. Ta is a metal used for high-quality superconducting resonators in quantum processors, but also lack of investigation. All these three metal elements are so-called "refractory metals" because of the high melting point among all materials and extraordinarily resistant to wear.

The treatment of ECs to anisotropic solids has be expaned by adding the possibility of calculating the ECs along the "stress-pressure" $T = 0$ K isotherm in the crystal parameter (within V-ZSISA) space and made it possible to go beyond ZSISA for systems in which atomic relaxations are one-dimensional. We have addressed Be as the simplest example of a HCP solid to explore the practical approach to investigate the thermoelasticiy in anisotropic solids. We also extended the code to run on architectures equipped with GPUs in order to accelerate the time-cosuming phonon calculations. Now we draw the main conclusions for each chapter in the following sections.

8.1 Tungsten

We presented the quasi-harmonic temperature and pressure dependent thermoelastic properties of tungsten calculated by `thermo_pw` using PAW pseudopotentials. The temperature dependent quasi-harmonic adiabatic ECs as well as the derived polycrystalline bulk, shear, and Young's moduli and Poisson's ratio have been compared with experiment at ambient pressure. The compressional and shear sound velocities, as well as the longitudinal and shear moduli, have been calculated as a function of pressure at the temperatures measured in the experiment of Qi et al. [158].

We find that the quasi-harmonic theory reproduces well the temperature dependent ECs

of tungsten at room pressure. The PBE and the PBEsol functionals give similar temperature dependences with PBEsol closer to experiment than PBE. Good agreement is also found for the temperature dependence of the polycrystalline elastic moduli, again with PBEsol closer to experiment than PBE.

The pressure and temperature dependence of the shear modulus of polycrystalline tungsten in the range of pressures measured in the experiment of Qi et al. [158] is reproduced very well by both PBE and PBEsol that are practically indistinguishable when a shift is used to facilitate the comparison with experiment. The pressure and temperature variations of the longitudinal module are instead described less accurately and also after a shift PBEsol and PBE predict a larger decrease with temperature than experiment. The PBEsol temperature derivative of the longitudinal module is slightly larger than the PBE one. These discrepancies are attributed to the temperature derivative of the adiabatic bulk modulus larger in the calculation than in experiment. As a consequence, the pressure and temperature dependences of the shear sound velocity are well reproduced by theory, while the compressional sound velocity as a function of pressure is well reproduced at low temperatures, but larger and larger differences are found at high temperatures. These conclusions hold for both PBE or PBEsol. Different functionals change the position of the elastic moduli or sound velocity curves, but not their slope nor their temperature variation. The reasons for the discrepancies between theory and experiment are presently unclear and might require an improvement of the theory or a revision of the experiment.

In this chapter we compared the elastic moduli and the sound velocities of polycrystalline tungsten at high pressure and high temperature with experiment and we demonstrated that these calculations are now routinely feasible in modern supercomputers. These parameters which are quite critical for high pressure and high temperature applications of materials are still missing from the literature for many metals. We hope that our efforts will stimulate further measurements and theoretical calculations in this direction.

8.2 Molybdenum

We presented the temperature and pressure dependent thermoelastic properties of molybdenum calculated by the `thermo_pw` software and PAW pseudopotentials. We find that the QHA predicts the temperature dependence of the ECs in much better agreement with experiments than the QSA. Furthermore we have used the QHA ECs to compute the pressure dependent compressional and shear sound velocities in polycrystalline molybdenum (and the corresponding bulk and shear moduli). In addition to the calculation at 300 K that is in good agreement with the experimental results of Liu et al., [112] we have calculated the low temperature (4 K) and the high temperature (1000 K, 1500 K, and 2000 K) pressure dependent curves, hoping that these calculations will stimulate an experimental investigation of these quantities.

For the sake of completeness, the phonon dispersions, the p-V equation of state at 300 K and 2000 K, the temperature dependent volume thermal expansion, the isobaric heat capacity, the adiabatic bulk modulus, and the average Grüneisen parameter for 0 kbar,

1000 kbar, 2000 kbar, and 3000 kbar have been calculated by the LDA, PBEsol, and PBE functionals, but since they are already available in the literature, we have moved them to the appendix.

8.3 Tantalum

We have presented the QHA TDECs of tantalum calculated within the PBE exchange and correlation energy and we have compared them with the QSA TDECs. We found a better agreement with experiment at low temperatures, up to 500 K, for the quantities C, C' and C_{44} that are measured in experiment. At high temperatures, experiments show a change of slope of the curves as a function of temperature that is not reproduced by our calculation. Comparing C_{11} and C_{12} the situation is less clear at low temperature and on a large temperature range from 0 K to 2000 K the QSA TDECs seem closer to experiment than the QHA ones. None of the two approximation however predicts a change of slope.

We have calculated also the pressure dependent elastic constants both at low temperature 5 K and for 300 K, 1000 K, and 1500 K. Although these data might have errors similar to those at 0 kbar, we hope that these data will stimulate a measurement of the tantalum EC at high temperature and pressure an information which is still missing from the literature.

8.4 Beryllium

We presented the QHA TDECs of beryllium calculated (within the V-ZSISA) in eight reference geometries along the "stress-pressure" 0 K isotherm and interpolated at $a(T)$. For C_{11} and C_{12}, atomic relaxations have been dealt mainly within the ZSISA approximation. We have verified using the QSA that the "stress-pressure" 0 K isotherm interpolation (V-ZSISA) gives results close to the interpolation made along the 0 kbar isobar. Moreover, we have compared the ZSISA approximation with the full free energy minimization (FFEM) with respect to the atomic positions, finding that for the present case ZSISA is a very good approximation. Comparison of our results with previous QSA and QHA calculations shows substantial agreement especially with Ref. [103] for the QSA and Ref. [161] for the QHA. Moreover, we provided the first estimate of the pressure dependent (up to 500 kbar) elastic constants at temperature of 500 K and 1000 K. We hope that these calculations will stimulate and support an experimental investigation of these quantities that are still unknown in beryllium.

The graphs of thermal expansion and isobaric heat capacity in the appendix (see also references [69, 134, 178, 107, 162] therein) show that QHA might be a reasonable approximation until 800 K where the QHA is able to reproduce the experimental results. In general QHA is expected to be accurate until 2/3 of the melting temperature so our data might require corrections above 1000 K [5], even if we have plotted them until 1500 K.

The calculations performed here of the QHA TCECs, required the phonon dispersion on $8 \times 30 = 240$ geometries (30 distorted configurations of 8 equilibrium geometries). With

much more effort, slightly more accurate calculations could have been done by computing the quasi-harmonic elastic constants taking as reference geometries all the two-dimensional mesh of a and c/a parameters. This calculation would require the phonon dispersions in $14 \times 7 \times 30 = 2940$ geometries (30 distorted configuration of a grid 14×7 of equilibrium geometries) and is presently beyond our computational resources, but it could become feasible soon. Presently, beryllium does not seem to require such an effort, but we have presented a workflow capable of going beyond both the V-ZSISA and ZSISA when necessary and it might be interesting to see if the conclusions reached in beryllium remain valid also for the other hcp metals. All methods used in this paper have been implemented in the `thermo_pw` software [38] and are publicly available.

8.5 GPU

We discussed a scheme to accelerate on the `GPUs` electronic structure codes based on plane waves and pseudopotentials. We have shown in the example of bcc tungsten that our scheme can be faster than the currently implemented `GPU` version when the system has small unit cells but requires a thick mesh of $\mathbf{k}$ points. The main idea is to apply the Hamiltonian to the wave-functions in parallel on many $\mathbf{k}$ points, one per `GPU` thread, so as to increase both the size of the data on which the `GPU` works at any given time and to give to the `GPU` a sufficient numerical workload to exploit all its SMs. Our method has been implemented in `CUDA Fortran` by partially rewriting the code and by using `GLOBAL` and `DEVICE` routines to parallelize the work of different `GPU` threads. We have discussed in detail the optimization of the Davidson algorithm, the application of the Kohn and Sham Hamiltonian and of the overlap matrix S to the wave-functions, and the preconditioned conjugate gradient algorithm which is used to solve the linear system of DFPT. In our example the application of H_{KS} and S to the wave-functions accounts for about one half of the total time with `CPUs` and about $1/3$ with the `GPUs`. For these operations our optimized `GPU` method is about 6 times faster than the standard `GPU` approach, and about twice as fast than the `CPUs` only calculation. The main limitation of the present implementation is that it does not support the reciprocal lattice vectors distribution among `CPUs`. It is instead possible to divide the $\mathbf{k}$ points in pools so that different `GPUs` acts on different pools. Finally, we underline the fact that when the system (and the FFT mesh) becomes large enough the `cuFFT` library routines become more efficient than our `DEVICE` routines and at that point the standard approach might become more convenient.

Our approach required a precise control of the `GPU` threads and math libraries (with `DEVICE` functions) that can be called from the `GPU`. Presently not many libraries offer this functionality and we hope that, in future, optimized `DEVICE` versions of math libraries will appear together with `FORTRAN` compatible interfaces. The substitution of our transformed routines with better optimized ones could further improve the speed of our code. As a last consideration we might ask if there are other ways to speed up the plane-waves pseudopotential codes for metallic cases as those that we need for our research. There are several option that one might explore from introducing a batched form of the `FFT` and of the linear

algebra routines, to using new FFT GPU libraries such as heFFTe. [85]. If these options would solve the problem pointed out in this paper within the standard GPU scheme remains to be investigated.

The implemented software is distributed within the GPL licence within the thermo_pw package. [38]

Appendices

Appendix A

Tungsten

In the present appendix, in addition to $\beta_V(p,T)$, we show $C_p(p,T)$, $B_S(p,T)$, and $\gamma(p,T)$ for several pressures p.

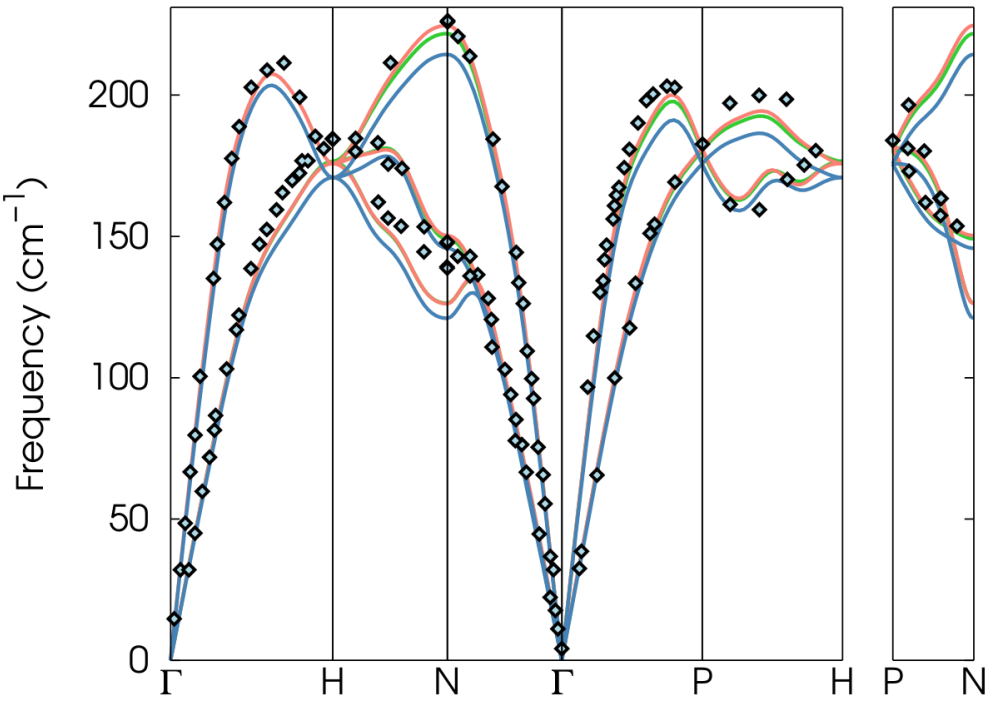

Figure A.1: Phonon dispersions interpolated at the 295 K lattice constant. The LDA (red curves), PBEsol (green curve), and PBE (blue curve) results are compared with the experimental inelastic neutron scattering data measured at 295 K (Refs. [105, 28, 29]).

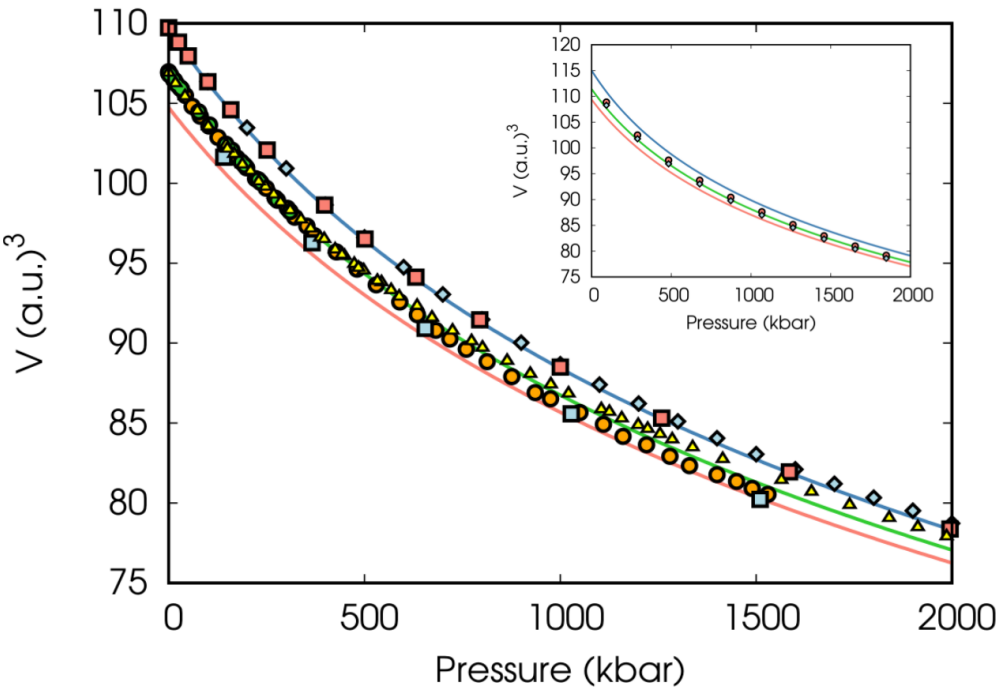

Figure A.2: V as a function of p at 300 K obtained by LDA (red), PBEsol (green), and PBE (blue) is compared with experiments (orange circles, [44] green circles, [110] and yellow triangles [51]) and previous calculations (blue diamonds (PBE) from Ref. [196], blue squares (LDA) from Ref. [166], and red squares (PBE) from Ref. [192]). In the inset the same curves at 3000 K are compared with the predictions of Refs. [48] (blue diamonds) and [110] (red circles).

A.1 Phonon dispersions

In Fig. A.1, we compare the phonon dispersions, interpolated at the 295 K lattice constant (reported in Table I of the paper), with inelastic neutron scattering data. [105, 28, 29]PBEsol and LDA frequencies are similar and show a good agreement with experiments while PBE gives frequencies lower than LDA (as found in other solids [36]), more distant from experiments. This conclusion agrees with Ref. [22, 43].

A.2 Equation of state

In Fig. A.2, we show the 300 K EOS. At low pressure, the PBEsol curve is in very good agreement with experiment, much more than PBE or LDA, as we have seen for the lattice constant. At higher pressures, the experimental data of Ref. [44] are well fitted by both LDA and PBEsol, while the recent measurements of Ref. [51] are closer to PBEsol. PBE is instead slightly above experiment. These results are like those found by Dewaele et al. [45] in zinc, molybdenum, and silver. Our PBE curve agrees with the linearized augmented plane wave

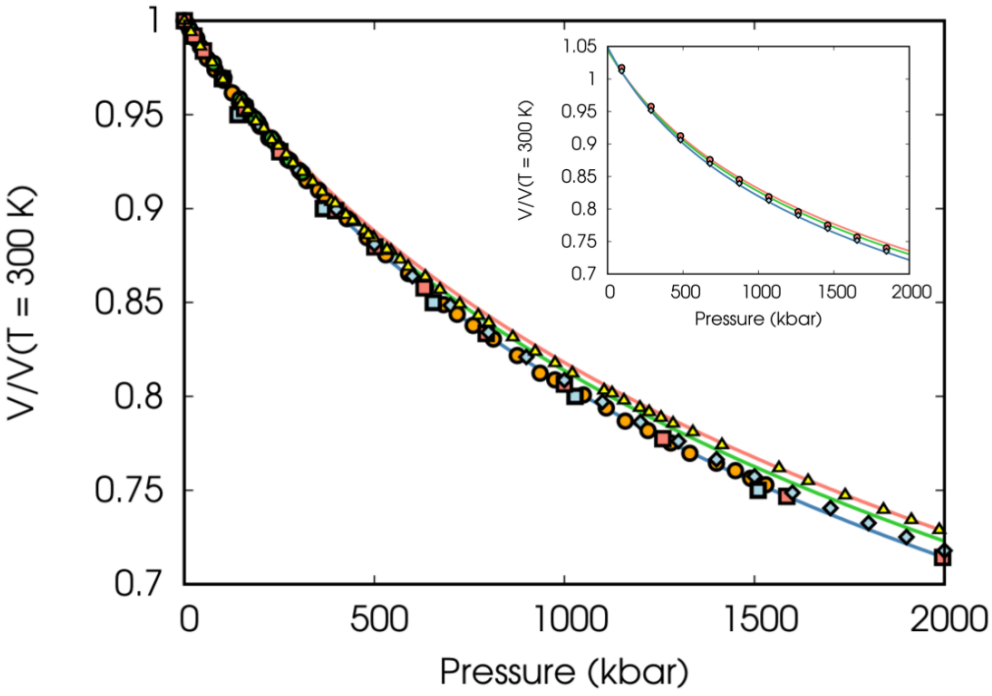

Figure A.3: V/V_0 as a function of p at 300 K obtained by LDA (red), PBEsol (green), and PBE (blue) is compared with experiments (orange circles, [44] green circles, [110] and yellow triangles [51]) and previous calculations (blue diamonds (PBE) from Ref. [196], and blue squares (LDA) from Ref. [166], and red squares (PBE) from Ref. [192]). In the inset the same curves at 3000 K are compared with the predictions of Refs. [48] (blue diamonds) and [110] (red circles).

(LAPW) all-electrons PBE calculation of Ref. [192] and with Ref. [196]. The LDA curve is instead slightly below the values of Ref. [166] especially at low pressure consistent with the 0.5% difference of the equilibrium lattice constants (see Table I of the paper).

To remove the effect of the different equilibrium volumes on the EOS, it is usual to plot the ratio V/V_0 (where V_0 is the volume at 300 K) against pressure. In this case one reaches different conclusions using the experimental data of Ref. [44] or those of Ref. [51] (see Fig. A.3). In the first case PBE agrees with the experimental data while the LDA and PBEsol EOS are above experiment. This is in agreement with Ref. [196] and at variance with Ref. [166]. In the second case, the experimental data of Ref. [51] seems to follow well PBEsol and LDA curves up to 2000 kbar. In the insets of Fig. A.2 and Fig. A.3 we compare the 3000 K EOS with the models of Refs. [48] and [110]. The two models agree with each other and with the ab-initio results. Also at this temperature, when $V(p,T)$ is plotted (Fig. A.2) PBEsol agrees with the models, while LDA is slightly below and PBE is slightly above. Instead, when V/V_0 is plotted (Fig. A.3) LDA remains higher than the other functionals and of the models data which are between PBE and PBEsol.

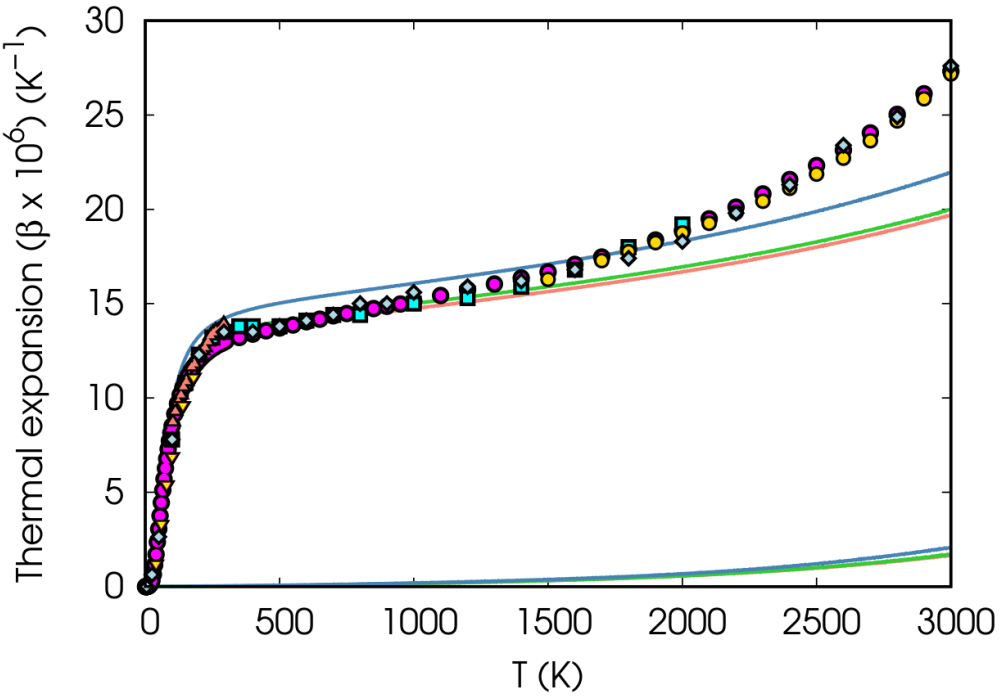

Figure A.4: Temperature dependent volumetric thermal expansion calculated by LDA (red curve), PBEsol (green curve), and PBE (blue curve) compared with the experimental data reported in Ref. [136] (red triangles), Ref. [170] (reversed yellow triangles), Ref. [131] (gold circles), Ref. [19] (magenta circles), Ref. [123] (cyan squares), and Ref. [185] (blue diamond). The thinner lines at the bottom indicate the differences between the thermal expansion calculated including or neglecting the electronic excitations term in the free energy.

A.3 Thermal expansion

In Fig. A.4, we compare with experiment the volumetric thermal expansion at zero pressure. PBEsol is in good agreement with LDA at all temperatures and both reproduce the experiment up to 1500 K. PBE is slightly above the other two functionals similar to the literature for other metals. [70] Comparing with literature, our LDA results agrees well with Ref. [43], while our PBE data are above the calculation of Ref.[196]. After 1500 K other effects, not included in our calculation, namely anharmonic phonon-phonon interactions and finite electronic temperature effects on the phonon frequencies are known to play a role. [196]

In Fig.A.4, we show the electronic thermal excitations contribution, determined from the difference between thermal expansions calculated including or neglecting the electronic free energy in Eq. 2.125 of the paper. Also for this contribution, the LDA and PBEsol curves coincide while PBE is slightly higher. There are not significant effects up to 1500 K, but at 3000 K the electronic contribution is about 1.6×10^{-6} (1/K) (LDA) and (PBEsol), 2.0×10^{-6} (1/K) (PBE).

In Fig. A.5, we show the thermal expansion at finite pressure. In this, as in the fol-

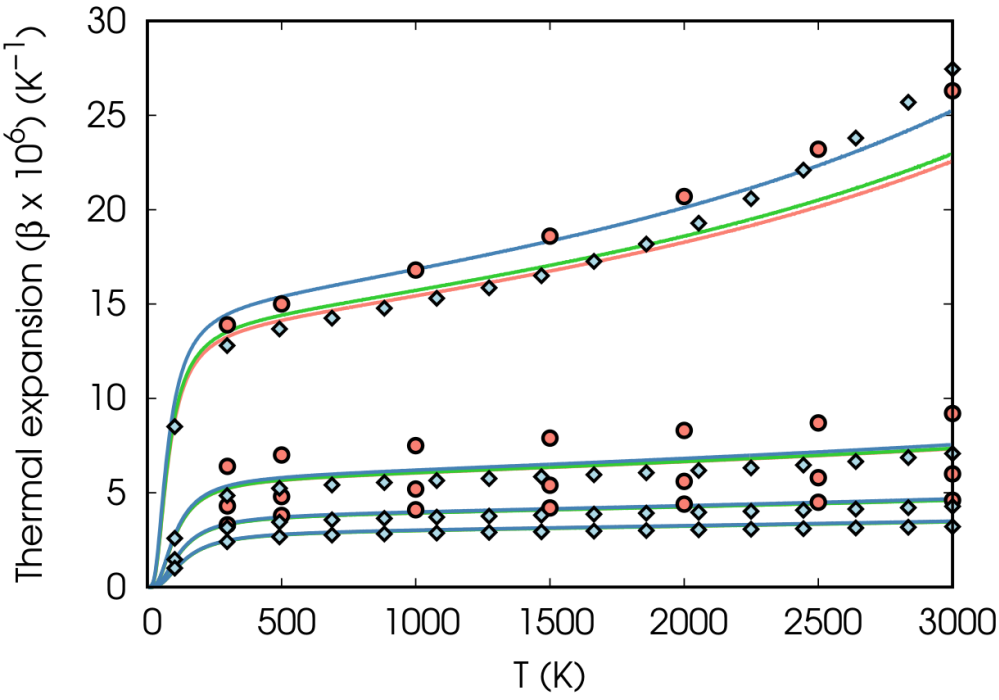

Figure A.5: Temperature dependent volumetric thermal expansion computed within the LDA (red line), PBEsol (green line), and PBE (blue line). The different curves (from top to bottom) correspond to pressures from 0 kbar to 3000 kbar in steps $\Delta p = 1000$ kbar. Theory is compared with the models of Refs. [48] (blue diamonds) and [110] (red circles).

lowing pressure dependent plots, we add to the free energy the anharmonic phonon-phonon contribution:

$$F_a = (a_0 + a_1 V)T^2, \tag{A.1}$$

whose parameters $a_0 = 2.66 \times 10^{-9}$ eV K^{-2} and $a_1 = -6.56 \times 10^{-10}$ eV Å^{-3} K^{-2} have been calculated in Ref. [196] with the PBE functional. We use the same parameters for all functionals. The comparison of Fig. A.5 and Fig. A.4 shows the effect of F_a at 0 kbar. Using PBEsol, it is 0.7×10^{-6} (1/K) at 1000 K and 3.0×10^{-6} (1/K) at 3000 K. The 0 kbar curves shows some differences between PBEsol (like LDA) and PBE that gradually decrease and vanish at high pressure. The values of the thermal expansion at finite pressures agree with the PBE results of Ref. [74] (not shown here). In the figure we compare our results with the models of Refs. [48] and [110]. The points of the model of Ref. [110] have been taken from their Table V, while those of the model of Ref. [48] have been calculated by us with the parameters given in their Table I. At zero pressure and up to 2000 K, LDA and PBEsol are in good agreement with the model of Ref. [48] while PBE matches better with the points of Ref. [110]. At finite pressure, our data become closer to those of Ref. [48] while the model of Ref. [110] predicts a slower decrease of the thermal expansion with pressure.

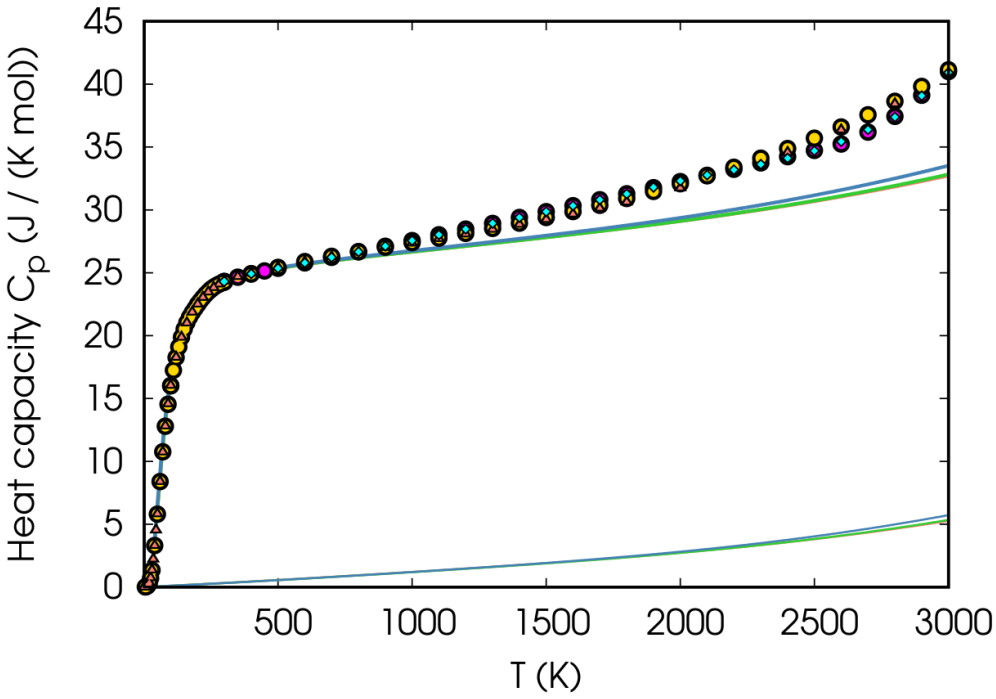

Figure A.6: LDA (red line), PBEsol (green line), and PBE (blue line) temperature dependent isobaric heat capacity compared with experiment from Ref. [194] (red triangles), Ref. [10] (gold circles), Ref. [27] (magenta circles), Ref. [11] (cyan diamonds). Thin lines at the bottom (with the same color conventions) indicate the contribution of electronic excitations to the heat capacity.

A.4 Isobaric heat capacity

In Fig. A.6, we compare the isobaric heat capacity with experiment. Here the differences among functionals are small and all of them agree with experiment up to 700 K. At higher temperatures the experimental data are consistently larger than theory. In the same figure, we plot separately the electronic excitations contribution. At 3000 K, it is about 5 J/(K · mol) with infinitesimal differences between functionals. At this temperature the quasi-harmonic contribution (the second term in Eq. 2.152) is about 3 J/(K · mol), while the difference between our calculation and experiment remains about 7 J/(K · mol). Adding the anharmonic phonon-phonon term of Ref. [196] (Eq. A.1), at 3000 K, C_p increases by about 5 J/(K · mol) (see Fig. A.7). Therefore, we agree with the conclusions of Grimvall et al. [71] that the large value of C_p above the Dulong-Petit limit can be explained by including electronic and anharmonic effects.

In Fig. A.7, we report the isobaric heat capacity at several pressures. With pressure increasing, the value of C_p decreases but remains well above the Dulong-Petit limit. We also show the electronic excitations contribution to C_V. This contribution decreases slowly with pressure: it is still 3.2 J/(K · mol) at 3000 K and 3000 kbar. Our results are compared with

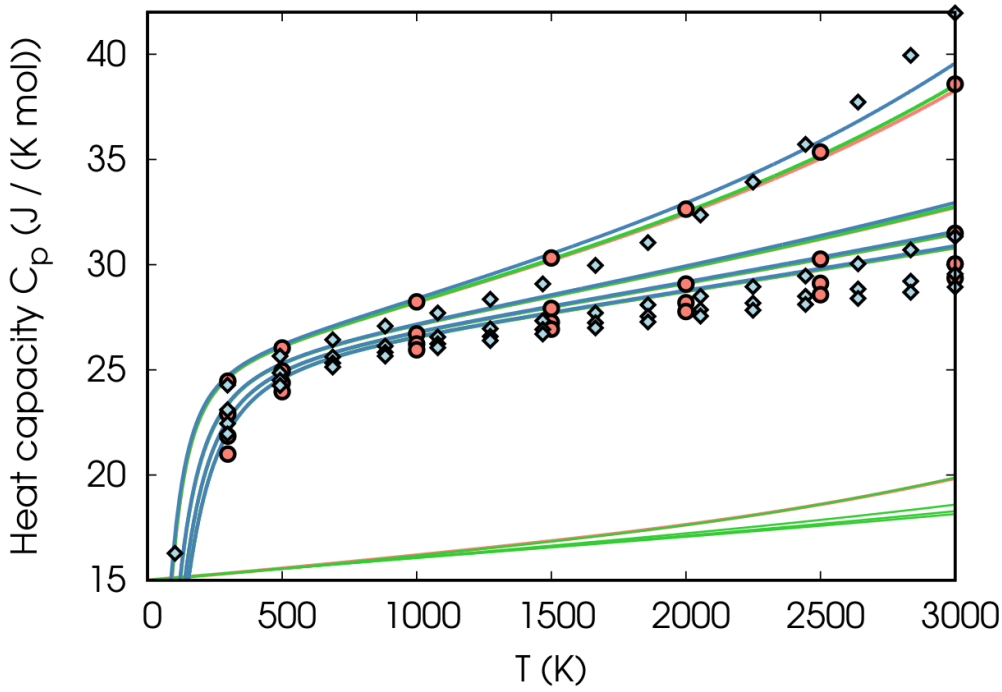

Figure A.7: LDA (red line), PBEsol (green line), and PBE (blue line) temperature dependent isobaric heat capacity. From top to bottom the curves correspond to pressures from 0 kbar to 3000 kbar in steps $\Delta p = 1000$ kbar. DFT calculations are compared with the models of Refs. [48] (blue diamonds) and [110] (red circles). The green lines at the bottom are the PBEsol electronic contribution to C_V at the four pressures (from top to bottom) shifted by 15 J/(K · mol).

the models of Ref. [48] and [110]. The two models, in agreement with each other, predict a faster convergence of C_p to the Dulong-Petit limit than our data.

We believe that this behavior is due to the different equations used for the volume dependence of the anharmonic phonon-phonon term in the models and in our pressure dependent pictures. Neglecting Eq. A.1, C_p at 3000 kbar and 3000 K is below the points of Ref. [48].

A.5 Bulk modulus

In Fig. A.8, we compare the adiabatic bulk modulus with experiment. The isothermal bulk modulus is plotted for reference. As discussed above, at 0 K, LDA overestimates while PBE underestimates the bulk modulus. PBEsol corrects a part of the LDA error but is still higher than experiment. Instead, the temperature dependence predicted by the three functionals is similar and in reasonable agreement with experiment. From 265 K to 2063 K, the adiabatic bulk modulus measured in Ref. [115] decreases by 305 kbar (9.8%) while the LDA, PBEsol, and PBE values are 293 kbar (8.7%), 279 kbar (8.6%), and 276 kbar (9.1%), respectively.

In Fig. A.9, we report the adiabatic bulk modulus at several pressures. In absolute

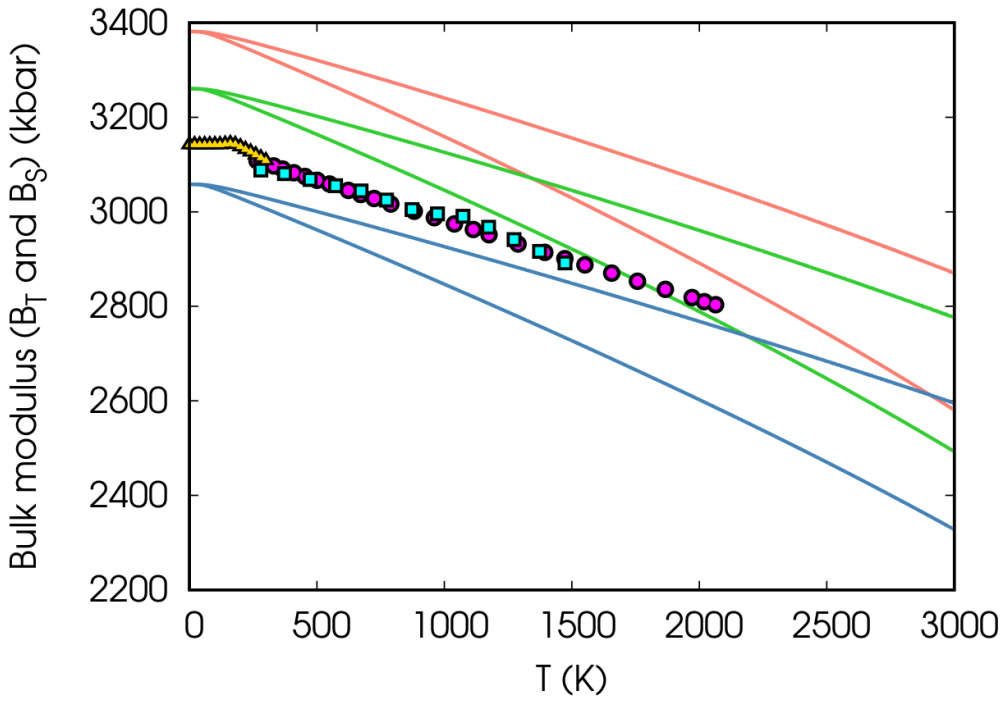

Figure A.8: Temperature dependent adiabatic and isothermal bulk moduli calculated within LDA (red line), PBEsol (green line), and PBE (blue line) compared with the experimental adiabatic data of Ref. [16] (filled cyan squares), Ref. [54] (empty gold triangles), and Ref. [115] (empty magenta cycles). For each functional the higher curve is the adiabatic bulk modulus.

values, the differences between functionals remain almost constant with pressure, while they decrease in percentage terms. For instance, at 0 K, the differences between LDA and PBEsol go from $\Delta B_S = 121$ kbar (3.5 %) at 0 kbar to $\Delta B_S = 159$ kbar (1.2 %) at 3000 kbar, while the differences between LDA and PBE go from $\Delta B_S = 323$ kbar (9.5 %) at 0 kbar to $\Delta B_S = 398$ kbar (3.0 %) at 3000 kbar. Comparing with the models of Refs. [48] and [110] that give equivalent results, the agreement is good but the DFT bulk moduli increase slightly faster than those of the models and at 3000 kbar also PBE is above the model points. With temperature, the model points of Ref.[48] decrease faster than DFT and at 3000 K and 0 kbar PBE is above. For predicting the behaviour of the bulk modulus PBE seems the best functional.

A.6 Gruneisen parameter

In Fig. A.10, we report the temperature dependent average Grüneisen parameter for several pressures. LDA and PBEsol coincide at all pressures, while PBE is higher at 0 kbar. The models of Ref. [48] and [110] have different pressure dependence mirroring the thermal expansion. At zero pressure and room temperature the ab-initio average Grüneisen param-

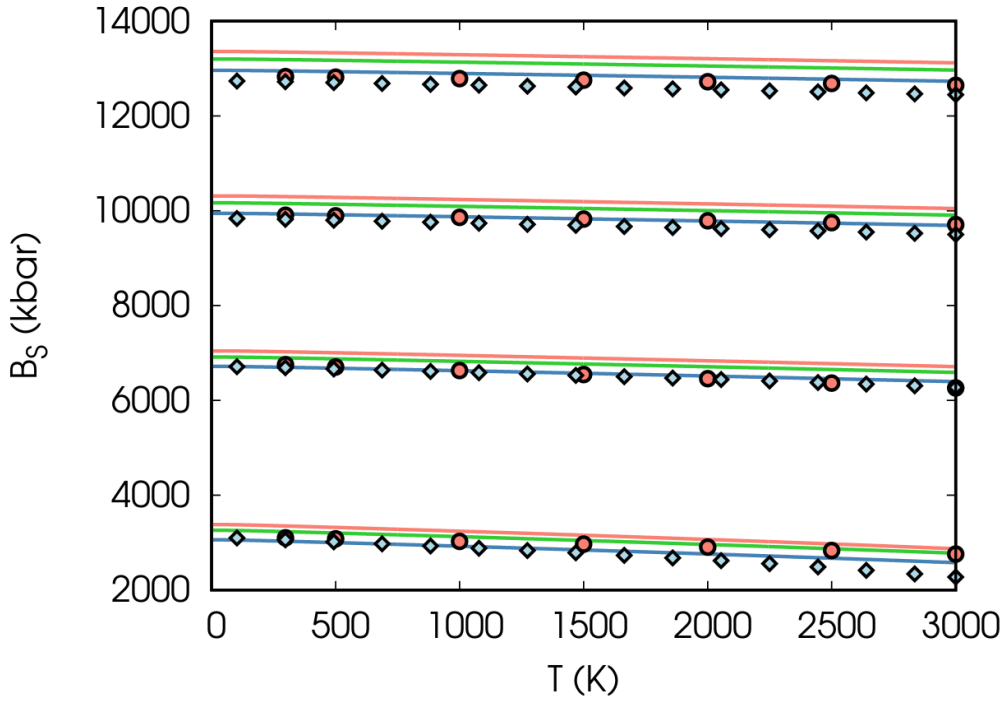

Figure A.9: Temperature dependent adiabatic bulk modulus calculated within the LDA (red lines), PBEsol (green lines), and PBE (blue lines). From bottom to top the curves correspond to pressures from 0 kbar to 3000 kbar in steps $\Delta p = 1000$ kbar. DFT calculations are compared with the model predictions of Ref. [110] (red circles) and of Ref. [48] (blue diamonds).

eter is similar to Ref. [110] and higher than Ref. [48]. Since the DFT values decrease with temperature while the model values increase, at high temperatures, our values are like those of Ref. [48]. With pressure, the differences between our values and the model of Ref. [48] decreases without vanishing completely.

A.7 Elastic moduli and sound velocities

The longitudinal and shear moduli calculated with PBEsol and PBE are shown in Figs. A.11 and A.12. The PBEsol curves are much closer to experiment than the PBE ones, but none of them reproduce accurately the experiment on the scale of this figure. Here it is difficult to compare the pressure and temperature dependence. In the main text, errors at 298 K are removed by a rigid shift of all curves to facilitate the comparison. We note that the PBEsol (PBE) shifts of about 128 kbar (437 kbar) and 122 kbar (204 kbar) for the longitudinal and shear moduli correspond to 2 % (8 %) and 7 % (12 %), respectively.

The compressional and sound velocities calculated with PBEsol and PBE are shown in Figs. A.13 and A.14. Here, with the exact density we would expect a percentage error equal

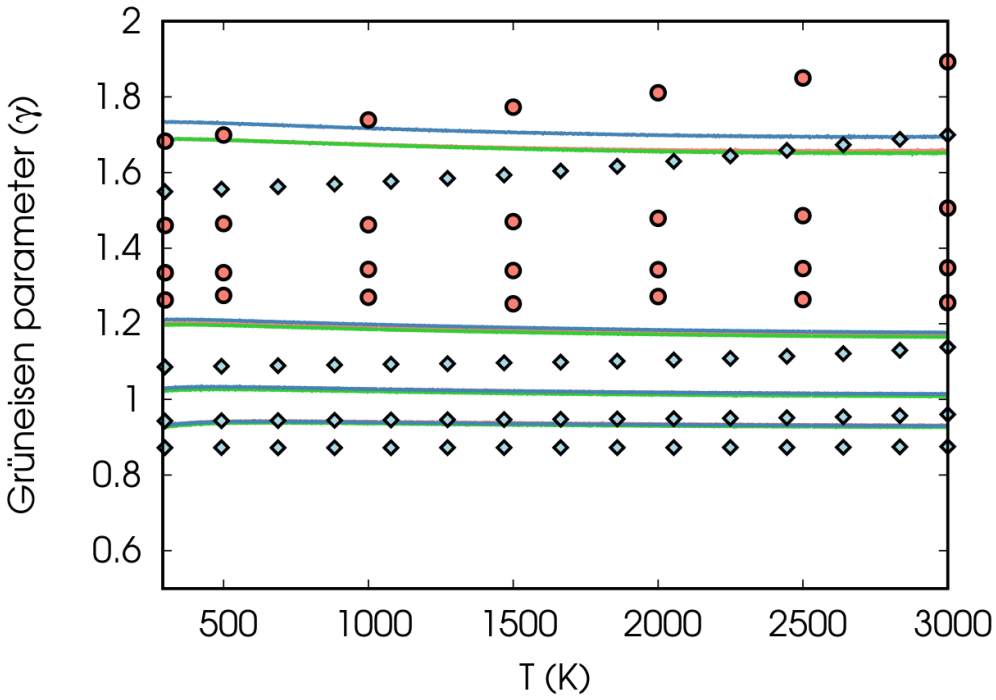

Figure A.10: Temperature dependent average Grüneisen parameter calculated within the LDA (red line below the green line), PBEsol (green line) and PBE (blue line). From top to bottom the curves correspond to pressures from 0 kbar to 3000 kbar in steps $\Delta p = 1000$ kbar. DFT calculations are compared with the model predictions of Refs. [48] (blue diamonds) and [110] (red circles).

to half the error of the elastic moduli. The presence of the density in the expression of the sound velocity slightly increases the PBEsol errors and decrease the PBE ones, since both the longitudinal and shear moduli are lower than experiment and PBEsol overestimates the density while PBE underestimates it. The PBEsol (PBE) shifts of the compressional sound velocity are 65 m/s (146 m/s) corresponding to 1 % (3 %), while the shifts of the shear sound velocity is 113 m/s (149 m/s) corresponding to 4 % (5 %).

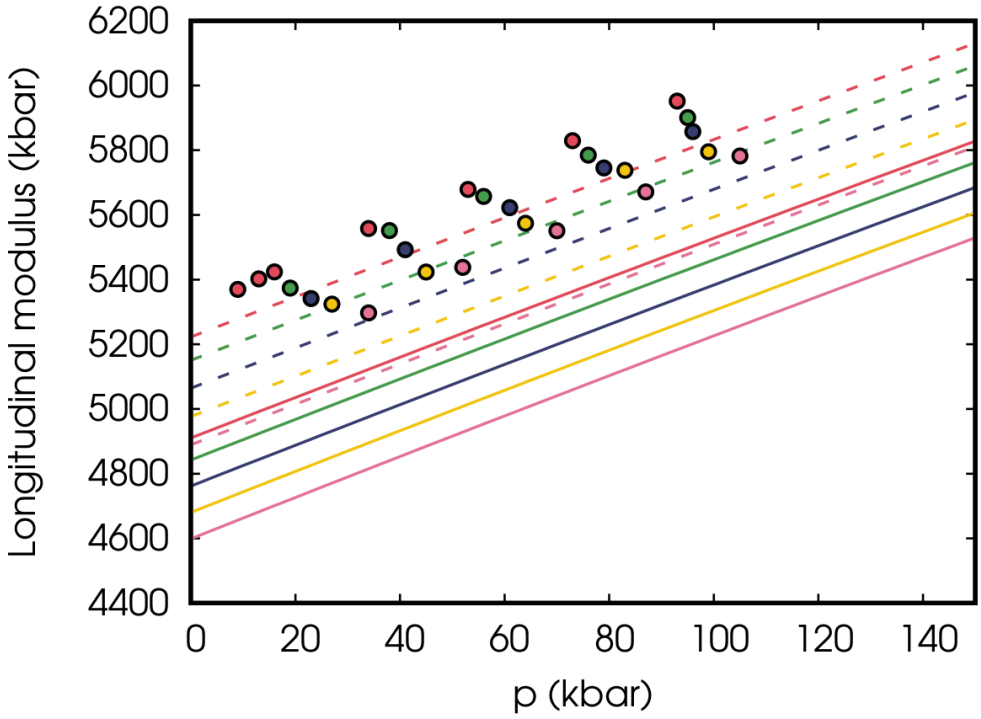

Figure A.11: Temperature dependent PBEsol (dashed lines) and PBE (solid lines) longitudinal modulus calculated within the quasi-harmonic approximation as a function of pressure for several temperatures (red 298 K, green 473 K, blue 673 K, yellow 873 K, and pink 1073 K). The circles (with the same color code) are the data of Ref.[158], measured at the same temperatures and calculated as $L = B_S + 4/3G_S$ from the B_S and G_S in their Table III.

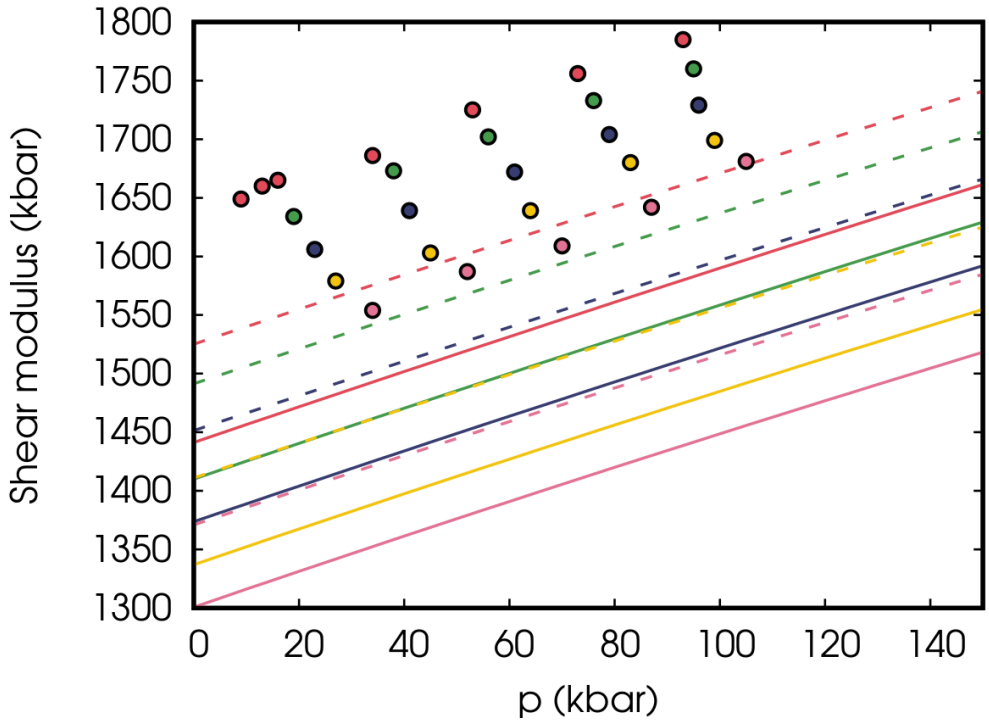

Figure A.12: Temperature dependent PBEsol (dashed lines) and PBE (solid lines) shear modulus calculated within the quasi-harmonic approximation as a function of pressure for several temperatures (red 298 K, green 473 K, blue 673 K, yellow 873 K, and pink 1073 K). The circles (with the same color code) are the data of Ref.[158], measured at the same temperatures (from their Table III).

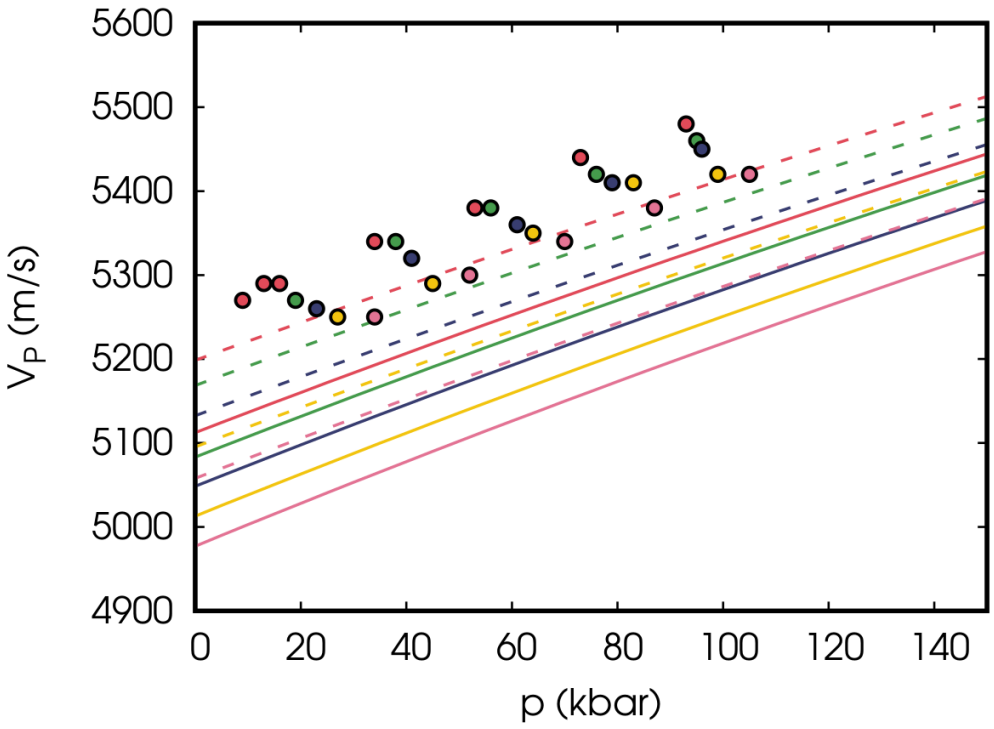

Figure A.13: Temperature dependent PBEsol (dashed lines) and PBE (solid lines) compressional sound velocity (V_P) calculated within the quasi-harmonic approximation as a function of pressure for several temperatures (red 298 K, green 473 K, blue 673 K, yellow 873 K, and pink 1073 K). The circles (with the same color code) are the data of Ref.[158], measured at the same temperatures.

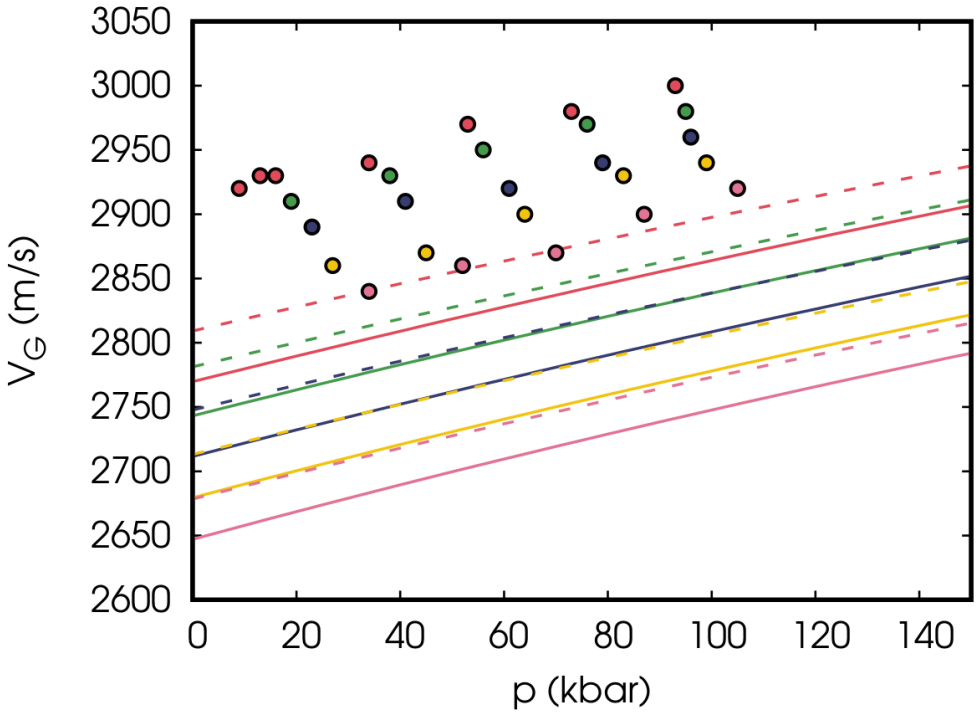

Figure A.14: Temperature dependent PBEsol (dashed lines) and PBE (solid lines) shear sound velocity (V_G) calculated within the quasi-harmonic approximation as a function of pressure for several temperatures (red 298 K, green 473 K, blue 673 K, yellow 873 K, and pink 1073 K). The circles (with the same color code) are the data of Ref.[158], measured at the same temperatures.

Appendix B

Molybdenum

In the present appedix, in addition to $\beta_V(p,T)$, we show $C_p(p,T)$, $B_S(p,T)$, and $\gamma(p,T)$ for several pressures p.

B.1 Phonon dispersion

In Fig. B.1, we compare the theoretical phonon dispersions, interpolated at the 295 K lattice constant obtained accounting for zero point and thermal expansion effects (see the values in Table 1 of the paper), with inelastic neutron scattering data. [155, 197] LDA and PBEsol give similar frequencies in good agreement with experiment except at the H point where we find a relatively large error. PBE gives frequencies lower than LDA (as found in other solids [36, 65]), and hence more distant from experiment. As for gold, platinum and tungsten, for molybdenum phonon dispersions, LDA or PBEsol are preferable to PBE. This conclusion is in agreement with Ref. [167, 26]. Instead, Ref. [198] finds PBE phonon dispersions closer to experiment than ours.

B.2 Thermal equation of state

In Fig. B.2, we show the 300 K equation of state. Our PBE curve agrees with the linearized augmented plane wave (LAPW) all-electrons PBE calculation of Ref. [192] and with the PW91 [151] results of Ref. [198]. The experimental results are all in good agreement among themselves with the shock wave data arriving beyond 2000 kbar. At each pressure, the PBE curve overestimates the volume, while LDA underestimate it as we have discussed for zero pressure. The PBEsol volume is still slightly underestimated at zero pressure, but the agreement with experiment increases with pressure. The same behaviour is found at 2000 K as we show in the inset. Here we compare our equation of state with the models of Ref. [177, 49] and [109]. The two models agree with each other and with the ab-initio results especially using PBE and PBEsol.

In Fig. B.3 we present the equation of state removing the error due to the equilibrium volume by plotting V/V_0 as a function of pressure (here V_0 is the equilbrium volume at

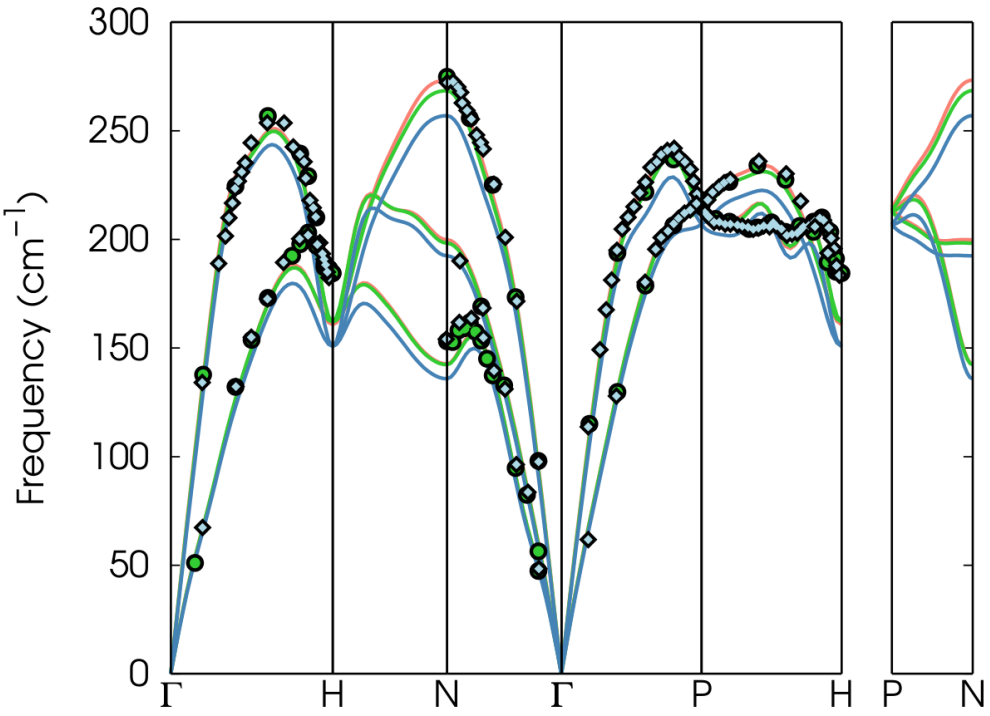

Figure B.1: Phonon dispersions interpolated at the 295 K lattice constant. The LDA (red curves), PBEsol (green curve), and PBE (blue curve) results are compared with the experimental inelastic neutron scattering data measured at 295 K (Ref. [155] blue diamonds and Ref.[197] green circles).

300 K, close to that reported in Table 1 of the paper). As in the case of tungsten, here the picture changes, with PBE that follows the experimental data in all the pressure range. Both LDA and PBEsol are in this case slightly above the experiment. In the inset we show the equation of state at 2000 K and compare with the model data presented in the inset of Fig. B.2. At this temperature the model points are equally close to PBE and PBEsol. At zero pressure the theoretical data are slightly below the model point of Ref. [109] reflecting the underestimation of the thermal expansion with respect to experiment (see below).

B.3 Thermal expansion

In Fig. B.4, we compare with experiment the thermal expansion at zero pressure. We have reported only the commonly accepted data, as those of Refs. [136, 18, 97, 130] and not the new measurements proposed by Ref. [201]. Our LDA and PBEsol data match the accepted values up to 1000 K while PBE is slightly higher. The PW91 data of Ref. [198] (not reported here) are more close to our LDA data, than to the PBE data and match the experimental thermal expansion up to 1500 K. After these temperatures, anharmonic phonon-phonon interaction effects are expected to become important and therefore our ab-initio data cannot

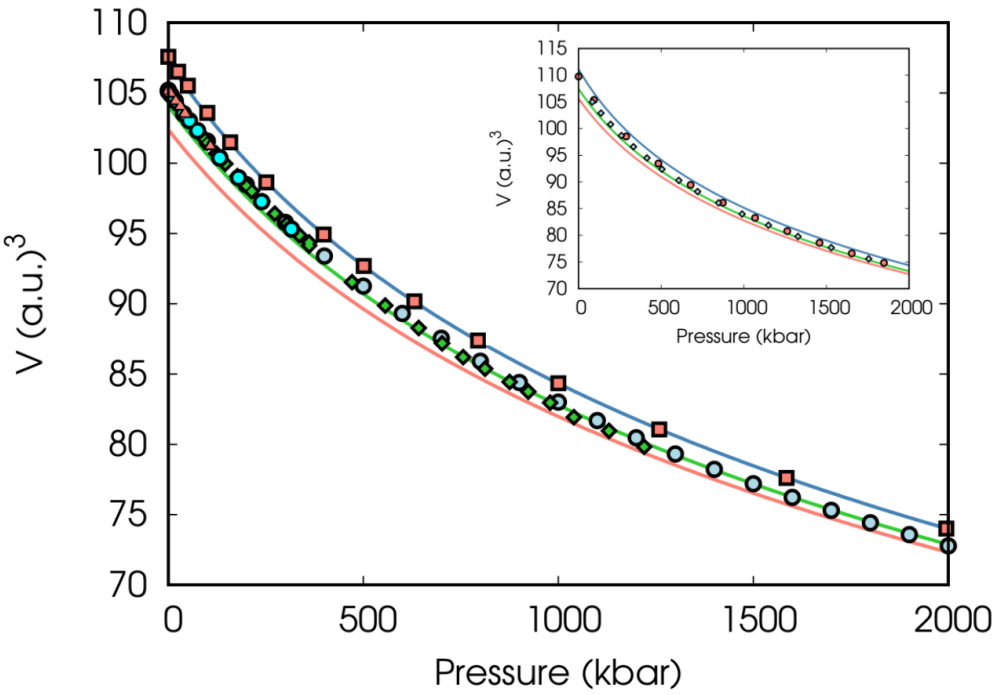

Figure B.2: V as a function of p at 300 K obtained by LDA (red), PBEsol (green), and PBE (blue) compared with experiment (blue circles [79], cyan circles, [109] red triangles, [201] and green diamonds [45]) and previous calculations (red squares (PBE) from Ref. [192]). In the inset the same curves at 2000 K compared with the predictions of Ref. [109] (red circles) and of Ref. [49] (blue diamonds).

follow experiment. In the picture we show also the electronic excitation contribution to the thermal expansion, calculated adding or neglecting the electronic term in the free energy. As can be seen from the figure at 3000 K it is of the order of 510^{-6} (1/K), but at 1500 K its contribution is negligible.

In Fig. B.5, we show the thermal expansion at 0 kbar, 1000 kbar, 2000 kbar, and 3000 kbar and compare our data with the models of Ref. [109] and of Ref. [177]. For the first we use the data reported in their Tab. V, while for the latter we use the data reported in Tab. 7 for 0 kbar and 1000 kbar and data calculated by us with the parameters reported at pag.193 at 2000 kbar and 3000 kbar. In the same figure we report also the PW91 values of Ref. [198]. We find that the three functionals differ appreciably at 0 kbar, but the differences are smaller at higher pressures. The pressure dependence of the thermal expansion agrees with the PW91 findings of Ref. [198]. The points of the two models differ at high pressure, with the model of Ref. [109] that decreases more slowly with pressure. Our data agree very well with the model of Ref. [177] until about 1000 K, but our curves are below the model points at higher temperatures. This seems due to missing anharmonic phonon-phonon interaction terms in our calculation.

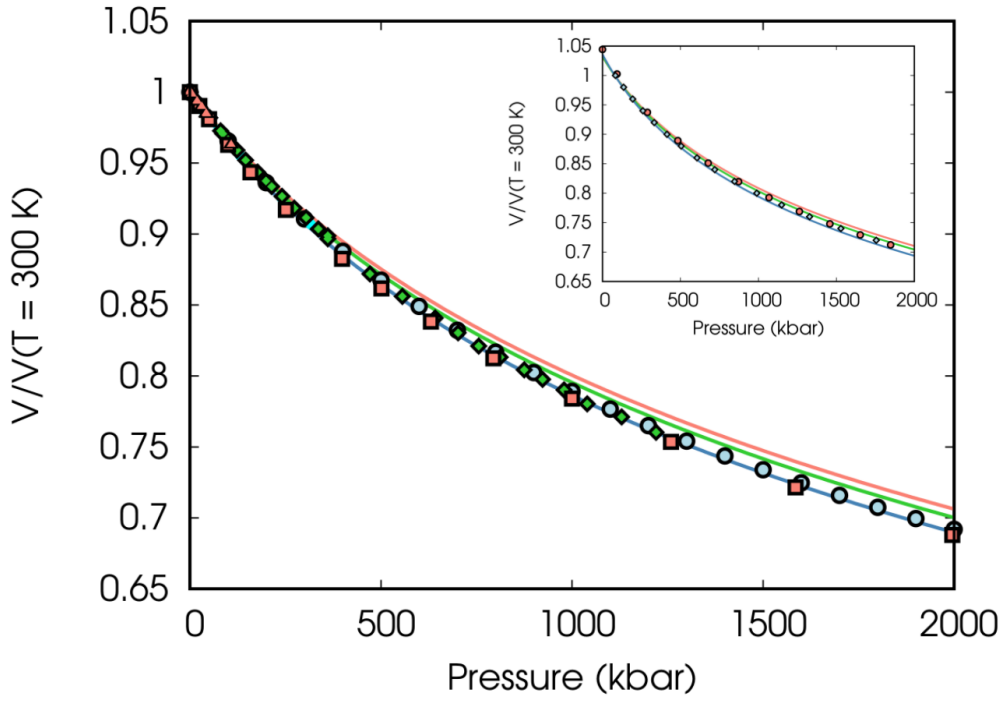

Figure B.3: V/V_0 as a function of p at 300 K obtained by LDA (red), PBEsol (green), and PBE (blue) compared with experiment (blue circles [79], cyan circles, [109] red triangles, [201] and green diamonds [45]) and previous PBE calculations (red [192] squares). In the inset the same curves at 2000 K compared with the predictions of Ref. [109] (red circles) and of Ref. [49] (blue diamonds).

B.4 Heat capacity

In Fig. B.6, we compare the isobaric heat capacity with experiment. The three functionals gives very similar values of this quantity and theory and experiment are in good agreement until about 1000 K. As can be seen from the figure at 2500 K our value of 33.2 J/(K· mol) has a contribution of electronic excitation of about 5.7 J/(K· mol), while the quasiharmonic term contributes for other 2.5 J/(K· mol), while the experimental value is 44.1 J/(K· mol) so that the anharmonic phonon-phonon interaction and possibly defects should give a contribution of about 10.9 J/(K· mol).

In Fig. B.7, we report the isobaric heat capacity at several pressures. In the same figure we show also the electronic contribution to which we added a fixed value of 15 J/(K · mol) for picture clarity. At zero pressure both models gives very similar results which reproduce well experiment, but the behaviour with pressure is different, with the model of Ref. [109] which converges faster to the Dulong-Petit limit. We find that the electronic contribution decrease slowly with pressure and added to the Dulong-Petit value gives a C_p higher than the point of Ref. [109]. It seems therefore that this model somewhat underestimates the electronic contribution to the specific heat at high pressures.

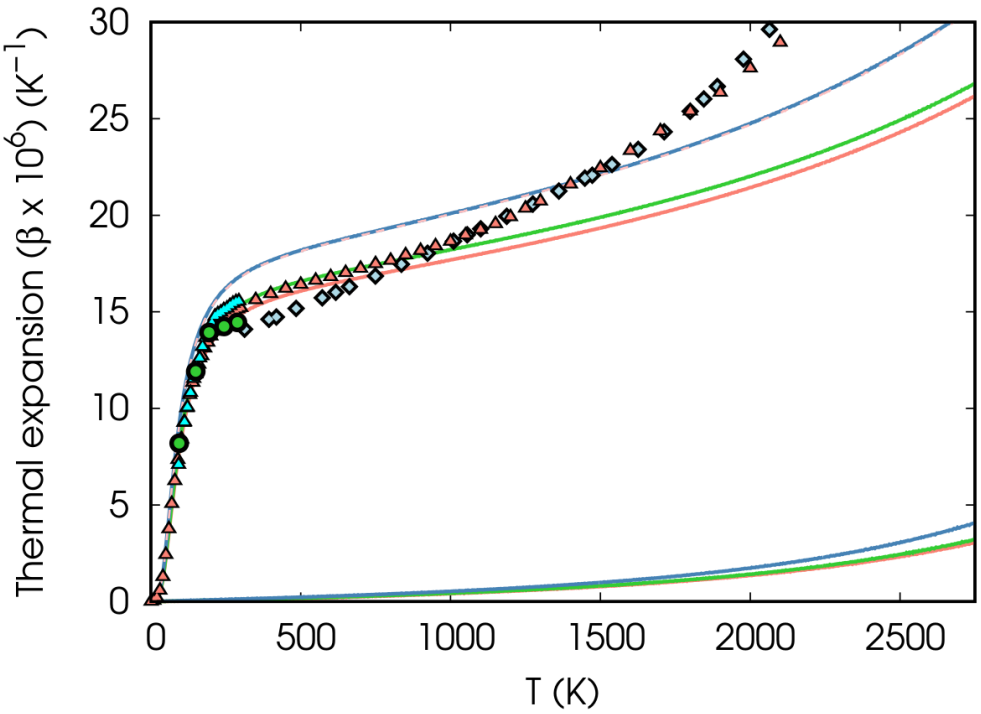

Figure B.4: Temperature dependent thermal expansion calculated by LDA (red curve), PBEsol (green curve), and PBE (blue curve) compared with the experimental data reported in Ref. [136] (cyan triangles) Ref. [97] (green circles), Ref. [130] (blue diamonds), Ref. [18] (red triangles). The thinner lines at the bottom indicate the differences between the thermal expansion calculated including or neglecting the electronic excitations term in the free energy. Pink dashed line on the PBE curve shows the result obtained with 8 geometries and $\Delta a = 0.02$ a.u.

.

B.5 Bulk modulus

In Fig. B.8, we compare the adiabatic bulk modulus with experiment. The isothermal bulk modulus is plotted for reference. The PBE bulk modulus is in very good agreement with experiment and also the temperature dependence seems to be well accounted for by theory. LDA and PBEsol instead overestimate the bulk modulus. The decrease of the experimental bulk modulus from 25 K to 2225 K is 410 kbar (16 %), while the LDA, PBEsol, and PBE values are 432 (15 %), 407 kbar (15 %), and 405 kbar (16 %), respectively. In Fig. B.9, we report the adiabatic bulk modulus at several pressures. Our data are compared with the models of Ref. [109] and of Ref. [49] (only at 0 kbar and 1000 kbar). In all the range of pressures the agreement between ab-initio values and model values is very good with PBE which remain always quite close to the model points and PBEsol and PBE slightly above. For this quantity the differences between functionals do not decrease with pressure.

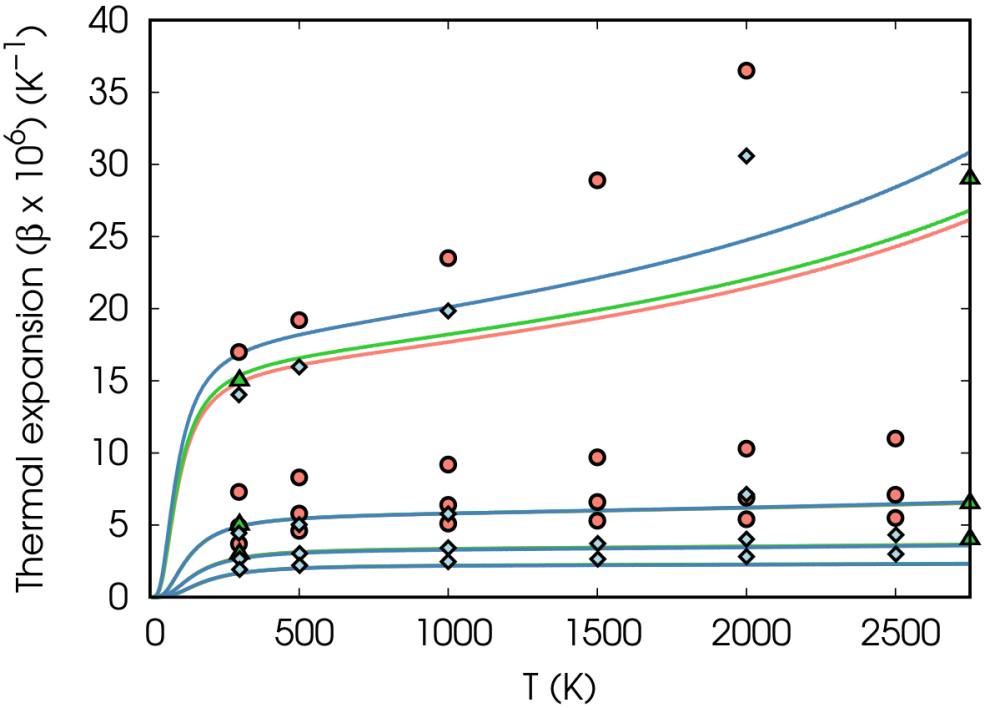

Figure B.5: Temperature dependent thermal expansion computed within the LDA (red line), PBEsol (green line), and PBE (blue line). The different curves (from top to bottom) correspond to pressures from 0 kbar to 3000 kbar in steps $\Delta p = 1000$ kbar. Theory is compared with the models of Ref. [109] (red circles) and of Ref. [177] (blue diamonds) and with the ab-initio PBE calculations of Ref. [198] (green triangles).

B.6 Grüneisen parameter

In Fig. B.10, we report the average Grüneisen parameter as a function of temperature and compare it with previous ab-initio calculation [198] an with the model data of Ref. [109] and of Ref. [49] The agreement with the PW91 calculation is quite good expecially at high pressure. The major difference is at 0 kbar and 300 K where the value of Ref. [198] is closer to the model of Ref. [49] while our value is closer to the model Ref. [109]. With temperature the model data and the ab-initio calculation increase faster than our values and at 0 kbar and 2750 K our value coincide with previous ab-initio result, but remains lower than both models. The model of Ref. [109] has average Grüneisen parameters decreasing much slowly with pressure than both the ab-initio results and the model of Ref. [49]. The ab-initio results however seems to remain more constant with temperature than the results of Ref. [49]. This in part could be due to the missing anharmonic phonon-phonon terms in the ab-initio calculation.

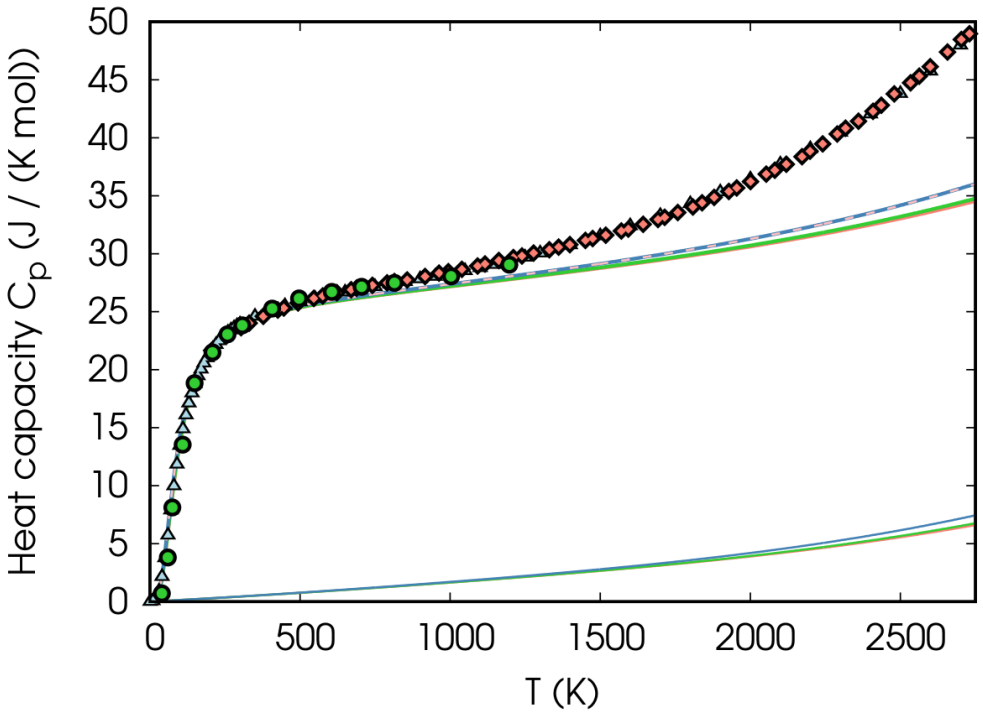

Figure B.6: LDA (red line), PBEsol (green line), and PBE (blue line) temperature dependent isobaric heat capacity compared with experiment from Ref. [97] (green circles), Ref. [72] (red diamonds) and Ref. [18] (blue triangles). Thin lines at the bottom (with the same color conventions) indicate the contribution of electronic themal excitations to the heat capacity. Pink dashed line on the PBE curve shows the result obtained with 8 geometries and $\Delta a = 0.02$ a.u.

.

B.7 Numerical issues

The choice of the interval between strains used to sample the energy might affect the final value of the elastic constants. We show in Fig. B.11 the dependence of the three elastic constants on this parameter. As can be seen from the figure, when the strain interval is small enough to avoid the high order terms in the energy versus strain curves that appear at large $\Delta\varepsilon$, the values of the elastic constants converge to a constant value. In principle, we should compute the limit for $\Delta\varepsilon \to 0$, but as can be seen in the curve for C_{11}, if the value of $\Delta\varepsilon$ is too small, the fit of the energy becomes also inaccurate. In the paper we used a value $\Delta\varepsilon = 0.005$, that gives values of elastic constants close to the limit of small $\Delta\varepsilon$ without introducing significant errors. We note that in these figures we are using an enlarged scale, but on the scale of elastic constants used in the paper, these curves appear almost flat.

We have also studied the dependence of our thermodynamic properties on the distance Δa among the geometries used to compute phonons. The Δa used in the paper is 0.1 a.u., but also a $\Delta a = 0.2$ a.u. gives very similar results as we show for PBE in Fig. B.4 and in

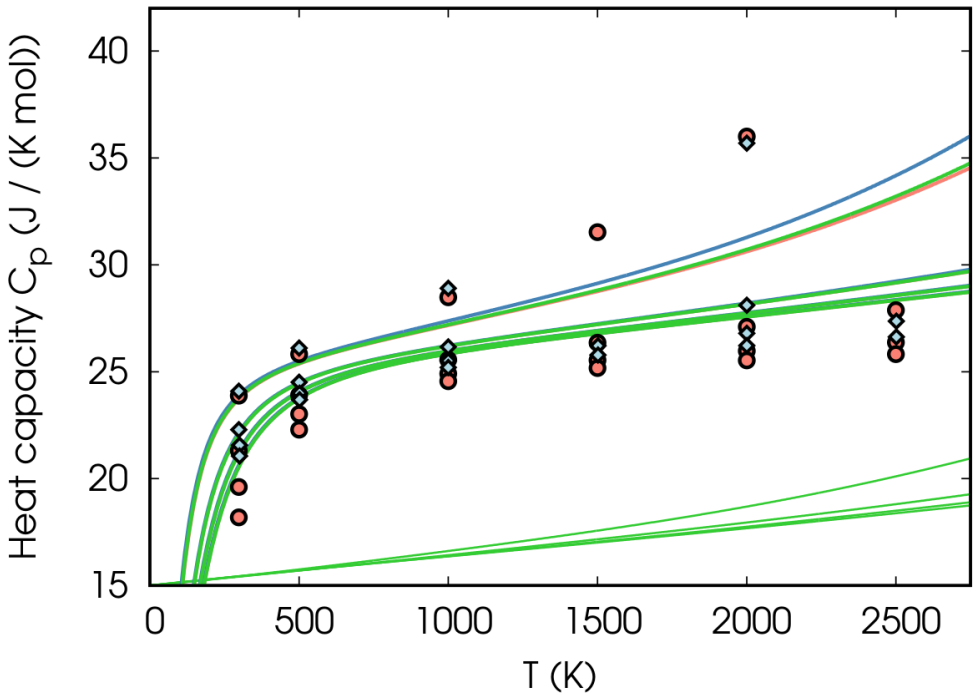

Figure B.7: LDA (red line), PBEsol (green line), and PBE (blue line) temperature dependent isobaric heat capacity. From top to bottom the curves correspond to pressures from 0 kbar to 3000 kbar in steps $\Delta p = 1000$ kbar. DFT calculations are compared with the model of Ref. [109] (red circles) and of Ref. [49] (blue diamond). The green lines at the bottom are the PBEsol electronic contribution to C_V at the four pressures (from top to bottom) shifted by 15 J/(K $\cdot$ mol).

Fig. B.6.

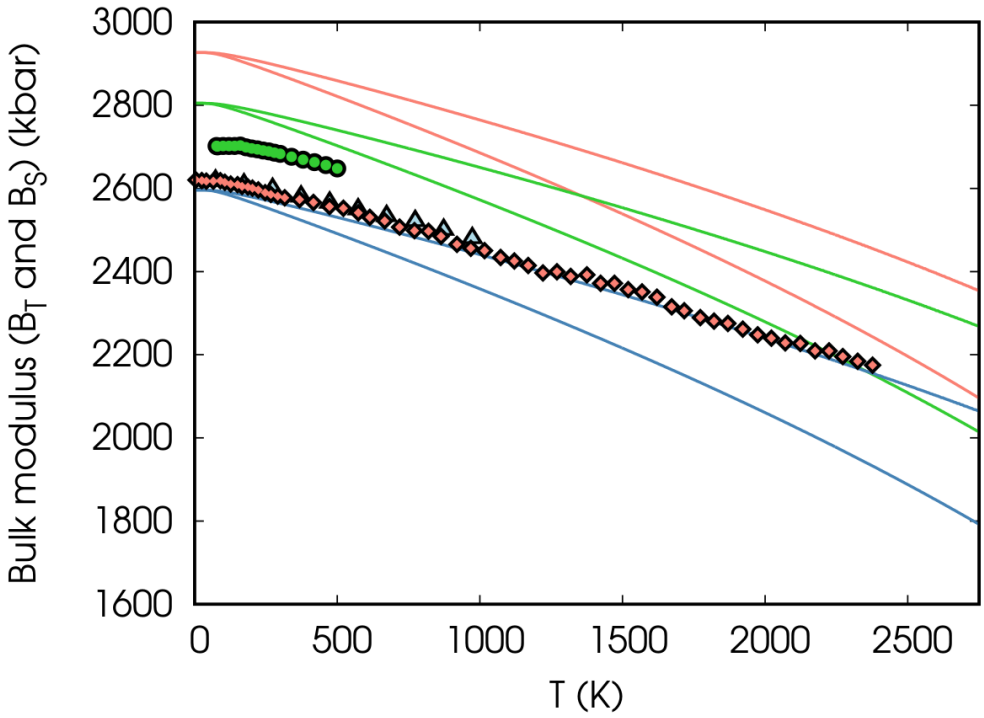

Figure B.8: Temperature dependent adiabatic and isothermal bulk moduli calculated within LDA (red line), PBEsol (green line), and PBE (blue line) compared with the experimental adiabatic data of Ref. [47] (blue triangles), Ref. [20] (green circles) and Ref. [21] (red diamonds). For each functional the higher curve is the adiabatic bulk modulus.

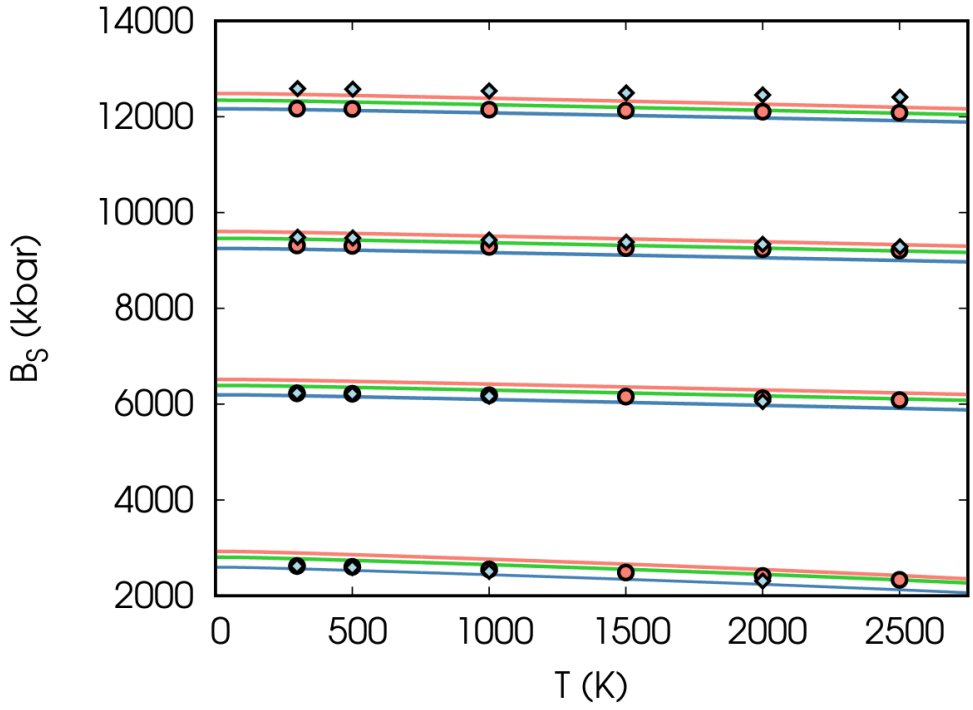

Figure B.9: Temperature dependent adiabatic bulk modulus calculated within the LDA (red lines), PBEsol (green lines), and PBE (blue lines). From bottom to top the curves correspond to pressures from 0 kbar to 3000 kbar in steps $\Delta p = 1000$ kbar. DFT calculations are compared with the model predictions of Ref. [109] (red circles) and of Ref. [177] (blue diamond).

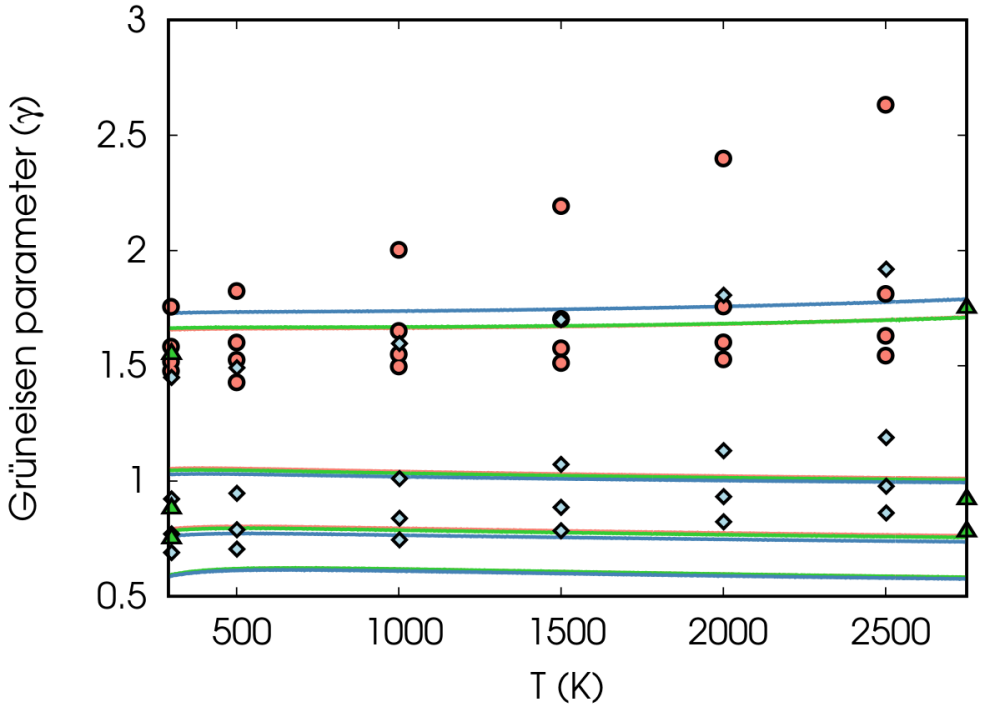

Figure B.10: Temperature dependent average Grüneisen parameter calculated within the LDA (red line below the green line), PBEsol (green line) and PBE (blue line). From top to bottom the curves correspond to pressures from 0 kbar to 3000 kbar in steps $\Delta p = 1000$ kbar. DFT calculations are compared with the model predictions of Ref. [109] (red circles) and of Ref. [49] (blue diamond) and with the ab-initio PBE calculations of Ref. [198] (green triangles).

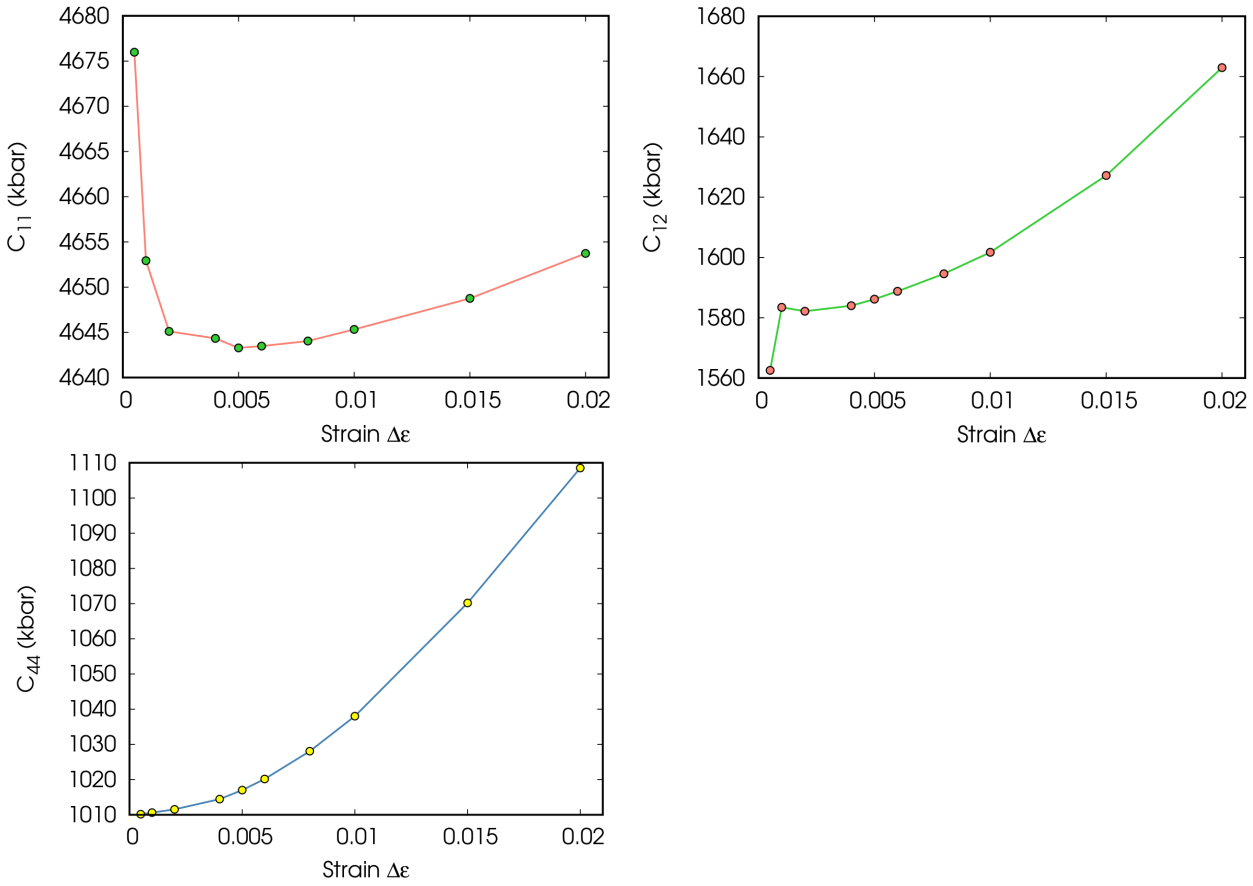

Figure B.11: Value of the $T = 0$ K elastic constants calculated with different values of the strain interval for each strain type.

Appendix C

Beryllium

This appendix presents some thermodynamic quantities calculated for beryllium: the equation of state, the thermal expansion, the isobaric heat capacity, and the adiabatic bulk modulus as a function of temperature at room pressure. Some of the calculated properties, such as the thermal expansion, are useful in interpreting the temperature dependence of the elastic constants, whereas others are presented for the sake of completeness. These thermodynamic quantities are already present in the literature and selected results from experiments and previous calculations are also marked in the figures for reference. The phonon frequencies calculated with the present pseudopotentials have been shown in Ref. [107] and are not reported here.

C.1 Thermodynamic properties

In Tab. C.1 we report, for each of the 11 geometries studied along the "stress-pressure" 0 K isotherm, the corresponding pressure, crystal parameters and volume. The geometries for which we have computed the QHA elastic constants are also indicated.

In Fig. C.1 we show the LDA EOS at 0 K and at 1500 K calculated with the interpolation of the free-energy on the two dimensional 14×7 grid and compared with the experimental data.

The c/a parameter along the "stress-pressure" isotherm at 0 K is shown in Fig. C.2 and compared with previous experimental measurements and previous calculation. Both theory and experiment predict an increase of c/a with pressure. Quantitatively, there is good agreement with the calculation of Ref. [162].

In Fig. C.3 we present the thermal expansion tensor and the volume thermal expansion. The thermal expansion of beryllium is quite small compared to other metals [69] and is well reproduced by our calculation at least until 1000 K. At higher temperatures, the experimental α_3 seems to increase slightly faster than our calculation, pointing to the presence of anharmonic effects beyond the QHA not accounted for by our calculation. The thermal expansion tensor has been calculated from the free-energy interpolated on the two dimensional grid of a, c/a. The volume thermal expansion is then compared with the curve obtained

Table C.1: The "stress-pressure" 0 K isotherm. In the configurations with * we have computed the QHA TDECs. For all other values of pressure we have interpolated them.

geometry	pressure (kbar)	a (a.u.)	c/a	V $(\text{a.u})^3$
1	1659	3.494	1.608	59.40
2	1259*	3.594	1.602	64.41
3	932	3.694	1.597	69.71
4	666*	3.794	1.593	75.34
5	452	3.894	1.589	81.25
6	282*	3.994	1.585	87.45
7	147*	4.094	1.580	93.89
8	43*	4.194	1.576	100.69
9	-39*	4.294	1.570	107.65
10	-101*	4.394	1.564	114.91
11	-150*	4.494	1.558	122.46

from the calculation of the free energy on the 11 geometries along the "stress-pressure" 0 K isotherm. The agreement of the two calculations is reasonably good. Similar thermal expansions have also been shown by Shao et al. [171] and for the volume thermal expansion by Luo et al. [116]. Both are in good agreement with our data.

The presence of anharmonic effects is confirmed also by the isobaric heat capacity (Fig. C.4) which is reproduced accurately by the QHA calculation until 800 K. The isobaric heat capacity has been calculated both in the two-dimensional parameter grid and along the 'stress-pressure" curve. The two curves coincide so we show only one curve in Fig. C.4. The reported experimental data are from Ref. [81] and from a critical assessment of many experimental data. [18] The two sets of data are quite close to each other. A theoretical result similar to our has been reported in Ref. [116].

The isothermal and the isoentropic bulk modulus calculated from the EOS applied to the 11 geometries along the "stress-pressure" 0 K isotherm is shown in Fig. C.5 and compared with that derived from the QHA TDECs. As can be seen from the figure there is a very good agreement if the elastic constants are interpolated using geometries $7-11$ symmetric about the minimum, but when we use all the 8 calculated elastic constants for the interpolation some shift of the bulk modulus (of the order of 32 kbar (3%) at 0 K) is found. The bulk modulus derived from EOS is instead stable passing from 5 to 11 geometries. Very small or no difference is found instead on the figures in the paper if we use 5 or 8 sets of elastic constants for the interpolation. For reference we report also the isothermal and adiabatic bulk modulus calculated in Ref. [162] which is sligtly higher than ours but has a very similar temperature dependence. Ref. [103] presents an adiabatic bulk modulus smaller than ours at 0 K but with a similar temperature dependence. The experimental data of Ref. [165] have instead a stronger decrease with temperature than the theoretical reports. Recent data on polycrystalline beryllium reported in Ref. [133] have still high uncertainty. We show in the figure the region in which their measurements are located.

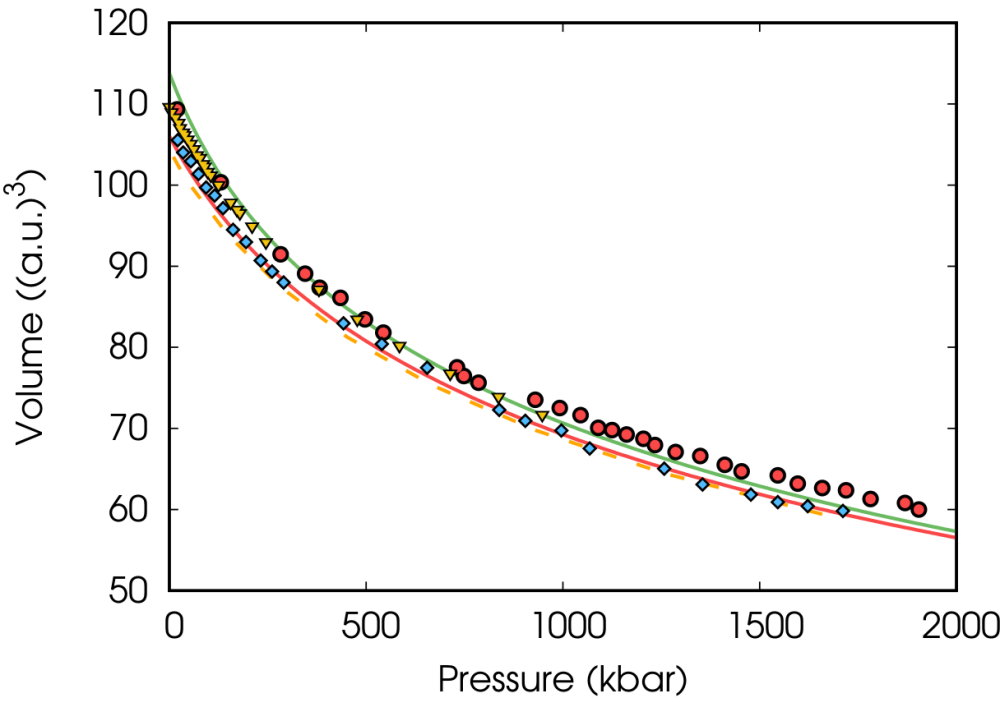

Figure C.1: Equation of state calculated with our parameters at 4 K (red line) and 1500 K (green line) compared with experimental data of Ref. [52] (red points), Ref. [134] (blue diamond), and Ref. [106] (yellow triangles). The "stress-pressure" 0 K isotherm is shown with a dashed orange line.

A flowchart in Fig. C.6 illustrates the calculations of various elastic constants for HCP metals in the `thermo_pw` software. Starting from the SCF calculations on each geometry ξ_i in a two-dimensional grid of HCP lattice parameters and interpolating, a stress-pressure curve is obtained by minimizing the Gibbs energy in Eq.(3) of the paper and obtaining several equilibrium geometries along the curve. In these, we compute the temperature and pressure dependent thermodynamic properties via SCF and phonon calculations. SCF and phonon calculation has to be computed also on strained geometries in order to obtain the ZSISA QHA ECs at fixed structures. In this step one can replace the ZSISA QHA ECs with the FFEM QHA ECs by determining the atomic coordinates from the minimum of free energy. With crystal parameters $\xi(T,P)$ and the thermal expansion $\alpha(T,P)$ obtained from the SCF+phonon calculations on the grid geometries, V-ZSISA QHA ECs are polynominally interpolated. Using the relation between isothermal and adiabatic elastic constants (Eq.(11) of the paper), we obtain the adiabatic ones that can be compared with experiments. In the second column, the QSA elastic constants are derived from the energy calculations of strained geometries of the grid unperturbed geometries. If the energy calculations are substituted by free energy, we could also get QHA elastic constants without the V-ZSISA approximation (not used in the thesis).

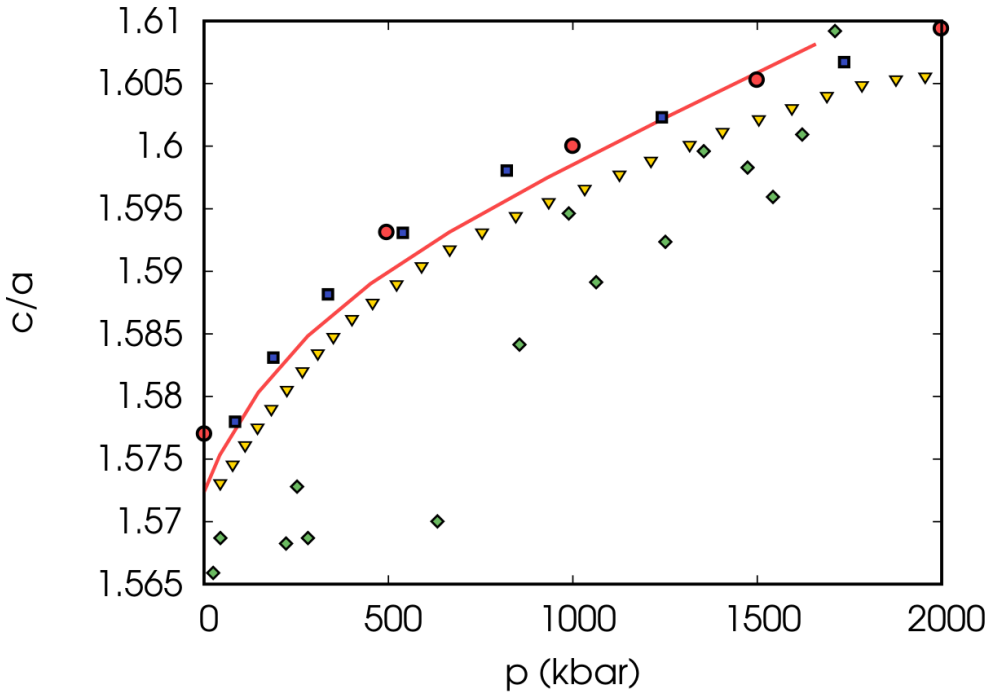

Figure C.2: c/a ratio as a function of pressure at 0 K (red line) compared with experimental data of Ref. [195] (red points) and of Ref. [134] (blue diamond) and with the theoretical calculations of Ref. [162] (blue squares) and Ref.[178] (yellow triangles).

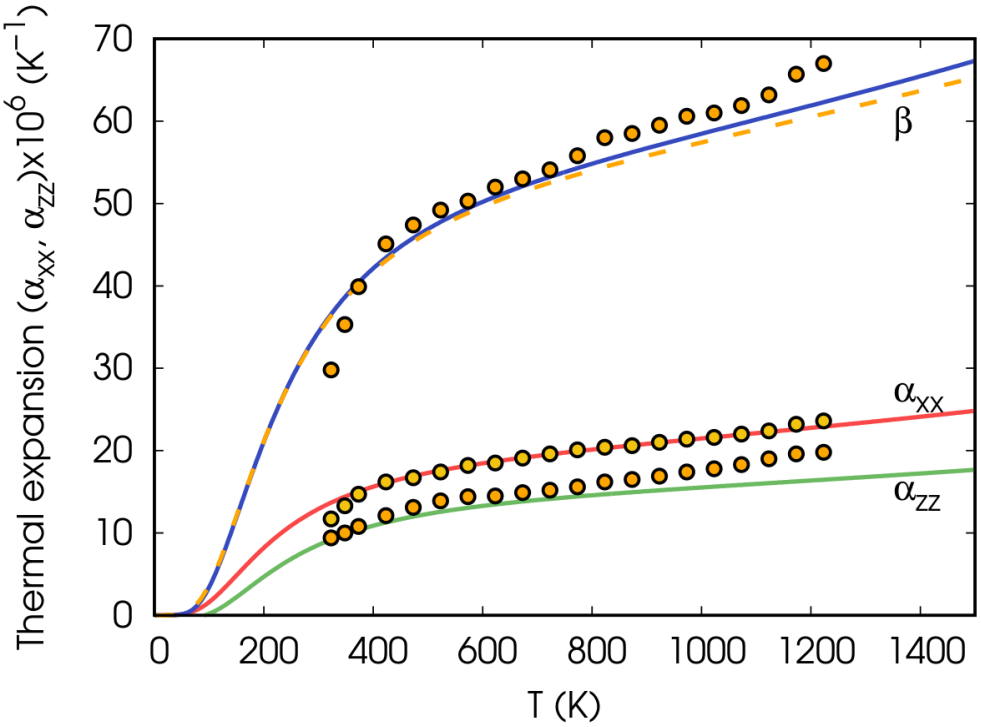

Figure C.3: Thermal expansion tensor of beryllium (red α_{xx} and green α_{zz} lines) calculated in the present work compared with the experimental data of Ref. [69]. The volume thermal expansion $\beta = 2\alpha_{xx} + \alpha_{zz}$ is also shown (blue line) and compared with the one calculated using only the 11 geometries along the "stress-pressure" 0 K isotherm (dashed orange line).

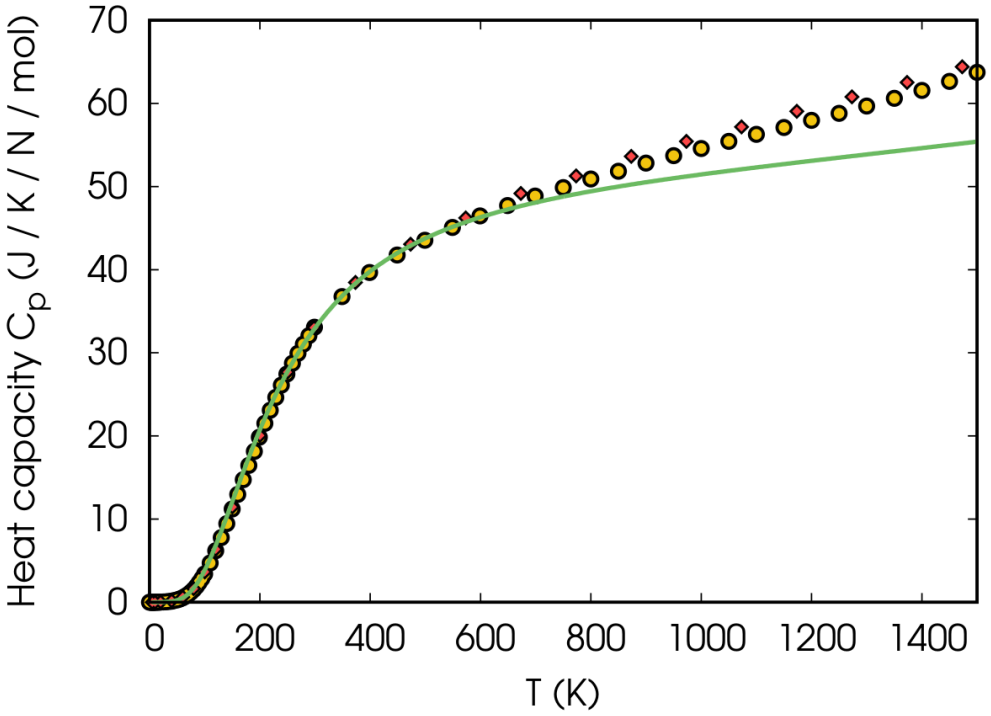

Figure C.4: Isobaric heat capacity per cell (green line) compared with the experimental data in Ref. [81] (red diamond) and with the values recommended Ref. [18] from a critical evaluation of the experimental data (yellow circles).

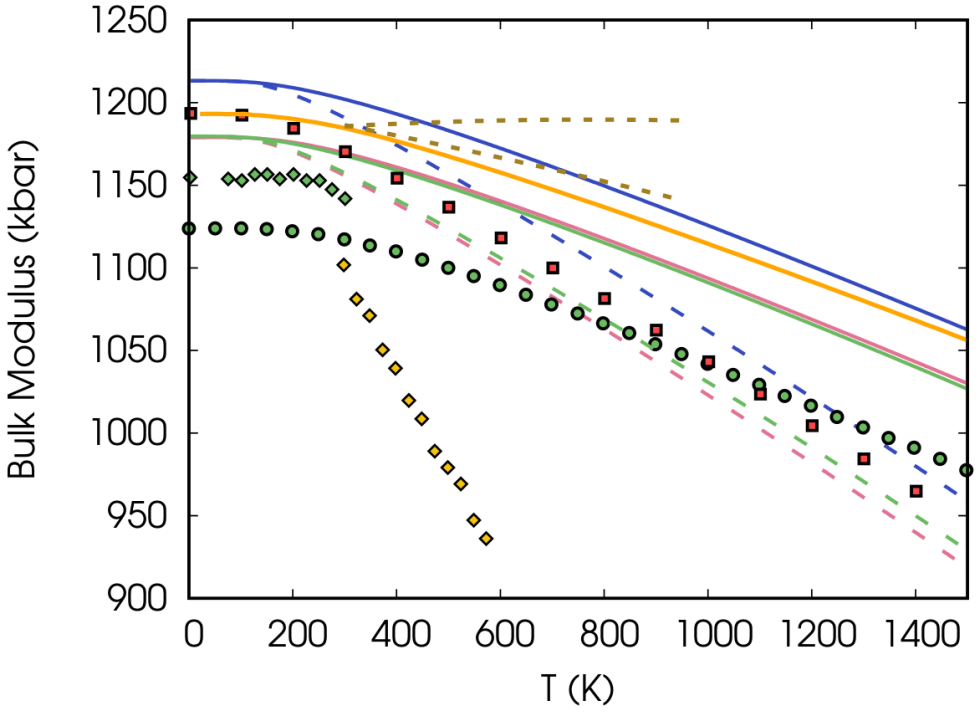

Figure C.5: Isothermal (dashed lines) and adiabatic (continuos lines) bulk modulus as a function of temperature calculated from the equation of state (red lines) by fitting the free energy along the "stress-pressure" 0 K isotherm with a fourth-order Birch-Murnaghan equation. The green (blue) lines are the bulk modulus obtained from the interpolation of the QHA elastic constants in 5 (8) geometries. The red squares (orange line) indicate the PBE isothermal (adiabatic) bulk modulus predicted in Ref. [162] The green dots is the bulk modulus predicted by Ref. [103]. The green (yellow) diamonds are the experimental values of Refs. [173] (Ref. [165]). The two dashed olive lines show the region where recent experimental values of the bulk modulus of polycristalline beryllium have been found. [133]

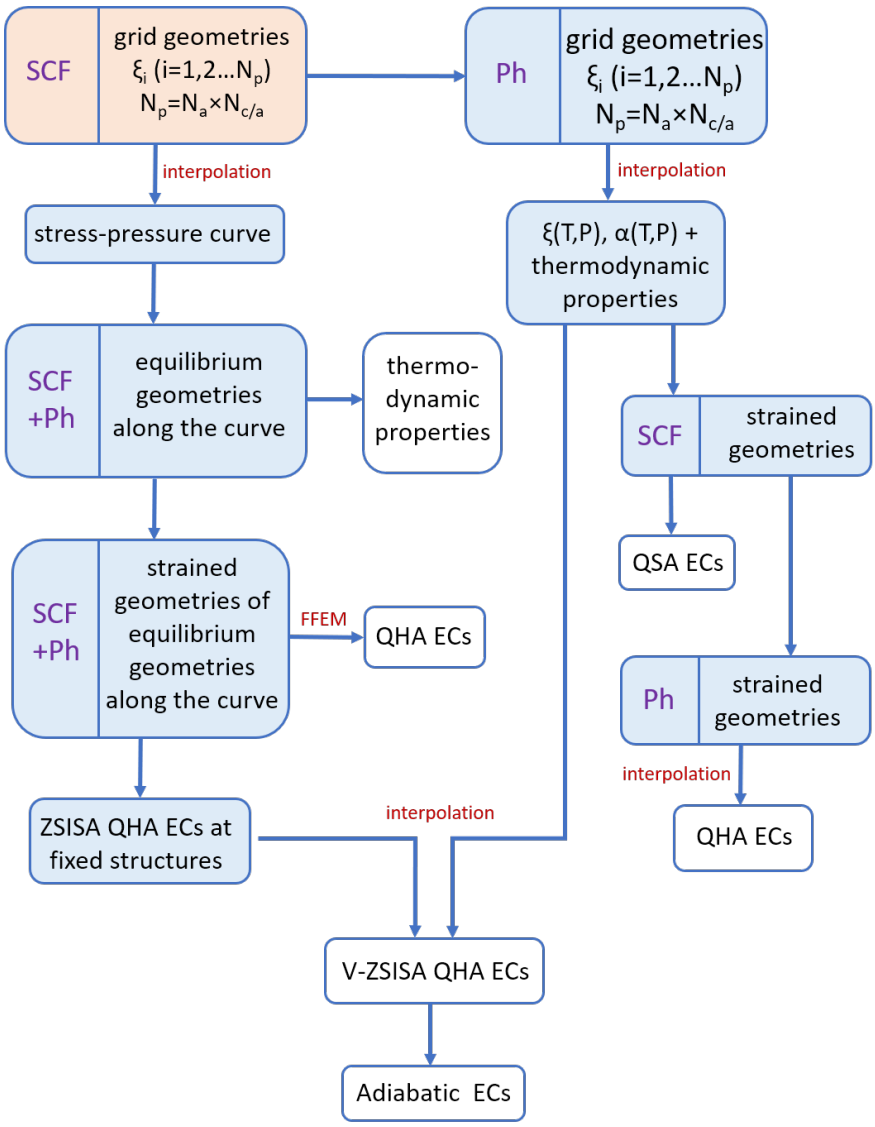

Figure C.6: The flowchart of elastic constants calculations of hcp metals in **thermo_pw**. "SCF" and "Ph" on the left side of the bar represent doing a self-consistent field (SCF) calculation of DFT energy and/or phonon calculations at the corresponding structures.

Appendix D

GPU and CUDA Fortran

The CUDA architecture is built around a scalable array of multithreaded Streaming Multiprocessors (SMs). Each SM has a set of execution units and a set of registers and can operate on variables contained in the GPU memory. CUDA Fortran allows the allocation of data on the GPU (called DEVICE in this context), the transfer of data from and to the GPU and the writing of routines that can run on the GPU (called GLOBAL or DEVICE), in many different threads, each one working on different data. This is possible also with OpenACC and openMP compiler directives we have opted for CUDA Fortran since in this moment there is a large basis of installed supercomputers equipped with NVIDIA GPUs that can run code written in CUDA Fortran and also the one available to us is in this category. The use of OpenACC and openMP that could be required to make our code transferable to GPUs of other vendors might be considered in the future if necessary.

In CUDA Fortran, to run on the GPU, one declares the routines with ATTRIBUTES(GLOBAL) or ATTRIBUTES(DEVICE). Both run on the GPU, but the first can be called from the CPU host with the triple chevron syntax (<<<,>>>) to specify the number of threads blocks and threads per block that are employed. In general thread blocks can be arranged in a three dimensional grid with variable size in each dimension. The second can be called from the GLOBAL routines on the data already selected for the current thread. CUDA makes four pieces of information available to each thread: the thread index (threadIdx), the block index (blockIdx), the size and shape of a block (blockDim), and the size and shape of a grid (gridDim). This information can be used to choose the variables the current thread will work on.

To give an order of magnitude, the Volta (Ampère) GPU architecture has 84 (108) SMs each capable of running up to 32 threads that is $32 \times 84 = 2688$ (3456) threads can run simultaneously on the GPU, however each thread block must run the same instructions on different data, while different thread blocks can execute different instructions. The code is independent from the GPU architecture on which it will run and can require even bigger grids and block sizes whose threads are run in sequence on the available SMs.

Bibliography

[1] Picture from https://en.wikipedia.org/wiki/Tensor.

[2] `OpenACC GPU` port of `VASP.6.2.0` is mentioned here: `https://www.vasp.at/wiki/index.php/OpenACC_GPU_port_of_VASP`.

[3] `GPU` support in `Abinit` is mentioned here: `https://docs.abinit.org/INSTALL_gpu`, 2024.

[4] N. L. Allan, T. H. K. Barron, and J. A. O. Bruno. The zero static internal stress approximation in lattice dynamics, and the calculation of isotope effects on molar volumes. *The Journal of Chemical Physics*, 105(18):8300–8303, Nov. 1996.

[5] P. B. Allen. Anharmonic phonon quasiparticle theory of zero-point and thermal shifts in insulators: Heat capacity, bulk modulus, and thermal expansion. *Physical Review B*, 92(6):064106, Aug. 2015.

[6] C. E. Anderson and F. R. Brotzen. Elastic constants of tantalum-tungsten alloys. *Journal of Applied Physics*, 53(1):292–297, Jan. 1982.

[7] E. Anderson, Z. Bai, C. Bischof, S. Blackford, J. Demmel, J. Dongarra, J. Du Croz, A. Greenbaum, S. Hammarling, A. McKenney, and D. Sorensen. *LAPACK Users' Guide*. Society for Industrial and Applied Mathematics, Philadelphia, PA, third edition, 1999.

[8] J. W. Arblaster. Thermodynamic properties of beryllium. *Journal of Phase Equilibria and Diffusion*, 37(5):581–591, 2016.

[9] J. W. Arblaster. Thermodynamic Properties of Tantalum. *Journal of Phase Equilibria and Diffusion*, 39(2):255–272, Apr. 2018.

[10] J. W. Arblaster. Thermodynamic Properties of Tungsten. *Journal of Phase Equilibria and Diffusion*, 39(6):891–907, Dec. 2018.

[11] I. Barin and G. Platzki. *Thermochemical data of pure substances*. VCH, Weinheim; New York, 1995.

[12] S. Baroni, S. de Gironcoli, A. Dal Corso, and P. Giannozzi. Phonons and related crystal properties from density-functional perturbation theory. *Reviews of Modern Physics*, 73(2):515–562, July 2001.

[13] S. Baroni, P. Giannozzi, and A. Testa. Green's-function approach to linear response in solids. *Physical Review Letters*, 58(18):1861–1864, May 1987.

[14] T. H. K. Barron and M. L. Klein. Second-order elastic constants of a solid under stress. *Proceedings of the Physical Society*, 85(3):523, 1965.

[15] C. Bercegeay and S. Bernard. First-principles equations of state and elastic properties of seven metals. *Physical Review B*, 72(21):214101, Dec. 2005.

[16] B. T. Bernstein. Elastic Properties of Polycrystalline Tungsten at Elevated Temperatures. *Journal of Applied Physics*, 33(6):2140–2140, June 1962.

[17] P. E. Blöchl. Projector augmented-wave method. *Physical Review B*, 50:17953–17979, Dec 1994.

[18] V. Y. Bodryakov. Correlation of temperature dependencies of thermal expansion and heat capacity of refractory metal up to the melting point: Molybdenum. *High Temperature*, 52(6):840–845, 2014.

[19] V. Y. Bodryakov. Correlation of temperature dependences of thermal expansion and heat capacity of refractory metal up to the melting point: Tungsten. *High Temperature*, 53(5):643–648, Sept. 2015.

[20] D. I. Bolef and J. De Klerk. Elastic Constants of Single-Crystal Mo and W between 77° and 500°K. *Journal of Applied Physics*, 33(7):2311–2314, July 1962.

[21] P. Bujard, R. Sanjines, E. Walker, J. Ashkenazi, and M. Peter. Elastic constants in Nb-Mo alloys from zero temperature to the melting point: experiment and theory. *Journal of Physics F: Metal Physics*, 11(4):775–786, 1981.

[22] C. Bungaro, S. de Gironcoli, and S. Baroni. Theory of the Anomalous Rayleigh Dispersion at H/W(110) Surfaces. *Physical Review Letters*, 77(12):2491–2494, Sept. 1996.

[23] S. M. Cardonne, P. Kumar, C. A. Michaluk, and H. D. Schwartz. Tantalum and its alloys. *International Journal of Refractory Metals and Hard Materials*, 13(4):187–194, 1995.

[24] P. Carrier, R. Wentzcovitch, and J. Tsuchiya. First-principles prediction of crystal structures at high temperatures using the quasiharmonic approximation. *Physical Review B*, 76(6):064116, Aug. 2007.

[25] C. Cazorla, M. J. Gillan, S. Taioli, and D. Alfè. Ab initio melting curve of molybdenum by the phase coexistence method. *The Journal of Chemical Physics*, 126(19):194502, 2007.

[26] C. Cazorla, M. J. Gillan, S. Taioli, and D. Alfè. Melting curve and Hugoniot of molybdenum up to 400 GPa by ab initio simulations. *Journal of Physics: Conference Series*, 121(1):012009, 2008.

[27] M. W. Chase and National Institute of Standards and Technology (U.S.). *NIST-JANAF thermochemical tables*. American Chemical Society ; American Institute of Physics for the National Institute of Standards and Technology, Maryland and New York, 1998.

[28] S. Chen and B. Brockhouse. Lattice vibrations of tungsten. *Solid State Communications*, 2(3):73–77, Mar. 1964.

[29] S.-H. Chen. *Neutron Scattering Studies of Lattice Vibrations in Metals*. PhD thesis, McMaster University, 1964.

[30] S. J. Clark, M. D. Segall, C. J. Pickard, P. J. Hasnip, M. I. J. Probert, K. Refson, and M. C. Payne. First principles methods using CASTEP. *Zeitschrift für Kristallographie - Crystalline Materials*, 220(5-6):567–570, 2005.

[31] R. E. Cohen and O. Gülseren. Thermal equation of state of tantalum. *Physical Review B*, 63(22):224101, 2001.

[32] H. Cynn and C.-S. Yoo. Equation of state of tantalum to 174 GPa. *Physical Review B*, 59(13):8526–8529, Apr. 1999.

[33] A. Dal Corso. Density-functional perturbation theory with ultrasoft pseudopotentials. *Physical Review B*, 64(23):235118, Nov. 2001.

[34] A. Dal Corso. Density functional perturbation theory within the projector augmented wave method. *Physical Review B*, 81(7):075123, Feb. 2010.

[35] A. Dal Corso. `pslibrary`. can be found at the webpage https://github.com/dalcorso/pslibrary, Mar. 2010.

[36] A. Dal Corso. Ab initio phonon dispersions of transition and noble metals: effects of the exchange and correlation functional. *Journal of Physics: Condensed Matter*, 25(14):145401, mar 2013.

[37] A. Dal Corso. Pseudopotentials periodic table: From H to Pu. *Computational Materials Science*, 95:337–350, 2014.

[38] A. Dal Corso. `thermo_pw`. can be found at the webpage https://github.com/dalcorso/thermo_pw, Mar. 2014.

[39] A. Dal Corso. Elastic constants of beryllium: a first-principles investigation. *Journal of Physics: Condensed Matter*, 28(7):075401, 2016.

[40] A. Dal Corso and S. de Gironcoli. Ab initio phonon dispersions of Fe and Ni. *Physical Review B*, 62(1):273–277, July 2000.

[41] D. Datta and M. S. Gordon. Accelerating coupled-cluster calculations with GPUs: An implementation of the density-fitted CCSD(t) approach for heterogeneous computing architectures using OpenMP directives. *Journal of Chemical Theory and Computation*, 19(21):7640–7657, 2023.

[42] E. R. Davidson. The iterative calculation of a few of the lowest eigenvalues and corresponding eigenvectors of large real-symmetric matrices. *Journal of Computational Physics*, 17(1):87–94, 1975.

[43] A. Debernardi, M. Alouani, and H. Dreyssé. *Ab initio* thermodynamics of metals: Al and W. *Physical Review B*, 63(6):064305, Jan. 2001.

[44] A. Dewaele, P. Loubeyre, and M. Mezouar. Equations of state of six metals above 94 GPa. *Physical Review B*, 70(9):094112, Sept. 2004.

[45] A. Dewaele, M. Torrent, P. Loubeyre, and M. Mezouar. Compression curves of transition metals in the mbar range: Experiments and projector augmented-wave calculations. *Physical Review B*, 78(10):104102, 2008.

[46] R. di Meo, A. Dal Corso, P. Giannozzi, and S. Cozzini. Calculation of Phonon Dispersions on the Grid Using Quantum ESPRESSO. 2009.

[47] J. M. Dickinson and P. E. Armstrong. Temperature dependence of the elastic constants of molybdenum. *Journal of Applied Physics*, 38(2):602–606, 1967.

[48] P. I. Dorogokupets and A. R. Oganov. Ruby, metals, and MgO as alternative pressure scales: A semiempirical description of shock-wave, ultrasonic, x-ray, and thermochemical data at high temperatures and pressures. *Physical Review B*, 75(2):024115, Jan. 2007.

[49] P. I. Dorogokupets, T. S. Sokolova, B. S. Danilov, and K. D. Litasov. Near-absolute equations of state of diamond, Ag, Al, Au, Cu, Mo, Nb, Pt, Ta, and W for quasi-hydrostatic conditions. *Geodynamics & Tectonophysics*, 3(2):129–166, 2012.

[50] L. Dubrovinsky, T. Boffa-Ballaran, K. Glazyrin, A. Kurnosov, D. Frost, M. Merlini, M. Hanfland, V. B. Prakapenka, P. Schouwink, T. Pippinger, and N. Dubrovinskaia. Single-crystal x-ray diffraction at megabar pressures and temperatures of thousands of degrees. *High Pressure Research*, 30(4):620–633, 2010.

[51] L. Dubrovinsky, N. Dubrovinskaia, E. Bykova, M. Bykov, V. Prakapenka, C. Prescher, K. Glazyrin, H.-P. Liermann, M. Hanfland, M. Ekholm, Q. Feng, L. V. Pourovskii, M. I. Katsnelson, J. M. Wills, and I. A. Abrikosov. The most incompressible metal osmium at static pressures above 750 gigapascals. *Nature*, 525(7568):226–229, 2015.

[52] W. J. Evans, M. J. Lipp, H. Cynn, C. S. Yoo, M. Somayazulu, D. Häusermann, G. Shen, and V. Prakapenka. X-ray diffraction and Raman studies of beryllium: Static and elastic properties at high pressures. *Physical Review B*, 72(9):094113, Sept. 2005.

[53] J.-L. Fattebert, C. F. A. Negre, J. Finkelstein, J. Mohd-Yusof, D. Osei-Kuffuor, M. E. Wall, Y. Zhang, N. Bock, and S. M. Mniszewski. Hybrid programming-model strategies for GPU offloading of electronic structure calculation kernels. *The Journal of Chemical Physics*, 160(12):122501, Mar. 2024.

[54] F. H. Featherston and J. R. Neighbours. Elastic Constants of Tantalum, Tungsten, and Molybdenum. *Physical Review*, 130(4):1324–1333, May 1963.

[55] M. Foata-Prestavoine, G. Robert, M.-H. Nadal, and S. Bernard. First-principles study of the relations between the elastic constants, phonon dispersion curves, and melting temperatures of bcc Ta at pressures up to 1000 GPa. *Physical Review B*, 76(10):104104, Sept. 2007.

[56] M. Frigo and S. G. Johnson. The design and implementation of FFTW3. *Proceedings of the IEEE*, 93(2):216–231, 2005. Special issue on "Program Generation, Optimization, and Platform Adaptation".

[57] G. Fugallo, M. Lazzeri, L. Paulatto, and F. Mauri. Ab initio variational approach for evaluating lattice thermal conductivity. *Physical Review B*, 88(4):045430, 2013.

[58] H. Fukui, A. Yoneda, S. Kamada, H. Uchiyama, N. Hirao, and A. Q. R. Baron. Single crystal elasticity and equation of state of tantalum up to 54 GPa. *Journal of Applied Physics*, 132(5):055902, Aug. 2022.

[59] P. Giannozzi, O. Andreussi, T. Brumme, O. Bunau, M. B. Nardelli, M. Calandra, R. Car, C. Cavazzoni, D. Ceresoli, M. Cococcioni, N. Colonna, I. Carnimeo, A. D. Corso, S. d. Gironcoli, P. Delugas, R. A. DiStasio, A. Ferretti, A. Floris, G. Fratesi, G. Fugallo, R. Gebauer, U. Gerstmann, F. Giustino, T. Gorni, J. Jia, M. Kawamura, H.-Y. Ko, A. Kokalj, E. Küçükbenli, M. Lazzeri, M. Marsili, N. Marzari, F. Mauri, N. L. Nguyen, H.-V. Nguyen, A. Otero-de-la Roza, L. Paulatto, S. Poncé, D. Rocca, R. Sabatini, B. Santra, M. Schlipf, A. P. Seitsonen, A. Smogunov, I. Timrov, T. Thonhauser, P. Umari, N. Vast, X. Wu, and S. Baroni. Advanced capabilities for materials modelling with quantum ESPRESSO. *Journal of Physics: Condensed Matter*, 29(46):465901, 2017.

[60] P. Giannozzi, S. Baroni, N. Bonini, M. Calandra, R. Car, C. Cavazzoni, D. Ceresoli, G. L. Chiarotti, M. Cococcioni, I. Dabo, A. D. Corso, S. d. Gironcoli, S. Fabris, G. Fratesi, R. Gebauer, U. Gerstmann, C. Gougoussis, A. Kokalj, M. Lazzeri, L. Martin-Samos, N. Marzari, F. Mauri, R. Mazzarello, S. Paolini, A. Pasquarello, L. Paulatto, C. Sbraccia, S. Scandolo, G. Sclauzero, A. P. Seitsonen, A. Smogunov,

P. Umari, and R. M. Wentzcovitch. QUANTUM ESPRESSO: a modular and open-source software project for quantum simulations of materials. *Journal of Physics: Condensed Matter*, 21(39):395502, Sept. 2009.

[61] P. Giannozzi, O. Baseggio, P. Bonfà, D. Brunato, R. Car, I. Carnimeo, C. Cavazzoni, S. de Gironcoli, P. Delugas, F. Ferrari Ruffino, A. Ferretti, N. Marzari, I. Timrov, A. Urru, and S. Baroni. Quantum ESPRESSO toward the exascale. *The Journal of Chemical Physics*, 152(15):154105, 04 2020.

[62] P. Giannozzi, S. de Gironcoli, P. Pavone, and S. Baroni. Ab initio calculation of phonon dispersions in semiconductors. *Physical Review B*, 43(9):7231–7242, Mar. 1991.

[63] X. Gong and A. Dal Corso. Ab initio quasi-harmonic thermoelasticity of molybdenum at high temperature and pressure. *The Journal of Chemical Physics*, 160(24):244703, June 2024.

[64] X. Gong and A. Dal Corso. High-temperature and high-pressure thermoelasticity of hcp metals from ab initio quasiharmonic free energy calculations: The beryllium case. *Physical Review B*, 110(9):094109, Sept. 2024.

[65] X. Gong and A. Dal Corso. Pressure and temperature dependent ab-initio quasi-harmonic thermoelastic properties of tungsten. *Journal of Physics: Condensed Matter*, 36(28):285702, Apr. 2024.

[66] X. Gong and A. Dal Corso. An alternative GPU acceleration for a pseudopotential plane-waves density functional theory code with applications to metallic systems. *Computer Physics Communications*, 308:109439, Mar. 2025.

[67] X. Gonze, B. Amadon, G. Antonius, F. Arnardi, L. Baguet, J.-M. Beuken, J. Bieder, F. Bottin, J. Bouchet, E. Bousquet, N. Brouwer, F. Bruneval, G. Brunin, T. Cavignac, J.-B. Charraud, W. Chen, M. Côté, S. Cottenier, J. Denier, G. Geneste, P. Ghosez, M. Giantomassi, Y. Gillet, O. Gingras, D. R. Hamann, G. Hautier, X. He, N. Helbig, N. Holzwarth, Y. Jia, F. Jollet, W. Lafargue-Dit-Hauret, K. Lejaeghere, M. A. L. Marques, A. Martin, C. Martins, H. P. C. Miranda, F. Naccarato, K. Persson, G. Petretto, V. Planes, Y. Pouillon, S. Prokhorenko, F. Ricci, G.-M. Rignanese, A. H. Romero, M. M. Schmitt, M. Torrent, M. J. van Setten, B. V. Troeye, M. J. Verstraete, G. Zérah, and J. W. Zwanziger. The abinit project: Impact, environment and recent developments. *Computer Physics Communications*, 248:107042, 2020.

[68] X. Gonze and C. Lee. Dynamical matrices, Born effective charges, dielectric permittivity tensors, and interatomic force constants from density-functional perturbation theory. *Physical Review B*, 55(16):10355–10368, Apr. 1997.

[69] P. Gordon. A high temperature precision x-ray camera: Some measurements of the thermal coefficients of expansion of beryllium. *Journal of Applied Physics*, 20(10):908–917, 1949.

[70] B. Grabowski, T. Hickel, and J. Neugebauer. Ab initio study of the thermodynamic properties of nonmagnetic elementary fcc metals: Exchange-correlation-related error bars and chemical trends. *Physical Review B*, 76:024309, Jul 2007.

[71] G. Grimvall, M. Thiessen, and A. F. Guillermet. Thermodynamic properties of tungsten. *Physical Review B*, 36(15):7816–7826, Nov. 1987.

[72] A. F. Guillermet and G. Grimvall. Analysis of thermodynamic properties of molybdenum and tungsten at high temperatures. *Physical Review B*, 44(9):4332–4340, Sept. 1991.

[73] O. Gülseren and R. E. Cohen. High-pressure thermoelasticity of body-centered-cubic tantalum. *Physical Review B*, 65(6):064103, Jan. 2002.

[74] Z.-C. Guo, F. Luo, X.-L. Zhang, C.-Y. Yuan, C.-A. Liu, and L.-C. Cai. First-principles calculations of elastic, phonon and thermodynamic properties of W. *Molecular Physics*, 114(23):3430–3436, Dec. 2016.

[75] P. Haas, F. Tran, and P. Blaha. Calculation of the lattice constant of solids with semilocal functionals. *Physical Review B*, 79:085104, Feb 2009.

[76] D. R. Hamann, M. Schlüter, and C. Chiang. Norm-conserving pseudopotentials. *Physical Review Letters*, 43(20):1494–1497, 1979.

[77] A. Hao and Y. Zhu. First-principle investigations of structural stability of beryllium under high pressure. *Journal of Applied Physics*, 112(2):023519, 2012.

[78] M. Hestenes and E. Stiefel. Methods of conjugate gradients for solving linear systems. *Journal of Research of the National Bureau of Standards*, 49(6):409, 1952.

[79] R. S. Hixson and J. N. Fritz. Shock compression of tungsten and molybdenum. *Journal of Applied Physics*, 71(4):1721–1728, Feb. 1992.

[80] P. Hohenberg and W. Kohn. Inhomogeneous electron gas. *Physical Review*, 136(3):B864–B871, 1964.

[81] J. W. Holladay. *Heat Capacity of Beryllium.* Defense Metals Information Center, Battelle Memorial Institute, 1959.

[82] X. Huang, F. Li, Q. Zhou, Y. Meng, K. D. Litasov, X. Wang, B. Liu, and T. Cui. Thermal equation of state of molybdenum determined from in situ synchrotron x-ray diffraction with laser-heated diamond anvil cells. *Scientific Reports*, 6(1):19923, 2016.

[83] W. P. Huhn, B. Lange, V. W.-z. Yu, M. Yoon, and V. Blum. GPU acceleration of all-electron electronic structure theory using localized numeric atom-centered basis functions. *Computer Physics Communications*, 254:107314, Sept. 2020.

[84] M. Hutchinson, P. Fleurat-Lessard, A. Anciaux-Sedrakian, D. Stosic, J. Bédorf, and S. Tariq. *Plane-Wave Density Functional Theory*, chapter 7, pages 135–172. John Wiley & Sons, Ltd, 2016.

[85] Innovative Computing Laboratory (ICL) and University of Tennessee. The highly efficient FFT for exascale (heFFTe) library, 2024.

[86] Innovative Computing Laboratory (ICL) and University of Tennessee. MAGMA, 2024.

[87] C.-J. W. Jian-Bing Gu and C.-J. W. Jian-Bing Gu. High-pressure structure and elastic properties of tantalum single crystal: First principles investigation. *Chinese Physics B*, 25(12):126103–126103, Dec. 2016.

[88] B. B. Karki, R. M. Wentzcovitch, S. de Gironcoli, and S. Baroni. *Science*, 286:1705, 1999.

[89] B. B. Karki, R. M. Wentzcovitch, S. de Gironcoli, and S. Baroni. High-pressure lattice dynamics and thermoelasticity of MgO. *Phys. Rev. B*, 61:8793, 2000.

[90] K. W. Katahara, M. H. Manghnani, and E. S. Fisher. Pressure derivatives of the elastic moduli of niobium and tantalum. *Journal of Applied Physics*, 47(2):434–439, Feb. 1976.

[91] K. W. Katahara, M. H. Manghnani, and E. S. Fisher. Pressure derivatives of the elastic moduli of BCC Ti-V-Cr, Nb-Mo and Ta-W alloys. *Journal of Physics F: Metal Physics*, 9(5):773–790, May 1979.

[92] K. W. Katahara, M. H. Manghnani, L. C. Ming, and E. S. Fisher. bcc transition metals under pressure: results from ultrasonic interferometry and diamond-cell experiments. [Nb–Mo, Ta–W]. Technical Report CONF-760716-4, Argonne National Lab., IL (USA), 1976.

[93] T. Katsura and Y. Tange. A simple derivation of the Birch–Murnaghan equations of state (EOSs) and comparison with EOSs derived from other definitions of finite strain. *Minerals*, 9(12):745, 2019.

[94] G. P. Kerker. Non-singular atomic pseudopotentials for solid state applications. *Journal of Physics C: Solid State Physics*, 13(9):L189, 1980.

[95] P. Keuter, D. Music, V. Schnabel, M. Stuer, and J. M. Schneider. From qualitative to quantitative description of the anomalous thermoelastic behavior of V, Nb, Ta, Pd and Pt. *Journal of Physics: Condensed Matter*, 31(22):225402, Mar. 2019.

[96] A. Khein, D. J. Singh, and C. J. Umrigar. All-electron study of gradient corrections to the local-density functional in metallic systems. *Physical Review B*, 51(7):4105–4109, Feb. 1995.

[97] R. K. Kirby, T. A. Hahn, and B. D. Rothrock. *American Institute of Physics Handbook 3rd edn*, volume 4. McGraw-Hill, New York, New York, USA, 1973.

[98] L. Kleinman and D. M. Bylander. Efficacious form for model pseudopotentials. *Physical Review Letters*, 48(20):1425–1428, 1982.

[99] L. Koči, Y. Ma, A. R. Oganov, P. Souvatzis, and R. Ahuja. Elasticity of the superconducting metals V, Nb, Ta, Mo, and W at high pressure. *Physical Review B*, 77(21):214101, June 2008.

[100] W. Kohn and L. J. Sham. Self-consistent equations including exchange and correlation effects. *Physical Review*, 140(4):A1133–A1138, 1965.

[101] L. Koči, Y. Ma, A. R. Oganov, P. Souvatzis, and R. Ahuja. Elasticity of the superconducting metals V, Nb, Ta, Mo, and W at high pressure. *Physical Review B*, 77(21):214101, June 2008.

[102] G. Kresse and D. Joubert. From ultrasoft pseudopotentials to the projector augmented-wave method. *Physical Review B*, 59(3):1758–1775, 1999.

[103] K. Kádas, L. Vitos, R. Ahuja, B. Johansson, and J. Kollár. Temperature-dependent elastic properties of α-beryllium from first principles. *Physical Review B*, 76(23):235109, 2007.

[104] S. B. Lang. *Sourcebook of pyroelectricity*, volume 2. CRC Press, 1974.

[105] A. Larose and B. N. Brockhouse. Lattice vibrations in tungsten at 22 °C studied by neutron scattering. *Canadian Journal of Physics*, 54(17):1819–1823, 1976.

[106] A. Lazicki, A. Dewaele, P. Loubeyre, and M. Mezouar. High-pressure–temperature phase diagram and the equation of state of beryllium. *Physical Review B*, 86(17):174118, 2012.

[107] M. Lazzeri and S. de Gironcoli. Ab-initio dynamical properties of the Be(0001) surface. *Surface Science*, 402–404:715–718, May 1998.

[108] R. G. Leisure, D. K. Hsu, and B. A. Seiber. Elastic properties of tantalum over the temperature range 4–300 K. *Journal of Applied Physics*, 44(8):3394–3397, Aug. 1973.

[109] K. D. Litasov, P. I. Dorogokupets, E. Ohtani, Y. Fei, A. Shatskiy, I. S. Sharygin, P. N. Gavryushkin, S. V. Rashchenko, Y. V. Seryotkin, Y. Higo, K. Funakoshi, A. D. Chanyshev, and S. S. Lobanov. Thermal equation of state and thermodynamic properties of molybdenum at high pressures. *Journal of Applied Physics*, 113(9):093507, 2013.

[110] K. D. Litasov, P. N. Gavryushkin, P. I. Dorogokupets, I. S. Sharygin, A. Shatskiy, Y. Fei, S. V. Rashchenko, Y. V. Seryotkin, Y. Higo, K. Funakoshi, and E. Ohtani. Thermal equation of state to 33.5 GPa and 1673 K and thermodynamic properties of tungsten. *Journal of Applied Physics*, 113(13):133505, Apr. 2013.

[111] J. Liu and P. B. Allen. Internal and external thermal expansions of wurtzite ZnO from first principles. *Computational Materials Science*, 154:251–255, Nov. 2018.

[112] W. Liu, Q. Liu, M. L. Whitaker, Y. Zhao, and B. Li. Experimental and theoretical studies on the elasticity of molybdenum to 12 GPa. *Journal of Applied Physics*, 106(4):043506, 2009.

[113] Z.-L. Liu, L.-C. Cai, X.-R. Chen, Q. Wu, and F.-Q. Jing. Ab initio refinement of the thermal equation of state for bcc tantalum: the effect of bonding on anharmonicity. *Journal of Physics: Condensed Matter*, 21(9):095408, 2009.

[114] S. G. Louie, S. Froyen, and M. L. Cohen. Nonlinear ionic pseudopotentials in spin-density-functional calculations. *Phys. Rev. B*, 26:1738–1742, Aug 1982.

[115] R. Lowrie and A. M. Gonas. Single-Crystal Elastic Properties of Tungsten from 24° to 1800°C. *Journal of Applied Physics*, 38(11):4505–4509, Oct. 1967.

[116] F. Luo, L.-C. Cai, X.-R. Chen, F.-Q. Jing, and D. Alfè. Ab initio calculation of lattice dynamics and thermodynamic properties of beryllium. *Journal of Applied Physics*, 111(5):053503, 2012.

[117] K. J. H. Mackay and N. A. Hill. Lattice parameter and hardness measurements on high purity beryllium. *Journal of Nuclear Materials*, 8(2):263–264, Mar. 1963.

[118] C. Malica and A. Dal Corso. Temperature-dependent atomic B factor: an ab initio calculation. *Acta Crystallographica Section A*, 75(4):624–632, 2019.

[119] C. Malica and A. Dal Corso. Quasi-harmonic temperature dependent elastic constants: applications to silicon, aluminum, and silver. *Journal of Physics: Condensed Matter*, 32(31):315902, 2020.

[120] C. Malica and A. Dal Corso. Temperature dependent elastic constants and thermodynamic properties of BAs: An ab initio investigation. *Journal of Applied Physics*, 127(24):245103, 2020.

[121] C. Malica and A. Dal Corso. Quasi-harmonic thermoelasticity of palladium, platinum, copper, and gold from first principles. *Journal of Physics: Condensed Matter*, 33(47):475901, 2021.

[122] C. Malica and A. Dal Corso. Finite-temperature atomic relaxations: Effect on the temperature-dependent C44 elastic constants of Si and BAs. *The Journal of Chemical Physics*, 156(19):194111, May 2022.

[123] F. Mandl. American Institute of Physics Handbook 3rd edn. *Physics Bulletin*, 24(8):492–492, Aug. 1973.

[124] R. Masuki, T. Nomoto, R. Arita, and T. Tadano. Full optimization of quasiharmonic free energy with an anharmonic lattice model: Application to thermal expansion and pyroelectricity of wurtzite GaN and ZnO. *Physical Review B*, 107(13):134119, Apr. 2023.

[125] M. A. Mathis, A. Khanolkar, L. Fu, M. S. Bryan, C. A. Dennett, K. Rickert, J. M. Mann, B. Winn, D. L. Abernathy, M. E. Manley, D. H. Hurley, and C. A. Marianetti. Generalized quasiharmonic approximation via space group irreducible derivatives. *Physical Review B*, 106(1):014314, July 2022.

[126] H. Mei, F. Wang, J. Li, and L. Kong. Elastic anisotropy and its temperature dependence for cubic crystals revealed by molecular dynamics simulations. *Modelling and Simulation in Materials Science and Engineering*, 31(6):065013, 2023.

[127] Message Passing Interface Forum. *MPI: A Message-Passing Interface Standard Version 4.0*, jun 2021.

[128] M. Methfessel and A. T. Paxton. High-precision sampling for brillouin-zone integration in metals. *Physical Review B*, 40:3616–3621, Aug 1989.

[129] A. Migliori, H. Ledbetter, D. J. Thoma, and T. W. Darling. Beryllium's monocrystal and polycrystal elastic constants. *Journal of Applied Physics*, 95(5):2436–2440, 2004.

[130] A. P. Miiller and A. Cezairliyan. Thermal expansion of molybdenum in the range 1500–2800 k by a transient interferometric technique. *International Journal of Thermophysics*, 6(6):695–704, 1985.

[131] A. P. Miiller and A. Cezairliyan. Thermal expansion of tungsten in the range 1500-3600 K by a transient interferometric technique. *International Journal of Thermophysics*, 11(4):619–628, July 1990.

[132] L. Ming and M. H. Manghnani. Isothermal compression of bcc transition metals to 100 kbar. *Journal of Applied Physics*, 49(1):208–212, Jan. 1978.

[133] M.-H. Nadal and L. Bourgeois. Elastic moduli of beryllium versus temperature: Experimental data updating. *Journal of Applied Physics*, 108(3):033512, Aug. 2010.

[134] K. Nakano, Y. Akahama, and H. Kawamura. X-ray diffraction study of Be to megabar pressure. *Journal of Physics: Condensed Matter*, 14(44):10569, Oct. 2002.

[135] R. E. Newnham. *Properties of Materials: Anisotropy, Symmetry, Structure.* Oxford University Press, Oxford, New York, Jan. 2005.

[136] F. C. Nix and D. MacNair. The Thermal Expansion of Pure Metals. II: Molybdenum, Palladium, Silver, Tantalum, Tungsten, Platinum, and Lead. *Phys. Rev.*, 61(1-2):74–78, Jan. 1942.

[137] Nvidia Corp. The cufft device extensions (cufftdx) library, 2022.

[138] Nvidia Corp. *NVIDIA HPC SDK Version 23.7 Documentation*, 2023.

[139] Nvidia Corp. cuBLAS, the cuda basic linear algebra subroutine library, 2024.

[140] NVIDIA Corp. cuFFT API Reference v12.4, 2024.

[141] Nvidia Corp. cuSOLVER, a gpu accelerated library for decompositions and linear system solutions for both dense and sparse matrices, 2024.

[142] NVIDIA Corp., P. Vingelmann, and F. H. Fitzek. CUDA, release: 10.2.89, 2020.

[143] J. F. Nye. *Physical properties of crystals.* Oxford science publications, 1985.

[144] J. F. Nye. *Physical Properties of Crystals: Their Representation by Tensors and Matrices.* Oxford University Press, 1985.

[145] OpenACC-Standard.org. The openacc application programming interface ver 3.3, 2022.

[146] D. Orlikowski, P. Söderlind, and J. A. Moriarty. First-principles thermoelasticity of transition metals at high pressure: Tantalum prototype in the quasiharmonic limit. *Physical Review B*, 74(5):054109, Aug. 2006.

[147] M. Palumbo and A. Dal Corso. Lattice dynamics and thermophysical properties of h.c.p. Os and Ru from the quasi-harmonic approximation. *Journal of Physics: Condensed Matter*, 29(39):395401, Aug. 2017.

[148] M. Palumbo and A. Dal Corso. Lattice dynamics and thermophysical properties of h.c.p. Re and Tc from the quasi-harmonic approximation. *Physica Status Solidi (b)*, 254(9):1700101, 2017.

[149] J. P. Perdew, K. Burke, and M. Ernzerhof. Generalized gradient approximation made simple. *Physical Review Letters*, 77:3865–3868, Oct 1996.

[150] J. P. Perdew, A. Ruzsinszky, G. I. Csonka, O. A. Vydrov, G. E. Scuseria, L. A. Constantin, X. Zhou, and K. Burke. Restoring the density-gradient expansion for exchange in solids and surfaces. *Physical Review Letters*, 100:136406, Apr 2008.

[151] J. P. Perdew and Y. Wang. Accurate and simple analytic representation of the electron-gas correlation energy. *Physical Review B*, 45(23):13244–13249, 1992.

[152] J. P. Perdew and A. Zunger. Self-interaction correction to density-functional approximations for many-electron systems. *Physical Review B*, 23:5048–5079, May 1981.

[153] V. Philipps. Tungsten as material for plasma-facing components in fusion devices. *Journal of Nuclear Materials*, 415(1, Supplement):S2–S9, Aug. 2011.

[154] W. E. Pickett. Pseudopotential methods in condensed matter applications. *Computer Physics Reports*, 9(3):115–197, 1989.

[155] B. M. Powell, P. Martel, and A. D. B. Woods. Lattice dynamics of niobium-molybdenum alloys. *Physical Review*, 171(3):727–736, 1968.

[156] W. H. Press, S. A. Teukolsky, W. T. Vetterling, and B. P. Flannery. *Numerical recipes in FORTRAN 90: the art of parallel scientific computing.* Cambridge University Press, 2nd ed edition, 1996.

[157] X. Qi, N. Cai, T. Chen, S. Wang, and B. Li. Experimental and theoretical studies on the elasticity of tungsten to 13 GPa. *Journal of Applied Physics*, 124(7):075902, Aug. 2018.

[158] X. Qi, N. Cai, S. Wang, and B. Li. Thermoelastic properties of tungsten at simultaneous high pressure and temperature. *Journal of Applied Physics*, 128(10):105105, Sept. 2020.

[159] X. Qi, S. Wang, S. Chen, N. Cai, and B. Li. Anomalous elastic behavior of tantalum at high pressures: Experimental and theoretical studies. *International Journal of Refractory Metals and Hard Materials*, 101:105691, Dec. 2021.

[160] A. M. Rappe, K. M. Rabe, E. Kaxiras, and J. D. Joannopoulos. Optimized pseudopotentials. *Physical Review B*, 41(2):1227–1230, 1990. Publisher: American Physical Society.

[161] G. Robert, P. Legrand, and S. Bernard. Multiphase equation of state and elastic moduli of solid beryllium from first principles. *Physical Review B*, 82(10):104118, Sept. 2010.

[162] G. Robert and A. Sollier. Equation of state and elastic properties of beryllium from first principles calculations. *Journal de Physique IV (Proceedings)*, 134:257–262, Aug. 2006.

[163] J. Romero, E. Phillips, G. Ruetsch, M. Fatica, F. Spiga, and P. Giannozzi. A Performance Study of Quantum ESPRESSO's PWscf Code on Multi-core and GPU Systems. In S. Jarvis, S. Wright, and S. Hammond, editors, *High Performance Computing Systems. Performance Modeling, Benchmarking, and Simulation*, pages 67–87, Cham, 2018. Springer International Publishing.

[164] S. Rostami and X. Gonze. Approximations in first-principles volumetric thermal expansion determination. *Physical Review B*, 110(1):014103, July 2024.

[165] W. D. Rowlands and J. S. White. The determination of the elastic constants of beryllium in the temperature range 25 to 300 °C. *Journal of Physics F: Metal Physics*, 2(2):231, 1972.

[166] A. L. Ruoff, C. O. Rodriguez, and N. E. Christensen. Elastic moduli of tungsten to 15 Mbar, phase transition at 6.5 Mbar, and rheology to 6 Mbar. *Physical Review B*, 58(6):2998–3002, Aug. 1998.

[167] S. Y. Savrasov and D. Y. Savrasov. Electron-phonon interactions and related physical properties of metals from linear-response theory. *Physical Review B*, 54(23):16487–16501, 1996.

[168] L. Schimka, R. Gaudoin, J. Klimeš, M. Marsman, and G. Kresse. Lattice constants and cohesive energies of alkali, alkaline-earth, and transition metals: Random phase approximation and density functional theory results. *Physical Review B*, 87(21):214102, 2013.

[169] O. Schütt, P. Messmer, J. Hutter, and J. VandeVondele. *GPU-Accelerated Sparse Matrix–Matrix Multiplication for Linear Scaling Density Functional Theory*, chapter 8, pages 173–190. John Wiley & Sons, Ltd, 2016.

[170] J. Shah and M. Straumanis. Thermal expansion of tungsten at low temperatures. *Journal of Applied Physics*, 42(9):3288–3289, 1971.

[171] T. Shao, B. Wen, R. Melnik, S. Yao, Y. Kawazoe, and Y. Tian. Temperature dependent elastic constants for crystals with arbitrary symmetry: Combined first principles and continuum elasticity theory. *Journal of Applied Physics*, 111(8):083525, 2012.

[172] G. V. Sin'ko and N. A. Smirnov. Relative stability and elastic properties of hcp, bcc, and fcc beryllium under pressure. *Physical Review B*, 71(21):214108, 2005.

[173] J. F. Smith and C. L. Arbogast. Elastic constants of single crystal beryllium. *Journal of Applied Physics*, 31(1):99–102, 1960.

[174] M. Smith, A. Tamerus, and P. Hasnip. Portable acceleration of materials modeling software: CASTEP, GPUs, and OpenACC. *Computing in Science & Engineering*, 24(1):46–55, 2022.

[175] P. Söderlind and J. A. Moriarty. First-principles theory of Ta up to 10 Mbar pressure: Structural and mechanical properties. *Physical Review B*, 57(17):10340–10350, May 1998.

[176] N. Soga. Comparison of Measured and Predicted Bulk Moduli of Tantalum and Tungsten at High Temperatures. *Journal of Applied Physics*, 37(9):3416–3420, Aug. 1966.

[177] T. S. Sokolova, P. I. Dorogokupets, and K. D. Litasov. Self-consistent pressure scales based on the equations of state for ruby, diamond, mgo, b2–nacl, as well as au, pt, and other metals to 4 mbar and 3000 k. *Russian Geology and Geophysics*, 54(2):181–199, 2013.

[178] H.-F. Song and H.-F. Liu. Modified mean-field potential approach to thermodynamic properties of a low-symmetry crystal: Beryllium as a prototype. *Physical Review B*, 75(24):245126, 2007.

[179] F. Spiga and I. Girotto. phiGEMM: A CPU-GPU Library for Porting Quantum ESPRESSO on Hybrid Systems. In *2012 20th Euromicro International Conference on Parallel, Distributed and Network-based Processing*, pages 368–375, Feb. 2012.

[180] R. Stedman, Z. Amilius, R. Pauli, and O. Sundin. Phonon spectrum of beryllium at 80K. *Journal of Physics F: Metal Physics*, 6(2):157–166, 1976.

[181] S. Taioli, C. Cazorla, M. J. Gillan, and D. Alfè. Melting curve of tantalum from first principles. *Physical Review B*, 75(21):214103, 2007.

[182] M. P. Teter, M. C. Payne, and D. C. Allan. Solution of schr\"odinger's equation for large systems. *Physical Review B*, 40(18):12255–12263, 1989.

[183] B. Thakur, X. Gong, and A. Dal Corso. Ab initio thermodynamic properties of iridium: A high-pressure and high-temperature study. *Computational Materials Science*, 234:112797, 2024.

[184] B. Thakur, X. Gong, and A. Dal Corso. Thermodynamic properties of rhodium—a first principle study. *AIP Advances*, 14(4):045229, 2024.

[185] Y. S. Touloukian, R. K. Kirby, R. E. Taylor, and P. D. Desai. *Thermal Expansion: Metallic Elements and Alloys*. Springer, New York, 1975 edition, 2014.

[186] N. Troullier and J. L. Martins. Efficient pseudopotentials for plane-wave calculations. *Physical Review B*, 43(3):1993–2006, Jan. 1991.

[187] D. Valent and P. Swarztrauber. FFTPACK 5.1, 2022.

[188] D. Vanderbilt. Soft self-consistent pseudopotentials in a generalized eigenvalue formalism. *Physical Review B*, 41:7892–7895, Apr 1990.

[189] E. Walker and P. Bujard. Anomalous temperature behaviour of the shear elastic constant C_{44} in tantalum. *Solid State Communications*, 34(8):691–693, May 1980.

[190] R. C. Walker and A. W. Götz, editors. *Electronic Structure Calculations on Graphics Processing Units: From Quantum Chemistry to Condensed Matter Physics*. John Wiley & Sons, Ltd, 2016.

[191] D. C. Wallace. *Thermodynamics of Crystals*. Dover Publications, 1998.

[192] Y. Wang, D. Chen, and X. Zhang. Calculated Equation of State of Al, Cu, Ta, Mo, and W to 1000 GPa. *Physical Review Letters*, 84(15):3220–3223, Apr. 2000.

[193] Y. Wang, J. J. Wang, H. Zhang, V. R. Manga, S. L. Shang, L.-Q. Chen, and Z.-K. Liu. A first-principles approach to finite temperature elastic constants. *J. Phys.: Condens. Matter*, 22:225404, 2010.

[194] G. K. White and S. J. Collocott. Heat Capacity of Reference Materials: Cu and W. *Journal of Physical and Chemical Reference Data*, 13(4):1251–1257, Oct. 1984.

[195] J. Wu, F. González-Cataldo, and B. Militzer. High-pressure phase diagram of beryllium from ab initio free-energy calculations. *Physical Review B*, 104(1):014103, 2021.

[196] S. Xiang, F. Xi, Y. Bi, J. Xu, H. Geng, L. Cai, F. Jing, and J. Liu. *Ab initio* thermodynamics beyond the quasiharmonic approximation: W as a prototype. *Physical Review B*, 81(1):014301, Jan. 2010.

[197] J. Zarestky, C. Stassis, B. N. Harmon, K. M. Ho, and C. L. Fu. Temperature dependence of the vibrational modes of molybdenum. *Physical Review B*, 28(2):697–701, 1983.

[198] Z.-Y. Zeng, C.-E. Hu, L.-C. Cai, X.-R. Chen, and F.-Q. Jing. Lattice dynamics and thermodynamics of molybdenum from first-principles calculations. *The Journal of Physical Chemistry B*, 114(1):298–310, 2010.

[199] Z.-Y. Zeng, C.-E. Hu, X.-R. Chen, X.-L. Zhang, L.-C. Cai, and F.-Q. Jing. Density functional theory investigation of the phonon instability, thermal equation of state and melting curve of mo. *Phys. Chem. Chem. Phys.*, 13(4):1669–1675, 2011.

[200] Z.-Y. Zeng, C.-E. Hu, W. Zhang, Z.-W. Niu, and L.-C. Cai. Dynamical stability of mo under high pressure and high temperature. *Journal of Applied Physics*, 116(13):133518, 2014.

[201] Y. Zhao, A. C. Lawson, J. Zhang, B. I. Bennett, and R. B. Von Dreele. Thermoelastic equation of state of molybdenum. *Physical Review B*, 62(13):8766–8776, 2000.

Acknowledgments

I'm greatly indebted to my supervisor Prof. Dr. Andrea Dal Corso who made this thesis possible. He provided me his scientific insights, knowledge, guidance, and continuous corrections always with patience.

Many thanks to all professors in condensed matter area in SISSA for teaching me advanced physics courses. In particular, I would like to express my sincere gratitude to the student secretaries for their kind help during my stay in Trieste. I thank all the students I have met in the last four years.

I also want to show my deep appreciation and concern to my parents in the distance.

The final thanks go to my best friends Hang in Trieste, Yibo and Lei in Leuven, Binjiao in Shenzhen and Qihan in Shanghai who share all my joys and sorrows.